Propulsion System Concepts for Silent Aircraft

by

Alexis Manneville

B.S., Ecole Polytechnique (France), 2001

Submitted to the Department of Aeronautics and Astronautics
in partial fulfillment of the requirements for the degree of

MASTER OF SCIENCE IN AERONAUTICS AND ASTRONAUTICS

at the

MASSACHUSETTS INSTITUTE OF TECHNOLOGY

June 2004

Author_____
Department of Aeronautics and Astronautics
May 21, 2004

Certified by_____
Professor Zoltán Spakovszky
C.R. Soderberg Assistant Professor of Aeronautics and Astronautics
Thesis Supervisor

Accepted by_____
Professor Edward M. Greitzer
H.N. Slater Professor of Aeronautics and Astronautics
Chairman, Committee on Graduate Students

Propulsion System Concepts for Silent Aircraft

by

Alexis Manneville

Submitted to the Department of Aeronautics and Astronautics
on May 21, 2004, in partial fulfillment of the
requirements for the degree of
Master of Science in Aeronautics and Astronautics

Abstract

The noise emitted by commercial aircraft is a major inhibitor of the growth of commercial air transport and is a critical environmental issue in air transportation.

A functionally-silent aircraft is envisioned to achieve a step change in airframe and propulsion system noise reduction (30 EPNdB). This thesis addresses the assessment of low-noise propulsion system concepts suggested to enable such a functionally-silent aircraft.

The propulsion system concepts of ultra-high bypass ratio turbofan engines, a distributed propulsion system, and silent engine air-brakes are evaluated in light of their noise signatures and propulsion system performance. These propulsion system concepts are assessed using simple analytic models and existing semi-empirical noise prediction methods.

Ultra-high bypass ratio turbofan engine cycles are predicted to achieve the 30 dB jet noise reduction goal. This noise reduction is possible with bypass ratios of order 70 for separate flow exhaust nozzles and of order 40 for a mixed flow exhaust nozzle. Such large bypass ratios result in a significant decrease in specific fuel consumption. However, the cost for a step change in jet noise reduction is a dramatic drop in specific thrust which requires larger engine diameters, and hence yields penalties in weight and installation drag. For a given noise goal, the study shows that an advanced technology engine cycle achieves a specific thrust similar to current technology engine cycles but enables a lower specific fuel consumption.

In order to embed such ultra-high bypass ratio engines in a blended-wing-body airframe, a distributed propulsion system consisting of 10 core engines driving a total number of 30 fans via gearboxes and shafts is suggested. A feasibility study shows that this configuration can achieve the noise reduction goal with a trade-off between transmission losses, gearbox weight, and turbomachinery losses. Such a propulsion system allows to exhaust the low speed jet along the trailing edge of the wing in a single high-aspect ratio nozzle. This exhaust system integrated in the airframe is predicted to entail a 5% loss in thrust but suggests an additional 4 dB reduction in perceived jet noise.

To achieve a quiet descent without high-drag devices, an engine air-brake system with variable geometry turbomachinery is suggested to control changes in impulse of the air flow through the propulsion system. For a blended-wing-body aircraft in clean configuration, the drag generated by the air-brake system enables an approach on a 4.5° glide slope angle at 84 m/s. On a preliminary basis it is found that the low fan rotational speeds of the engine air-brake yield a 10 dB reduction in fan noise on approach.

A distributed propulsion system with engine air-brake capability is delineated and a total reduction in jet noise of 34 EPNdB is predicted at takeoff. On approach, a reduction in airframe noise of 32 EPNdB is estimated for a blended-wing-body aircraft with aerodynamically smooth lifting surfaces, boundary layer ingestion, and silent engine air-brakes.

Thesis Supervisor: Professor Zoltán Spakovszky
Title: C.R. Soderberg Assistant Professor of Aeronautics and Astronautics

Acknowledgments

This research has been a challenging but most rewarding experience. It would not have been possible without the help of many people.

First, I would like to thank my advisor Professor Zoltán Spakovszky for his invaluable guidance and encouragement throughout my research and the writing of this thesis.

I would like to acknowledge Déborah Pilczer who began the research on a functionally-silent aircraft. Her work and her assistance in running ANOPP have been very valuable for my research. I am also very grateful to Justin Jaworski for his insightful and thorough suggestions during the writing of this thesis. I wish him luck in the continuation of this research project.

I acknowledge Professor Drela for his assistance in running MISES and MTFLOW, and Professor Darmofal who provided the data from the wind tunnel tests of the blended-wing-body aircraft model. I would like to thank Robert Liebeck for sharing his valuable knowledge of the blended-wing-body aircraft.

This work was funded by NASA Langley Research Center under grant NAS 1-02044 Dr. Russel H. Thomas contract monitor. This support is gratefully acknowledged.

I am grateful to the professors and students of the MIT Gas Turbine Laboratory, thanks to whom I have discovered various fascinating aspects of aeronautics. I would like to thank my officemates, particularly Vincent, Déborah, Justin, Josep, Boris, and Parthiv for their friendship and cheerfulness. I am also deeply grateful to all of my friends from MIT who made Boston a great place to live.

Finally, I would like to thank my family and friends for their support. They have continually encouraged and trusted me throughout the years.

And last, but certainly not least, I thank Marine for her wholehearted support and affection.

Contents

List of Figures

List of Tables

Nomenclature

Roman

A	Flow-path or jet area
$\dot{m}$	Mass flow rate
P_t	Total pressure
P	Static pressure
T_t	Total temperature
T	Static temperature
c	Speed of sound
V	Flow velocity
u	Axial flow velocity
M	Mach number
N_f	Number of fans
N_j	Number of jets
D	in Chapter 3, fan or jet diameter; in Chapter 4, Drag
L	Lift
T or F	Thrust
f	frequency
St	Strouhal number
Re	Reynolds number
V_s	Aircraft stall velocity
u_0	Aircraft flight velocity
L	Nozzle axial length
C_D	in Chapter 4, Drag coefficient; in Chapter 3 and Appendix B, Nozzle discharge coefficient
C_L	Lift coefficient
C_{fg}	Nozzle gross thrust coefficient
$C_{SD_{req}}$	Required Silent Drag coefficient
$C_{D_{fan}}$	Drag coefficient based on the fan inlet area

C_p	Pressure coefficient
U	Blade speed
r	With subscript, radius; Alone, blade hub-to-rip ratio
W	Acoustic power

Greek

α	in Chapter 4, angle of attack; in Appendix A, bypass ratio
π	Total Pressure ratio across the component indicated in subscript
τ	Total Temperature ratio across the component indicated in subscript
η	Polytropic efficiency of the component indicated in subscript
θ	Approach profile glide slope angle
Ψ	Blade loading coefficient
Φ	Blade flow parameter
σ	in Sections 4.3 and 4.4, blade row solidity at meanline; in Section 4.2, wing loading
γ	Blade row stagger angle at meanline
ρ	Flow density

Subscripts

$_a$	quantity at ambient conditions
$_d$	behind π: inlet total pressure recovery
$_b$	relative to the combustor
$_{nc}$	relative to the core nozzle
$_{nb}$	relative to the bypass nozzle
$_r$ or $_{des}$	reference quantity computed at design point

Acronyms

ANOPP	Aircraft Noise Prediction Program
TSFC	Thrust Specific Fuel Consumption
ST	Specific Thrust
SPL	Sound Pressure Level

OASPL	Overall Sound Pressure Level
EPNL	Effective Perceived Noise Level
EPNdB	Effective Perceived Noise Level Decibels
BPR	Bypass Ratio
FPR	Fan Pressure Ratio ($= \pi_{LPC} \cdot \pi_{HPC}$)
OPR	Overall Pressure Ratio
UHBPR	Ultra-High Bypass Ratio
AR	Aspect Ratio
HARN	High Aspect Ratio Nozzle
NPR	Nozzle Pressure Ratio
DEN	Distributed Exhaust Nozzle
LPC	Low-Pressure Compressor
HPC	High-Pressure Compressor
HPT	High-Pressure Turbine
LPT	Low-Pressure Turbine
TOGW	Take-off Gross Weight

Stations Numbering

Cycle Analysis

0	Far field - Ambient conditions
2	Fan inlet
2.5	LPC exit / HPC inlet
3	HPC exit / Combustor inlet
4	Combustor exit / HPT inlet
4.5	HPT exit / LPT inlet
6	LPT exit / Core exhaust nozzle throat or mixer inlet
8	Fan exit / Bypass exhaust nozzle throat or mixer inlet
Mix	Mixer exit
9	Mixed flow exhaust nozzle

High Aspect Ratio Nozzle

0	Nozzle inlet

1	Nozzle exit

Windmilling Engine Air-Brake

0	Far field - Ambient conditions
1	Rotor blade-row inlet
2	Rotor blade-row exit
8	Nozzle exit

Chapter 1

Introduction

1.1 The Silent Aircraft Initiative

1.1.1 Motivation and Objectives

Since the beginning of the turbojet engine era in the 1950s, noise emitted by commercial aircraft has been one of the most critical environmental issues associated with air transportation. The development of high bypass ratio turbofan engines, simultaneously driven by the need for improved aircraft performance and more stringent noise regulations, led to significant noise reductions. As a result, the number of people living in areas exposed to unacceptably high aircraft noise in the USA has dropped significantly, from more than 7 million in 1975 to approximately 600,000 in the year 2000 (Erickson (2000)). However, air traffic growth tends to offset these benefits, and a surge in the number of noise abatement procedures and curfews imposed on airports or penalties to airlines has been recently observed (Huff (2000)). Local communities often object to any airport expansion that would increase their exposure to aircraft noise. In the future, these constraints are likely to become a major inhibitor of the growth of air transport. More stringent regulations will be required to preserve the environment and the quality of life of people living in the vicinity of airports.

Within this context, there is an incentive to achieve a revolutionary step in aircraft noise reduction. This is the objective of the "Silent Aircraft Initiative". By definition, noise levels emitted by a "Silent Aircraft" are such that its operations are not perceived as annoying or intrusive by the community. Considering background noise levels in typical well-populated areas (60 to 65 dB), this objective requires a reduction of 25 to 30 dB compared to current aircraft noise levels.

Such an aircraft is envisioned to

1. greatly improve the quality of life in the neighborhood of airports by suppressing noise pollution at its source, and

2. transform commercial air transportation by relieving operational constraints and costs associated with noise.

This enables further traffic growth by abolishing curfews and making nighttime operations possible. Many economical advantages are expected. For example, the value of real estate close to airports is expected to greatly improve. Soundproofing expenses can be alleviated. Assuming that related safety issues can be solved, airports can be moved closer to city centers, saving time and ground transportation expenses for millions of travelers each year.

There are many technical challenges posed by these ambitious goals. Aircraft are traditionally developed to meet performance and cost requirements. Environmental issues are considered secondary as long as constraints imposed by regulations can be satisfied. This explains the incremental reduction of noise emissions observed in the aviation history. New progressively introduced technologies typically allow noise reductions of the order of 3 to 5 dB. In order to achieve noise emission levels enabling a "Silent Aircraft", significant changes in aircraft and propulsion system design are required. Noise must be included early as a prime design variable in a multidisciplinary design process. Unconventional configurations and new technologies must be considered. Innovative concepts must be invented and their feasibility assessed. In order to significantly reduce propulsion system noise, jet velocities and fan rotational speeds have to be dramatically reduced. This inevitably requires higher bypass ratio engines. Integration issues associated with such large engines must be addressed at the system level (weight and drag penalties). Assuming that propulsion system noise levels meet the reduction target for a "Silent Aircraft", airframe noise becomes the dominant noise source. Significantly reducing this noise component inevitably requires new airframe configurations. An aircraft capable of safely landing without deploying noisy devices such as flaps and slats is envisioned. Increasing the glide slope angle on approach can further reduce the noise perceived on the ground. This imposes challenging operational constraints. To achieve these goals, it is clear that airframe and engines must be much more closely integrated than it is currently done on commercial aircraft.

This thesis attempts to assess concepts enabling a low-noise propulsion system and to delineate design implications for a functionally-silent aircraft.

1.1.2 Previous Results

Previous research undertaken within the framework of the "Silent Aircraft Initiative" has been carried out by Pilczer (2003). This work focused on:

- assessing concepts enabling a step change in airframe noise reduction. Pilczer (2003) designates these ideas as "Quiet Lift" concepts.
- delineating preliminary design implications of "Quiet Lift" concepts for a functionally-silent

aircraft.

Review of "Quiet Lift" Concepts

Aerodynamically-Smooth Lifting Surfaces. In current aircraft designs, high-lift devices such as flaps and slats are deployed in the approach configuration. This entails discontinuities in the spanwise lift distribution that generate noisy flow structures.

To alleviate this airframe noise component, a blended-wing body type aircraft with aerodynamically-smooth lifting surfaces is envisioned. Wing self-noise generated by turbulent flow structures scattered at the wing trailing edge and wing-tip edge then becomes the dominant airframe noise source.

According to Pilczer (2003), a blended-wing body configuration with aerodynamically-smooth lifting surfaces is suggested to yield a 28 EPNdB reduction for a standard approach path. An additional reduction of 6 EPNdB can be achieved by following a 9° glide slope angle.

Hidden Trailing Edge and Boundary Layer Ingestion. An integrated engine-wing trailing edge design is envisioned to ingest boundary layer fluid from the suction and pressure sides of the wing through mail-slot inlets. "Hiding" the wing trailing edge inhibits the scattering of the relatively thick wing boundary layers at the trailing edge, thus further reducing airfoil self-noise emissions. The ingestion of high entropy fluid by the propulsion system detrimentally increases the specific fuel consumption but reduces the airframe wake size. As suggested by Ko et al. (2003) and Hanlon (2003), this can yield improvements in overall efficiency and have a beneficial impact on flight range.

Pilczer (2003) shows that the hidden trailing edge concept enables an additional reduction of 3 EPNdB in trailing edge noise. This is achieved for an optimum mail-slot spanwise extent of 60% of the aircraft span. This configuration yields a 5% improvement in range.

Design Implications

A blended-wing body type aircraft with aerodynamically smooth lifting surfaces and boundary layer ingestion is suggested to be a promising baseline for a functionally-silent aircraft. Airframe noise reductions of 30 EPNdB are predicted on approach.

However, both "Quiet Lift" concepts mentioned above yield a reduction in airframe drag during approach. Thus, additional drag needs to be generated in a quiet manner on approach. These "Silent Drag" requirements are quantified as a function of aircraft size, approach speed, and glide slope angle.

1.2 Scope of Thesis, Research Questions and Objectives

This thesis focuses on assessing low-noise propulsion system concepts that are expected to enable a functionally-silent aircraft. First, low-noise propulsion system concepts are introduced. Then, the research questions and objectives are presented.

1.2.1 Low-Noise Propulsion System Concepts

Silent thrust concepts propose to reduce jet mixing noise and fan noise components dominant at high engine power settings during takeoff.

Silent drag concepts are aimed at generating drag in a quiet manner in order to:

1. compensate for the drag reduction as a consequence of quiet lift concepts,
2. reduce the noise footprint on the ground by enabling steeper approach glide slope angles.

Silent Thrust

Ultra-High Bypass Ratio Turbofan Engines. The mixing of high-speed jets with surrounding air is a primary source of noise generated by the propulsion system. Significant progress has been made by changing from turbojet to turbofan engine cycles. Further noise reductions have been achieved by increasing the bypass ratio of turbofan engines to values of approximately 8, which is representative of engines currently in service. According to Lighthill's analogy, jet noise scales with the eighth power of the jet velocity. Thus, in order to achieve a large jet noise reduction, jet velocity must be dramatically reduced. For the same thrust output, this requires an increase in mass flow rate such that the bypass ratio needs to be increased to values of order 30 to 60. Such an increase in bypass ratio improves uninstalled specific fuel consumption but yields lower specific thrust, hence very large engine diameters. This inevitably raises integration issues.

Distributed Propulsion System Embedded in the Airframe. Embedding and distributing the propulsion system in the airframe is envisioned to:

1. enable the implementation of the hidden trailing edge concept,
2. allow acoustic shielding and control of turbomachinery noise,
3. improve aircraft and propulsion system performance by mitigating weight and drag penalties associated with ultra-high bypass ratio engine cycles.

Embedding ultra-high bypass ratio engines in the blended-wing-body airframe requires a departure from conventional engine configurations. Instead of using a few large engines, the propulsion

system can be distributed along the span inside the blended-wing-body airframe using a large number of small engines. Multiple fans driven by a common core engine through gearboxes and shafts are also envisioned. Gearboxes can enable fan noise reduction and efficiency improvement by decoupling the fan and the low pressure turbine rotational speeds.

It is envisioned to exhaust the low velocity jet along the trailing edge of the wing through a high aspect ratio nozzle. High aspect ratio jets are a promising means to further reduce jet noise. However, high aspect ratio nozzles inevitably entail higher thrust losses than conventional round nozzles. A spanwise distributed jet exhaust can be used to enhance aerodynamic performance and control authority by applying thrust vectoring or circulation control techniques.

Silent Drag - Windmilling Engine Air-Brake

In order to follow a given approach profile, an aircraft must dissipate its potential and kinetic energy. Conventional aircraft configurations use high-lift devices and landing gear to generate the required drag on approach. The quiet lift concepts assessed by Pilczer (2003) invariably lead to a decrease in drag. Thus, the capability to generate additional drag in a quiet manner is crucial to enable a functionally-silent aircraft. Silent drag generation is envisioned to allow the silent aircraft to follow conventional approach procedures and not disrupt air traffic patterns. Further silent drag generation can enable steeper approach glide slope angles, yielding a reduced noise footprint on the ground.

During approach, the turbofan engines are running at idle speed, producing thrust. At such low engine power settings, the fan noise levels are of the same order of magnitude as airframe noise. Operating the fan in windmilling mode is envisioned to generate silent drag by extracting power from the airflow. To operate the fan in windmilling mode, the fan blade stagger angle needs to be adjusted such that variable pitch turbomachinery is required. The rotating speed of the fan in windmilling mode is expected to decrease relative to a fan operating at low engine power setting, leading to potentially lower fan noise emissions. The power extracted must be dissipated, for example, by a hydrodynamic break that controls the shaft rotational speed.

1.2.2 Research Questions and Objectives

The research objectives of this thesis are:

1. to quantitatively assess the potential jet noise reduction using ultra-high bypass ratio turbofan engines and to investigate associated airframe integration issues,

2. to assess the feasibility of a distributed propulsion system with an integrated airframe/exhaust system,

3. to evaluate the viability of the windmilling engine air-brake concept in terms of performance, noise signature and turbomachinery requirements.

In more detail, this thesis attempts to address the following research questions:

- What are the cycle characteristics of a turbofan jet engine necessary to achieve a step change in jet noise reduction?
- What noise reduction can be achieved using ultra-high bypass ratio engine cycles with mixer nozzles?
- How does an ultra-high bypass ratio cycle affect propulsion system performance?
- What propulsion system configurations allow to embed ultra-high bypass ratio engines in the airframe?
- What is the performance and noise signature of a distributed propulsion system with a high aspect ratio nozzle?
- How much drag can be generated using a windmilling engine air-brake?
- What is the noise signature of a fan operating in windmilling mode?
- What are the turbomachinery requirements for a windmilling engine air-brake?
- On a preliminary basis, what would the propulsion system for a functionally-silent aircraft look like?

1.3 Thesis Contributions

Ultra-High Bypass Ratio Engine Cycles for a Step Change in Jet Noise Reduction

A modeling framework using a first-principles-based engine cycle deck coupled to semi-empirical propulsion system noise prediction methods (Stone's jet noise and Heidmann's fan noise modules in ANOPP) is developed and validated against engine cycle data and aircraft noise certification data. This framework is used to assess the performance and noise signature of ultra-high bypass ratio engine cycles. The noise reduction potentials of separate flow and mixed flow exhaust nozzles are investigated, and the influence of engine technology level on the noise reduction potential of ultra-high bypass ratio cycles is analyzed. The results suggest that an advanced technology engine with mixed flow exhaust nozzle can achieve the silent aircraft jet noise reduction goals at takeoff (-30 EPNdB). A bypass ratio of 42 is envisioned, which entails a 18% decrease in specific fuel consumption compared to the candidate baseline blended-wing-body engine. However, this results in a 42% drop in specific thrust, yielding a twofold increase in engine cross-sectional area.

Distributed Propulsion System Concepts

In order to embed the propulsion system in a blended-wing-body airframe, distributed propulsion system concepts are investigated. The embodiment of such engine configurations is analyzed in the light of the geometrical constraints imposed by the blended-wing-body airframe. For an engine cycle of bypass ratio 42, a total number of 30 fans is required to satisfy these constraints.

Propulsion system configurations with multiple small engines and multiple fans driven by a common core engine are evaluated based on their impact on propulsion system performance (i.e. weight and efficiency penalties). It is suggested that configurations with 6 or 10 core engines driving a total number of 30 fans meet the installation specifications with a trade-off between gearbox weight penalties and turbomachinery losses due to Reynolds number effects.

Increasing the number of fans from 3 (for the baseline configuration) to 30 at a constant tip Mach number yields a perceived fan noise reduction of the order of 2 dB due to the beneficial shift of the fan noise spectrum towards higher frequencies.

Reducing the number of jets from 3 to 1 is predicted to yield a 2 dB reduction in perceived jet noise resulting from the shift of the jet noise spectrum towards lower frequencies.

Experimental measurements and data of high aspect ratio jet noise reported in literature are used to develop a prediction tool capable of determining the trends in jet noise reduction as a function of jet aspect ratio. For a jet aspect ratio of 30 to 50, a jet noise reduction of 2 to 3 dB in overall sound pressure level in the plane containing the minor axis of the nozzle is predicted.

Thrust losses in high aspect ratio nozzles are estimated using three-dimensional CFD computations. For simple nozzle geometries, thrust losses can be maintained below 5% if flow separation can be avoided. High exhaust aspect ratios (20 to 40) can be achieved without flow separation by maintaining the ratio of exit to inlet aspect ratio below 1.5. For larger values of this ratio, separation invariably occurs and higher thrust losses are observed.

Silent Drag - Windmilling Engine Air-Brake

The drag requirements for a quiet approach are quantified and the concept of a windmilling engine air-brake system is assessed in the light of aerodynamic performance and acoustic signature. To first order, the required Silent Drag coefficient is suggested to be independent of aircraft size. High aerodynamic performance of blended-wing-body airframe is critical to achieve approach velocities of 75 to 85 m/s in clean configuration with a 10 to 30% stall margin, compared to 100 m/s for a conventional aircraft configuration. Predictions show that low approach velocities are necessary to achieve the airframe noise reduction goals. If 40% of the drag of a bluff body can be generated using engine air-brakes, the approach glide slope angle can be increased to 4.5°. This increase in glide slope leads to a 30 dB reduction in airframe noise perceived on the ground, compared to a 28 dB reduction for a blended-wing-body aircraft with aerodynamically smooth lifting surfaces on

a standard approach profile (3° glide slope angle).

A one-dimensional compressible flow model of a ducted blade-row with variable pitch geometry is developed to assess the drag generation potential of the engine air-brake. For blade tip Mach numbers of order 0.3, a drag coefficient based on the fan inlet area of 0.4 (i.e. 40% of the drag of a bluff body of identical cross-sectional area) is predicted.

In order to refine this assessment, a two-dimensional viscous blade-to-blade analysis using MISES is performed. Results show that a drag coefficient of 0.45 can be achieved for blade tip Mach numbers larger than 0.2, provided that the blade stagger angle is properly adjusted.

The noise signature of the windmilling engine air-brake is estimated on a preliminary basis using Heidmann's fan noise prediction method and an improved version of the Mugridge-Morfey model for rotor self-noise reported by Gliebe (2002). Compared to the fan noise levels at low engine power setting on approach, both predictions suggest that the engine air-brake yields fan noise reductions of order 10 dB in sound pressure level, due to lower blade tip Mach numbers, despite thicker boundary layers and airfoil wakes.

1.4 Thesis Outline

The concept of ultra-high bypass ratio turbofan engine is investigated in Chapter 2. The methodology is first described, followed by aerothermodynamic and acoustic studies of various engine cycle configurations. Finally, propulsion system design implications are discussed.

In Chapter 3, concepts potentially enabling the integration of the propulsion system in the airframe are assessed. Various distributed propulsion system configurations are compared based on their impact on propulsion system performance. High aspect ratio jet noise is analyzed and the thrust losses in high aspect ratio nozzles are quantified. A distributed propulsion system embedded in a blended-wing-body airframe is then outlined.

In Chapter 4, the drag generation capability of the silent windmilling engine air-brake concept is assessed using a meanline compressible flow analysis and viscous blade-to-blade computations. The noise signature of windmilling fans is then estimated using Heidmann's fan noise prediction method and an improved version of the Mugridge-Morfey model for rotor self-noise reported by Gliebe (2002).

Conclusions and recommendations for future work are discussed in Chapter 5.

Chapter 2

Ultra-High Bypass-Ratio Engine Cycles for a Step Change in Jet Noise Reduction

2.1 Introduction and Objectives

2.1.1 Introduction

According to Lighthill's acoustic analogy (Lighthill (1952)), jet noise scales with the 8^{th} power of the jet velocity. In order to achieve a step change in jet noise reduction, jet velocity must therefore be dramatically reduced. For a given thrust output, reducing the jet velocity inevitably requires a larger engine mass flow and hence a higher bypass ratio.

The aircraft noise reductions achieved over the last 30 years were essentially driven by a gradual increase in engine cycle bypass ratios. First, the commercial jet engine cycle evolved from turbojets to the first generation of low bypass ratio turbofans. High-bypass ratio turbofan engines were developed next with bypass ratios currently ranging up to 8. To meet the stringent noise regulations, this trend will continue in the future: engines designed for the A380 will have a bypass ratio close to 9, and the bypass ratios of engines for the 7E7 are expected to be even higher. This evolution is mostly driven by the quest for improved fuel efficiency. As engine technology improves, engine thermal efficiency increases and higher bypass ratios can be achieved. Higher bypass ratios yield a lower jet velocity and a consequently higher propulsive efficiency. Thus, the overall efficiency of the propulsion system increases, leading to a lower uninstalled specific fuel consumption. However, higher bypass ratios yield lower specific thrusts, hence larger engine diameters at constant thrust. Larger engine diameters directly lead to increased installation drag, which tends to offset gains in

cycle propulsive efficiency. Propulsion systems are currently designed to achieve an optimum trade-off between installation losses and cycle performance, leading to minimum installed thrust specific fuel consumption.

More recently, however, noise considerations have been increasingly influencing engine design. For example, the bypass ratio of the GP7200 engine powering the A380 had to be increased (see Flug Revue (2002)) to satisfy the stringent noise constraints at London's Heathrow airport. This resulted in a 1.2% drop in fuel efficiency, corresponding to a 200 nautical miles reduction in aircraft range and a 10 tons weight penalty (see Antoine and Kroo (2002); Antoine (2003)).

Achieving the jet noise reductions necessary for a silent aircraft will require much larger values of the bypass ratio, and trade-offs between aircraft performance and jet noise emissions will become more pronounced. A back-of-the-envelope calculation[1] shows that bypass ratios of order 25 to 40 are required to achieve a 30 dB jet noise reduction. To achieve such "ultra-high" bypass ratios, advanced engine technology is required and system level penalties induced by the large size of these engines (fan, nacelle and pylon weight, installation drag) also have to be taken into account.

In this chapter, noise is considered the prime design criterion for a turbofan cycle, and the concept of ultra-high bypass ratio engines is assessed. For this purpose, a first-principles-based turbofan engine cycle deck is coupled to NASA's Aircraft Noise Prediction Program (ANOPP) to predict the Effective Perceived Noise Level (EPNL) due to propulsion system noise sources at takeoff.

2.1.2 Objectives

The objectives of this chapter are:

- to quantitatively estimate the engine cycle characteristics required to achieve the silent aircraft goals in jet noise reduction, and
- to assess the impact of ultra-high bypass ratio engine cycles on propulsion system performance.

The jet noise reduction potential of mixer nozzles is evaluated. The influence of the engine technology level is discussed. In order to facilitate engine integration within the airframe as envisioned in Chapter 3, the engine size needs to be minimized by maximizing specific thrust while meeting noise reduction objectives. Fan noise is not included in this study: it is assumed that, for embedded engines or engines mounted on the top of a blended-wing body configuration, fan noise can be effectively shielded (Clark and Gerhold (1999); Antoine and Kroo (2002)) and passively or actively

[1] According to the jet noise scaling law deduced from Lighthill's acoustic analogy (Lighthill (1952)), a 30 dB reduction in jet noise requires a decrease of the jet velocity by a factor $10^{\frac{3}{8}} \approx 2.4$. Assuming constant static thrust, this corresponds to an increase in mass flow by the same factor. For a constant core size, this increase in mass flow would require an approximately equivalent increase in bypass ratio. Starting from a value of 9 (current engine technology), the required bypass ratio would be in the 20-25 range; starting from a value of 15 (advanced engine technology), the bypass ratio can roughly be estimated around 35-40.

controlled with acoustic liners. Thus, jet noise remains as the most challenging propulsion system noise source to be reduced at takeoff.

2.2 Methodology

A modeling framework has been developed that is capable of predicting the propulsion system noise at takeoff for any given turbofan cycle and airframe characteristics. The effective perceived noise level (EPNL) is evaluated at prescribed measurement points (or "observers") located in the far field. Engine performance metrics such as Thrust Specific Fuel Consumption (TSFC) and Specific Thrust are also computed by the model. This section describes the methods and underlying assumptions used in the modeling, and the validation and calibration of the model.

2.2.1 Model Description and Assumptions

The modeling framework consist of four modules that are coupled to one another:

1. Given a design point, a cycle analysis is first conducted, yielding cycle performance metrics such as specific thrust and TSFC.

2. The engine is sized to meet a given thrust requirement at design point, setting the fan inlet and exhaust areas.

3. The off-design performance of the engine during takeoff is then computed.

4. The aircraft takeoff trajectory is determined by ANOPP's flight dynamics module (see Zorumski (1982)). Jet noise emissions are then computed using Stone's prediction method (see Stone (1974) and Stone and Montegani (1980)) at each position along the trajectory. Fan noise can also be computed by applying Heidmann's prediction method (see Heidmann (1975)). The radiated pressure field is propagated to the observers by ANOPP's atmospheric propagation module. Finally, the sound pressure level history is post-processed by ANOPP to yield the effective perceived noise level (EPNL) at the observer location (see Zorumski (1982)).

The assumptions underlying the modeling framework are as follows (detailed description of these four modules and their interaction can be found in Appendix A):

- The thermodynamic cycle analysis is based on conservation of energy:
  - the power required to drive the fan and the low-pressure compressor equals the power delivered by the low-pressure turbine,
  - the power required to drive the high-pressure compressor equals the power delivered by the high-pressure turbine,

– the net enthalpy flux across the combustor equals the heat added by the fuel combustion.

- Off-design performance computations are performed by applying first principles (mass flow and energy conservation) and thermodynamic analysis of engine components. It is assumed that polytropic efficiencies of rotating components are constant and that the flow is always choked at both high- and low-pressure turbines inlets (see Appendix A.2 or Mattingly (1996) for more details).
- In both the cycle analysis and the engine performance calculations, gas properties are assumed constant across the components.
- In the case of the mixed flow exhaust nozzle, the bypass and core flows are fully mixed in a constant area mixer and are then expanded through a converging nozzle. A control volume analysis of the constant area-mixer enables the determination of the mixed flow state at both design and off-design conditions by applying conservation of mass, momentum, and energy.
- Noise shielding effects are neglected in the noise prediction.

2.2.2 Model Validation and Calibration

Validation Process

The model is validated at three different levels using:

- the engine cycle analysis tool GasTurb (Kurzke (2001)),
- engine data (Pratt & Whitney JT9D data (Mattingly (1996)) and Rolls-Royce Trent data (Jane's Aero-Engines (2003))),
- airframe characteristics and takeoff noise certification data (Airbus A318 to A340-600 (Jane's All the World's Aircraft (2003))).

First, the cycle analysis and engine sizing are performed for a JT9D engine cycle. Predicted total temperatures and total pressures at different engine stations across the engine agree within 5 to 10% with experimental data reported in Mattingly (1996) and GasTurb's output for the same case. Fuel and air mass flows and thrust output are accurately rendered by the model.

Most discrepancies can be attributed to the assumption of constant gas properties across rotating components and the lack of data on the actual component efficiencies. More details and measures of the errors are given in Appendix A.1.3 (Tables A.2 and A.3). Results of the cycle analysis for the baseline advanced engine proposed in Liebeck et al. (1996) for the blended-wing-body aircraft are also compared to the cycle performance predicted using GasTurb in Appendix A.1.3 (Tables A.4 and A.5). Errors in jet temperatures and velocities, engine mass flow, and specific fuel consumption predicted by the cycle analysis relative to GasTurb's prediction are less than 10%.

Off-design performance predictions performed by the off-design module and GasTurb are compared over a range of flight conditions and power settings. The baseline blended-wing-body engine cycle is considered. Results of these parametric studies are given in Appendix A.2.3.

For variations in flight Mach number of ± 0.2 relative to the design point, and variations in turbine inlet temperature of ± 200 K relative to the design inlet temperature, the off-design performance module predicts the thrust output, fuel consumption, and flow state at the exhaust nozzles with a reasonable accuracy. The correct trends are captured. For larger variations in operating conditions relative to the design point, the accuracy of the prediction decreases. This is essentially due to the assumption of constant polytropic efficiency of the rotating components. GasTurb uses generic fan, compressor, and turbine maps.

Finally, the entire framework is run for aircraft and engines for which data are available, and predicted noise levels are compared to certification data at flyover and sideline certification measurement points.

First, the takeoff of an A300 (airframe aerodynamic data from Boiffier (2000)) with JT9D engines at 4 different takeoff gross weights is simulated. Both fan noise and jet noise are taken into account in the noise predicion. Independently of takeoff weight, sideline noise is overestimated by approximately 3 dB and flyover noise by 7 dB. This noise over-prediction is partly due to the uncertainty on flaps setting and throttle scheduling during takeoff and also to the fact that fan noise shielding is not taken into account. However, the increase in noise with takeoff weight is well captured. Details of this study are given in Appendix A.3.2, in Figure A-6.

In order to gain greater confidence in the robustness of the model, the entire framework is run for all aircraft in the Airbus family for which certification noise level at takeoff and airframe specifications are available (Jane's All the World's Aircraft (2003)). Engine type, takeoff thrust, bypass ratio, and overall pressure ratio, as well as aircraft takeoff weight and wing area, are found in Jane's Aero-Engines (2003). However, the model requires more detailed inputs[2] which are not available for all engines and airframes considered here. Thus, for each type of aircraft, airframe aerodynamic characteristics and takeoff speeds are assumed to be the same as for the A300 (Boiffier (2000)). Engine cycle design point is taken at sea level static (SLS) conditions, on a hot day (ISA+15 K). Unknown engine cycle characteristics are deduced from Mattingly (1996) for the current engine technology level. For a given bypass ratio and overall pressure ratio, the fan pressure ratio is deduced by minimizing the specific fuel consumption at the design point. Jet noise alone is taken into account in the noise prediction.

The top plot in Figure 2-1 compares the runway length required to lift off simulated by the flight dynamics module to the takeoff field length given in aircraft specifications (from Jane's All

[2]Such as: fan pressure ratio, component polytropic efficiencies, turbine inlet temperatures at takeoff, design point, rotation and initial climb speeds, lift and drag coefficients for different flap settings

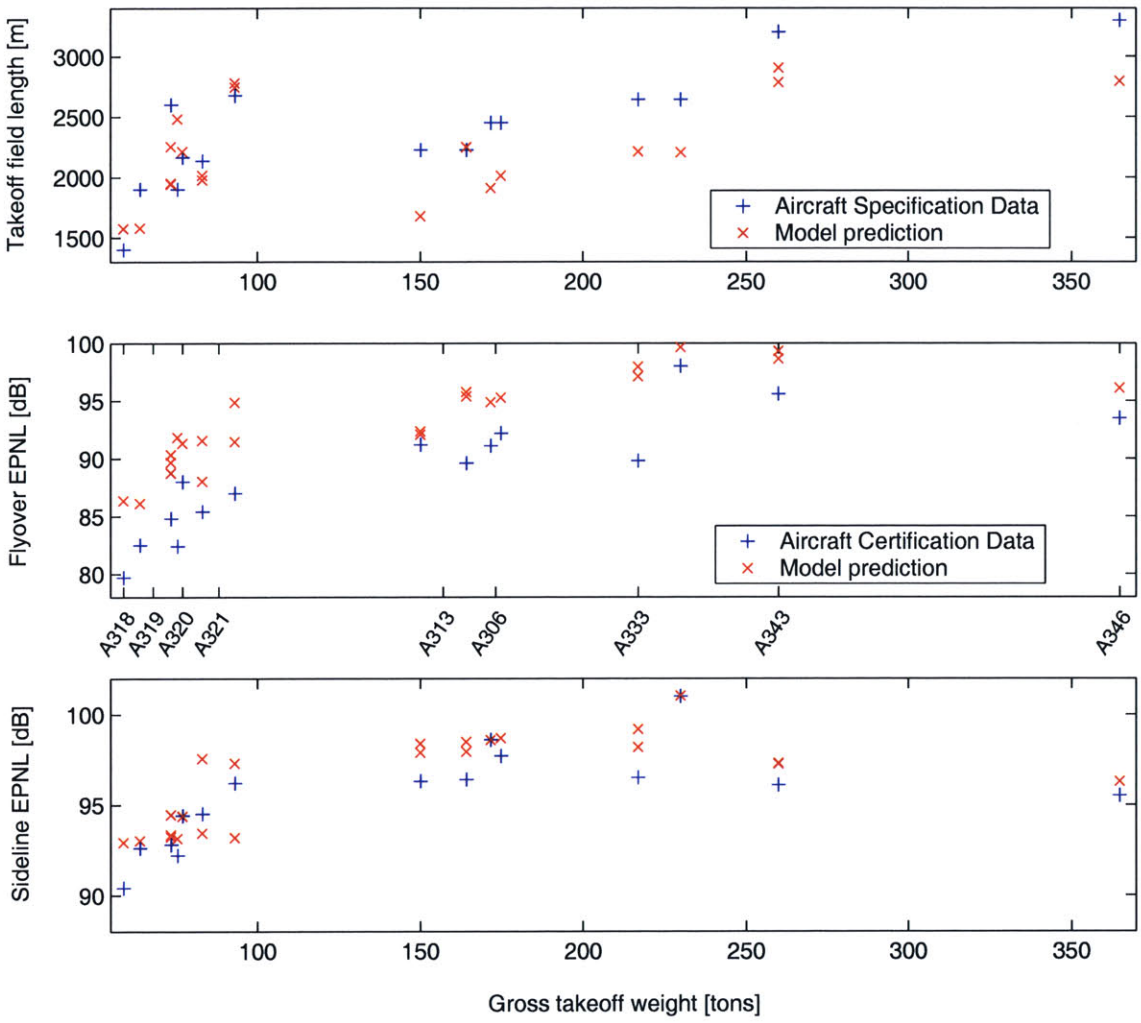

Figure 2-1: Comparison of model prediction (red) to aircraft specifications or certification data (blue) for takeoff field length (top), flyover EPNL (middle) and sideline EPNL (bottom). Data from Jane's All the World's Aircraft (2003).

the World's Aircraft (2003)). The relative error in runway length is plotted in Figure 2-2. For most narrow-body aircraft, the predicted runway length is within $\pm 20\%$ of the aircraft specifications. For wide-body aircraft, the runway length is underestimated by approximately 10%. This discrepancy is due to the uncertainty on flaps and power settings, takeoff speeds, and airframe characteristics. However, Figure 2-1 suggests that the model captures the correct trend in takeoff length.

The comparison of the predicted absolute EPNL with certification data is also presented in the middle (flyover) and bottom (sideline) plots of Figure 2-1. The framework clearly renders the trend in EPNL with takeoff gross weight. A +3 dB shift is applied to the predicted EPNL in an attempt to render the fact that fan noise was neglected, assuming equal contributions from jet and fan noise sources towards the total EPNL. Errors in predicted flyover and sideline noise relative to certification

data are plotted in Figure 2-1. At the flyover measurement point, the noise level is systematically overestimated by the model. The maximum overestimate is 9.5 dB, but the average error is 4.6 dB. At the sideline measurement point, the noise level is predicted within ±3 dB of the certification data, and the average error is 1.3 dB. These average relative errors are acceptable considering the assumptions underlying this study.

However, even if absolute noise levels seem to be captured for some of the configurations, this must be considered as fortuitous since noise shielding effects and fan noise are not computed here.

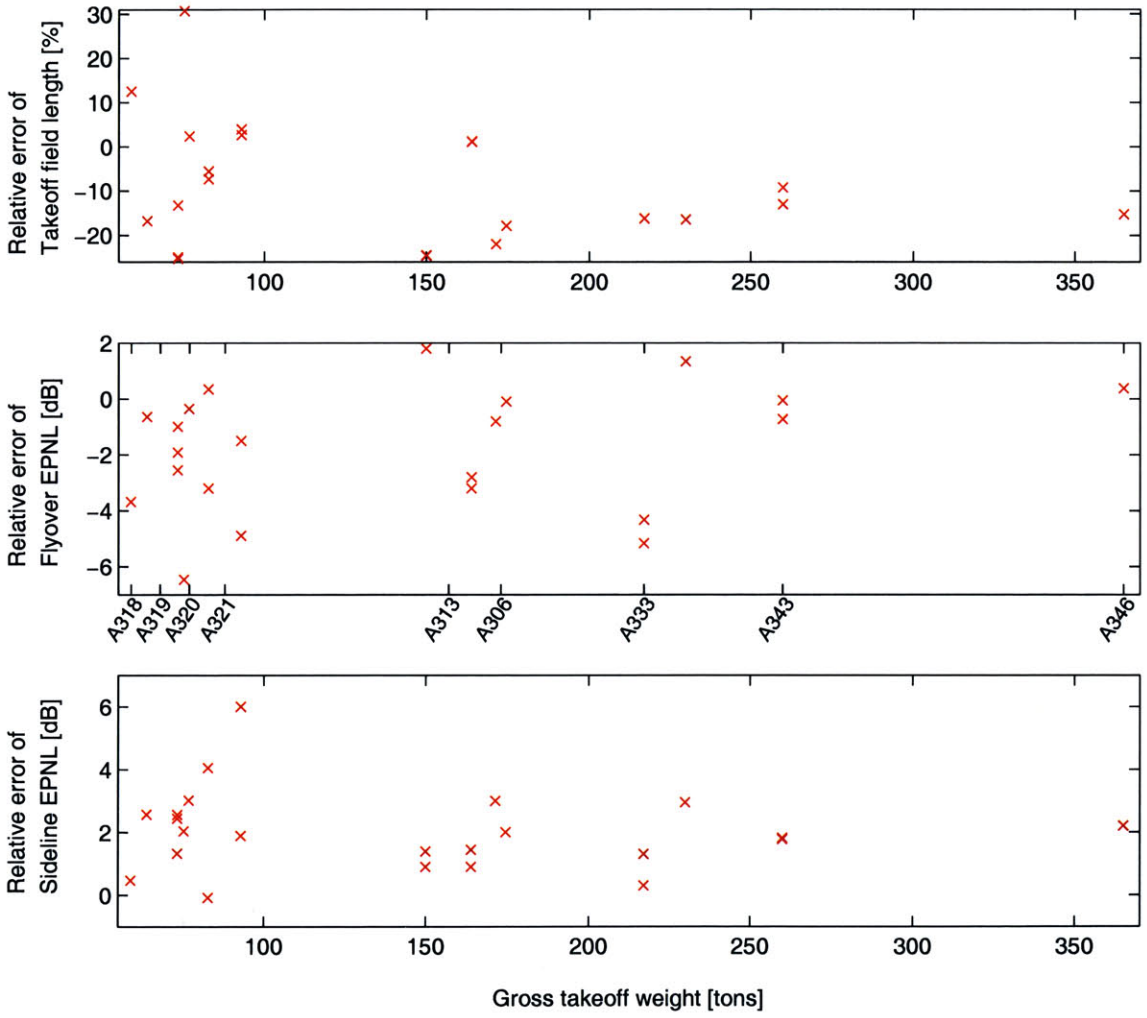

Figure 2-2: Model prediction error for takeoff field length (top), flyover EPNL (middle) and sideline EPNL (bottom) relative to aircraft specifications and certification data. Data from Jane's All the World's Aircraft (2003).

The main limitation of the model lies in the off-design engine performance prediction. The accuracy of the prediction drops for operating conditions (flight Mach number, engine power setting, ambient conditions) significantly different from the design point ($M_0 \pm 0.2$, $T_{t4} \pm 200$ K). Thus, for

a turbofan engine cycle designed at takeoff, specific fuel consumption at cruise conditions cannot be accurately predicted. This is mainly due to the assumption of constant polytropic efficiency of the rotating components underlying the off-design prediction method. Fan, compressor, and turbine maps are required to improve the accuracy of the prediction.

The main conclusion from this study is that trends in jet noise emissions are correctly rendered by the model. Thus, all noise assessments have to be conducted on a relative basis.

Calibration of Jet Noise Prediction Tool

Since relative variations in noise levels are correctly rendered by the model, calibrating the model output for a well-known reference configuration should relate noise level variations relative to this reference to the absolute EPNL scale.

The A340-600 powered by Trent 500 engines is chosen as reference. According to available noise certification data reported in Jane's All the World's Aircraft (2003), it is the quietest aircraft in the same weight category as the blended-wing-body aircraft. The total flyover EPNL for this airframe/engine combination is 93.5 dB. Assuming that fan and jet noise contribute equally to the noise radiation and are the two most dominant noise sources, the flyover EPNL of jet noise alone can be estimated at 90.5 dB. The following procedure is applied to obtain a best estimate of the reference noise level:

- The design point is taken at sea level static (SLS) conditions on a hot day (ISA+15 K).
- The overall pressure ratio and bypass ratio of the Trent 500 are obtained from Jane's Aero-Engines (2003).
- The fan pressure ratio is adjusted to minimize fuel consumption at design point.
- The turbine inlet temperature is adjusted so the specific thrust matches engine specifications.
- The components efficiencies are deduced from Mattingly (1996) assuming current engine technology level.
- The same aerodynamic characteristics as the A300 (from Boiffier (2000)) are assumed.

Cycle characteristics of the Trent 500 engine are presented in Table 2.1.

The flyover noise level predicted by the model for the reference airframe/engine combination is subtracted from all subsequent flyover noise assessments. Thus, a predicted relative EPNL of 0 dB corresponds to an absolute EPNL of 90.5 dB. The EPNL of 60 dB required to enable a functionally-silent aircraft translates into a jet noise reduction target of 30.5 dB.

Quantity	Symbol	Value
Overall Pressure Ratio	OPR	37.3
Bypass Ratio	BPR	7.5
Specific Thrust	ST	0.83
Fan polytropic efficiency*	η_{Fan}	0.86
Low-pressure compressor polytropic efficiency*	η_{LPC}	0.88
High-pressure compressor polytropic efficiency*	η_{HPC}	0.88
High-pressure turbine polytropic efficiency*	η_{HPT}	0.87
Low-pressure turbine polytropic efficiency*	η_{LPT}	0.89
Turbine Inlet Temperature$^+$	T_{t4}	1600 K
Inlet pressure recovery*	π_d	0.98
Combustor pressure ratio*	π_b	0.94
Core nozzle pressure ratio*	π_{nc}	0.98
Bypass nozzle pressure ratio*	π_{nb}	0.98

Table 2.1: Cycle parameters of the Trent 500 engine obtained from Jane's Aero-Engines (2003). Parameters noted by a * are deduced from Mattingly (1996). $^+$: T_{t4} is adjusted to match the specific thrust.

2.3 Results

The modeling framework presented in Section 2.2 requires the following inputs:

- propulsion system cycle parameters (OPR, FPR, BPR, T_{t4}, total thrust, number of engines),
- propulsion system component efficiencies,
- airframe design variables (TOGW, Wing Area),
- airframe performance parameters (lift and drag coefficients, rotation speed).

In order to focus the study on ultra-high bypass ratio engine cycles, the following assumptions are made.

Constant Airframe Characteristics. Changes in propulsion system inevitably induce variations in airframe weight, lift and drag characteristics. However, taking these effects into account requires a multidisciplinary framework including weight and aerodynamic modeling.

Airframe characteristics are assumed constant throughout the present study. A blended-wing body configuration is considered. Indeed, this configuration is a good candidate to achieve the low airframe noise objectives for a silent aircraft (see Section 1.1.2 or Pilczer (2003) for more details). Using data reported by Liebeck et al. (1996), aerodynamic characteristics in clean configuration, takeoff weight and takeoff speeds are input in the model.

Constant Propulsion System Characteristics. The total thrust required at takeoff is directly related to the aircraft takeoff weight. Therefore, it is considered here as a constant requirement for

the propulsion system. As cycle parameters are varied, specific thrust is computed and engines are sized at design point by adjusting the design mass flow to match the required thrust.

The engine component efficiencies, maximum turbine inlet temperature, and overall pressure ratio reported in Liebeck et al. (1996) for the baseline blended-wing-body engine are considered. Additional cycle characteristics required by the model and not given in Liebeck et al. (1996) are deduced from Mattingly (1996). The cycle characteristics are summarized in Table 2.2.

In the model, the low-pressure compressor pressure ratio includes the fan pressure ratio. Thus, as the fan pressure ratio varies, it is assumed that the low-pressure compressor is adjusted to keep the overall pressure ratio constant.

Constant Takeoff Procedure. The engine power setting is kept at full-power throughout the takeoff maneuver.

2.3.1 Methodology

Under the above assumptions, jet noise and propulsion system performance can be predicted for given fan pressure ratios and bypass ratios. Separate or mixed flow exhaust nozzles can be compared. Various engine technology levels can be analyzed.

In order to assess the impact of ultra-high bypass ratio engine cycles on jet noise emissions and propulsion system performance, following studies are carried out:

1. For the advanced engine technology level suggested in Liebeck et al. (1996), a parametric study in fan pressure ratio and bypass ratio is first performed for both separate flow and mixed flow exhaust nozzles. Observed trends in jet noise and engine performance enable to outline three relevant cycle configurations for a given bypass ratio.

2. The noise reduction potential of the mixed flow exhaust nozzle is then assessed.

3. Finally, the influence of engine technology level on jet noise reduction potential is analyzed.

2.3.2 Influence of Fan Pressure Ratio and Bypass Ratio on Jet Noise Emissions and Cycle Performance

A parametric study in fan pressure ratio and bypass ratio is performed for both separate flow and mixed flow exhaust nozzles for an advanced engine technology level corresponding to the baseline blended-wing-body engine suggested in Liebeck et al. (1996). Corresponding cycle characteristics are summarized in Table 2.2. As in Liebeck et al. (1996), the design point is at sea level conditions on a hot day (ISA+15 K) for a flight Mach number of 0.2.

Quantity	Symbol	Value
Fan polytropic efficiency	η_{Fan}	0.94
Low-pressure compressor polytropic efficiency	η_{LPC}	0.925
High-pressure compressor polytropic efficiency	η_{HPC}	0.92
High-pressure turbine polytropic efficiency	η_{HPT}	0.90
Low-pressure turbine polytropic efficiency	η_{LPT}	0.90
Turbine Inlet Temperature	T_{t4}	2000 K
Overall Pressure Ratio	OPR	67.5
High-pressure compressor pressure ratio	π_{HPC}	25
Inlet pressure recovery*	π_d	0.99
Combustor pressure ratio*	π_b	0.96
Core nozzle pressure ratio*	π_{nc}	1
Bypass nozzle pressure ratio*	π_{nb}	0.99

Table 2.2: Cycle parameters for the baseline blended-wing-body engine suggested in Liebeck et al. (1996). Parameters noted by a * are deduced from Mattingly (1996).

Cycle Limits and Trends in Jet Noise Emission and Cycle Performance for Separate Flow Exhaust Nozzles

Contours of constant relative flyover EPNL, specific thrust, and fuel consumption are plotted as a function of fan pressure ratio and bypass ratio in Figure 2-3 for separate flow exhaust nozzles.

Cycle Limits. For a given bypass ratio, there is an upper limit in fan pressure ratio for which all available power extracted from the core by the low-pressure turbine is consumed to drive the fan such that the net mechanical power of the core vanishes. In the limit, the bypass flow velocity reaches a maximum and the core flow velocity vanishes.

A lower limit in fan pressure ratio is also observed. In this case, most of the core power is transferred to the core jet kinetic energy. Only a small fraction of this power must be transferred to the bypass flow to overcome duct pressure losses and close the cycle. In the limit, the bypass flow velocity vanishes and the core flow velocity reaches a maximum.

These two limiting cases are plotted in black in Figure 2-3. Close to these cycle limits, the specific thrust drops and the specific fuel consumption sharply rises, yielding poor cycle performance. At the lower cycle limit, very high jet noise levels are observed due to the high speed and the high temperature of the core jet. At the upper cycle limit, the bypass jet is faster than the core jet, i.e. the velocity profile is "inverted". In this case, noise levels cannot be computed by Stone's jet noise prediction method (see Stone (1974) and Stone and Montegani (1980)) currently available.

Trends in Jet Noise and Cycle Performance. For a given bypass ratio, fuel consumption reaches a minimum and specific thrust reaches a maximum for a certain fan pressure ratio between the two cycle limits outlined above.

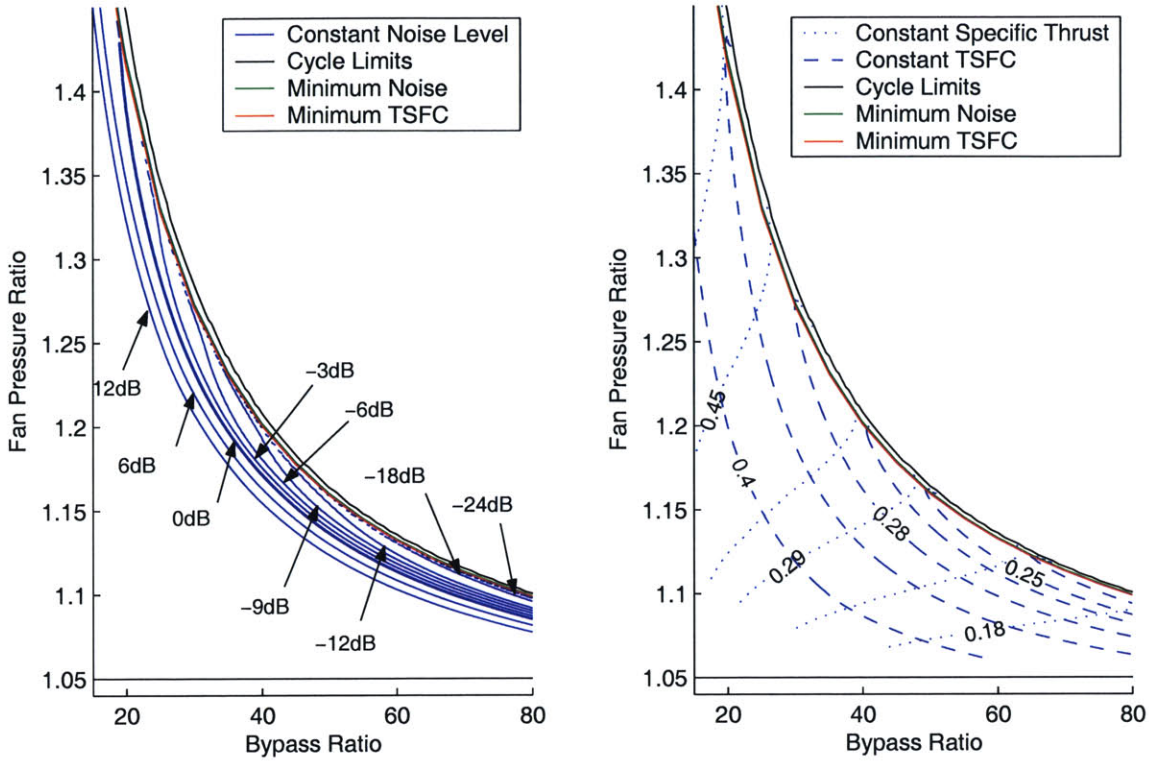

Figure 2-3: Contours of constant noise level (left), specific thrust (right, dotted), and specific fuel consumption (right, dashed) as a function of fan pressure ratio and bypass ratio for separate flow exhaust nozzles. TSFC is in kg/(hr.kg).

At the high bypass ratios considered here, increasing the fan pressure ratio yields a decrease in core jet velocity greater than the associated increase in bypass jet velocity. Thus, the jet noise level decreases with increasing fan pressure ratio until both jets have equal velocities. Higher fan pressure ratios then further increase the bypass jet velocity and decrease the core jet velocity, hence an inverted velocity profile. Such jet configurations are expected to generate even lower noise levels. However, these cases cannot be predicted with the currently available method. Therefore, the cycle leading to equal jet velocities is denoted as the "minimum noise" configuration with separate exhaust nozzles. This configuration (in green in Figure 2-3) is achieved for a fan pressure ratio slightly larger than that leading to minimum TSFC and maximum specific thrust (in red in Figure 2-3).

The trends in engine performance observed here are well-known: it can be shown (see Mattingly (1996)) that, for a given bypass ratio, an optimum fan pressure ratio exists which minimizes the thrust specific fuel consumption and maximizes the specific thrust. For an ideal turbofan cycle, this occurs when both jet velocities are equal. For non-ideal cycles, this optimum occurs for a core jet velocity larger than the bypass jet velocity.

This raises the issue of determining the design fan pressure ratio for a given bypass ratio. Tra-

ditionally, the fan pressure ratio is adjusted to minimize specific fuel consumption. However, this study suggests that lower jet noise levels can be achieved by increasing the fan pressure ratio. The cost in specific fuel consumption for this noise reduction is less than 0.1%. A quantitative estimate of this jet noise reduction and of its impact on engine cycle performance is given in Section 2.3.3.

Cycle Limits and Trends in Jet Noise Emission and Cycle Performance for Mixed Flow Exhaust

Cycle Limits. In the case of mixed flow exhaust, the range of fan pressure ratios leading to a feasible cycle is narrower than for separate flow exhaust nozzles. This is essentially due to the additional constraint of equal core and bypass flow static pressures at the mixer inlet when the bypass and core flows are not choked at this station. This is illustrated in Figure 2-4, which shows the upper and lower cycle limits (black curves) as well as contours of constant noise level, specific thrust, and fuel consumption as a function of fan pressure ratio and bypass ratio.

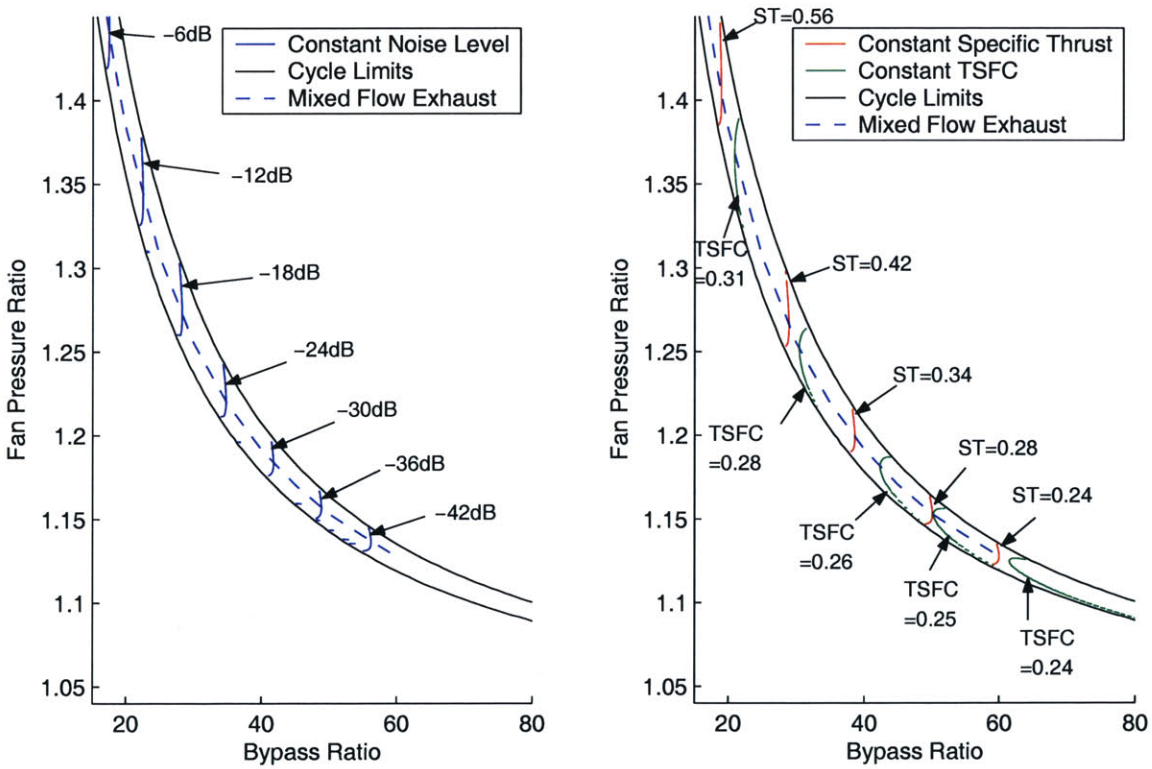

Figure 2-4: Contours of constant noise level (left), specific thrust (right, red), and specific fuel consumption (right, green) as a function of fan pressure ratio and bypass ratio for mixed flow exhaust. TSFC is in kg/(hr.kg).

Trends in Jet Noise and Cycle Performance. For a given bypass ratio, the fan pressure ratio maximizing specific thrust also minimizes specific fuel consumption. Cycle performance deteriorates as the fan pressure ratio tends toward cycle limits. Compared to the optimum cycle performance for the same bypass ratio, specific fuel consumption at the cycle limit is multiplied by more than three and specific thrust is divided by five.

On the other hand, the fan pressure ratio has a weak influence on mixed jet velocity, hence jet noise. Thus, with a mixed flow exhaust, there is no significant trade-off between jet noise emissions and engine cycle performance at a given bypass ratio. Therefore, it is suggested to adjust the fan pressure ratio to achieve minimum specific fuel consumption and maximum specific thrust (dashed blue curve in Figure 2-4).

Conclusions

The parametric studies in terms of fan pressure ratio and bypass ratio for both separate flow and mixed flow exhaust nozzles reveal three relevant cycle configurations at a given bypass ratio:

1. with separate flow exhaust nozzles, the cycle yielding the minimum specific fuel consumption and maximum specific thrust is referred to from now on as the "minimum TSFC" cycle configuration,

2. with separate flow exhaust nozzles, the cycle yielding a uniform exhaust profile is referred to as the "minimum noise" cycle configuration,

3. with mixed flow exhaust nozzles, the cycle yielding optimum engine performance is referred to as the "mixed flow exhaust" cycle configuration.

For a given engine technology level, selecting one of these three cycle configurations automatically sets the dependence of fan pressure ratio with bypass ratio. This dependence is marked by the red ("minimum TSFC") and green curves ("minimum noise") in Figure 2-3 and by the dashed blue curve in Figure 2-4 ("mixed flow exhaust").

2.3.3 Noise Reduction Potential of Advanced UHBPR Engines with Separate and Mixed Flow Exhaust Nozzles

In this study, the noise reduction potential and cycle performance of the three cycle configurations outlined in Section 2.3.2 are compared for the advanced engine technology level suggested in Liebeck et al. (1996).

Figure 2-5 compares the relative flyover noise level, fuel consumption, specific thrust, and engine cross-sectional area as a function of bypass ratio for these three cycle configurations. The -30.5 EPNdB noise goal is indicated by the dotted black line.

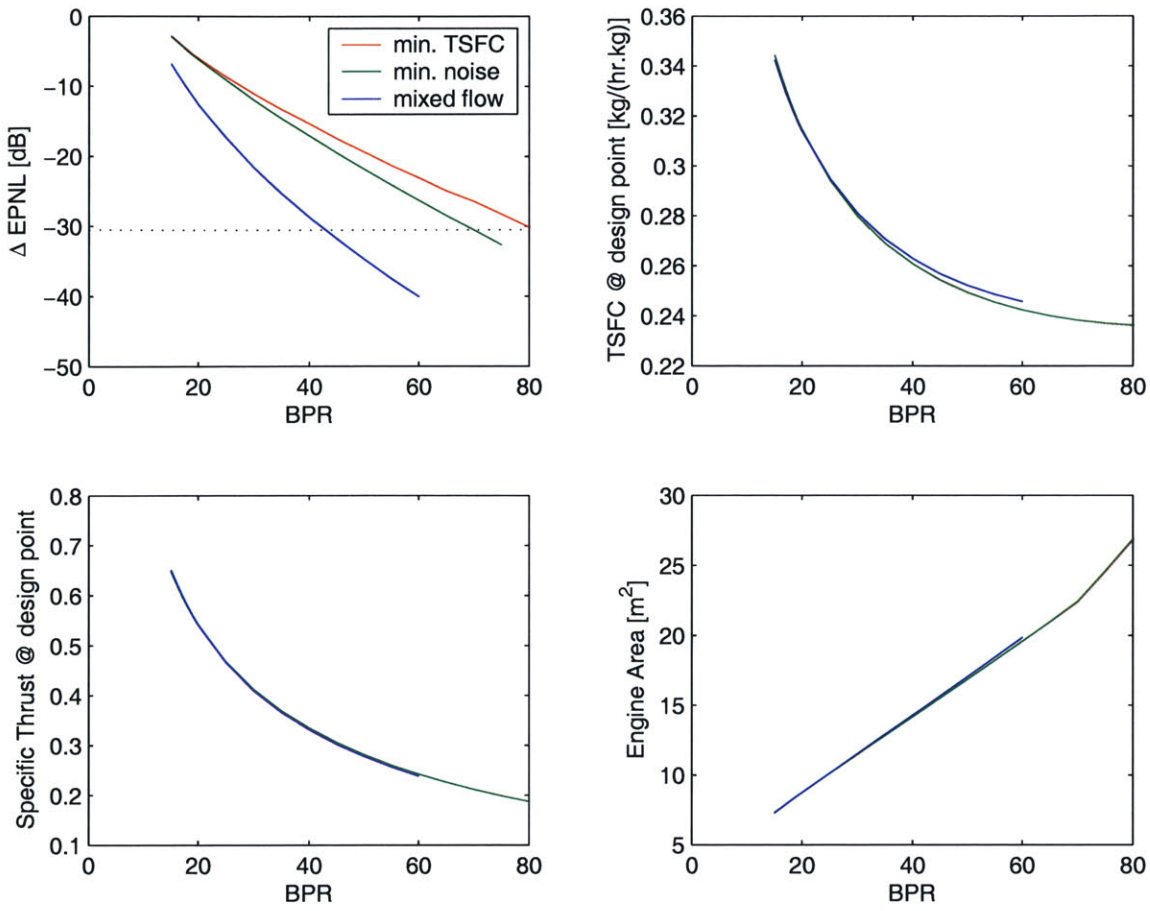

Figure 2-5: Noise reduction potential and engine performance as a function of bypass ratio for "minimum TSFC" (red), "minimum noise" (green), and "mixed flow exhaust" (blue) configurations: Advanced technology engine.

The following comments can be made on these results:

- "Minimum TSFC", "minimum noise", and "mixed flow exhaust" cycle configurations reach the noise goal for bypass ratios of 80, 69, and 42, respectively.
- Relative to the "minimum TSFC" cycle, the "minimum noise" cycle achieves a jet noise reduction of 3 EPNdB at a bypass ratio of 60. For bypass ratios lower than 30, no significant difference in jet noise levels is observed. This effect is due to the increasing sensitivity of the core jet velocity to fan pressure ratio as the bypass ratio increases. Although this effect is small, it achieves the noise goal with a 14% lower bypass ratio.
- Relative to both configurations with separate flow exhaust nozzles, the mixer nozzle achieves a jet noise reduction rising from 3 EPNdB at a bypass ratio of 20 to more than 15 EPNdB at bypass ratios higher than 50. This effect is due to the enhanced uniformity in jet temperature

and density resulting from the mixing of the core and bypass streams. For the same thrust output, lower sound pressure levels are radiated by a uniform jet compared to co-annular jets of different densities. Furthermore, the length scale driving the jet noise peak frequency of co-annular jets is the diameter of the hot core flow, whereas for a single jet this length scale is the diameter of the jet (see Zorumski (1982), Stone (1974), and Stone and Montegani (1980)). As a result, the jet noise peak frequency is lower for the mixed jet than for co-annular jets. The spectrum is shifted toward lower frequencies that are less annoying to the human ear. This further reduces the EPNL. This effect increases with bypass ratio since frequencies below 50 Hz are not even taken into account in the EPNL calculation.

- Trends in specific fuel consumption and specific thrust (hence, engine cross-sectional area) with increasing bypass ratio are similar for the three different configurations. In particular, for the "minimum TSFC" and "minimum noise" configurations, these performance metrics are equivalent to within 0.1% for a given bypass ratio. Thus, the noise reduction enabled by the "minimum noise" cycle relative to the "minimum TSFC" is achieved at almost no cost in cycle performance. By adjusting the the Mach number of the core flow at the mixer inlet for each bypass ratio, the "mixed flow exhaust" configuration can achieve lower or higher performance levels compared to configurations with separate flow exhaust nozzles. However, the magnitude of this effect in specific fuel consumption is less than 2%, which is small compared to the sensitivity of cycle performance to bypass ratio. Thus, at this level of analysis, it can be assumed that all three configurations perform equally in terms of specific thrust and specific fuel consumption for a given bypass ratio.

The predictions clearly show that mixer nozzles are powerful means to reduce jet noise EPNL.

In order to assess the impact of jet noise reduction on the cycle performance of the different cycle configurations, bypass ratio, specific fuel consumption, specific thrust, and engine cross-sectional area are plotted as a function of the jet noise reduction in Figure 2-6.

The bypass ratio required to achieve a given noise reduction using a mixer nozzle is 20 to 50% lower than using separate flow exhaust nozzles. Thus, for a given noise reduction, the "mixed flow exhaust" configuration achieves a higher specific thrust, leading to smaller engines, but also yields a higher specific fuel consumption. This trade-off will be further discussed later in this chapter.

The following can be concluded from this study:

1. Ultra-high bypass ratio engine cycles can achieve the target jet noise reduction while simultaneously inducing a 20 to 30% reduction in specific fuel consumption at the cost of a 40 to 60% drop in specific thrust, leading to engines 50 to 80% larger in diameter.

2. The mixed flow exhaust configuration enables jet noise reduction that lowers the required bypass ratio by 40% for a given noise goal. Compared to configurations with separate flow

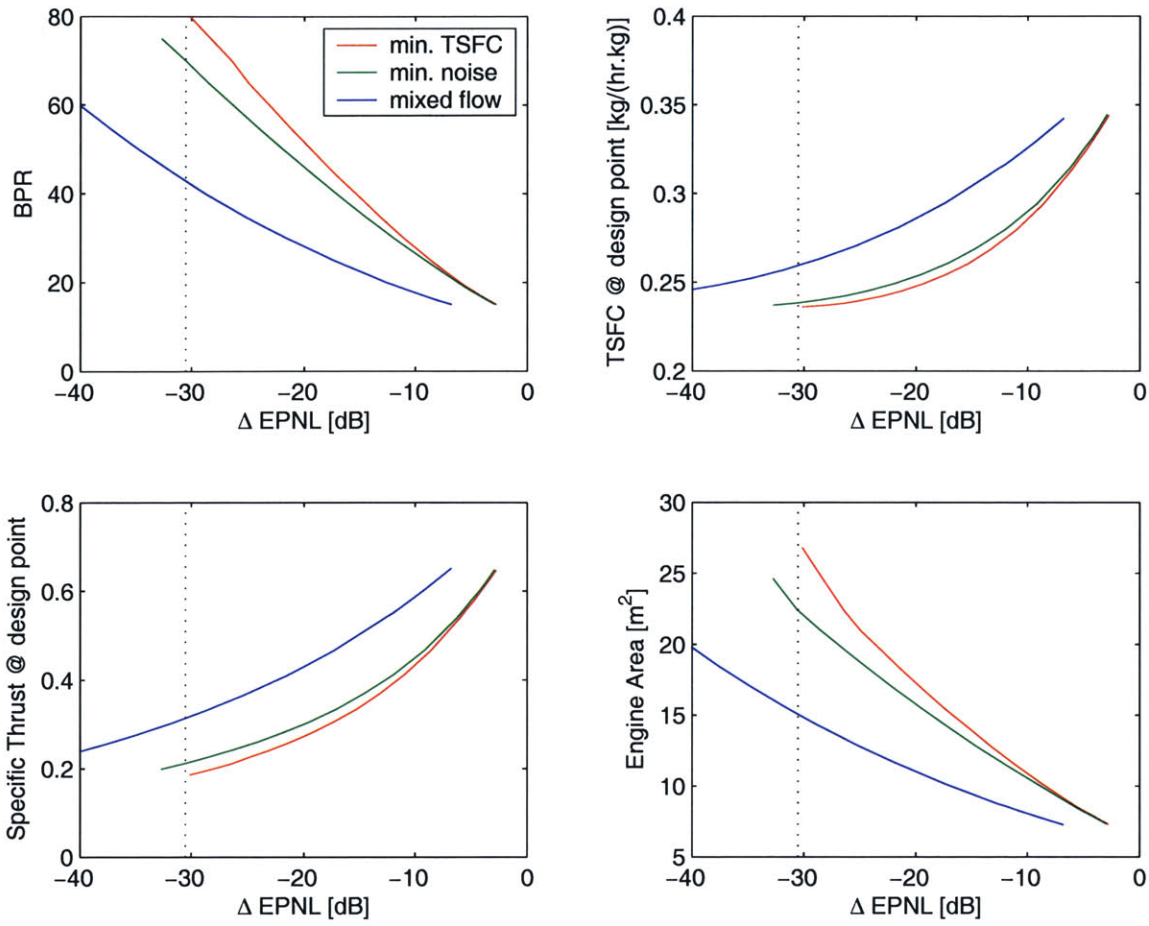

Figure 2-6: Bypass ratio and engine performance as a function of jet noise reduction for "minimum TSFC" (red), "minimum noise" (green), and "mixed flow exhaust" (blue) configurations: Advanced technology engine.

exhaust nozzles, this translates into 30% smaller engines cross-sectional areas, thus enabling easier integration within the airframe.

2.3.4 Influence of Engine Technology Level on Noise Reduction Potential

It can be argued that the efficiencies, overall pressure ratio, and maximum turbine inlet temperature suggested by Liebeck et al. (1996) for the baseline blended-wing-body engine are optimistic. In order to assess the sensitivity of the jet noise reduction potential of ultra-high bypass ratio engine cycles to engine technology level, a study similar to that performed in Section 2.3.3 is repeated for an engine at a current technology level. The Trent 500 engine technology is used. The corresponding cycle parameters are summarized in Table 2.1.

With the current engine technology level, the bypass ratio can be increased up to about 35 for the "mixed flow exhaust" and "minimum TSFC" cycle configurations. However, for the "minimum

noise" cycle configuration, noise levels cannot be computed for bypass ratios larger than 20 because the core jet velocity becomes lower than the bypass jet velocity beyond a certain flight speed. Figure

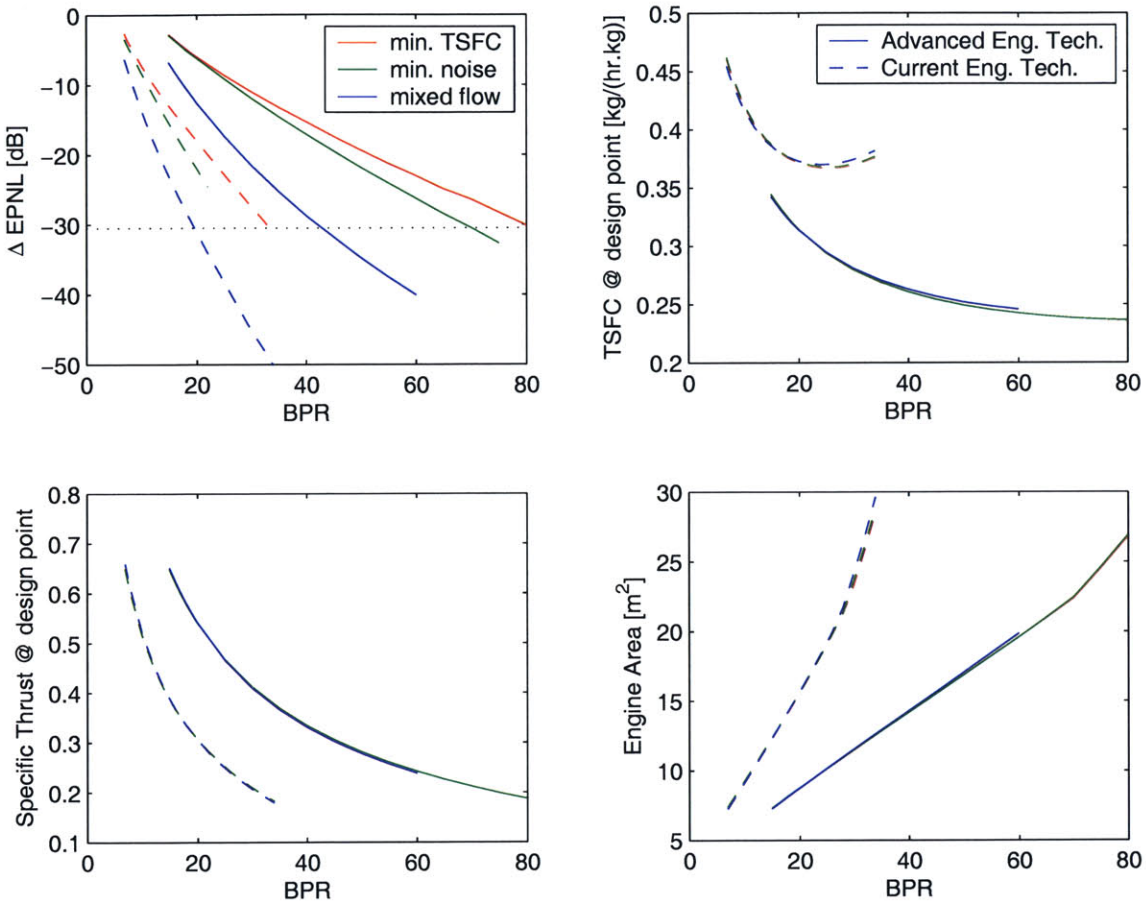

Figure 2-7: Noise reduction potential and engine performance as a function of bypass ratio for "minimum TSFC" (red), "minimum noise" (green), and "mixed flow exhaust" (blue) configurations: Advanced (solid) and Current (dashed) engine technology levels.

2-7 compares the cycle performance and noise reduction potential for the "current" technology level and the "advanced" technology level as a function of bypass ratio.

As observed in Section 2.3.3 for the advanced technology engine, the three different cycle configurations yield similar cycle performance for a given bypass ratio.

As expected, the performance of the current technology engine is much lower than that of the advanced technology engine. For a given bypass ratio, the specific fuel consumption is 10 to 40% higher and the specific thrust is 40 to 60 lower, resulting in 30 to 50% larger engine diameters.

As the bypass ratio increases, the specific thrust decreases faster for the current technology engine than for the advanced technology engine. For bypass ratios above 25, the fuel consumption of the current engine starts increasing, whereas it continues to decrease for the advanced engine. As the

fan pressure ratio decreases with increasing bypass ratio, duct and nozzle losses become dominant, yielding a decrease in cycle thermal efficiency that offsets the increase in cycle propulsive efficiency due to lower jet velocities.

However, as the bypass ratio increases, jet noise levels decrease faster for the current engine compared to the advanced engine. The 30.5 EPNdB reduction objective is reached for a bypass ratio of 33 for the separate flows exhaust case ("minimum TSFC" configuration) and a bypass ratio of only 20 with the mixer nozzle. These bypass ratios are more than half of those required with advanced technology engine.

In order to compare the jet noise reduction potentials of the current and advanced technology levels, the cycle performances of both engine technology levels are plotted as a function of the jet noise level in Figure 2-8.

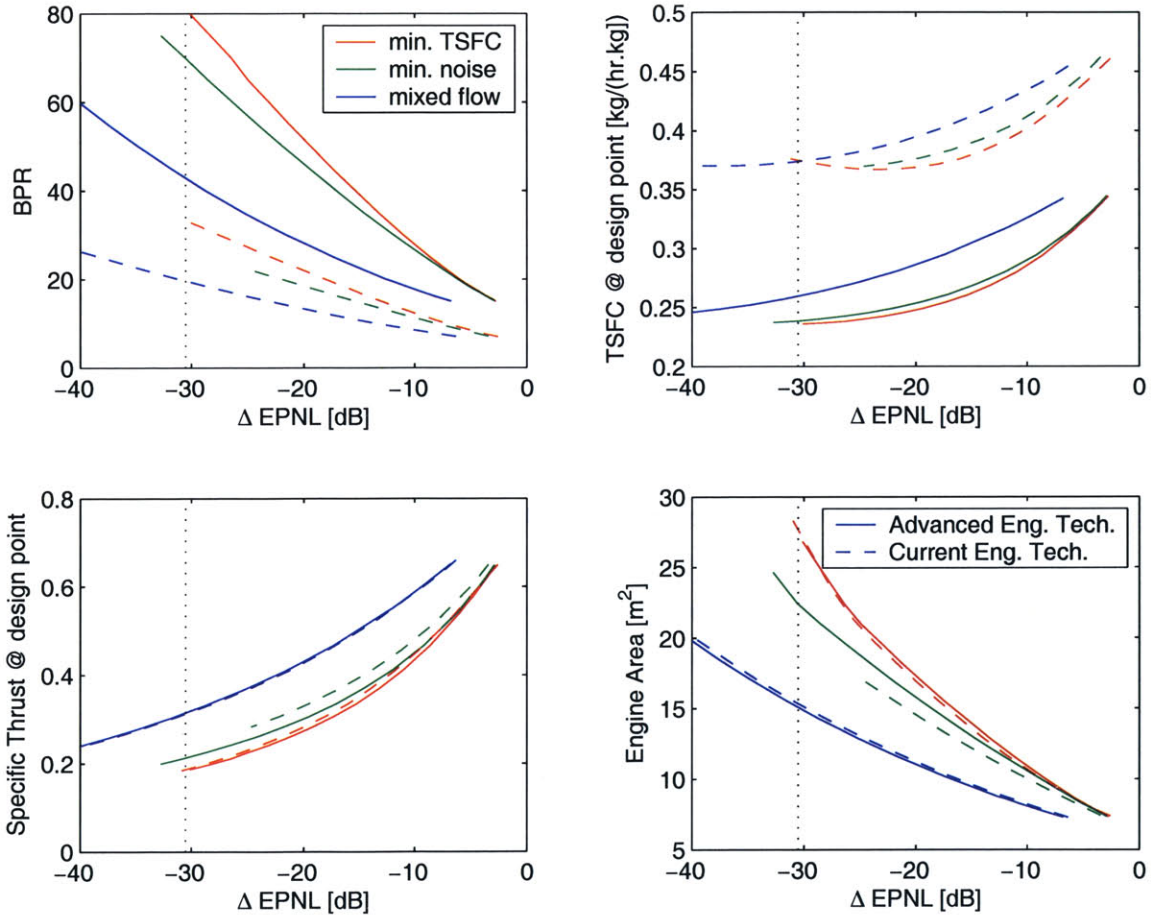

Figure 2-8: Bypass ratio and engine performance as a function of jet noise reduction for "minimum TSFC" (red), "minimum noise" (green), and "mixed flow exhaust" (blue) configurations: Advanced (solid) and Current (dashed) engine technology levels.

For a given noise reduction and cycle configuration, the specific thrust levels of the current and

the advanced technology engines differ by less than 2%. Thus, the higher rates at which jet noise and specific thrust decrease with increasing bypass ratio for the current technology compared to the advanced technology compensate each other. This shows that, within the range considered here, the engine technology level has little impact on the specific thrust for a given noise goal. The major improvement enabled by the advanced technology level engine lies in its higher fuel efficiency: the current technology engine cannot achieve the specific fuel consumption of the baseline advanced technology engine (bypass ratio of 19.5, "minimum TSFC" cycle configuration). On the other hand, as previously observed, the current technology engine requires 50% lower bypass ratios compared to the advanced technology engine to achieve the noise reduction goal. This trade-off is further discussed next.

2.4 Conclusions

2.4.1 Discussion of Results

This study shows that the concept of ultra-high bypass ratio engine can achieve the reduction in flyover jet noise required to enable a functionally-silent aircraft. Two major design trends can be outlined:

1. For a given engine technology level and noise reduction goal, cycle configurations with mixed flow exhaust nozzles require bypass ratios 20 to 50% lower than cycle configurations with separate flow exhaust nozzles. Mixed flow exhaust nozzle cycle configurations achieve higher specific thrusts but yield higher a TSFC.

2. For a given noise reduction, the "advanced" technology level engine requires a bypass ratio approximately twice as large as the "current" technology level engine but achieves 30 to 40% lower specific fuel consumption levels. Specific thrust is almost independent of engine technology level for a given noise reduction.

In order to assess these trends more quantitatively, characteristics of the different cycle designs leading to a 30 EPNdB jet noise reduction are compared in Table 2.3. The results yield the following

Technology level	Advanced				Current	
Cycle configuration	Baseline BWB	min. TSFC	min. noise	mixed flow	min. TSFC	mixed flow
Bypass ratio	19.5	80	69	42	33	19.2
$\Delta TSFC$	0	-26%	-25%	-18%	+18%	+18%
ΔST	0	-66%	-61%	-41.9%	-65%	-42.3%
Engine Area [m^2]	7.3	26.8	22.1	14.8	27.2	15.0

Table 2.3: Cycle configurations leading to a jet noise reduction of 30 EPNdB.

conclusions:

- For the advanced technology level engine, configurations with separate flow exhaust nozzles enable an additional 7% decrease in specific fuel consumption compared to the configuration with mixed flow exhaust (from -18 to -25%). However, the additional drop of 19% in specific thrust (from -42 to -61%) yields engines with 50% larger cross-sectional areas (14.8 to 22.1 m^2, i.e. from three times to twice the area of the baseline engine). Large engine areas create challenges for engine integration, especially if the propulsion system has to be embedded in the airframe. Thus, cycle configurations with mixed flow exhaust nozzles are very promising to achieve the jet noise reduction goals: compared to configurations with separate flow exhaust nozzles, 40% lower bypass ratios and 35% lower engine cross-sectional areas are required. Compared to the baseline engine configuration, a 18% reduction in specific fuel consumption is achieved.

- The current technology engine achieves the jet noise reduction goal for bypass ratios 50% lower than the advanced technology engine. For a given noise goal, similar specific thrust levels are achieved by both advanced and current engines. Thus, similar diameters, hence weight and drag penalties, can be expected for both engine technology levels for a given jet noise goal. However, relative to the baseline engine, the current technology engine yields a 18% increase in specific fuel consumption compared to a 18% decrease for the advanced technology engine. Thus, for advanced technology engine, weight and drag penalties are mitigated by the reduction in specific fuel consumption. For the current technology engine, these penalties and the larger specific fuel consumption add up and inevitably have a detrimental impact on the overall aircraft performance.

2.4.2 Preliminary Propulsion System Design Implications for a Silent Aircraft

Preliminary design implications for the design of the propulsion system enabling a functionally-silent aircraft are given based on previous results. These implications are the following:

1. An engine cycle with mixed flow exhaust is suggested. For a given jet noise goal, this cycle configuration requires lower bypass ratios and achieves higher specific thrust levels than cycle configurations with separate flow exhaust nozzles.

2. The most advanced engine technology available should be applied. A given jet noise goal can then be achieved for lower specific fuel consumption than with a less advanced engine technology level. This improvement in TSFC mitigates the weight and drag penalties associated with the large increase in engine size.

3. The jet noise reduction goal at takeoff can be achieved by using a turbofan engine cycle with mixed flow exhaust nozzle. A bypass ratio of 42 and a fan pressure ratio of 1.183 are required if the advanced engine technology level suggested in Liebeck et al. (1996) can be reached. This engine cycle is suggested to have an 18% lower fuel consumption compared to the baseline blended-wing-body engine. However, its 42% lower specific thrust inevitably requires a twofold increase in cross-sectional area, from 7.3 m^2 for the baseline to 14.8 m^2, assuming a configuration with 3 pod-mounted engines. This engine configuration constitutes the baseline ultra-high bypass ratio (UHBPR) engine. The challenges posed by its integration in the airframe are addressed in Chapter 3.

2.4.3 Modeling Limitations and Suggested Improvements

All engine performance assessments are made at design point, which is at sea level on a hot day at a flight Mach number of 0.2. A refined assessment would consist in selecting the fan pressure ratio for minimum TSFC at cruise conditions, where specific fuel consumption and specific thrust are crucial for the aircraft performance. It is expected that the thrust lapse (ratio of thrust at cruise over thrust at takeoff for a given power setting) decreases with increasing bypass ratio. Level flight at cruise conditions then require higher power setting and therefore higher fuel consumption. Thus, engine performance at cruise is expected to drop faster with increasing bypass ratio than what was observed in the present study. The current model requires refinement to reliably compute engine performance for operating points far from the design point. It is suggested to include components maps in the off-design performance module. If cycles selected in this study based on their takeoff noise reduction potential show excessively poor performance at cruise compared to the baseline engine, it is then necessary to consider variable cycle engines. In particular, variable bypass ratios will be required to achieve optimum performance at cruise. Also, fan pressure ratios will have to be adjusted using, for example, variable pitch blading.

With the expected reduction in jet noise, the fan and core noise are expected to become the dominant propulsion system noise sources. It is suggested that fan noise propagating forward and core noise can be efficiently shielded by embedding the propulsion system in the blended-wing-body airframe. However, fan noise propagating rearward needs to be dramatically reduced. Passive and active noise control methods and low-noise fan designs are envisioned to address this issue.

The engine cycle configurations suggested here should be assessed at the system level by estimating the impact of increasing the engine bypass ratio on the gross weight and range of the aircraft. This would refine the design implications for a silent aircraft delineated here. However, assessing the impact of ultra-high bypass ratio engines on the system performance would require a much more complex and multidisciplinary model capable of

1. estimating the cruise specific fuel consumption more accurately,

2. taking installation losses such as nacelle drag into account, and

3. modeling weight penalties due to the mixer nozzle and larger engines and evaluating their impact on aircraft performance.

Such a model would also refine the noise prediction by taking into account the changes in gross weight and aerodynamic performance in the calculation of the takeoff trajectory.

The assessment of the concept of ultra-high bypass ratio engines should be further refined by considering jet noise level at the sideline measurement point. Directivity and flight effects might lead to different trends than those observed at the flyover measurement point considered here. Another metric based on the area of the noise footprint on the ground could be used with the motivation to minimize the area outside the borders of the airport where noise exceeds the noise goal.

Chapter 3

Distributed Propulsion System Concepts

3.1 Introduction and Objectives

3.1.1 Introduction

In order to achieve the jet noise reduction goal, the ultra-high bypass ratio (UHBPR) cycle suggested in Chapter 2 requires a cross-sectional flow-path area approximately twice as large as that of the baseline blended-wing-body engine. For a configuration of three pod-mounted engines similar to the baseline configuration, UHBPR engines require a 30% larger fan diameter compared to the baseline engine. An increase in fan size inevitably entails a large increase in nacelle weight and installation drag, hence detrimental penalties in terms of aircraft performance. Moreover, as fan diameter increases, the bypass duct internal surface available for acoustic treatment decreases relative to the fan inlet area, yielding a lower fan noise reduction potential from acoustic liners.

A distributed propulsion system embedded in the the blended-wing-body airframe is envisioned to:

1. alleviate the weight and drag penalties associated with pod-mounted propulsion system configurations,

2. effectively shield and control turbomachinery noise,

3. enable the concept of "hidden trailing edge" by ingesting the wing surface boundary layer through a mail-slot inlet. This is expected to yield improvements in aircraft range up to 10% and airframe noise reduction on approach up to 3 dB (see Pilczer (2003) or Section 1.1.2),

4. enable integrated airframe/exhaust system concepts aimed at reducing jet noise such as "distributed exhaust nozzles" (i.e. nozzles splitting the exhaust jet into a large number of small jets) and "high aspect ratio nozzles" (i.e. nozzles exhausting a high aspect ratio jet).

The embodiment of UHBPR engines raises many challenges. In particular, the fan diameter must satisfy geometrical constraints imposed by the blended-wing-body airframe. To address this issue, configurations with multiple small engines and/or multiple fans driven by a common core engine through gearboxes and shafts are suggested. However, small engines yield larger viscous losses due to the Reynolds number effect, and gearboxes introduce weight penalties and shaft power transmission losses. Also, integrated airframe/exhaust system configurations impose weight penalties and introduce thrust losses. Finally, ingesting the boundary layer has a detrimental impact on the cycle performance.

3.1.2 Objectives

The objectives of this chapter are:

- to investigate various engine configurations enabling the embodiment of the propulsion system in a blended-wing-body airframe,
- to evaluate the noise reduction potential of distributed propulsion systems and "distributed exhaust nozzles" (DEN),
- to assess the noise reduction potential of "high aspect ratio nozzles" (HARN) and to estimate the associated thrust losses,
- to delineate, on a preliminary basis, a distributed propulsion system for a silent aircraft.

3.1.3 Approach

The internal dimensions of the trailing edge of the blended-wing-body airframe are first determined. The physical layout of the embedded propulsion system is then deduced from these geometrical constraints and the flow-path areas required by the UHBPR engine cycle.

For this propulsion system layout, various configurations employing multiple small engines and multiple fans driven by a common core engine are then compared to each other based on weight penalty and impact on engine performance. The fan noise signature of a distributed propulsion system with a large number of small fans is assessed.

Integrated airframe/exhaust system concepts are then assessed based on their noise signature and expected thrust losses. First, the noise reduction potential of distributed exhaust nozzles is evaluated using available data and jet noise prediction methods. Noise emitted by high aspect ratio jets is then assessed. For this purpose, a literature review is conducted, and existing data together

with scaling laws are used to modify Stone's jet noise prediction method to render the observed decrease in jet noise with increasing jet aspect ratio. Thrust losses induced by various geometries of high aspect ratio nozzles (HARN) are estimated using viscous three-dimensional computational fluid dynamics.

Finally, design implications for a low-noise distributed propulsion system embedded in the blended-wing-body airframe are outlined.

3.2 Embedded Propulsion System Layout

3.2.1 Methodology

The thermodynamic cycle analysis of UHBPR engine cycle with a mixed flow exhaust nozzle determines the engine flow-path area at the following engine stations:

- propulsion system inlet (A_1)
- fan inlet (A_2)
- mixer nozzle inlet (A_{mix})
- nozzle exit (A_9)

The envisioned propulsion system ingests the air mass flow required by the UHBPR engine cycle through a mail-slot inlet located on the suction side of the blended-wing-body airframe and exhausts a low-velocity jet from the wing trailing edge. Assuming nozzle, core engine, and inlet axial lengths, the locations of the nozzle inlet, fan inlet, and mail-slot inlet are deduced. The internal geometry of the blended-wing-body airframe is analyzed at these locations, and geometrical constraints imposed by the airframe on the propulsion system dimensions are quantified. The flow-path area of the UHBPR engine cycle at these stations is then "distributed" to satisfy these geometrical constraints. Finally, the resulting embedded propulsion system layout is outlined.

3.2.2 Integration Constraints of a Blended-Wing-Body Airframe

Figure 3-1 shows the interior arrangement of the baseline blended-wing-body aircraft configuration. It is suggested that the propulsion system can be embedded in the trailing edge of the wing, currently the "unpressurized afterbody" and "emergency egress tunnels" areas, without imposing drastic modifications to the inner wing fuel tanks, and the cabin and cargo areas. This allows a maximum propulsion system length of approximately 8 m. Typical inlet and core engine lengths of 1 m and 3 m are assumed respectively. The exhaust system is expected to also play the role of a mixer nozzle for the UHBPR engine cycle. To achieve fully-mixed core and bypass flows, the

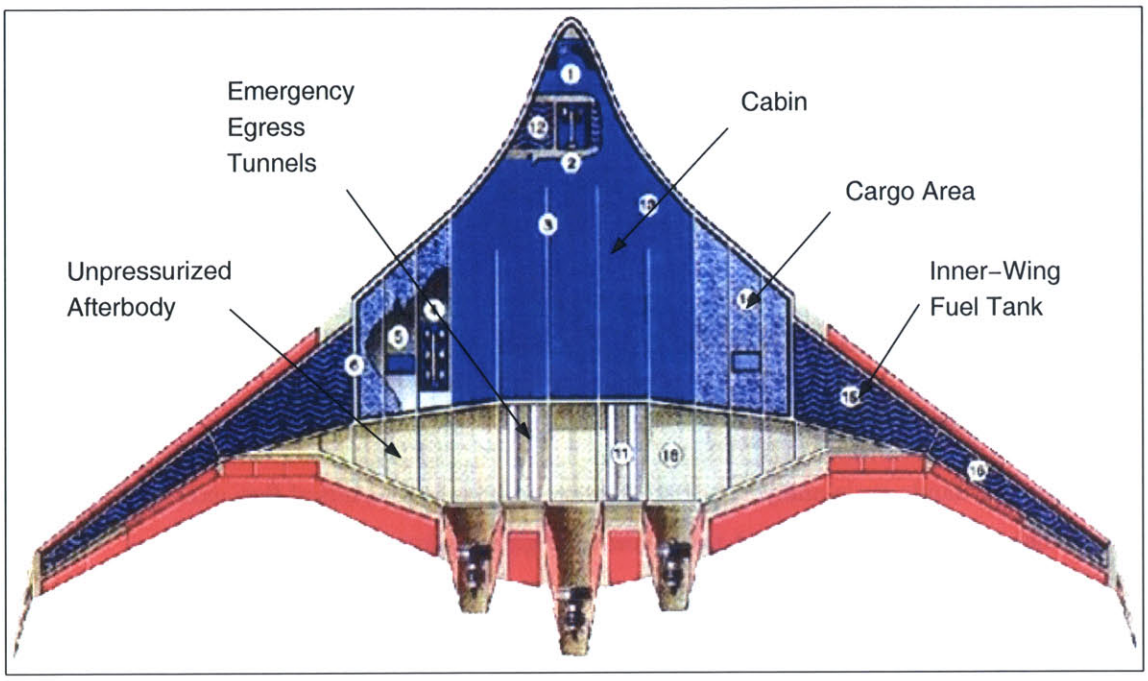

Figure 3-1: Interior arrangement of the blended-wing-body aircraft (from Liebeck et al. (1996)).

maximum possible nozzle length is required. Thus, a nozzle length of 4 m is assumed. The spanwise extent of the propulsion system is limited to leave room for control surfaces at the trailing edge of the wing and to avoid structural issues at the wing leading edge.

Figure 3-2 shows the resulting axial locations and maximum allowed spanwise extents of the mail-slot inlet, the fan inlet, the nozzle inlet, and the nozzle exit for a propulsion system embedded in the blended-wing-body airframe.

The space available to embed the propulsion system inside the airframe needs to be determined at these locations. For this purpose, a three-dimensional model of the blended-wing-body aircraft is "cut" by curved surfaces at the mail-slot inlet, fan inlet, and nozzle inlet. The resulting cross-sections are shown on Figure 3-3. Assuming a rectangular propulsion system layout, the maximum area that the propulsion system can occupy in each cross-section is indicated in white.

3.2.3 Embodiment of UHBPR Engines in a Blended-Wing-Body Airframe

The total flow-path areas of the UHBPR engine cycle prescribed in Chapter 2 are reported in Table 3.1. These data are presented with their corresponding geometrical constraints of the blended-wing-body airframe obtained in Section 3.2.2.

Because of the axisymmetric geometry of the fans and the presence of spinners at the fan centers,

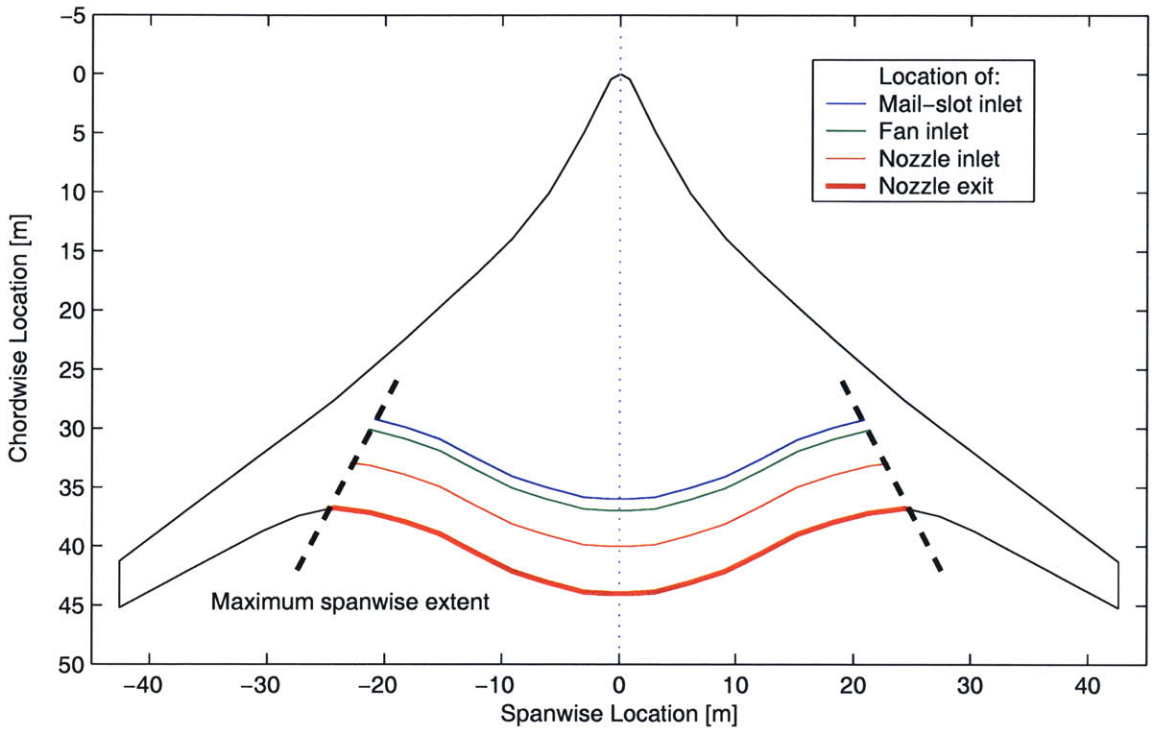

Figure 3-2: Mail-slot inlet, fan inlet, nozzle inlet, and nozzle exit locations and maximum allowable spanwise extent.

the total rectangular area occupied by the fans (A_{rect}) is larger than the total flow-path area of the fan inlet (A_2). For N_f fans of diameter D_f, $A_{rect} = (N_f D_f) \cdot D_f$. Introducing the fan blade hub-to-tip ratio r, the diameter of each fan is

$$D_f = \sqrt{\frac{4}{\pi} \cdot \frac{A_2/N_f}{\sqrt{1-r^2}}}. \tag{3.1}$$

Thus,

$$A_{rect} = \frac{4}{\pi} \frac{A_2}{\sqrt{1-r^2}}. \tag{3.2}$$

With $r = 0.3$, this yields $A_{rect} \approx 1.4 A_2$. To enable the embodiment of fans in the airframe, the cross-section of the fan inlet must satisfy the constraints imposed by the airframe dimensions.

Using data presented in Table 3.1, the layout of an embedded propulsion system configuration satisfying the geometrical constraints imposed by the blended-wing-body airframe dimensions can be outlined. The maximum rectangular areas allowed at the mail-slot inlet, the fan inlet, and the nozzle inlet are 31%, 6% and 35% larger, respectively, than the areas required by the UHBPR engine cycle. Thus, the fan inlet is likely to be the most geometrically constraining station.

Based on this observation, the propulsion system layout is determined at the different stations

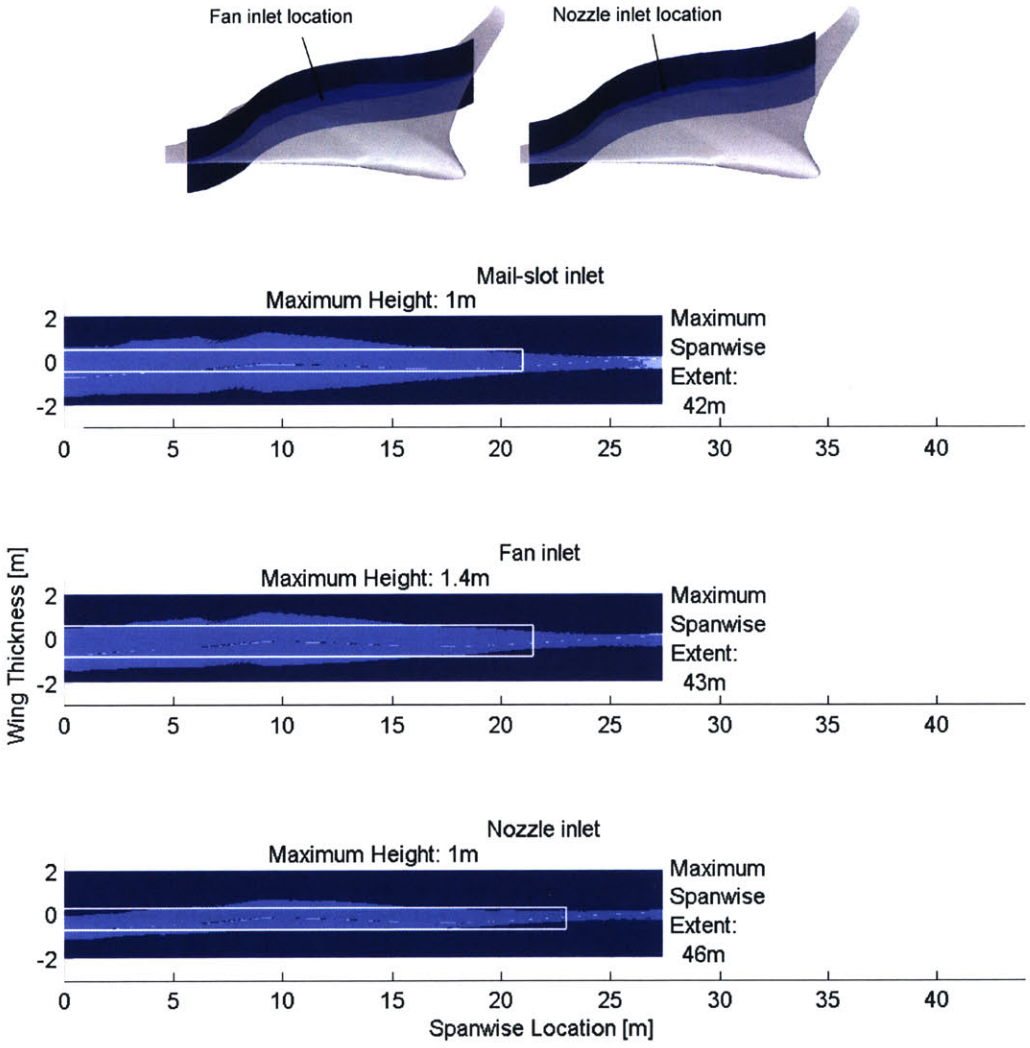

Figure 3-3: Cross-sections of the blended wing body airframe at the mail-slot inlet, the fan inlet, and the exhaust nozzle inlet.

by applying the following procedure:

Fan Inlet

The maximum fan diameter corresponds to the maximum height allowed at the fan inlet: $D_{f_{max}} = 1.4$ m. The minimum fan diameter is reached for the maximum spanwise extent $w_{2_{max}}$. The required fan inlet rectangular area then yields: $D_{f_{min}} = \frac{A_{rect}}{w_{2_{max}}} = 1.32$ m. Thus,

$$1.32\ m < D_f < 1.4\ m. \tag{3.3}$$

	UHBPR cycle requirements	Airframe dimensions	
Station	Area [m^2]	maximum span-wise extent [m]	maximum height [m]
Mail-slot inlet	32.1	42	1
Fan inlet (flow-path)	40.4	43	1.4
Fan inlet (A_{rect})	56.6	43	1.4
Nozzle inlet	34.1	46	1
Nozzle exit	36.3	50	-

Table 3.1: Total area requirements for the ultra-high bypass ratio cycle and airframe dimensions at the corresponding location.

For a given fan diameter, the number of fans is: $N_f \frac{A_{rect}}{D_f^2}$. For the minimum and maximum fan diameters, this yields $28.8 < N_f < 32.6$, i.e:

$$29 \leq N_f \leq 32. \tag{3.4}$$

A total number of 30 fans is selected in order to enable various multiple engine/fan propulsion system configurations. Such propulsion system configurations are developed further in the next section.

In a 30-fan configuration, the total spanwise extent of the fan inlet is 41.2 m. The height of the fan inlet is equal to the fan diameter: $D_f = 1.37$ m.

Mail-Slot Inlet

The spanwise extent of the mail-slot inlet is assumed equal to that of the fan inlet. From the flow-path area at this station, the height of the mail-slot inlet is:

$$h_1 = A_1/w_1 = 0.78\ m. \tag{3.5}$$

Both constraints on spanwise extent and height are satisfied.

Nozzle Inlet and Exit

In order to determine the appropriate nozzle geometry, thrust losses induced by integrated airframe/exhaust systems need to be assessed. This study is performed later in this chapter.

At this stage, it can be noticed that the nozzle inlet aspect ratio must be between 34 and 62 to satisfy the geometrical constraints imposed by the blended-wing-body airframe.

3.2.4 Conclusions

This study shows that the ultra-high bypass ratio engine cycle delineated in Chapter 2 can be embedded in the airframe of the blended-wing-body provided that a configuration with thirty 1.37m-diameter fans is adopted. The mail-slot inlet ingests the wing surface boundary layer over a spanwise extent corresponding to 48% of the aircraft span.

At this stage, means to enable a distributed propulsion system configuration with 30 fans are required, and the geometry of the exhaust system needs to be determined.

3.3 Multiple Engine/Fan Propulsion System Configurations

3.3.1 Introduction

In order to achieve the embedded propulsion system layout described in Section 3.2, a drastic departure from conventional propulsion system configurations is required. In particular, the most constrictive requirement imposed by the blended-wing-body airframe is that the total fan inlet area must be distributed among 30 fans as required by the UHBPR engine cycle from Chapter 2.

Configurations with a large number of small engines and multiple fans driven by a common core engine are assessed in this section.

3.3.2 Approach

Expected advantages and drawbacks of multiple engine/fan configuration are first outlined. Various distributed propulsion system configurations with multiple small engines and multiple fans driven by a common core engine are then compared to each other using the following metrics:

- weight penalty
- shaft power transmission losses
- core engine mass flow (Reynolds number effect losses)
- fan gearbox power requirements

3.3.3 Multiple Small Engines

The idea of using multiple small engines to power the silent aircraft simply consists in splitting the total required thrust output among a large number of small engines. For a constant fan hub-to-tip ratio and a given total fan area requirement, the fan diameter is inversely proportional to the square root of the number of engines. For example, increasing the number of engines from 3 to 30 yields a decrease in fan diameter from 4.3 m to 1.37 m for the given UHBPR cycle.

To first order, large pod-mounted engines must be proportionally scaled down to achieve the right fraction of the total thrust. However, as the core engine size decreases, the Reynolds number also decreases and viscous losses in turbomachinery components increase. Thus, small core engines achieve lower thermal efficiencies compared to larger core engines. This "Reynolds number effect" inevitably produces a drop in cycle performance for small core engines, i.e. higher specific fuel consumption and lower specific thrust.

Moreover, it is expected that multiple small engines entail a weight penalty compared to configurations with a small number of large engines. The weight of engine accessories and engine parts do not scale proportionally to the engine thrust output (cube-square scaling law). Therefore, the total weight of multiple small engines is likely to be larger than the weight of a few large engines for the same total power.

The concept of multiple small engines may also benefit from economical (economies of scale for engine manufacturers) and passenger safety (increased redundancy) standpoints, but potential drawbacks from the operational point of view must also be taken into account (increased maintenance costs for airlines). These trade-offs are similar to those already existing between 2- and 4-engine aircraft and will not be further discussed in this study.

3.3.4 Multiple Fans Driven by a Common Core Engine

The idea of multiple fans driven by a common core engine aims to alleviate the main issues associated with the concept of multiple small engines presented above. With a conventional turbofan configuration, the only way to simultaneously decrease fan diameter and achieve a given bypass ratio is to reduce the size of the engine. This leads to a lower thrust output that has to be compensated by an increased number of engines. It is suggested that the total fan inlet area required for a certain bypass ratio given a thrust output be distributed among multiple fans driven by a common core engine. The core engine shaft power output is transmitted to the fans via gearboxes and shafts. The multiple fan concept allows a decrease in required fan diameter at constant bypass ratio and core engine size. To satisfy the geometrical constraints imposed by the blended-wing-body airframe at the fan inlet outlined in Section 3.2, the fans are distributed spanwise in parallel.

This idea alleviates the penalty in core efficiency due to Reynolds number effects but raises new challenges. First, gearboxes required to mechanically transfer power from the core engine to the fans inevitably introduce shaft power transmission losses that must be taken into account in the cycle analysis. In the case of a large number of fans driven by a common core engine, these losses accumulate through each gearbox and significantly alter the overall propulsion system performance. The first gearbox directly driven by the core engine has to withstand the total shaft power output from the core engine. These gearboxes are expected to be heavier than gearboxes driving a single fan. In the limit of a single core engine driving a large number of fans, excessive shaft power transmission

losses and weight penalty are expected to offset the benefits of the higher thermal efficiency of the larger core engine. In this limiting case, a single large core engine is envisioned as a power generator to drive the fans by electric motors. Replacing shafts and gearboxes by electric wires is expected to yield a large weight reduction. However,

1. total power losses due to the double mechanical/electrical power conversion are expected to be significantly higher than mechanical power losses in gearboxes and shafts, and

2. for a similar power output, electric motors are excessively heavy compared to conventional turbomachinery. For example, state-of-the-art superconducting electric engines of 5 and 36.5 MW power output are expected to weight 7 and 70 tons respectively (see Jaworski (2004) and American Superconductor (2003)). This represents an approximately tenfold increase in propulsion system weight compared to conventional turbomachinery of same power output.

Finally, multiple fans driven by a common core engine inevitably introduce additional turbomachinery complexity. This is expected to pose reliability, maintenance, and cost issues.

3.3.5 Evaluation of Multiple Engine/Fan Propulsion System Configurations

The key metrics to evaluate an embedded propulsion system are:

- weight penalty due to the large number of core engines, transmission shafts, and gearboxes,
- shaft power transmission losses, scaling with the number of fans driven by a common core engine,
- Reynolds number effects, scaling with the core engine size,
- fan gearbox power requirements.

For reference, power input into gearboxes developed for the ADP and PW8000 projects are 30 MW and 24 MW respectively (see Flug Revue (1998)), with mechanical efficiencies of order 99.5%. Considering likely improvements in gearbox technology, the maximum fan gearbox power input is limited to 40 MW for this study. The following propulsion system configurations are compared with respect to these metrics in Table 3.2. Configurations B and A are conventional pod-mounted three-engine setups for the baseline blended-wing-body engine cycle and the ultra-high bypass ratio engine cycle given in Chapter 2, respectively. Configurations D1 to D4 are distributed propulsion system configurations for the ultra-high bypass ratio engine cycle. To enable distributed propulsion system embodiment, each configuration has a total of thirty 1.37m-diameter fans as suggested in Section 3.2. The number of core engines and fans driven by a common core engine varies from one configuration to another. These propulsion system configurations are sketched in Figure 3-4.

Config-uration	No. of core engines	No. of fans per core	D_f [m]	$\dot{m}_{core}$ [kg/s]	Gearbox power [MW]
B	3	1	3.3	68	48.7
A	3	1	4.3	56.4	38.8
D1	2	15	1.37	84.6	58.2
D2	6	5	1.37	28.2	19.4
D3	10	3	1.37	16.9	11.6
D4	30	1	1.37	5.6	3.9

Table 3.2: Comparison of propulsion system configurations A, B, and D1-4.

Increasing the number of core engines (from A to D2-D3-D4) significantly reduces the required fan gearbox power but yields smaller core engines, hence larger viscous losses. With less than 3 core engines (configuration D1), the required gearbox power exceeds the upper limit of 40 MW, which is considered achievable without excessive weight penalty. For a given fan diameter, increasing the number of fans driven by a common core engine (D4-D3-D2-D1) requires larger, hence more efficient, core engines. However, this inevitably increases the shaft power transmission losses and requires larger, heavier gearboxes. The configuration with multiple small engines (D4) entails a large drop in efficiency due to Reynolds number effect and introduces a weight penalty due to the large number of core engines (cube-square law). On the other hand, relatively light gearboxes can be used because of the relatively low gearbox power requirement.

3.3.6 Conclusions

Multiple fan/engine configurations enable the embodiment of the propulsion system in the blended-wing-body airframe by significantly reducing the required fan diameter and permitting propulsion system layouts geometrically compatible with the airframe geometry.

Configurations involving only multiple small engines (D1) or a large number of fans driven by a few core engines (D4) are likely to yield poor propulsion system performance due to excessively high viscous losses due to Reynolds number effect (D4) or high shaft power transmission losses and large required gearbox power (D4). The trends in shaft power transmission losses, Reynolds number effect, and required gearbox power suggest that propulsion system configurations combining multiple small engines and multiple fans driven by a common core engine (D2-D3) can achieve a compromise between the different weight and efficiency penalties.

In order to further assess multiple fan/engine propulsion system configurations, the current study can improved as follows. First, the total weight of the propulsion system needs to be estimated for given gearbox power input, total number of core engines, fans, shafts and gearboxes. Next, the impact of multiple fan/engine configurations on engine cycle performance can be quantified by modifying the tools developed in Chapter 2 to account for Reynolds number effects (for example,

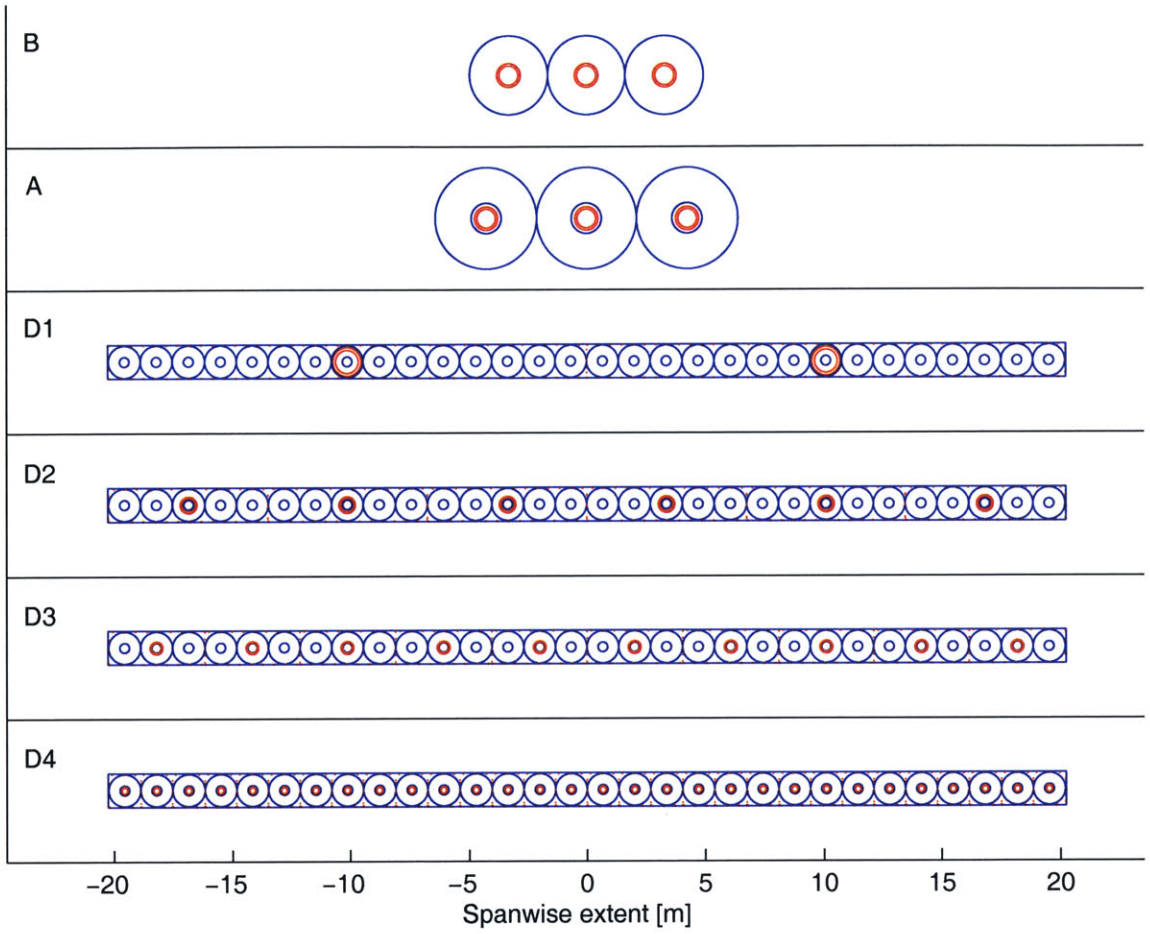

Figure 3-4: Fan inlet layout for propulsion system configurations A, B, and D1-4 (see Table 3.2). Blue: fan - Red: core engine.

by computing the component efficiencies as a function of the core engine size) as well as shaft power transmission losses.

3.4 Noise Signature of Multiple Fans

3.4.1 Introduction

The study performed in Section 3.2 shows that a configuration with a total of thirty 1.37m-diameter fans in parallel is required to embed the propulsion system in the blended-wing-body airframe. In Section 3.3, multiple engine/fan configurations enabling this propulsion system layout are outlined.

The impact of configurations with a large total number of fans on fan noise signature is assessed in this section. As the fan diameter decreases at constant blade tip Mach number, the total fan noise acoustic power is constant, but the rotating speed increases of each fan, leading to higher blade

passing frequency, hence higher fan noise frequencies. A favorable frequency shift above the range of maximum sensitivity of the human ear is expected to yield lower perceived noise level.

Potential noise reduction benefits resulting from this frequency shift effect are quantified in this section.

3.4.2 Methodology

Fan noise EPNL is computed at takeoff for a blended-wing-body aircraft with baseline and UHBPR engines. The modeling framework presented in Chapter 2 first computes fan rotating speed, fan mass flow, and fan blade loading during the takeoff maneuver. The fan noise is then predicted using Heidmann's semi-empirical method (see Heidmann (1975), Groeneweg et al. (1991), Zorumski (1982)). In Heidmann's method, it is assumed that the acoustic power radiated by tone and broadband noise sources follows the scaling law:

$$W \propto A_f(\Delta T_t/T_t)^a M_{tip}^b, \tag{3.6}$$

where A_f is the fan flow-path area, $\Delta T_t/T_t$ is related to the blade loading, and M_{tip} is the blade tip Mach number. In Kontos et al. (1996), the accuracy of Heidmann's fan noise prediction method is improved by adjusting constants and parameters to better render fan noise experimental measurements. These improvements are applied in the following noise predictions ("GE method" in ANOPP).

In order to model multiple fan propulsion system configurations, the total fan flow-path area A_2 is distributed into N_f fans of area $A_f = A_2/N_f$. The fan flow coefficient $\Phi = \frac{u_2}{U_{tip}}$ and the blade loading coefficient $\Psi = \frac{\Delta h_t}{U_{tip}^2}$ characterize the level of technology of the blade design. Thus, Φ and Ψ are kept constant to establish a consistent technology level for various propulsion system configuration fan geometries.

Fixing Φ and Ψ also fixes the blade tip Mach number and blade loading (ΔT_t) for all fans. Therefore, the overall sound pressure level (OASPL) predicted by Heidmann's method for multiple fans with total area A_2 is independent of N_f. Only the spectral distribution of the total acoustic power varies with N_f. The fan noise peak frequency corresponds to the blade passing frequency: $f_{peak} = B \cdot \frac{\omega_1}{2\pi} = B \cdot \frac{M_{tip}}{D_f} \cdot \frac{c_0}{\pi}$, where B is the number of rotor blades, ω_1 is the low-pressure spool rotational speed, and D_f is the fan diameter. Since $D_f = \sqrt{\frac{4A_f}{\pi(1-r^2)}}$, the peak frequency scales with the square root of the number of fans with a constant number of blades and hub-to-tip ratio r.

3.4.3 Results

A parametric study is performed by increasing N_f from 1 to 64 for both the baseline blended-wing body and the UHBPR engine cycles. Broadband and tonal noise sources are taken into account in the computation. The reference EPNL corresponds to the baseline three-engine ($N_f = 3$) configuration.

The variations in EPNL relative to this reference are shown in Figure 3-5 as a function of the number

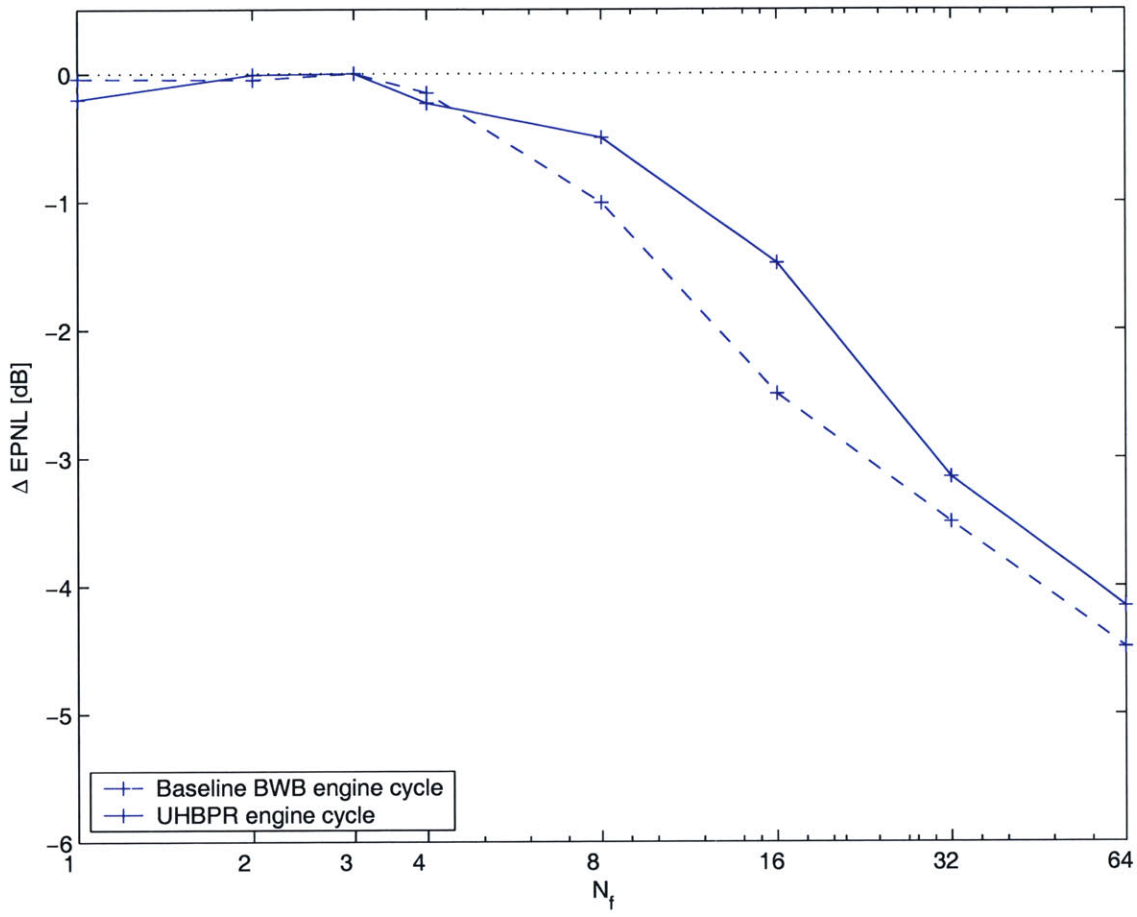

Figure 3-5: Variations in flyover fan noise EPNL for the baseline (dashed) and UHBPR (solid) engines as a function of the total number of fans using Heidmann's jet noise prediction method (with "GE method").

of fans.

The sensitivity of the human ear decreases for frequencies higher than 1 to 2 kHz. This fact is taken into account in the computation of the EPNL. For low number of fans ($N_f < 8$), the peak frequency lies in the 1-2 kHz band, yielding an EPNL effectively independent of N_f. As the number of fans increases, the EPNL decreases since the peak frequency exceeds the 1-2 kHz band as the fan noise spectrum is shifted toward higher frequencies.

3.4.4 Conclusions

Compared to a three engine configuration, this study suggests that the propulsion system configuration with 30 fans outlined in Sections 3.2 and 3.3 yields a reduction of approximately 3 dB in perceived fan noise at takeoff due to a beneficial frequency shift effect.

Considering the objectives of current fan noise reduction technologies, this is a significant noise reduction. However, further fan noise reductions are required to achieve the silent aircraft noise goals. For this purpose, active and passive noise control technologies and low-noise fan designs need to be developed. The effect of fan noise shielding enabled by the embedded propulsion system must also be assessed.

3.5 Distributed Exhaust Nozzles

3.5.1 Introduction

At this stage, the appropriate exhaust system for a distributed propulsion system embedded in the blended-wing-body airframe needs to be determined.

This section assesses the viability of the concept of distributed exhaust nozzle (DEN) for a silent aircraft based on a literature review and available jet noise prediction tools.

Distributed exhaust nozzles aim to reduce jet mixing noise by splitting the exhaust jet into a large number of small "jetlets" by discharging the flow through a nozzle of appropriate geometry, e.g. slots, orifices, or tubes.

This concept exploits two distinct phenomena involved in jet noise generation:

- splitting the large jet into many jetlets increases the total jet area exposed to ambient air, leading to a more rapid mixing. Suitably spaced jetlets then interact and coalesce into a single jet at lower velocity and temperature, resulting in lower jet mixing noise,

- the peak frequency of the jet mixing noise occurs at an approximately constant Strouhal number: $St = \frac{D_{jet} \cdot f_{peak}}{u_{jet}}$. Thus, for a constant jet velocity u_{jet} set by the nozzle pressure ratio, the peak frequency increases as the jet diameter decreases. For a sufficiently large number of small "jetlets", the jet noise peak frequency can be shifted beyond the range of frequencies for which the sensitivity of the human ear is maximum. This is expected to reduce the effective perceived jet noise level.

3.5.2 Previous Work on Distributed Exhaust Nozzles

The concept of DEN has been applied more or less successfully since the late 1950's. The initial objective was to develop noise suppression devices for turbojet engines.

Coles (1957) observed jet noise reductions of 5 dB with thrust losses of approximately 2% using exhaust nozzles with multiple slots generating 3 to 18 jetlets.

More recently, studies focused on DENs from an integrated airframe/exhaust system perspective. As reported by Kinzie et al. (2001), first generation DEN designs (generating 72 jetlets) demonstrated

a low suppression potential, but introduced 5% thrust losses compared to equivalent axisymmetric nozzles.

Using similar designs, Gaeta and Ahuja (2002) achieved reductions in overall sound pressure level (OASPL) of approximately 4 dB at the cost of large thrust losses (10%).

Improved designs generating 100 jetlets achieved reductions in OASPL of 10 dB with 10% of thrust losses (see Kinzie et al. (2002)). The jet mixing noise reduction was explained by the interaction of jetlets and a jet-jet shielding phenomenon.

3.5.3 Assessment of Frequency Shift Effects

Studies presented above do not clearly reveal any trend or scaling law describing the jet noise pattern radiated by DENs. From one study to another, results vary in terms of thrust losses and noise reduction. In order to predict the jet noise reduction potential of DEN, methods such as CFD and CAA accounting for jet-jet interaction and noise shielding effects are required.

However, it is suggested that the effect of the frequency shift due to DENs on perceived jet noise can be assessed with available semi-empirical jet noise prediction methods such as Stone's method (see Stone (1974); Stone and Montegani (1980)).

Methodology

In order to assess the perceived jet noise emitted by DENs using Stone's prediction method, following assumptions are required:

- A single jet of area A_{ex} is split into N_j jetlets of area A_{ex}/N_j with the same velocity, temperature, and density as the large jet. This arrangement is expected to yield thrust losses. According to state-of-the-art designs, it is assumed that for $N_j = 100$, the DEN yields 10% thrust losses.
- The interaction between the N_j jetlets is neglected.
- The jet-jet noise shielding is neglected.

In Stone's jet noise prediction method, the OASPL at 90° of polar angle is proportional to the jet area. Thus, the total OASPL emitted by N_j non-interacting jetlets of area A_{ex}/N_j is equal to the OASPL radiated by a single jet of area A_{ex}. Since the Strouhal number driving the jet noise peak frequency is constant, the jet noise peak frequency is proportional to $\frac{1}{D_j} \propto \sqrt{N_j}$.

The variations in flyover EPNL resulting from this jet noise frequency shift are computed using the modeling framework presented in Chapter 2 for a blended-wing-body aircraft with baseline and UHBPR engines.

3.5.4 Results

A parametric study is performed by increasing the number of jets from 1 to 128. According to the performance of current DEN designs, DENs generating a larger number of jetlets are expected to incur detrimental thrust losses. The increase in the number of jets yields a tenfold decrease in jet diameter from approximately 5 m to 0.5 m. Jet area decreases from 19 m^2 to 0.19 m^2. It is assumed that Stone's jet noise prediction method remains valid over this range of areas.

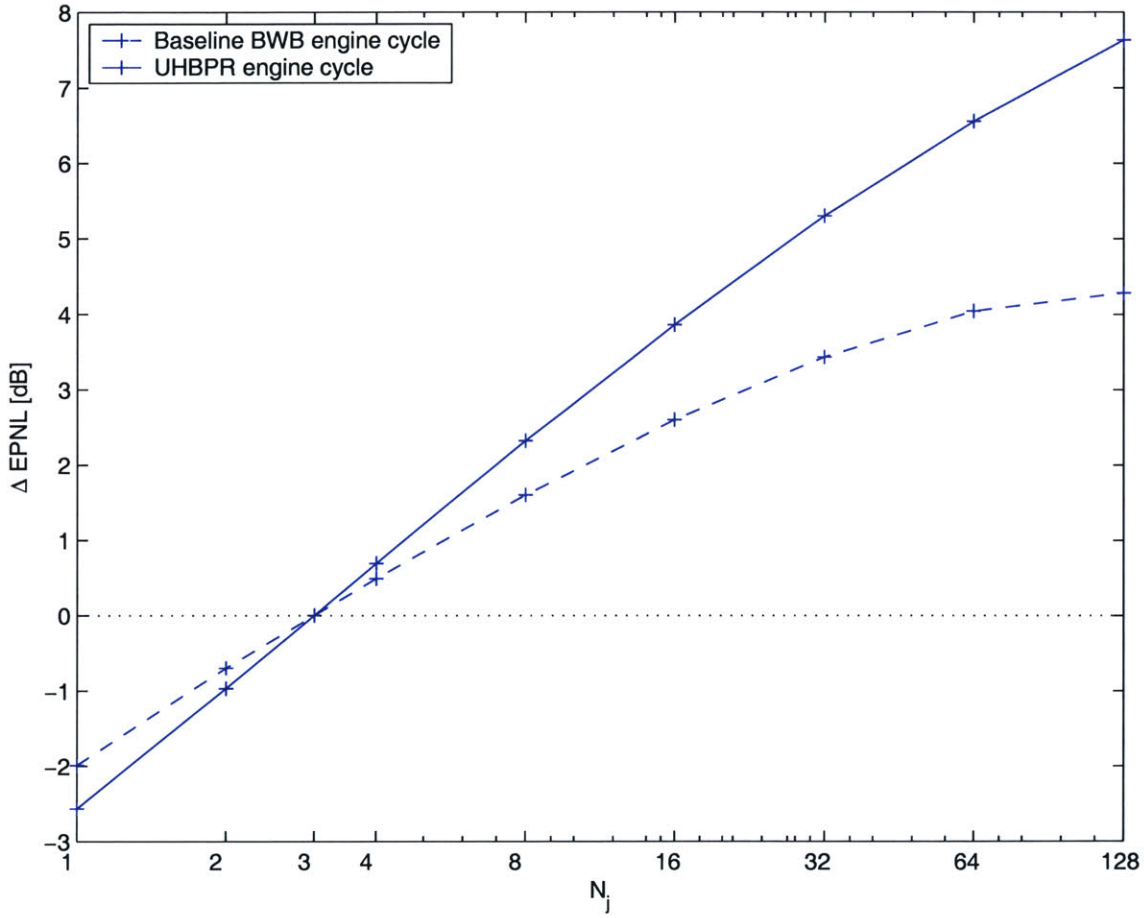

Figure 3-6: Variations in flyover jet noise EPNL for the baseline (dashed) and UHBPR (solid) engines as a function of the number of jets using Stone's jet noise prediction method.

Figure 3-6 shows the variation in EPNL relative to the reference configurations ($N_j = 3$) as a function of the number of jets.

For both engine cycles, the EPNL continually increases with the number of jets. The relatively large jet areas and low jet velocities achieved by the baseline and UHBPR engine cycles yield jet noise peak frequencies of approximately 100 Hz in 3-jet configurations. Thus, as the number of jets increases, the region of the spectrum with the higher sound pressure levels gets closer to the 1-2 kHz

frequency band, leading to an increase in perceived noise level. For 128 jets, this frequency shift effect raises EPNL levels by 4.2 dB and 7.5 dB for the baseline blended-wing-body engine cycle and the UHBPR engine cycle, respectively.

On the other hand, decreasing the number of jets from three to one yields a decrease in EPNL of approximately 2 dB for both engine cycles. In this case, perceived jet noise is decreased as the spectrum reaches peak frequencies of order 50 Hz.

3.5.5 Conclusions

Current distributed exhaust nozzle designs generating approximately 100 jetlets can achieve a 10 dB reduction in jet noise OASPL. This jet noise reduction is essentially due to jetlets interaction and jet-jet noise shielding effected (Kinzie et al. (2002)). However, these nozzle designs introduce thrust losses of approximately 10%.

For UHBPR engine cycles, it is suggested that the frequency shift effect associated with the generation of 100 non-interacting jetlets yields detrimentally increases the jet noise EPNL by approximately 7 dB. Further increasing the number of jetlets can result in a beneficial frequency shift effect but at the cost of detrimental thrust losses.

On the other hand, a reduction of 2 dB in EPNL can be achieved by merging the three initial jets into a single large jet producing low frequency noise.

A single large jet configuration is expected to achieve a better compromise than a DEN generating 100 jets in terms of jet noise reduction potential and exhaust system performance (i.e. thrust losses and weight penalty). The concept of high aspect ratio nozzle is suggested as a good candidate to enable an embedded exhaust system with a single large jet. Jet noise emissions and thrust losses induced by this type of nozzle geometry are assessed next.

3.6 High Aspect Ratio Nozzles

3.6.1 Introduction

The embedded propulsion system layout suggested in Section 3.2 requires a nozzle inlet aspect ratio of 34 to 62 to both satisfy the geometrical constraints imposed by the blended-wing-body airframe and provide the flow-path area necessary for the UHBPR engine cycle at this station. For the maximum spanwise extent allowed at the nozzle exit, i.e. 50 m, a nozzle height of 0.73 m is required to satisfy the total exhaust area of 36.3 m^2. This yields a maximum nozzle exit aspect ratio of 69.

Thus, a high aspect ratio nozzle (HARN) is envisioned to collect the bypass and core flows and distribute the propulsion system exhaust throughout the trailing edge of the blended-wing-body airframe.

The noise reduction potential of high aspect ratio jets is first assessed. For these jet geometries, the total jet area exposed to ambient air is larger than for axisymmetric jets. This is expected to induce quicker mixing, hence lower jet noise levels.

An evaluation of the impact of integrated airframe/exhaust systems on the propulsion system performance is crucial to assess the viability of the embedded propulsion system. Thus, thrust losses induced by high aspect ratio nozzles are estimated for various nozzles geometries.

3.6.2 Jet Noise of High Aspect Ratio Nozzles

The results of various experimental jet noise studies for a wide range of jet aspect ratios are used to develop a prediction tool capable of determining the trends in jet noise reduction as a function of jet aspect ratio.

Presentation and Analysis of Available Data

The aeroacoustics of high aspect ratio jets have been extensively studied over the last half-century. Coles (1959) described jet noise emission through rectangular slot nozzles of aspect ratio 14 and 100. Gruschka and Schrecker (1972) measured noise radiated by rectangular nozzles of aspect ratio 30, 60, and 120. More recently, Munro and Ahuja (2003a,b,c) analyzed jet noise emitted by rectangular slots of aspect ratio varying from 60 to 3000. A detailed literature review on this subject is presented in Appendix B.1.1. The following conclusions are deduced from this study.

Jets of relatively low aspect ratio (below 10 to 30) tend to radiate noise levels very similar to round jets of same velocity, temperature, and density.

The overall sound pressure levels (OASPL) emitted by jets of high aspect ratios (larger than 200) decrease with increasing aspect ratio. This trend is observed by Munro and Ahuja (2003a,b,c)) in the plane containing the nozzle minor axis, at a polar angle of 90° (i.e., perpendicular to the jet axis). This decrease in jet noise with increasing aspect ratio is attributed to a change in the length scale driving the noise generation and a change in convection Mach number (M_c) compared to circular jets. For intermediate values of the jet aspect ratio (from 20 to 100), available data show jet noise reductions of order 2 dB compared to round/low aspect ratio jet geometries.

In order to compare data from various studies, all available experimental results are converted to a common metric. This procedure is described in more details in appendix B.1.2. The available data are gathered in Table B.1 and plotted in Figure 3-7.

Three different behaviors of jet noise radiation as function of jet aspect ratio can be distinguished:

- For low aspect ratio ($1 < AR < 10$ *to* 30), data reported by Tam and Zaman (2000), Coles (1959), Maestrello and McDaid (1971), and Gruschka and Schrecker (1972) show that jet noise sound pressure level is approximately independent of the jet aspect ratio.

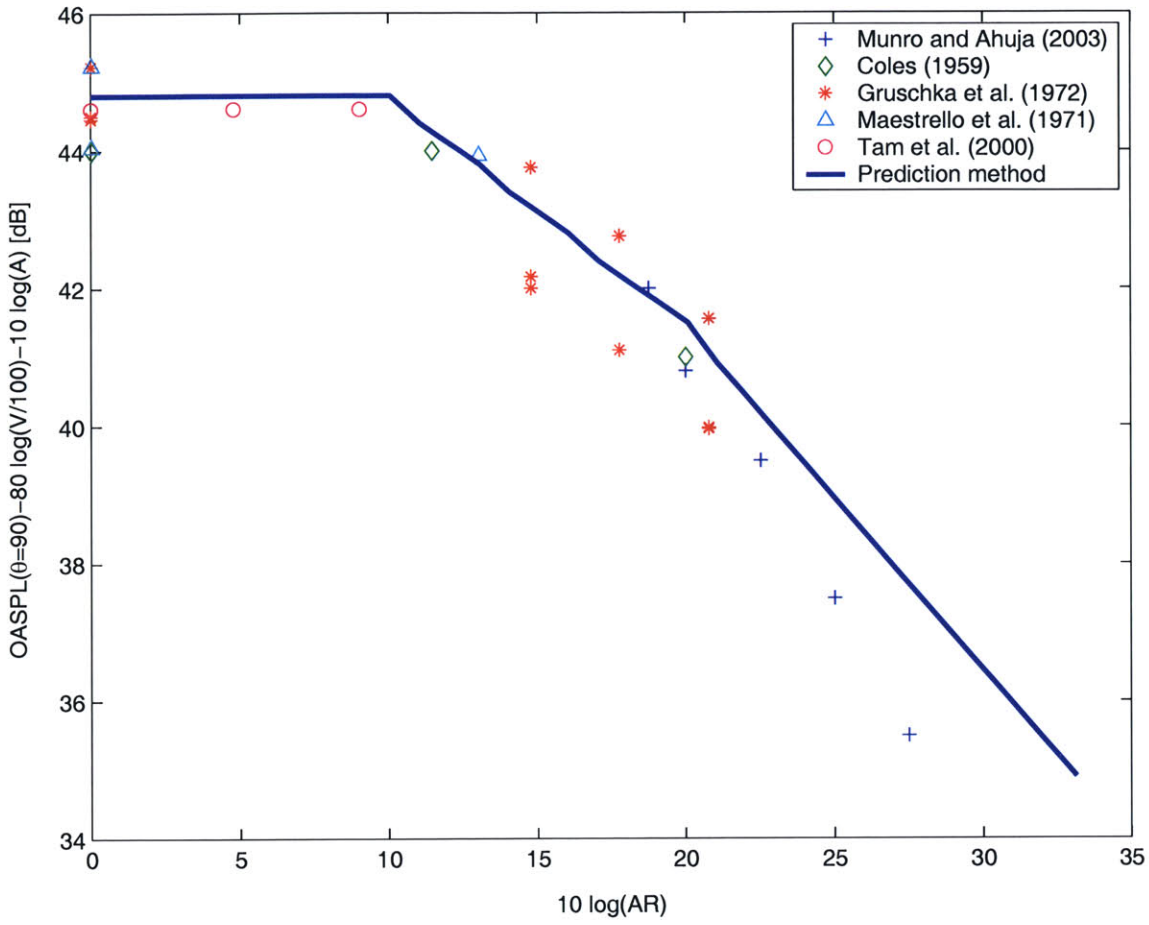

Figure 3-7: High aspect ratio jet noise data and prediction using the modified version of Stone's method as a function of jet aspect ratio.

- For high aspect ratios ($AR > 100$), data reported by Munro and Ahuja (2003a,b) show that the jet noise OASPL scales with jet aspect ratio, following the law: $OASPL \propto 10 \log AR^{-0.72}$.
- For intermediate aspect ratios ($\sim 30 < AR < 100$), a transition between the two precedent behaviors occurs. Over this range, the data reported by Gruschka and Schrecker (1972) show that the total acoustic power radiated by the jet scales with the jet aspect ratio, following the law: $P \propto 10 \log AR^{-0.36}$.

These different behaviors can be explained by changes in the length scale driving jet noise generation as the jet aspect ratio increases.

For circular jets, the length scale is related to the equivalent diameter: $D_{eq} = \sqrt{4A_{jet}/\pi} \approx 1.13\sqrt{A_{jet}}$. Both jet noise spectral distribution (through the Strouhal number $S_t = fD_{eq}/V_{jet}$) and the sound intensity ($I \propto A_{jet} \propto D_{eq}^2$) depend on this length scale.

For high aspect ratio jets, Munro and Ahuja (2003a,b) report that:

- the appropriate length scale driving jet noise generation becomes:

$$L_{eq} \propto \sqrt{A_{jet}} AR^{-1/4}, \tag{3.7}$$

- the convection Mach number decreases from $0.64M_{jet}$ for round jets to $0.36M_{jet}$.

Modifications to Stone's Jet Noise Prediction Method

Stone's jet noise prediction method is modified to estimate the jet noise OASPL and spectra as a function of jet aspect ratio. The details of the modifications are presented in Appendix B.1.3. The following assumptions are made. For jet aspect ratios larger than 100, the length scale and convection Mach number are modified as suggested by Munro and Ahuja (2003a,b). For jet aspect ratios from 10 to 100, it is assumed that the convection Mach number is the same as for round jets and that the length scale follows $L_{eq} \propto \sqrt{A_{jet}} AR^{-1/6}$.

The modifications in length scale and convection Mach number suggested by Munro and Ahuja (2003b,a) are inferred from the jet noise spectra and OASPL measured at a polar angle of 90° in the plane containing the minor axis of the nozzle. However, it is assumed that these changes in length scale and convection Mach number are valid at all azimuthal and polar angles. Jet noise measurements at other polar and azimuthal angles are needed to validate this assumption.

Results

Figure 3-7 compares the overall sound pressure level at a polar angle of 90° predicted by Stone's jet noise prediction method modified as presented above to available jet noise data. The discrepancy between the data and the prediction for high aspect ratio jets is due to the assumption that L_{eq} scales with $AR^{-1/4}$, leading to a sound intensity proportional to $AR^{-1/2}$, whereas data reported by Munro and Ahuja (2003a,b) suggest that jet noise OASPL scales with $AR^{-0.72}$.

In Figure 3-8, predicted spectra for different polar angles are compared to data presented in Munro and Ahuja (2003a). The peak frequency at 90° is correctly predicted, however, at lower polar angle significant discrepancies can be noticed in both peak frequency and sound pressure levels. This is mostly due to the assumption that the scaling laws observed at a polar angle of 90° are valid at any polar angle.

Conclusions

According to this study, high aspect ratio jets tend to radiate lower sound pressure levels than round jets of same area, velocity, density, and temperature. This trend is observed in the plane containing the jet minor axis. For a high aspect ratio nozzle distributed spanwise, this plane contains the azimuthal angles directed toward the ground. Thus, it is suggested that high aspect ratio nozzles

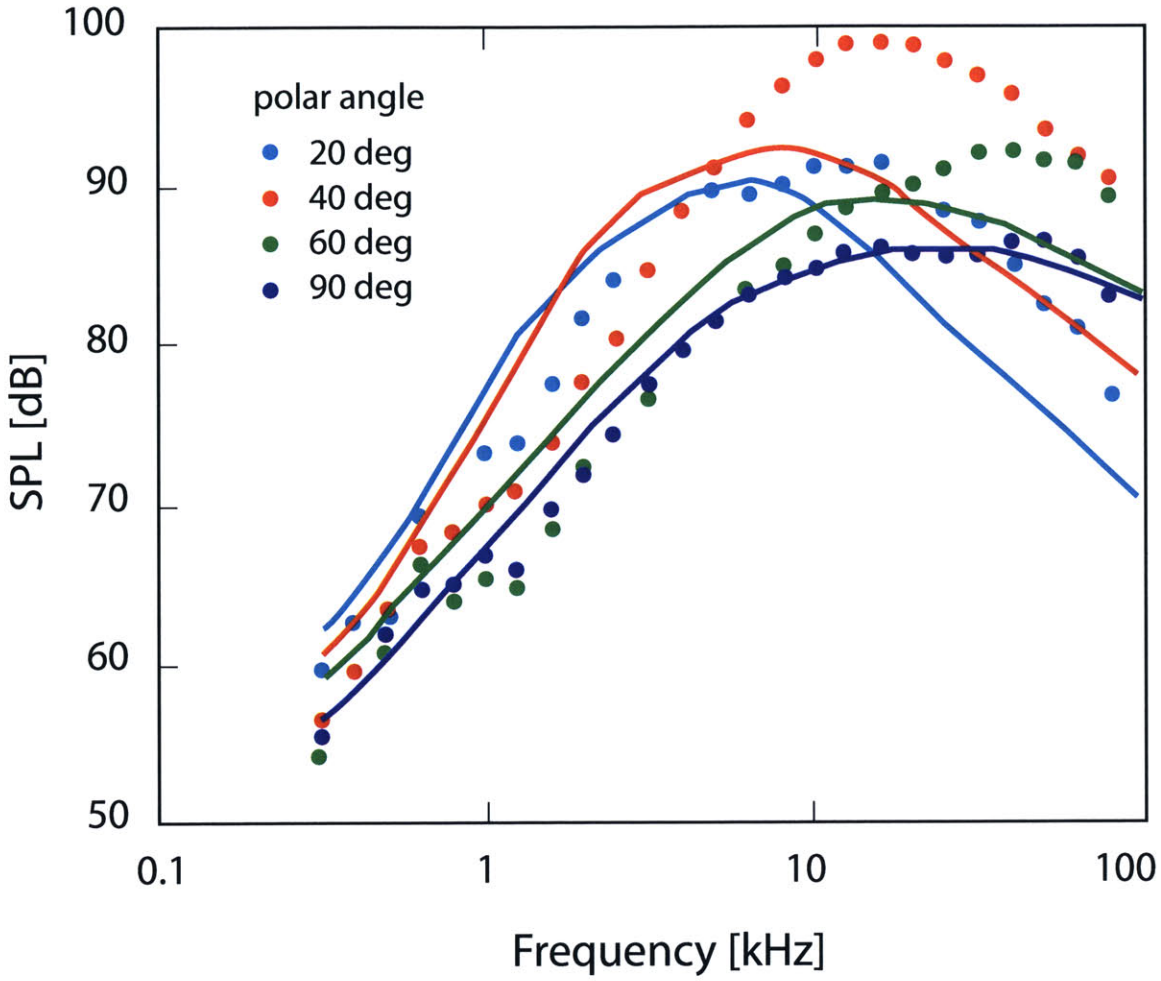

Figure 3-8: Spectral distribution and directivity for a nozzle of aspect ratio 260. Lines: prediction using the modified version of Stone's method - Dots: data from Munro and Ahuja (2003a).

can reduce flyover jet noise. For jet aspect ratios of 30 to 50, reductions in OASPL of 2 to 3 dB are expected.

Jets of intermediate aspect ratios (between 10 and 100) need to be further studied in order to determine the appropriate length scale and convection Mach number for these jet geometries. Directivity effects need to be assessed by performing measurements at various polar and azimuthal angles.

3.6.3 Thrust Losses in High Aspect Ratio Nozzles

Introduction

Exhaust nozzle performance is crucial to overall aircraft performance: a 1% decrease in nozzle gross thrust coefficient (C_{fg}) at cruise is equivalent to a 3% increase in specific fuel consumption (see

Johnson (1998)). For comparison, a 1% increase in nacelle drag or interference drag is equivalent to a 1% increase in SFC, and a 1% drop in inlet pressure recovery is equivalent to a 0.7% increase in SFC.

For a given exhaust area, high aspect ratio nozzles have a larger internal wetted area than conventional axisymmetric nozzles. A larger wetted area is expected to yield larger thrust losses due to larger skin friction.

Thus, a quantitative estimate of the impact of high aspect ratio nozzles on propulsion system performance is required to assess the viability of the embedded propulsion system. In this section, thrust and mass flow losses induced by HARNs are computed using three-dimensional computational fluid dynamics (CFD).

HARN geometry

High aspect ratio nozzles are represented by a duct of rectangular cross-section, as sketched in Figure 3-9.

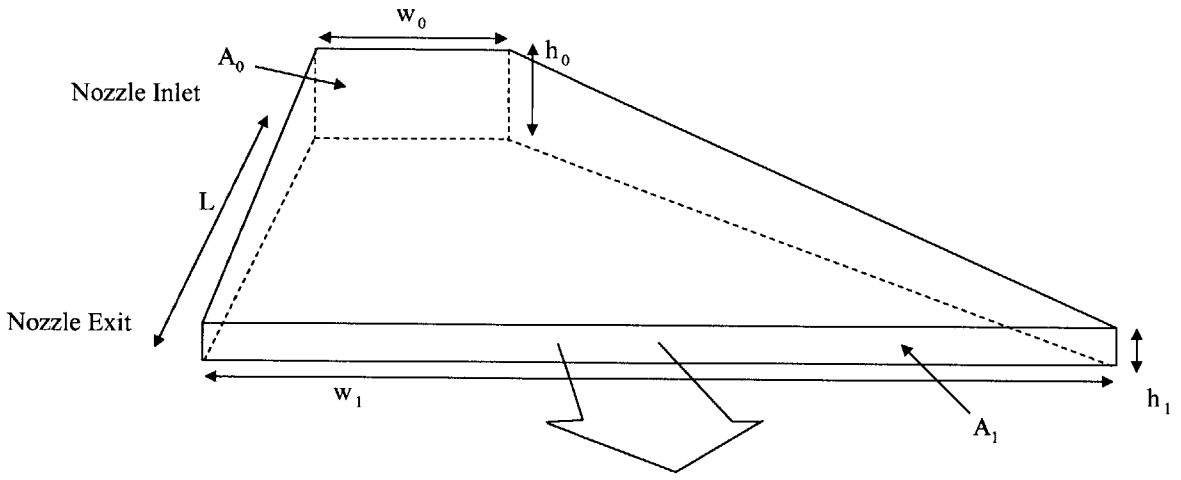

Figure 3-9: High aspect ratio nozzle geometry considered for the computation of the nozzle thrust losses.

This geometry is described by the following design parameters:

- L: nozzle axial length
- A_0: inlet area
- A_1/A_0: exit/inlet area ratio (< 1 for converging nozzle)
- AR_0: inlet aspect ratio
- AR_1/AR_0: exit aspect ratio / inlet aspect ratio

Nozzle Performance Computation

The key metrics for the evaluation of nozzle performance are:

- discharge coefficient, $C_D = \dot{m}_{actual}/\dot{m}_{ideal}$
- gross thrust coefficient, $C_{fg} = F_{actual}/F_{ideal}$

Ideal quantities are computed assuming isentropic expansion of the nozzle inlet total pressure through an orifice of same area as the nozzle exit.

Descriptions of the flow model, the nozzle meshing, the boundary conditions, the post-processing are given in Appendix B.2.1. A discussion of the accuracy of the results is given in Appendix B.2.2.

Thrust Losses for Various HARN Geometries

In order to assess the trends in thrust losses with variations in nozzle geometry, following test matrix is considered:

- $A_1/A_0 = 0.8$
- $A_0 = 20$ m^2
- $L = 4.5$ m and 9 m ($L^* = L/\sqrt{A_0} = 1$ and 2)
- $AR_0 = 1$, 5, and 10
- $AR_1/AR_0 = 1$, 5, and 20

This generates to 18 different geometries with exit aspect ratios (AR_1) ranging from 1 to 200. The performance of each of these nozzles is computed under four different operating conditions, typical of those encountered in UHBPR engines: nozzle pressure ratios of 1.3 and 1.8 and temperature ratio of 1.2 at takeoff conditions, nozzle pressure ratios of 2.2 and 2.8, and temperature ratio of 1.6 at cruise conditions. Discharge and gross thrust coefficients computed for all nozzle geometries are presented in Table 3.3.

Results are plotted in Figures 3-10 and 3-11 as a function of AR_1/AR_0, nozzle pressure ratio, and nozzle length, respectively.

Accuracy and Validity of Results

The uniform total pressure distribution imposed at the nozzle inlet (see boundary conditions in B.2.1) does not aptly describe the complex flow ingested by a real nozzle due to boundary layers at the walls. According to the sensitivity study of nozzle performance to upstream conditions presented in B.2.2, this effect introduces an uncertainty of approximately 2% on the discharge and gross thrust coefficients predicted for nozzles with $C_{fg} > 0.85$. For nozzles with $C_{fg} < 0.85$, the gross thrust

		$AR_0 = 1$			$AR_0 = 5$			$AR_0 = 10$		
NPR	L^*	AR_1	C_D	C_{fg}	AR_1	C_D	C_{fg}	AR_1	C_D	C_{fg}
1.3	1.0	1	0.991	0.985	5	0.989	0.980	10	0.987	0.976
1.8	1.0	1	0.994	0.987	5	0.992	0.983	10	0.992	0.982
2.2	1.0	1	0.999	0.989	5	0.997	0.989	10	0.996	0.987
2.8	1.0	1	1.001	0.998	5	0.999	0.992	10	0.998	0.980
1.3	2.0	1	0.989	0.980	5	0.986	0.974	10	0.983	0.969
1.8	2.0	1	0.991	0.983	5	0.989	0.979	10	0.988	0.977
2.2	2.0	1	0.997	0.993	5	0.994	0.979	10	0.992	0.979
2.8	2.0	1	0.998	0.992	5	0.996	0.989	10	0.994	0.976
1.3	1.0	5	0.928	0.867	25	0.815	0.698	50	0.742	0.621
1.8	1.0	5	0.939	0.886	25	0.838	0.730	50	0.771	0.652
2.2	1.0	5	0.951	0.907	25	0.853	0.752			
2.8	1.0	5	0.953	0.915	25	0.858	0.774			
1.3	2.0	5	0.973	0.949	25	0.928	0.869	50	0.879	0.792
1.8	2.0	5	0.981	0.959	25	0.940	0.890	50	0.900	0.824
2.2	2.0	5	0.990	0.973	25	0.950	0.903	50	0.913	0.844
2.8	2.0	5	0.988	0.960	25	0.952	0.899	50	0.916	0.852
1.3	1.0	20	0.768	0.615	100	0.584	0.416			
1.8	1.0	20	0.802	0.667	100	0.621	0.457			
2.2	1.0	20	0.823	0.700						
2.8	1.0	20	0.830	0.723						
1.3	2.0	20	0.891	0.805	100	0.758	0.610	200	0.671	0.505
1.8	2.0	20	0.913	0.840	100	0.795	0.664	200	0.710	0.556
2.2	2.0	20	0.930	0.864	100	0.817	0.693	200	0.732	0.587
2.8	2.0	20	0.935	0.870	100	0.825	0.725	200	0.741	0.611

Table 3.3: High Aspect Ratio Nozzle performance.

coefficients are predicted with an accuracy of 5%. This accuracy is acceptable considering the objective of this study.

For some nozzle geometries with high AR_1/AR_0 and $L^* = 1$, the computation did not properly converge.

Discussion of Results

From Figures 3-10 and 3-11, following trends can be outlined:

- Increasing the ratio of exit to inlet aspect ratio (AR_1/AR_0) has a detrimental impact on nozzle performance on the nozzle performance.
- Increasing the inlet aspect ratio (AR_0) yields increased thrust losses. The sensitivity to this parameter is low at low AR_1/AR_0 and becomes larger as AR_1/AR_0 increases.
- For $AR_1/AR_0 = 1$, the gross thrust coefficient decreases slightly (-0.5%) with increasing nozzle length.

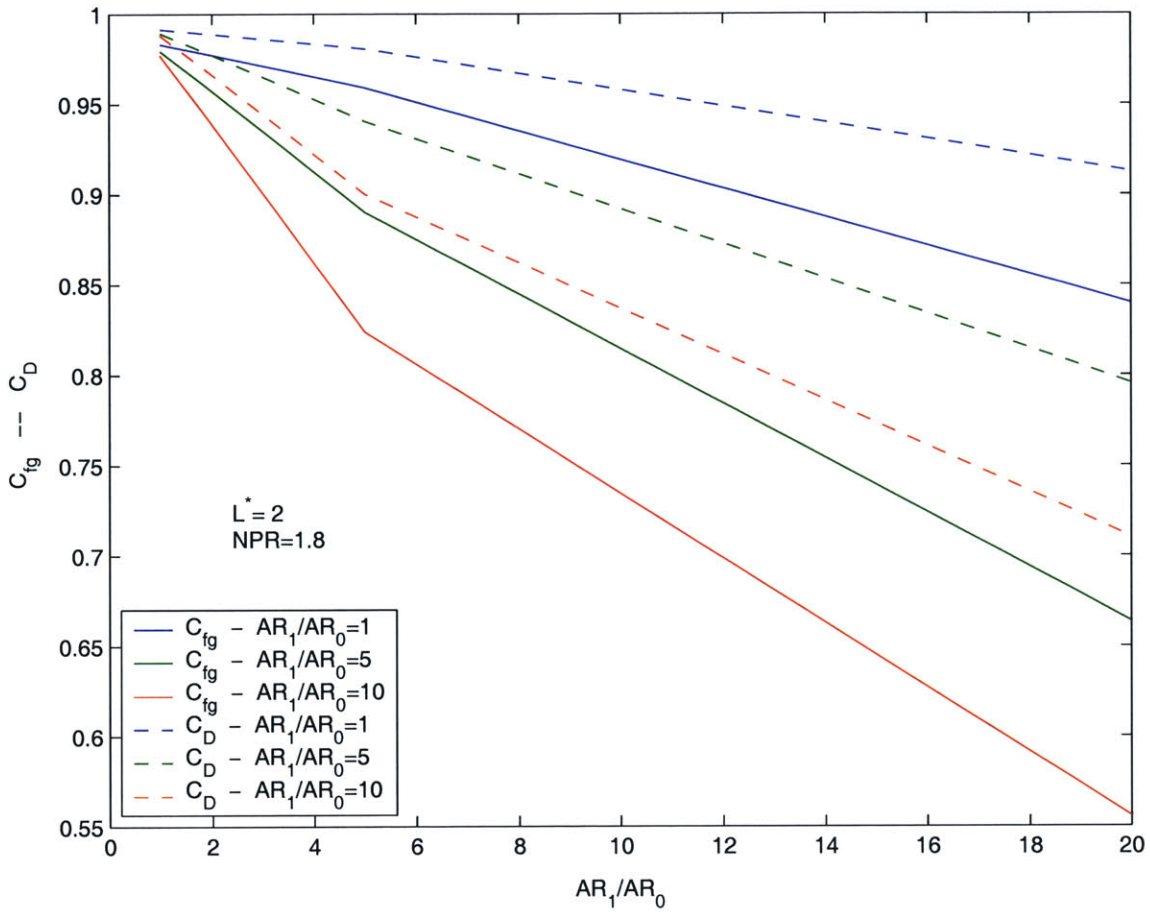

Figure 3-10: C_{fg} (solid) and C_D (dashed) as a function of AR_1/AR_0 for $AR_0 = 1$ (blue), 5 (green), and 10 (red). $L^* = 2$ and $NPR = 1.8$.

- For larger AR_1/AR_0, the performance of the nozzle greatly improves (+15% in C_{fg}) with increasing nozzle length.

Figure 3-12 shows the axial variations in cross-sectional area for different values of AR_1/AR_0. For $AR_1/AR_0 > 1$, the cross-sectional area of the nozzle initially increases, and then decreases. Thus, the nozzle behaves first as a diffuser, and then as a converging nozzle. This explains most of the trends observed above:

- as AR_1/AR_0 increases, separation occurs due to the adverse axial pressure gradient in the diverging section of the nozzle, leading to large thrust losses. For a given AR_1/AR_0, the diffusion increases as AR_0 increases, leading to stronger separation, and higher thrust losses. Longer nozzles mitigate this effect by reducing the adverse axial pressure gradient;

- for $AR_1/AR_0 = 1$, the HARN is a converging rectangular duct. The axial pressure gradient is always favorable and separation does not occur. Thus, the thrust losses are driven by the

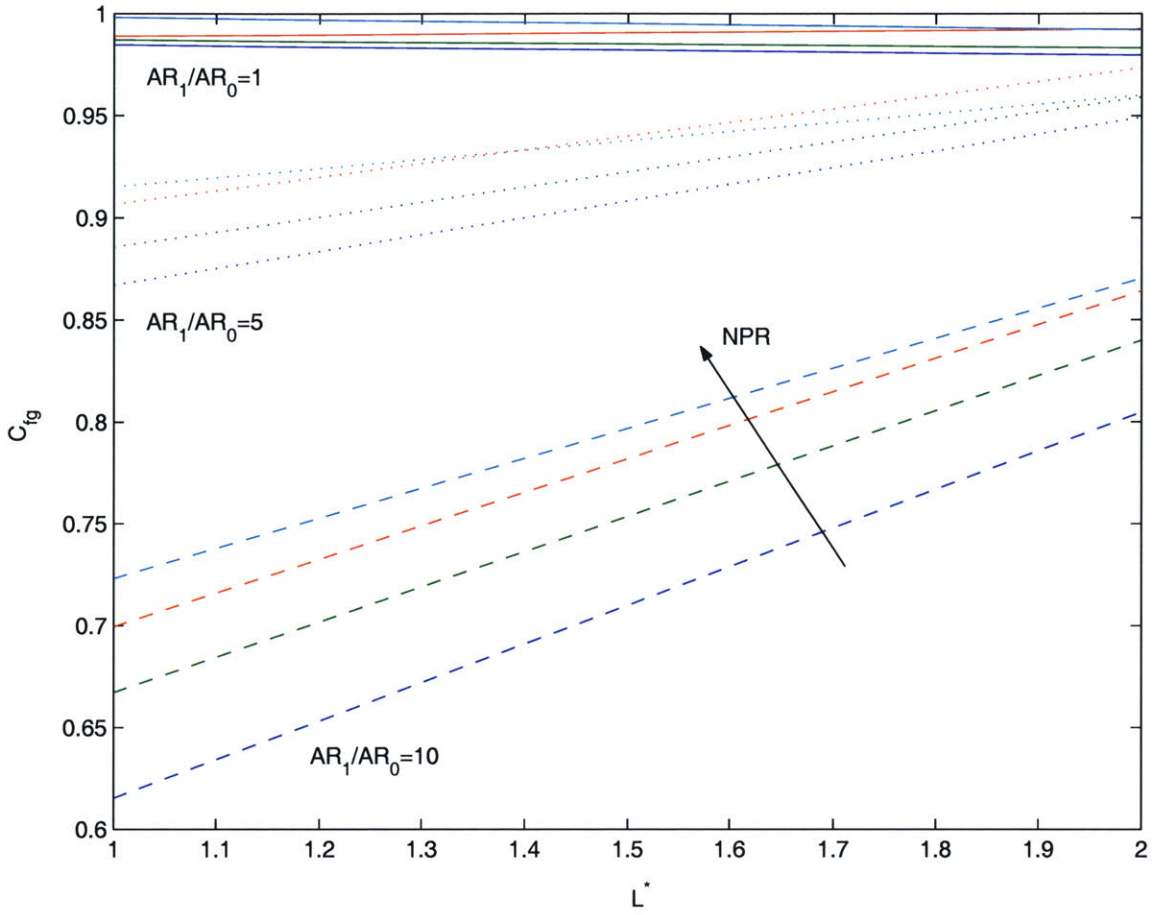

Figure 3-11: C_{fg} as a function of L^* for $AR_1/AR_0 = 1$ (solid), 5 (dotted) and 20 (dashed) and $NPR = 1.3$ (dark blue), 1.8 (green), 2.2 (red) and 2.8 (light blue). $AR_0 = 1$.

skin friction. Longer nozzles have a larger wetted area, hence larger thrust losses. However, these losses from skin friction are much smaller than losses due to separation. This explains the high performance of nozzles with low AR_1/AR_0.

To illustrate these observations, Figures 3-13 and 3-14 show the flow fields computed for nozzles of similar exit aspect ratios (20 and 25, respectively) but achieved with significantly different values of AR_1/AR_0 (20 and 5, respectively). The high AR_1/AR_0 nozzle shows a large area of low Mach number corresponding to a region of separation and recirculation, whereas recirculation develops in a much smaller area for the nozzle of lower AR_1/AR_0. As expected, the gross thrust coefficient of the nozzle with $AR_1/AR_0 = 20$ is significantly lower ($C_{fg} \approx 0.85$) than that of the nozzle with $AR_1/AR_0 = 5$ ($C_{fg} \approx 0.90$).

In the parametric study presented above, nozzle inlet area (A_0) is held constant at 20 m^2. The impact of the scale of the nozzle on the gross thrust coefficient is analyzed in B.2.2 (a study on

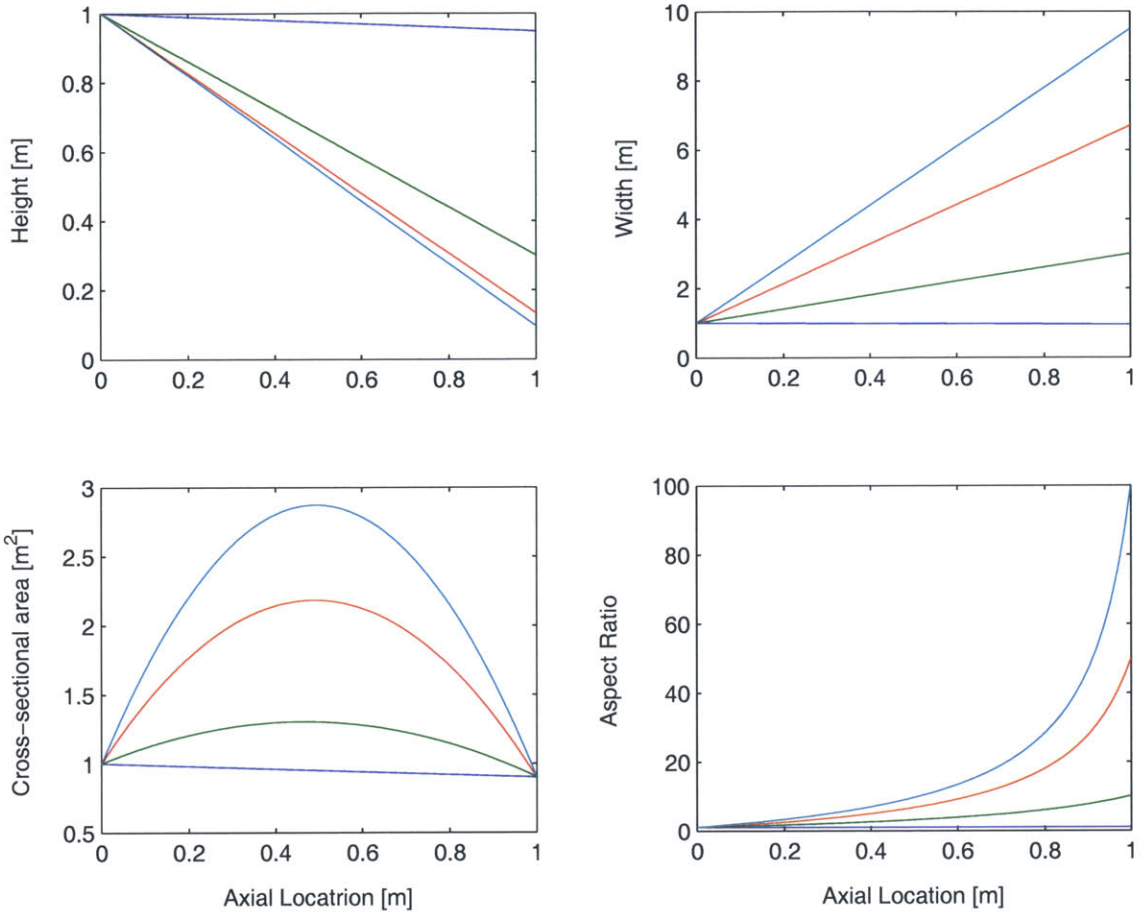

Figure 3-12: Axial variations of nozzle height, width, cross-sectional area and aspect ratio for $AR_1/AR_0 = 1$ (dark blue), 10 (green), 50 (red) and 100 (light blue); $AR_0 = 1$, $A_0 = 1$ m^2, $A_1/A_0 = 0.9$, $L = 1$ m.

viscosity ratio). For this analysis, AR_0, AR_1/AR_0, A_1/A_0, and the dimensionless nozzle length $L^* = L/\sqrt{A_0}$ are constant and the physical dimensions of the nozzle (length L, height, and width) are scaled by factors 1/2, 1/4 and 1/8, yielding inlet areas of $A_0 = 5$ m^2, 1.25 m^2 and 0.31 m^2 respectively. The trend in gross thrust coefficient shows that the performance of the nozzle increases with its size (this could be interpreted as a Reynolds number effect), but the variation of C_{fg} over almost two orders of magnitude in A_0 is only +0.15%. Since this effect is much smaller than the expected accuracy of the predictions, it is safe to assume that nozzle performance is nearly independent of nozzle size over the range covered here.

Sensitivity of nozzle performance to the area ratio A_1/A_0 cannot be assessed from the studies performed here. However, the value of 0.8 selected for the parametric study is typical of current technology nozzles.

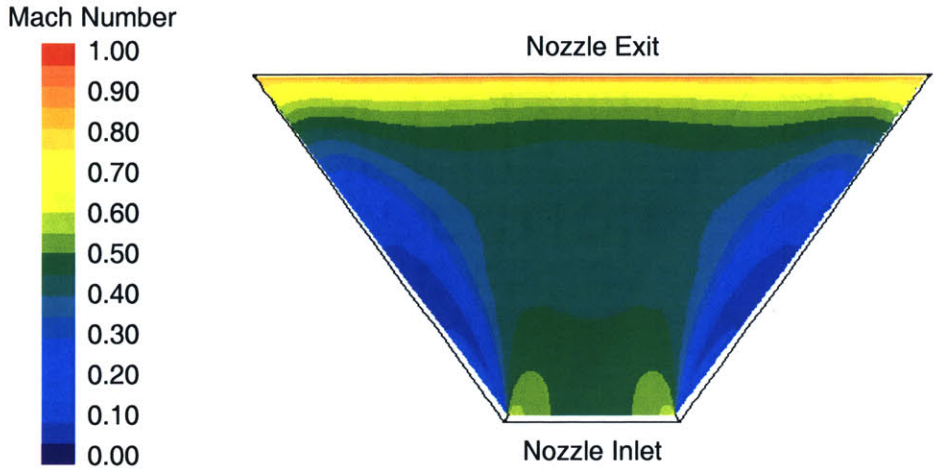

Figure 3-13: Contours of Mach number for the geometry: $AR_1/AR_0 = 20$, $AR_0 = 1$, $L^* = 2$, $NPR = 1.8$, $C_{fg} = 0.84$.

Conclusions

This study quantitatively assesses the thrust losses for various HARN geometries and delineates the trends in thrust losses for the main design parameters.

Separation occurs in the diverging section of nozzles with high values of AR_1/AR_0 and yields large thrust losses ($C_{fg} < 0.9$). Increasing the nozzle length decreases the strength of this separation, and yields lower thrust losses but leads to unrealistic lengths in terms of integration (more than 9m) and large weight penalties.

However, high nozzle exit aspect ratios AR_1 can be implemented with reasonably low thrust losses ($C_{fg} > 0.95$) if separation is avoided by selecting an inlet aspect ratio AR_0 as large as possible and keeping AR_1/AR_0 sufficiently small (below 1.5 in practice). Thrust losses are then essentially due to skin friction, and shorter nozzles are expected to yield higher gross thrust coefficients.

A prediction tool based on these results has been developed (see B.2.3) and can be coupled to the cycle analysis presented in Chapter 2 in order to account for thrust losses and discharge coefficients due to high aspect ratio nozzles.

The quantitative estimates of the thrust losses presented above are only valid for the nozzle geometries considered in this study. It is suggested that the performance of these HARN designs can be greatly improved. For example, the initial increase in cross sectional area can be reduced by using curved nozzle walls. If separation can be avoided, shorter and lighter nozzles inducing lower thrust losses can be envisioned.

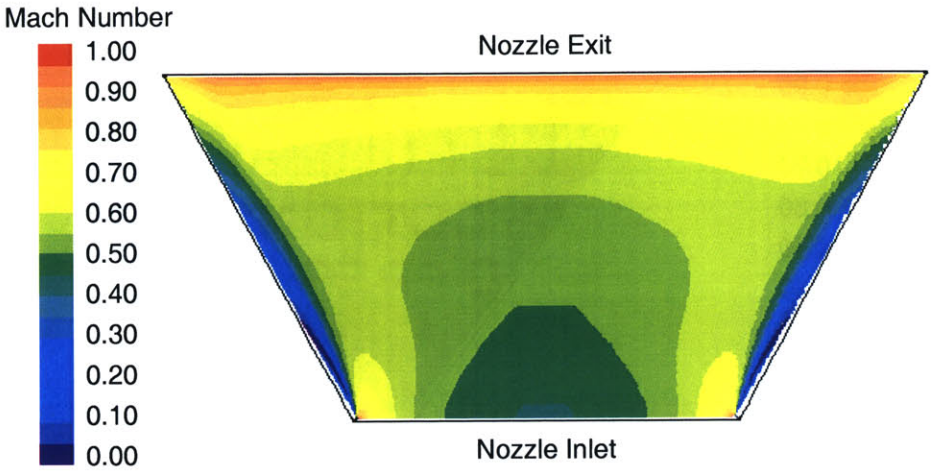

Figure 3-14: Contours of Mach number for the geometry: $AR_1/AR_0 = 5$, $AR_0 = 5$, $L^* = 2$, $NPR = 1.8$, $C_{fg} = 0.89$.

3.6.4 Design Implications for an Integrated Airframe/Exhaust System

As observed in Section 3.2, embedding the propulsion system requires a nozzle inlet aspect ratio of 34 to 62. For the exhaust area required by the UHBPR engine cycle, the maximum exit aspect ratio allowed by the blended-wing-body airframe geometry is 69, such that the maximum value of AR_1/AR_0 is 2. In order to achieve high gross thrust coefficients, the shortest possible nozzle for which separation does not occur must be selected. It is suggested that gross thrust coefficients larger than 0.95 can be achieved using a nozzle of length 4 m with a low value of $AR_1/AR_0 \approx 1.2$. This yields a nozzle exit aspect ratio of 40 to 50, hence jet noise reductions of 2 dB to 3 dB in overall sound pressure level.

3.7 Conclusions

3.7.1 Design Implications for a Distributed Propulsion System Configuration

The various studies performed in this chapter enable a preliminary sketch of a distributed propulsion system embedded in the blended-wing-body airframe.

A total of thirty 1.37m-diameter fans is required to both satisfy the geometrical constraints imposed by the blended-wing-body airframe and provide the flow-path area for the ultra-high bypass ratio engine cycle delineated in Chapter 2. A propulsion system configuration with 6 core engines driving 5 fans (D2 in Table 3.2) or 10 core engines driving 3 fans (D3 in Table 3.2) is suggested as a good compromise between shaft power transmission losses, total propulsion system weight,

and Reynolds number effects. Compared to a configuration with 3 fans, a 2 dB reduction in fan noise EPNL can be expected at takeoff, because of a beneficial frequency shift effect toward high frequencies. The mail-slot inlet ingests the wing surface boundary layer over a spanwise extent corresponding to 48% of the aircraft span. According to Pilczer (2003), this is expected to yield a entail a 2 dB reduction in trailing edge noise on approach and a 4 to 6% increase in aircraft range depending on the inlet axial Mach number.

The type of integrated airframe/exhaust system still needs to be determined. A distributed exhaust nozzle generating approximately 100 jetlets and a high aspect ratio nozzle exhausting a single jet of aspect ratio 30 to 50 are compared in Table 3.4 in terms of noise reduction potential (due to OASPL reduction and frequency shift effect), gross thrust coefficient, and weight penalty. Both nozzles are expected to yield weight penalties. These penalties are not quantified at this stage.

Configuration	HARN Single Jet	Baseline BWB engine config.	DEN
Number of Jets N_j	1	3	~ 100
$\Delta OASPL$ [dB]	-2 to -3	0	-10
$\Delta EPNL$ (frequ. shift) [dB]	-2	0	+7
C_{fg}	0.95	1	0.9
Weight penalty	Yes	No	Yes

Table 3.4: Comparison of various exhaust system configurations.

Both nozzles configurations can be integrated with the structure of the blended-wing-body trailing edge, resulting in similar weight savings. The HARN has a total perceived jet noise reduction potential of 4 to 5 dB, and only 3 dB for the DEN. The HARN creates half of the thrust losses induced by the DEN (5% instead of 10%). Thus, for a 1% decrease in C_{fg} (equivalent to a 3% increase in SFC, according to Johnson (1998)), the HARN achieves a reduction in perceived jet noise of approximately 1 dB, but the DEN achieves a reduction of only 0.3 dB.

According to these results, the high aspect ratio nozzle is the best candidate to enable an integrated airframe/propulsion system and an embedded propulsion system. This conclusion could change if significant improvements in DEN design are achieved, but the large exhaust areas required by UHBPR engine inevitably drive a detrimental frequency shift effect (7 dB increase in EPNL) as the large single jet is split into more than 100 jetlets.

Thus, the envisioned exhaust system consists of a single high aspect ratio nozzle exhausting a high aspect ratio low velocity jet distributed along the trailing edge of the wing. The nozzle inlet is fed by flows from all core engines and fans and therefore has to be geometrically compatible with the layout of the engines. The nozzle also plays the role of mixer required by the ultra-high bypass ratio engine cycle (see Chapter 2). The blended-wing-body geometry requires a nozzle inlet aspect ratio between 34 and 62. The aspect ratio of the fan inlet is equal to the number of fans, i.e. 30.

The separation observed in HARNs for large variations in aspect ratio from the inlet to the exit suggest that the nozzle inlet aspect ratio should be kept as close as possible to the fan inlet aspect ratio to avoid separation. Thus, a nozzle inlet aspect ratio of 34 is selected. In order to maintain the nozzle gross thrust coefficient above 0.95, the ratio of exit to inlet aspect ratio is set to 1.2. Thus, the nozzle exit aspect ratio is 41, and a 2.5 dB reduction in jet noise level can be expected in the plane containing the nozzle minor axis. It is suggested that a nozzle length of 4 m is required to avoid separation and enable full mixing of the bypass and core flows.

Dimensions and key characteristics of this preliminary embedded propulsion system configuration are presented in Table 3.5 for both 6 core engines and 10 core engines configurations.

Configuration	D2	D3
Number of fans per core	5	3
Number of core engines	6	10
Core mass flow [kg/s]	28.2	16.9
Fan gearbox power [MW]	19.4	11.6
Mail-slot inlet (h x w, AR)	0.78 m x 41.2 m, 53	
Total number of fans	30	
Fans diameter	1.37 m	
Fans inlet A_{rect} (h x w, AR)	1.37 m x 41.2 m, 30	
Nozzle inlet (h x w, AR)	1.0 m x 34.1 m, 34	
Nozzle exit (h x w, AR)	0.94 m x 38.5 m, 41	
Nozzle length	4 m	
Nozzle AR_1/AR_0	1.2	
Nozzle C_{fg}	0.95	
Reduction in Jet noise	-34 EPNdB	
Reduction in Fan noise	-2 EPNdB	

Table 3.5: Preliminary distributed propulsion system configurations to enable a functionally-silent aircraft.

Distributed propulsion system configurations D2 and D3 embedded in the blended-wing-body airframe are compared to conventional pod-mounted configurations for the baseline and ultra-high bypass ratio engines in Figures 3-15 and 3-16.

3.7.2 Modeling Limitations and Suggested Improvements

Mechanisms driving noise generation for high aspect ratio jets need to be further studied to confirm the trends observed in Section 3.6.2. In particular, the study should focus on jets of aspect ratio between 20 and 50, and directivity effects should be taken into account.

Using CFD, thrust losses induced by high aspect ratio nozzles could be computed for the geometries enabling propulsion system embodiment suggested in this study (i.e. $AR_0 = 34$, $AR_1 = 41$). More efficient and shorter nozzles could probably be designed.

Models capable of computing metrics involved in the evaluation of propulsion system config-

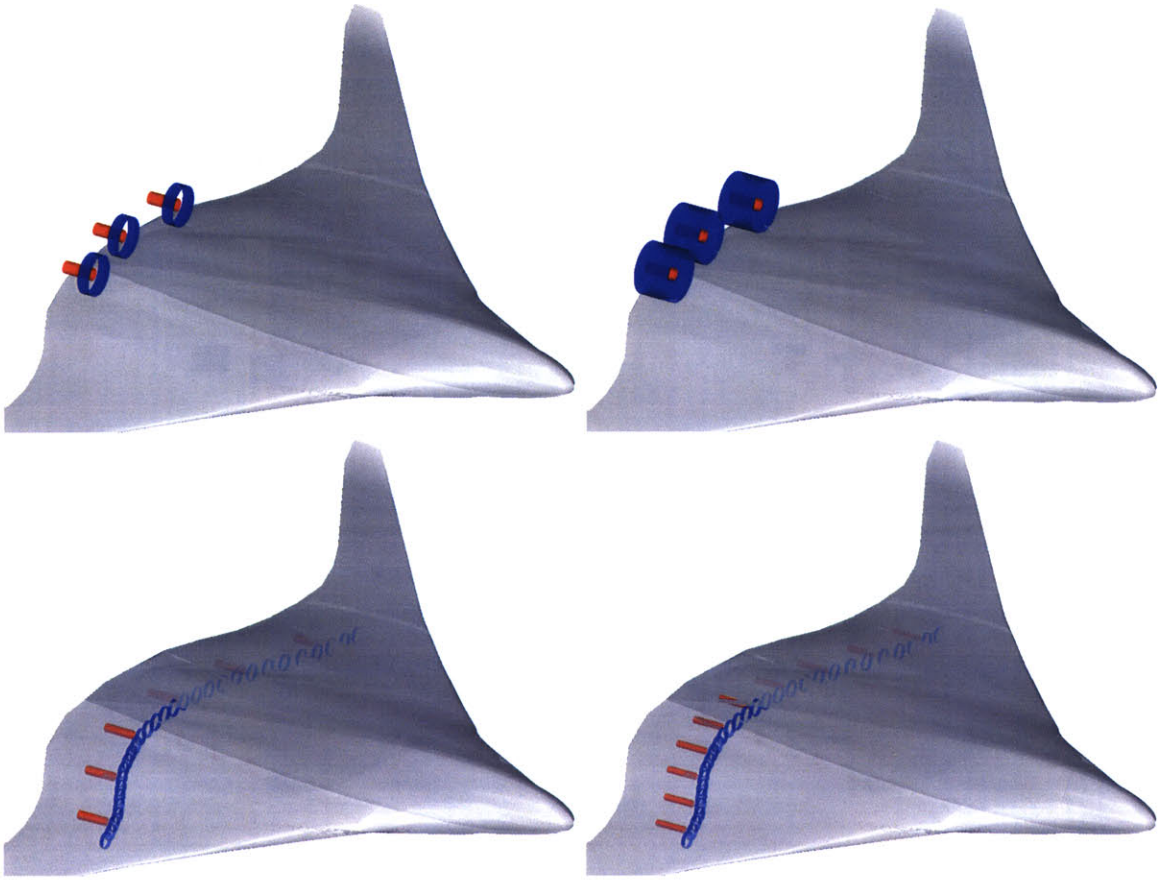

Figure 3-15: Comparison of baseline (top-left) and UHBPR (top-right) pod mounted engines, and UHBPR distributed propulsion system configurations with 6 core engines (D2, bottom-left) and 10 core engines (D3, bottom-right): side view. Core engines are shown in red, fans and nacelles are shown in blue.

urations should enable to assess the trade-offs between weight and thrust penalties, transmission losses, and Reynolds number effect. The impact of the embedded propulsion system on airframe aerodynamic performance should also be considered (wing flow disturbance induced by the mail-slot inlet and the height of the nozzle exit).

Engine cycle performance will be considerably altered by the embodiment of the engines. Ingestion of the wing surface boundary layer and mail-slot inlet geometry will inevitably lead to higher inlet distortion levels and lower inlet pressure recovery. Therefore, the study performed in Chapter 2 will need to be updated to take these effects into account. Reynolds number effects, transmission losses, and thrust losses due to the high aspect ratio may also be included in the study. This will yield to new cycle requirements and start a new iteration in the process of designing the embedded propulsion system enabling a functionally-silent aircraft.

Turbomachinery needs to be designed to tolerate the inlet distortion due to boundary layer

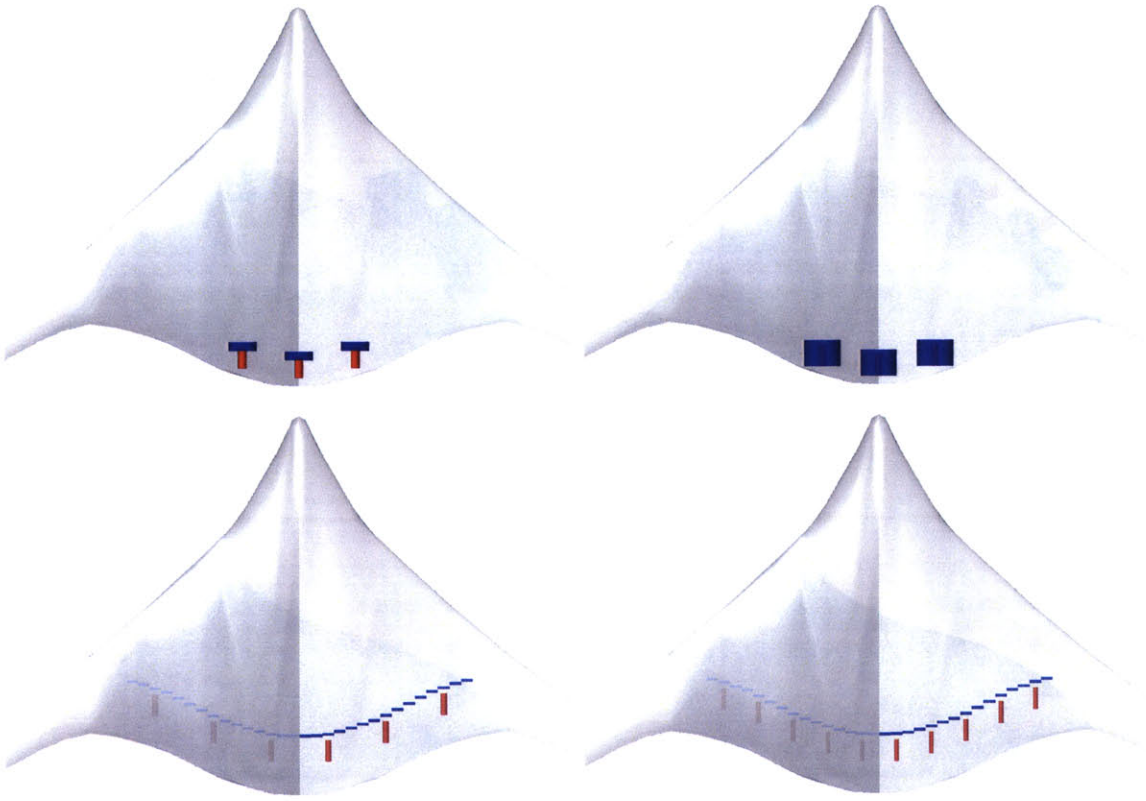

Figure 3-16: Comparison of baseline (top-left) and UHBPR (top-right) pod mounted engines, and UHBPR distributed propulsion system configurations with 6 core engines (D2, bottom-left) and 10 core engines (D3, bottom-right): top view. Core engines are shown in red, fans and nacelles are shown in blue.

ingestion and mail-slot geometry.

Finally, the analysis presented here assumed that the fan noise could be perfectly shielded. Refined studies will have to quantitatively assess the fan noise reduction potential of embedded propulsion system configurations and determine corresponding design implications including, but not limited to, low-noise fan design requirements, required surface for acoustic liners, use of active or passive noise control.

Chapter 4

Silent Drag - Windmilling Engine Air-Brakes

4.1 Introduction and Objectives

4.1.1 Introduction

"Quiet Lift" concepts such as aerodynamically smooth lifting surfaces and hidden trailing edge invariably reduce airframe drag. A distributed propulsion system embedded in the airframe alleviates nacelle and pylon drag. Landing in a low-drag (or "clean") configuration usually requires a shallower approach at higher speed. This not only raises safety and air traffic control issues but also yields higher approach noise levels and increases the noise footprint on the ground. Therefore, means to generate drag in a quiet manner, or "Silent Drag", need to be developed to allow steeper approaches.

Instead of dissipating the potential and kinetic energy of the aircraft through noisy flow structures created by high-lift devices, it is suggested that the engines operate in windmilling mode to generate the drag required on approach. Using variable pitch turbomachinery, fan blades can be employed as low efficiency turbine blades by adjusting the blade stagger angle. By extracting work from the flow, the total pressure decreases across the blade row, which results in a momentum deficit through the propulsion system. This momentum deficit yields a force acting opposite the flight direction on the aircraft, i.e. drag. Figure 4-1 depicts the engine air-brake concept.

The maximum drag that can be generated by extracting work from the flow is achieved when the total pressure drop across the blade row is equal to the dynamic pressure. The flow is therefore brought to stagnation at the blade row inlet. In this limiting case, there is no mass flow through the propulsion system and the exhaust velocity is zero. This can only be achieved if the fan blades completely block the flow path through the engine. The propulsion system then behaves like a bluff

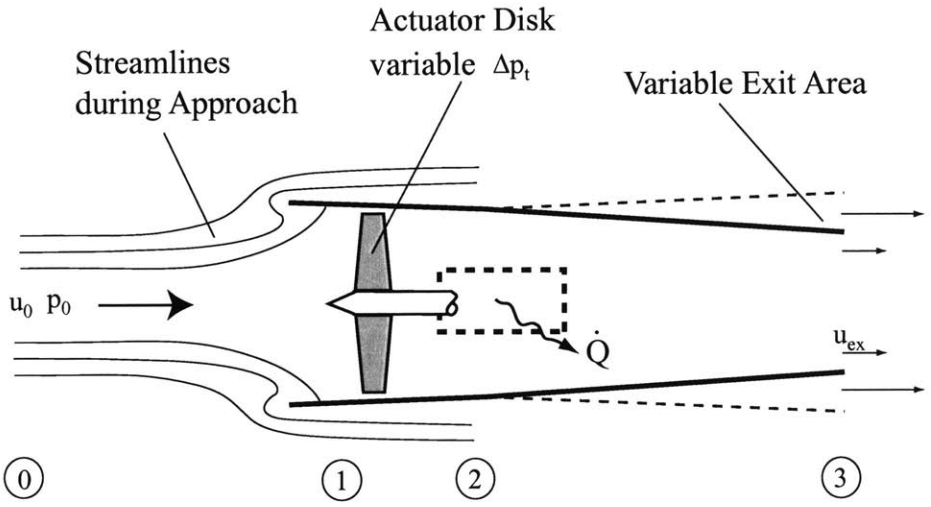

Figure 4-1: Windmilling engine air-brake concept to generate "Silent Drag".

body, and the resulting drag for incompressible flow becomes:

$$D = A_{fan} \cdot (P_1 - P_2), \tag{4.1}$$

where P_1 and P_2 are the static pressures upstream and downstream of the blade row, and A_{fan} is the fan inlet area. Since the flow is brought to stagnation at station 1,

$$P_1 = P_{t_1} = P_{t_0} = P_0 + \frac{1}{2}\rho u_0^2, \tag{4.2}$$

where u_0 is the flight velocity. Setting ambient pressure P_0 at the exhaust and zero axial velocity through the engine yield

$$P_2 = P_{t2} = P_0. \tag{4.3}$$

Thus,

$$P_1 - P_2 = \frac{1}{2}\rho u_0^2. \tag{4.4}$$

The total pressure drop across the blade row is also:

$$P_{t1} - P_{t2} = P_1 - P_2 = \frac{1}{2}\rho u_0^2. \tag{4.5}$$

Finally, the generated bluff body drag is:

$$D = \frac{1}{2}\rho u_0^2 A_{fan}. \tag{4.6}$$

and can be expressed in the form of a drag coefficient based on the fan inlet area:

$$C_{D_{fan}} = \frac{D}{\frac{1}{2}\rho u_0^2 A_{fan}} = 1. \tag{4.7}$$

$C_{D_{fan}} = 1$ is the maximum drag coefficient that the engine air-brake can achieve. In this case, the zero velocity at the engine exhaust induces unsteady flow structures due to vortex shedding. These unsteady flow structures generate undesirable low-frequency noise and must be avoided. A more detailed discussion of this issue is given in Sections 4.2 and 4.5.

The dissipated power corresponding to the drag generated by a bluff body of area A_{fan} is

$$P = D \cdot u_0 = \frac{1}{2}\rho u_0^3 A_{fan}. \tag{4.8}$$

A back-of-the-envelope calculation shows that a 310-ton aircraft (approximately the landing weight of the blended-wing-body aircraft) on a standard glide slope of 3° at an approach speed of 80 m/s needs to dissipate 12.7 MW. This power can be dissipated by a bluff body of area $A_{fan} = \frac{2}{u_0^2 \rho} mg \sin\theta =$ 41.4 m^2. This area corresponds to 4 fans with diameters of approximately 4 m.

The power extracted by the engine air-brake must be dissipated, for example, by a hydrodynamic break controlling the fan rotational speed. This air-brake system requires the capability to disengage the fan from the low-pressure spool using a clutch. For this purpose, a technology similar to that developed for the JSF lift-fan can be envisioned. Variable pitch fan blades have already been demonstrated on the Advanced Ducted Propulsor (see Flug Revue (1998)) to reverse thrust. The ability to quickly recover forward thrust is crucial for operational and passenger safety reasons, for example, in the case that the pilot needs to adjust the approach trajectory or abort a landing. This concept inevitably increases the complexity of both the propulsion system and engine control system and introduces maintenance and reliability issues.

4.1.2 Objectives

This chapter focuses on assessing the viability of an engine air-brake using the fan in windmilling mode to generate drag. The main objectives are:

- to quantify the drag generation capability of an engine air-brake concept and compare it to the drag that needs to be generated in a quiet manner to follow a given approach profile,
- to estimate the noise signature of the engine air-brake, and
- to delineate the preliminary design implications for a functionally-silent aircraft with an engine air-brake capability.

First, the "Silent Drag" required by a blended-wing-body airframe and a conventional aircraft to land in clean configuration is estimated for various approach profiles (landing speed and glide slope). Then, a meanline compressible flow model capable of computing the off-design behavior of a ducted rotor with variable pitch geometry is developed. Using this model, a preliminary estimate of the drag generated by a windmilling engine air-brake is obtained. A two-dimensional viscous analysis of the rotor blade passage flow in windmilling mode is performed using MISES computations (see Drela and Youngren (1998)) to refine the drag calculation. Finally, the fan noise signature of the engine air-brake is assessed on a preliminary basis using Heidmann's fan noise prediction method (see Heidmann (1975) and Zorumski (1982)) and the improved Mugridge-Morfey model for rotor self-noise reported by Gliebe (2002).

4.2 Silent Drag Requirements

4.2.1 Methodology

Problem Description

The steady-state force balance for an aircraft of mass m on approach with a velocity u_0 and a glide slope angle of θ becomes $mg\sin\theta = D_r - T$ along the trajectory, where D_r is the drag required to follow the prescribed path and T is the residual engine thrust. The force balance normal to the trajectory is $mg\cos\theta = L_r$, where L_r is the lift required to follow the approach profile.

The required drag D_r can be split into two components: the drag produced by the airframe in clean configuration D_p and the additional drag D_{add} that needs to be generated to keep the aircraft on a given approach profile. The required lift L_r can also be split into the lift produced by the airframe in clean configuration L_p and the additional lift L_{add} that needs to be generated to keep the aircraft on the approach profile. For current aircraft configurations, D_{add} and L_{add} are generated by high-lift and high-drag devices such as flaps, slats, and landing gear. In this study, it is assumed that the aircraft lands in clean configuration and that additional drag can be generated by the engine air-brakes on approach. Thus, all of the required lift must be produced by the clean airframe by adjusting the angle of attack:

$$L_r = L_p = C_L(\alpha)\frac{1}{2}\rho u_0^2 A_w, \tag{4.9}$$

where $C_L(\alpha)$ is the lift coefficient at an angle of attack α. A_w is the wing area on which the lift coefficient is based. The lift coefficient required to achieve L_r must remain below the maximum lift coefficient at which the airfoil stalls, i.e. $C_L < C_{L_{max}}$. If the required lift coefficient is larger than the $C_{L_{max}}$ in clean configuration, the prescribed approach profile cannot be achieved without stalling the aircraft or deploying high-lift devices. For a given glide slope angle, the stall velocity V_s

corresponding to $C_L = C_{L_{max}}$ is:

$$V_s = \sqrt{\frac{mg\cos\theta}{\frac{1}{2}\rho C_{L_{max}} A_w}}. \tag{4.10}$$

In practice, the approach speed is chosen such that $u_0 = 1.3 \cdot V_s$ to keep a reasonable stall margin for safety reasons.

Assuming that the required lift can be produced, the drag produced by the airframe is given by the drag polar $C_D(C_L)$:

$$D_p = C_D(C_L(\alpha))\frac{1}{2}\rho u_0^2 A_w. \tag{4.11}$$

The force balance along the trajectory then becomes:

$$mg\sin\theta = C_D(C_L(\alpha))\frac{1}{2}\rho u_0^2 A_w + D_{add} - T. \tag{4.12}$$

It is assumed that the additional required drag is generated by the engines in air-braking mode. Thus, the sum of additional drag and residual thrust corresponds to the net momentum flux through the propulsion system. The additional drag and residual thrust can therefore be grouped into a single term that characterizes the "Silent Drag" requirement:

$$SD_{req} = D_r - D_p = D_{add} - T. \tag{4.13}$$

This term is positive if "Silent Drag" must be generated by the engine air-brake and negative if thrust is required to keep the aircraft on the prescribed path. For $SD_{req} = 0$, the engine air-brake must compensate for the residual thrust produced by the core such that the mixed-out exhaust velocity is equal to the free stream velocity.

The required silent drag coefficient based on the wing area is then:

$$C_{SD_{req}} = \frac{D_r - D_p}{\frac{1}{2}\rho u_0^2 A_w} = \frac{mg\sin\theta}{\frac{1}{2}\rho u_0^2 A_w} - C_D(C_L(\alpha)). \tag{4.14}$$

The drag coefficient generated by the engine air-brake, $C_{D_{fan}}$, is based on the fan inlet area. In order to compare the drag generated to the silent drag requirement ($C_{SD_{req}}$), the drag coefficient based on the fan inlet area ($C_{D_{fan}}$) is converted into a drag coefficient based on the wing area (C_D) such that:

$$C_D = \frac{D}{\frac{1}{2}\rho u_0^2 A_w} = C_{D_{fan}}\frac{A_{fan}}{A_w}. \tag{4.15}$$

Discussion of the Influence of Aircraft Size on Silent Drag Requirements

The feasibility of the silent aircraft largely depends on the ability to produce the required silent drag. The following question then arises: how does the required Silent Drag on approach scale with aircraft size?

In this discussion, the aircraft size is characterized by a scale factor $k < 1$ such that $A_w = k \cdot A_{w_0}$ where A_{w_0} is the wing area of a reference aircraft. It is assumed that:

- The aircraft landing weight and total fan inlet area scale as $mg = k^\alpha \cdot m_0 g$ and $A_{fan} = k^\beta \cdot A_{fan_0}$, where α and β need to be determined. $m_0 g$ and A_{fan_0} are the landing weight and the total fan inlet area of the full-size aircraft, respectively.
- The airframe aerodynamic performance is independent of aircraft size.
- The airframe drag coefficient in clean configuration depends on the lift coefficient as follows: $C_D = b_1 + b_2 C_L + b_3 C_L^2$, where b_i are constants.

The Silent Drag coefficient required to keep an aircraft of size k on a glide slope angle θ at a speed u_0 is then:

$$C_{SD_{req}} = \frac{m_0 g \sin\theta}{\frac{1}{2}\rho u_0^2 A_{w_0}} \cdot k^{\alpha-1} - (b_1 + b_2 C_L + b_3 C_L^2). \tag{4.16}$$

The force balance normal to the aircraft trajectory yields $C_L = \frac{m_0 g \cos\theta}{\frac{1}{2}\rho u_0^2 A_{w_0}} \cdot k^{\alpha-1}$. Thus, the required silent drag coefficient can be rewritten:

$$C_{SD_{req}} = a_1 + a_2 \cdot k^{\alpha-1} + a_3 \cdot k^{2(\alpha-1)}, \tag{4.17}$$

where a_i are constants. Since $C_{D_{fan}}$ is independent of engine size, the drag coefficient produced by the engine air-brake is

$$C_D = C_{D_{fan}} \frac{A_{fan_0}}{A_{w_0}} \cdot k^{\beta-1} = c_0 \cdot k^{\beta-1}, \tag{4.18}$$

where c_0 is a constant. For a given specific thrust,

$$\frac{F}{F_0} = \frac{\dot{m}}{\dot{m}_0} = \frac{A}{A_0} = k^\beta. \tag{4.19}$$

The total thrust is set by the requirement that the aircraft must be able to take off with a minimum climb angle θ_{min} in the case of an engine failure. For small θ_{min}, this translates to:

$$\frac{n-1}{n}\frac{F}{mg} = \frac{D}{L} + \theta_{min}, \tag{4.20}$$

where n is the number of engines. Thus,

$$\frac{F}{F_0} = \frac{mg}{m_0 g} = k^\alpha. \tag{4.21}$$

Therefore, the exponents α and β are equal. To determine how $C_{SD_{req}}$ and C_D scale with aircraft size, α needs to be determined. It is assumed that the wing loading is independent of aircraft size.

Thus,

$$\sigma = mg/A_w = m_0 g/A_{w_0} \cdot k^{\alpha-1} \tag{4.22}$$

yields $\alpha = 1$. In Figure 4-2, the maximum landing weight and total takeoff thrust are plotted as a function of wing area for most current airliners (data from Jane's All the World's Aircraft (2003)). The aircraft landing weight is proportional to wing area, which justifies the assumption that wing

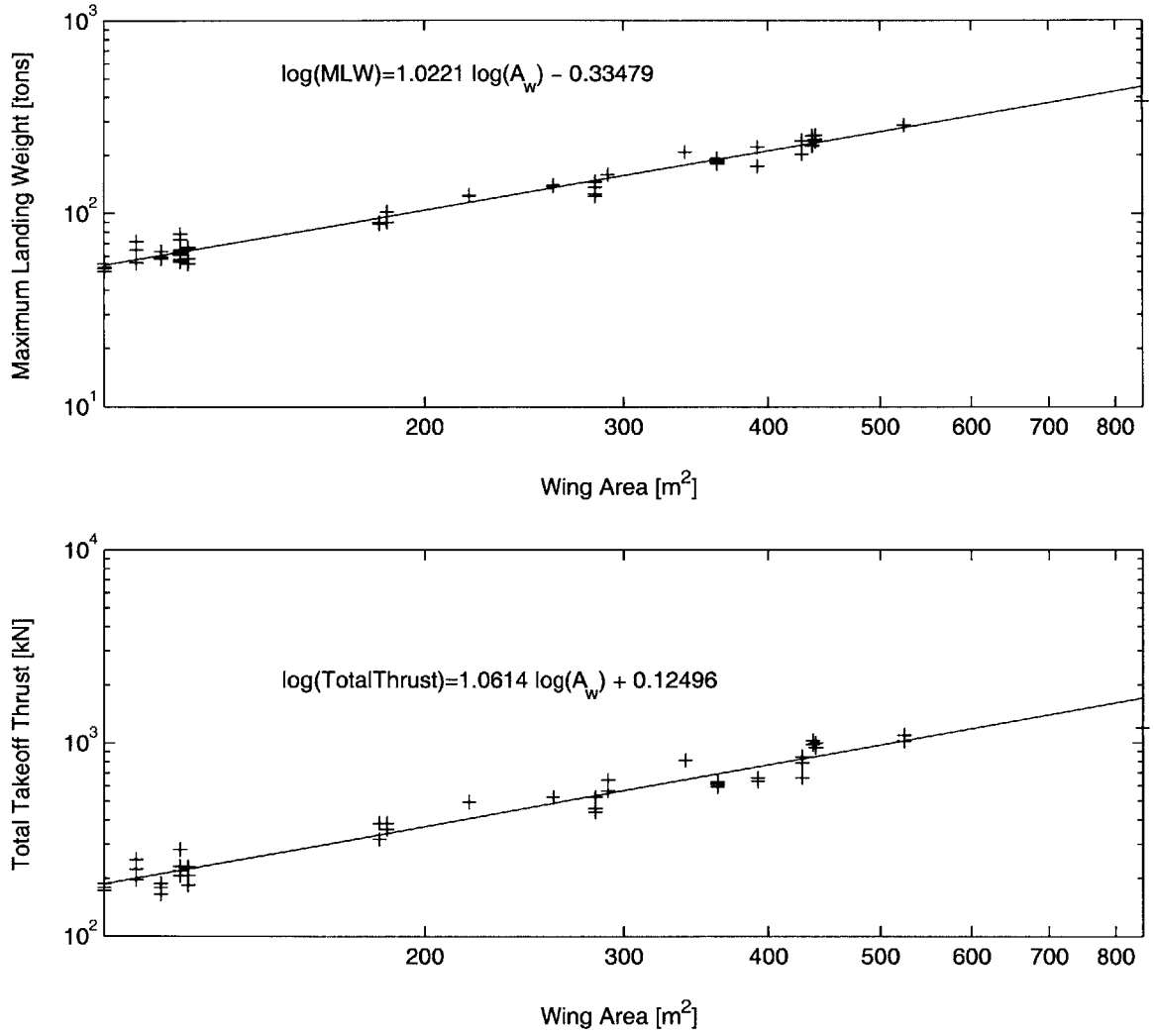

Figure 4-2: Maximum Landing Weight (top) and Total Takeoff Thrust (bottom) as a function of Wing Area for current airliners. Data from Jane's All the World's Aircraft (2003).

loading is constant to first order, and $\alpha = 1$. The trend observed in Figure 4-2 for the total thrust confirms that $\beta = \alpha = 1$.

According to Equations 4.17 and 4.18, the required Silent Drag and the drag produced by the engine air-brake are independent of aircraft size to first order.

Thus,

$$\sigma = mg/A_w = m_0 g/A_{w_0} \cdot k^{\alpha-1} \tag{4.22}$$

yields $\alpha = 1$. In Figure 4-2, the maximum landing weight and total takeoff thrust are plotted as a function of wing area for most current airliners (data from Jane's All the World's Aircraft (2003)). The aircraft landing weight is proportional to wing area, which justifies the assumption that wing

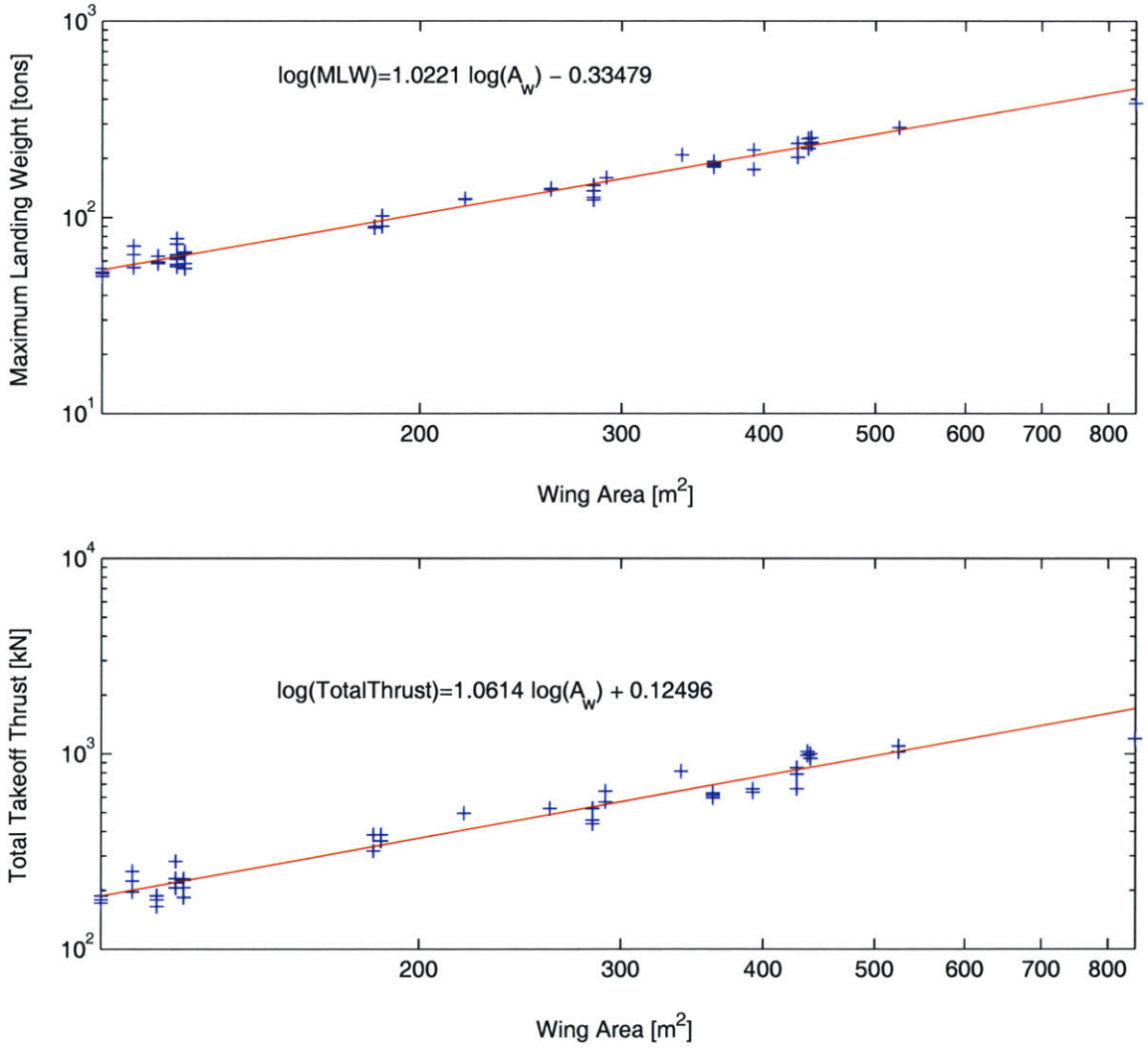

Figure 4-2: Maximum Landing Weight (top) and Total Takeoff Thrust (bottom) as a function of Wing Area for current airliners. Data from Jane's All the World's Aircraft (2003).

loading is constant to first order, and $\alpha = 1$. The trend observed in Figure 4-2 for the total thrust confirms that $\beta = \alpha = 1$.

According to Equations 4.17 and 4.18, the required Silent Drag and the drag produced by the engine air-brake are independent of aircraft size to first order.

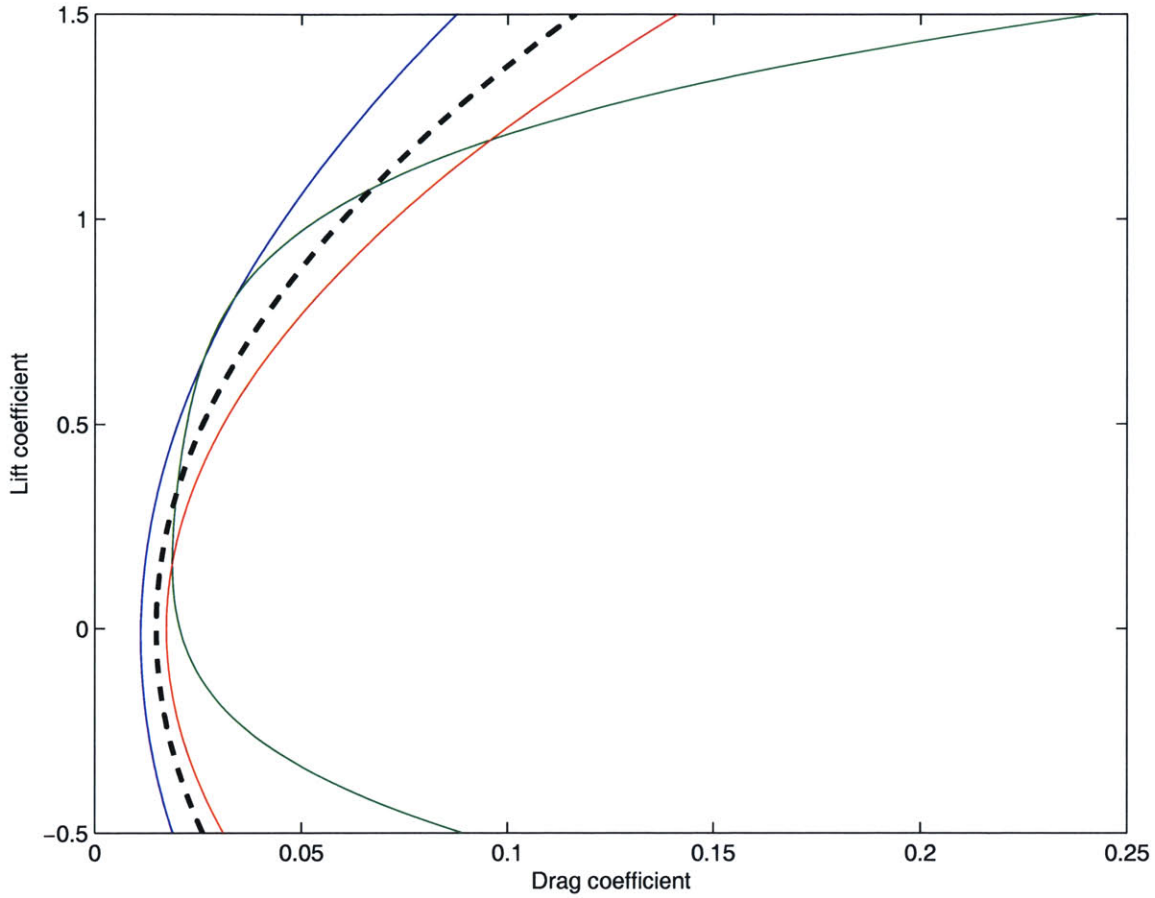

Figure 4-3: Drag polars for the blended-wing-body airframe in clean configuration at cruise conditions from Liebeck et al. (1996) (blue), from model wind tunnel tests by Darmofal (2003) (green), and for the A300 from Boiffier (2000) (red). Black line: best estimate of the drag polar used for the evaluation of the silent drag requirements.

the ultra-high bypass ratio engine cycle delineated in Chapter 2.

For both aircraft types, a parametric study is performed for glide slope angles θ between 3° and 6°. For each glide slope angle, the stall velocity V_s is determined using Equation 4.10. The silent drag requirement $C_{SD_{req}}$ is then computed for approach velocities equal to V_s, $1.1 \cdot V_s$ and $1.3 \cdot V_s$. A minimum stall margin of 30% is usually considered to reduce the risk of stalling the aircraft on approach. This requires $u_0 \geq 1.3 \cdot V_s$. However, it is assumed that the stall margin can be reduced to 10%, i.e. $u_0 \geq 1.1 \cdot V_s$, to enable steeper approach profiles. For $u_0 = V_s$, the aircraft stalls. Steeper and/or slower approach profiles cannot be achieved without high-lift and high-drag devices.

Approach velocities and corresponding silent drag requirements are plotted as a function of the glide slope angle in Figures 4-4 and 4-5 for the conventional and the blended-wing-body aircraft, respectively. Assuming that the engine air-brake generates 0%, 20%, 40%, and 60% of the drag of a bluff body with the same cross-sectional area (i.e. $C_{D_{fan}} = 0,\ 0.2,\ 0.4,\ 0.6$, respectively), the drag

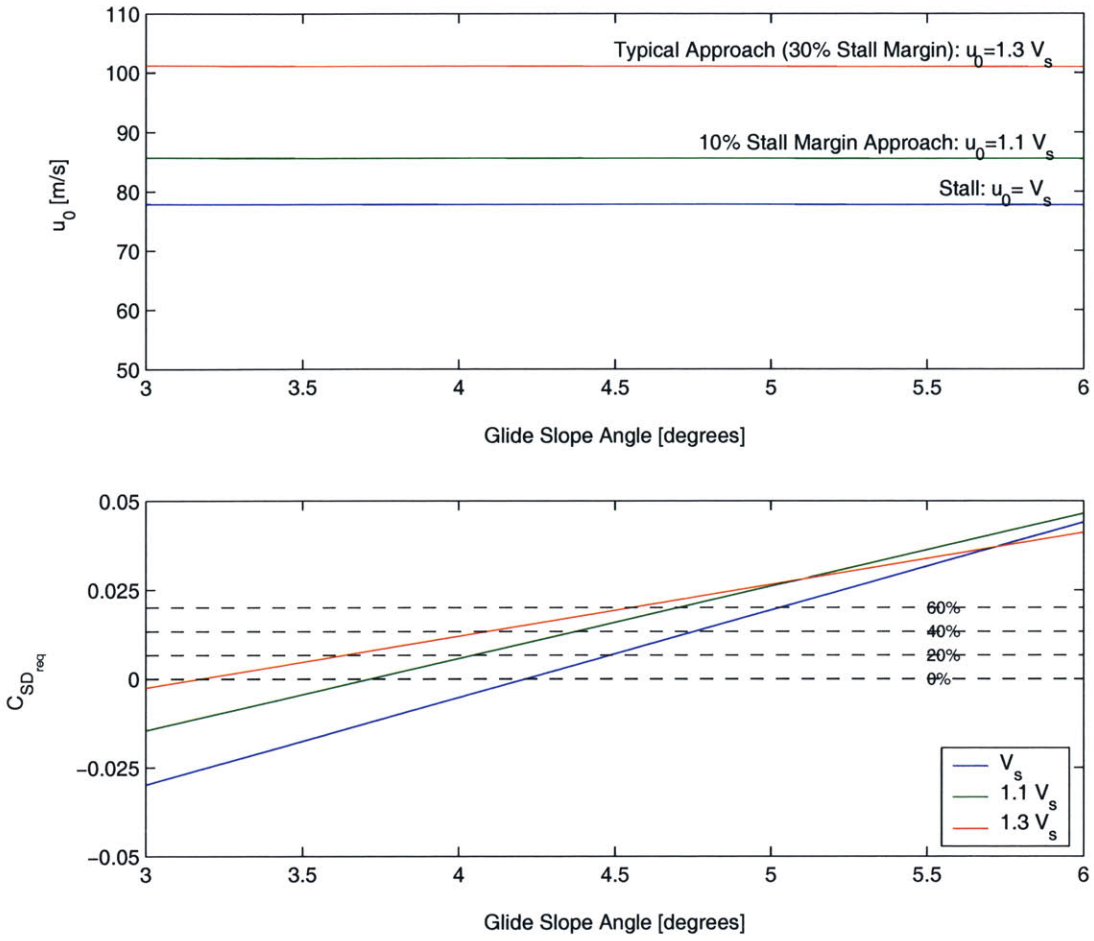

Figure 4-4: Approach velocities (top) and silent drag requirements (bottom) for approach stall margins of 0, 10, and 30% (in blue, green, and red, respectively) as a function of glide slope angle for a conventional aircraft in clean configuration. Black lines: engine air-brake drag assuming 0%, 20%, 40% and 60% of the drag of a bluff body with the same cross-sectional area.

glide slope angle increases to approximately 4°.

Assuming that the engine air-brake can generate 40% of the drag of a bluff body with the same cross-sectional area ($C_{D_{fan}} = 0.4$), glide slope angles for $u_0 = 1.3 \cdot V_s$ and $u_0 = 1.1 \cdot V_s$ increase to 4.6° and 5°, respectively, for the fan inlet area of ultra-high bypass ratio engines delineated in Chapter 2. According to Pilczer (2003), a 6 dB reduction in EPNL can be expected if the conventional approach pattern at $\theta = 3°$ and $u_0 = 1.3 \cdot V_s = 84$ m/s, is altered to a quiet descent at $\theta = 5°$ and $u_0 = 1.1 \cdot V_s = 71$ m/s enabled by a silent engine air-brake generating $C_{D_{fan}} = 0.4$.

When drag is generated by the engine air-brake, the exhaust velocity is lower than the flight velocity. This creates unsteady flow structures due to vortex shedding that generate low-frequency noise. If thrust is produced, jet noise is radiated. Thus, minimum noise radiation is achieved when the exhaust velocity matches the flight velocity. In this case, the engine air-brake does not produce

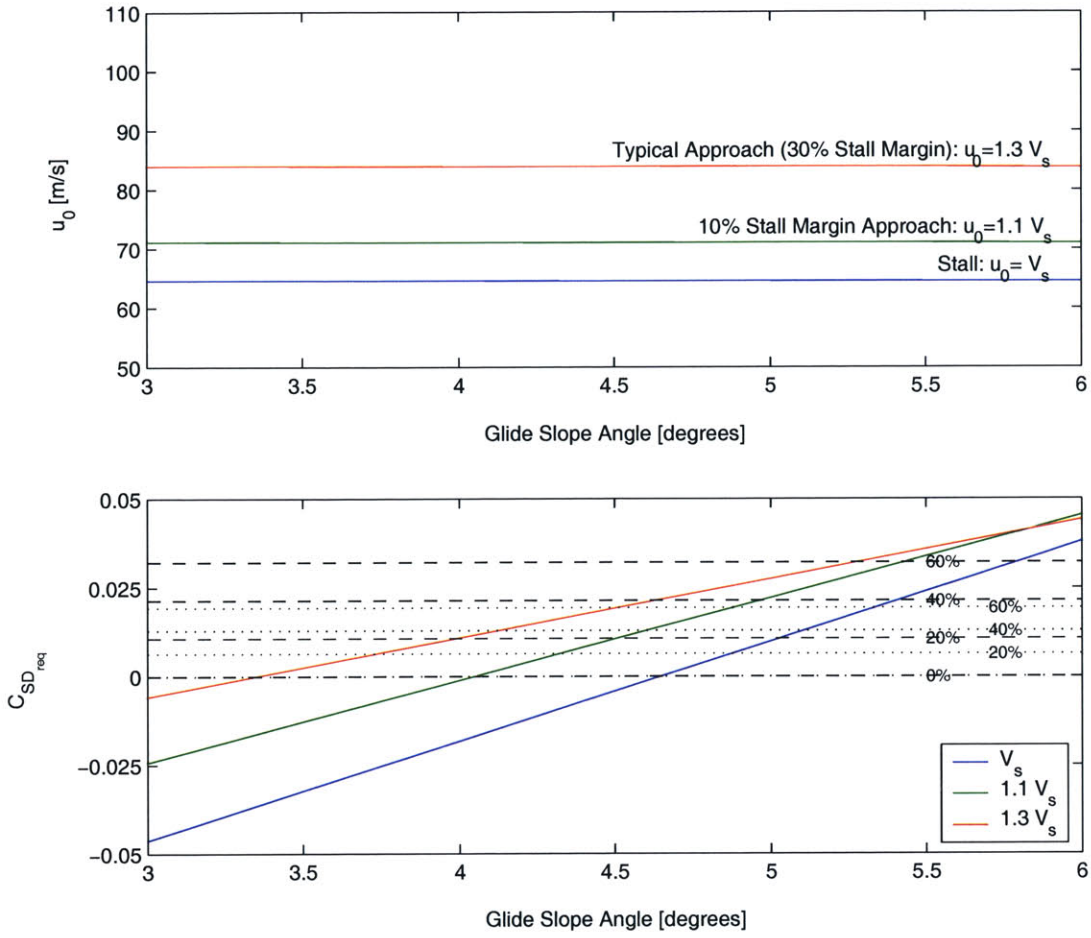

Figure 4-5: Approach velocities (top) and silent drag requirements (bottom) for approach stall margins of 0, 10, and 30% (in blue, green, and red, respectively) as a function of glide slope angle for a blended-wing-body aircraft in clean configuration. Black lines: engine air-brake drag assuming 0%, 20%, 40% and 60% of the drag of a bluff body with the same cross-sectional area. Dotted lines: baseline BWB engine, dashed lines: UHBPR engine.

drag ($C_D = 0$). The maximum glide slope angles then become 3.5° at $u_0 = 1.3 \cdot V_s$ and 4° at $u_0 = 1.1 \cdot V_s$. According to Pilczer (2003), this reduction of the glide slope angle by 0.5° at constant approach velocity yields a 1 dB increase in perceived trailing edge noise.

These observations suggests that a "minimum noise approach" exists between

- steep approaches achieved for $C_D > 0$ but yielding radiation of noise due vortex shedding and
- shallower approaches achieved for $C_D = 0$ leading to the reduction of vortex shedding and jet noise.

The optimum approach profile in terms of perceived noise can only be determined with refined assessments of airframe noise, silent drag requirements, engine air-brake drag generation, and engine air-brake noise signature (vortex shedding and fan noise).

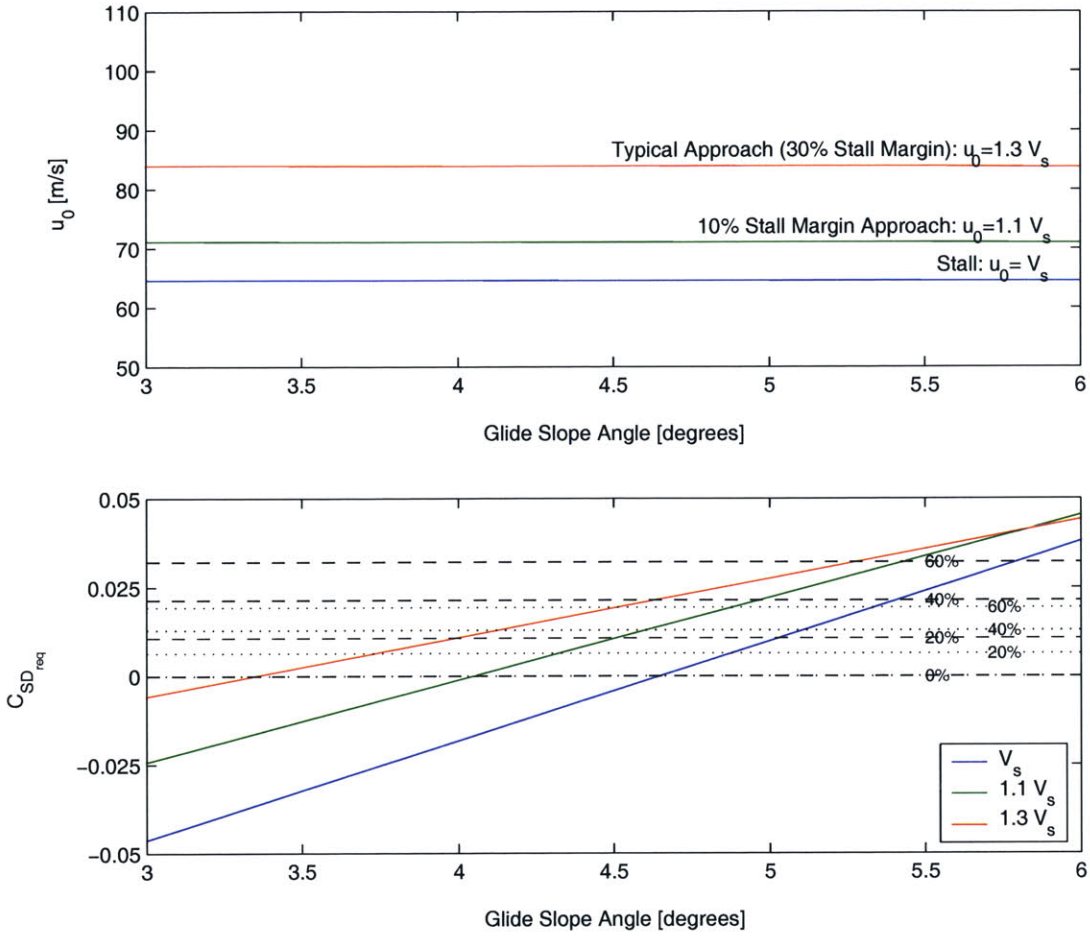

Figure 4-5: Approach velocities (top) and silent drag requirements (bottom) for approach stall margins of 0, 10, and 30% (in blue, green, and red, respectively) as a function of glide slope angle for a blended-wing-body aircraft in clean configuration. Black lines: engine air-brake drag assuming 0%, 20%, 40% and 60% of the drag of a bluff body with the same cross-sectional area. Dotted lines: baseline BWB engine, dashed lines: UHBPR engine.

drag ($C_D = 0$). The maximum glide slope angles then become 3.5° at $u_0 = 1.3 \cdot V_s$ and 4° at $u_0 = 1.1 \cdot V_s$. According to Pilczer (2003), this reduction of the glide slope angle by 0.5° at constant approach velocity yields a 1 dB increase in perceived trailing edge noise.

These observations suggests that a "minimum noise approach" exists between

- steep approaches achieved for $C_D > 0$ but yielding radiation of noise due vortex shedding and
- shallower approaches achieved for $C_D = 0$ leading to the reduction of vortex shedding and jet noise.

The optimum approach profile in terms of perceived noise can only be determined with refined assessments of airframe noise, silent drag requirements, engine air-brake drag generation, and engine air-brake noise signature (vortex shedding and fan noise).

4.3 Engine Air-Brake Meanline Flow Model

4.3.1 Introduction

According to Euler's turbine equation, work is done on the fluid by increasing the angular momentum. This results in a "positive turning" of the flow in compressor mode. Inversely, work is extracted from the fluid by decreasing the angular momentum. Thus, in order to operate in windmilling mode, a "negative turning" of the flow must be achieved. It is suggested that turning the fan blade by approximately 180° can achieve the required negative flow turning. This idea is illustrated in Figure 4-6.

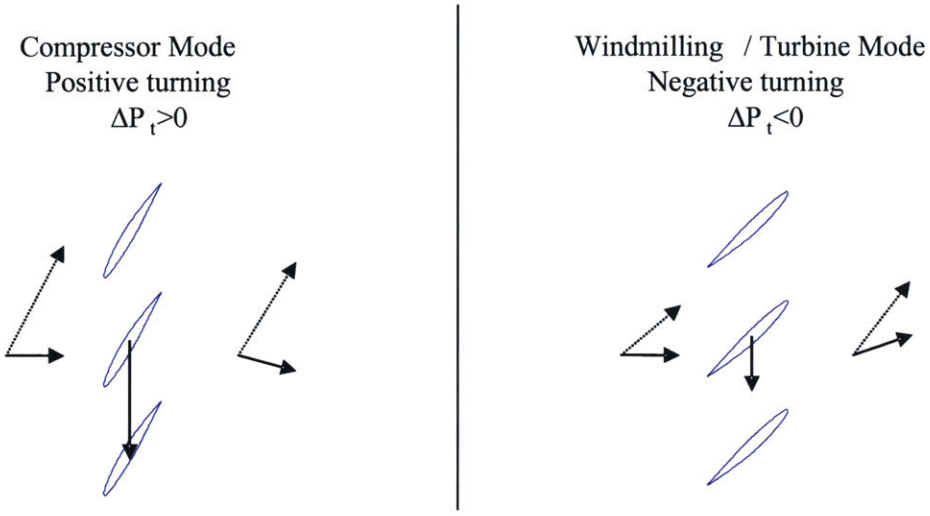

Figure 4-6: Compressor and windmilling operating modes for a rotor blade-row with variable stagger angle.

To assess the drag generation ability of such a windmilling engine air-brake, a compressible meanline flow model of a variable-pitch ducted blade row is developed. The methodology and underlying assumptions are first presented. The functionality of the model is then demonstrated by generating a standard fan map. Finally, a parametric study is performed for various blade stagger angles and wheel speeds in windmilling mode. The corresponding drag generated by the engine air-brake is computed.

4.3.2 Meanline Flow Model of a Variable Pitch Ducted Rotor

In the model presented here, the following stations are considered:

- station 0: far stream ambient conditions
- station 1: blade-row inlet

- station 2: blade-row exit
- station 3: duct exit

These stations are indicated in Figure 4-1. At each station, V_i, u_i, and v_i are the meanline, axial, and tangential flow velocities, respectively.

Blade-Row Loss and Turning Description

Blade-row deviation and loss are given over a range of incidence angles for 10° to 20° above and below the design incidence angle and for various blade Mach numbers. At a certain incidence, the blade stalls, leading to a rise in losses and deviation.

In windmilling mode, the flow incidence angle relative to the leading edge metal angle (i) is expected to be of order 180°. To compute the drag generated by the air-brake, the blade performance at such off-design incidences must be known. However, in windmilling mode and at fully stalled conditions, deviation becomes difficult to model. Therefore, the blade-row performance is described by flow turning instead of deviation. The loss buckets are assumed independent of the blade Mach number .

The following assumptions allow the definition of the blade-row turning and loss buckets for any incidence:

- The maximum positive turning is achieved at the design incidence angle (i^*) in compressor mode.
- Flow angles and velocities at the design point set the design diffusion factor. The design loss coefficient is then deduced and sets the minimum loss level.
- For a prescribed incidence angle i_s, the blade stalls. According to the definition of stall given in Cumpsty (1989), the loss coefficient increases by a factor of two relative to the minimum loss level achieved at the design point.
- The "full stall" incidence angle i_{fs} is defined such that the turning drops to zero and the loss coefficient reaches a maximum level. The blade then behaves as a bluff body and does not alter the flow direction.
- Over the range $-i_{fs} < i < i_{fs}$, the loss bucket and turning function are defined in the form of fourth order polynomials satisfying the previous constraints.
- The flow incidence angle relative to the trailing edge metal angle is given by: $i_{TE} = i + c + sgn(i)\pi$ where c is the blade camber (trailing edge metal angle minus leading edge metal angle), and $sgn(i) = 1$ if $i \geq 0$, and -1 if $i < 0$. In windmilling mode, i_{TE} is expected to be close to zero. Therefore, over the range $-i_{fs} < i_{TE} < i_{fs}$, the turning is assumed equal and opposite

to that achieved in compressor mode for $i = i_{TE}$, and losses are assumed equal to the ones occurring for $i = i_{TE}$.

- Finally, for incidences angles other than $-i_{fs} < i < i_{fs}$ and $-i_{fs} < i_{TE} < i_{fs}$, the blade is fully stalled: the turning is zero and the loss coefficient is equal to the maximum level previously determined.

Under these assumptions, the blade row is modeled as an actuator disk with generic turning and losses characteristics defined for any incidence. The resulting turning function and loss buckets are plotted in Figure 4-7. The design and stall incidences introduced above are indicated.

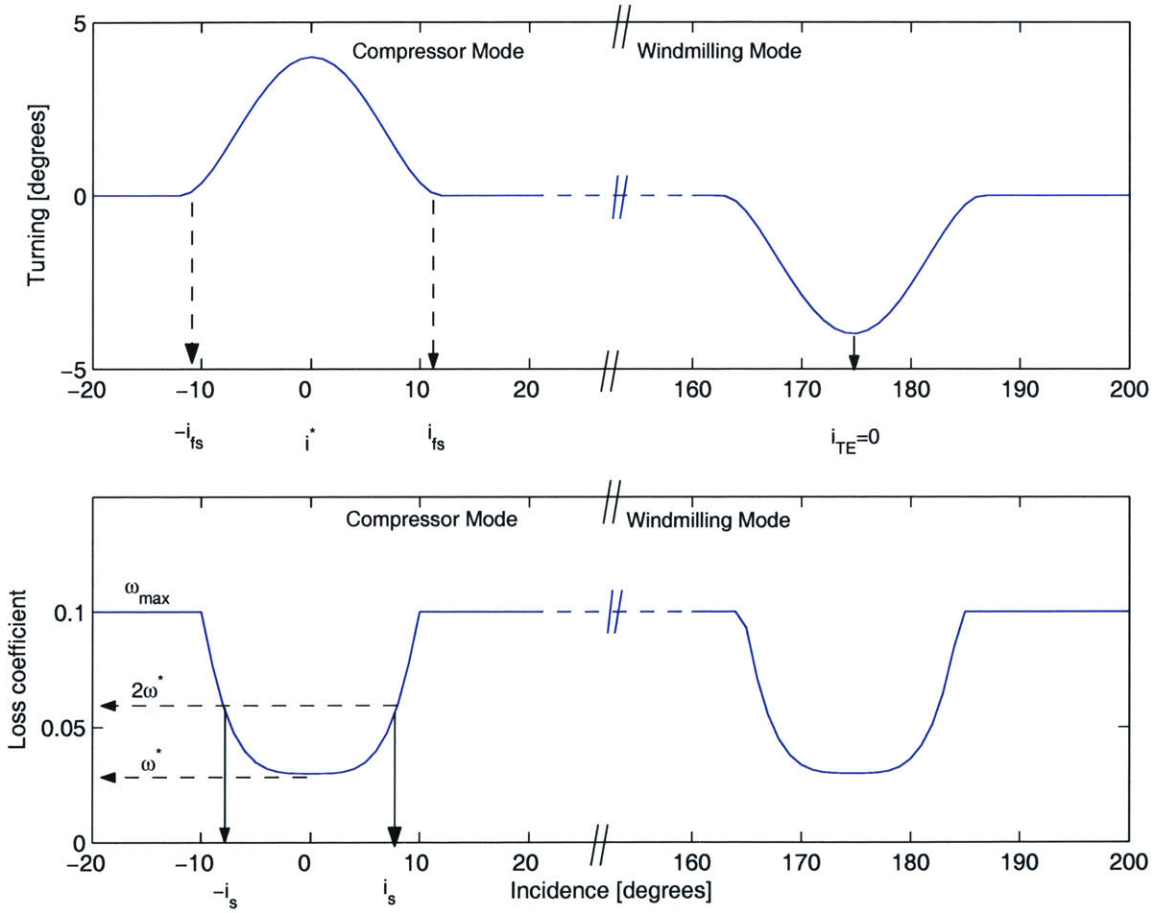

Figure 4-7: Generic turning function and loss buckets in compressor and windmilling operating modes.

Design Point

The blade-row characteristics and the duct geometry are set given design operating conditions. At off-design conditions, these blade-row characteristics and the duct geometry determine the operating

point.

In the case of a meanline compressible calculation, the duct geometry is characterized by relative variations in annulus area between the different stations.

The following inputs and design variables are required to set the design point:

- ambient conditions at design point: T_0, P_0, M_0
- blade tip speed: U_{tip}
- blade hub-to-rip ratio: $r = r_{hub}/r_{tip}$
- blade loading coefficient: $\Psi = \frac{\Delta h_t}{U^2}$
- blade flow parameter: $\Phi = u_1/U$, where u_1 is the axial velocity at the blade inlet
- blade row solidity at meanline: σ

The meanline compressible calculation at design point used in this model is very similar to that presented in Mattingly (1996). The main steps of this calculation and the underlying assumptions are as follows:

- Assuming isentropic inlet flow, the ambient conditions yield total pressure and temperature at station 1.
- From hub-to-tip ratio, the meanline radius is computed relative to the tip radius: $r_{mean}/r_{tip} = \sqrt{(1+r^2)/2}$. The blade speed at the meanline is then $U = r_{mean}/r_{tip} \cdot U_{tip}$. Δh_t and u_1 are deduced from Ψ and Φ, respectively.
- Assuming axial flow at station 1 (absolute flow angle $\alpha_1 = 0°$), the flow properties can be completely determined at this station in both absolute and relative frames of reference.
- Assuming constant meanline radius across the blade row, the tangential flow velocity at station 2 is deduced from Euler's turbine equation and Δh_t.
- Assuming the axial velocity constant across the blade row, the flow velocity triangle at station 2 is completely known. This enables the computation of the design diffusion factor: $D = 1 - V_{2r}/V_{1r} + |v_{1r} - v_{2r}|/(2\sigma V_{1r})$. Using the correlation between diffusion factor D and loss coefficient $\omega = \frac{P_{t1r}-P_{t2r}}{P_{t1r}-P_1} = \frac{1-\pi_r}{1-\left(1+\frac{\gamma-1}{2}M_{1r}^2\right)^{\frac{\gamma}{1-\gamma}}}$ (see Cumpsty (1989); Mattingly (1996)), the relative total pressure losses across the blade row π_r are deduced, and the flow state at station 2 can be completely determined.
- The blade leading edge metal angle γ_i is set by assuming zero incidence at design conditions. The blade trailing edge metal angle is computed employing Carter's rule and the blade row solidity: $\gamma_o = (4\beta_2\sqrt{\sigma} - \gamma_i)/(4\sqrt{\sigma} - 1)$. Assuming a circular camber line, the blade row meanline stagger angle and the blade camber are given by $\gamma = \frac{\gamma_i+\gamma_o}{2}$ and $\gamma_o - \gamma_i$, respectively.

- From the conservation of mass between stations 1 and 2, the variation of the annulus area across the blade row is $A_2/A_1 = \frac{\rho_1 u_1}{\rho_2 u_2}$.

- Finally, the flow at station 2 is exhausted through a converging nozzle at station 3. Assuming isentropic flow through the duct, $P_{t3} = P_{t2}$ and $T_{t3} = T_{t2}$. The nozzle flow is either choked ($M_3 = 1$) or ideally expanded to ambient pressure ($P_3 = P_0$). In either case, the flow properties at station 3 can be completely determined. From the conservation of mass between stations 1 and 3, the nozzle exit area relative to the fan inlet area is $A_3/A_1 = \frac{\rho_1 u_1}{\rho_3 u_3}$.

Off-Design Performance Calculation

Once the design point calculation is performed, the meanline blade camber and duct geometry (A_2/A_1 and A_3/A_1) are frozen. The off-design behavior of this ducted blade-row then needs to be determined under various operating conditions, in particular, in windmilling mode, to assess the drag generation capacity of the engine air-brake. For a variable-pitch ducted blade-row, an off-design operating point is completely defined by:

- off-design ambient conditions: T_0, P_0, M_0

- blade tip speed: U_{tip}

- meanline blade row stager angle: γ

If the nozzle has a variable geometry, the operating point is also influenced by the exhaust area setting, characterized by $A_3/A_{3_{des}}$.

In order to determine the flow state throughout the system at off-design conditions, the following method is applied:

- Starting with an initial guess of M_1, the flow state at station 1 is determined and the blade incidence is found from the wheel speed and the stagger angle.

- For this incidence, the flow turning and loss coefficient are computed according to the blade-row model described above. Using Euler's turbine equation, relative total pressure losses, and the conservation of mass across the blade-row, the flow state at station 2 can be determined.

- The flow state at station 3 is found from the total pressure and temperature at station 2 and the isentropic relations. From the flow velocity and density at stations 1 and 3 and the relative area A_3/A_1, the ratio $\dot{m}_3/\dot{m}_1$ can be computed.

- If $\dot{m}_3/\dot{m}_1 = 1$, mass conservation is satisfied from station 1 to 3, and the off-design performance computation is complete. Otherwise, the inlet Mach number needs to be adjusted as follows. If the mass flow at station 3 is too low ($\dot{m}_3/\dot{m}_1 < 1$), the pressure ratio across the blade row needs

to be raised by increasing the blade loading in compressor mode or decreasing it in windmilling mode. In both operating modes, increasing the pressure ratio invariably requires an increase in flow incidence by reducing M_1. If the mass flow at station 3 is too high ($\dot{m}_3/\dot{m}_1 > 1$), M_1 must be increased.

- A variable-area exhaust nozzle can be modeled with this method by imposing a given value of $\frac{A_3}{A_1} = \frac{A_3}{A_{3_{des}}} \cdot \frac{A_{3_{des}}}{A_1}$ when the mass flow at station 3 is computed relative to the mass flow at station 1. The solution scheme then adjusts M_1 such that mass conservation is satisfied throughout the entire system.

Model Output - Engine Air-Brake Drag Computation

The axial force F acting on the duct is opposite to the net axial momentum flux between station 0 and station 3, $F = \dot{m}(u_3 - u_0)$, where u_i are axial velocities and $\dot{m}$ is the total mass flow through the device. In particular, at station 1, $\dot{m} = \rho_1 u_1 A_1$, where ρ_1 and u_1 are given by the off-design computation. Since u_3 is also computed, F can be determined.

If $u_3 > u_0$, F is positive and forward thrust is produced. Thus, the drag generated by the engine air-brake in windmilling mode is:

$$D = \rho_1 u_1 A_1 (u_0 - u_3). \tag{4.23}$$

The physical size of the engine air-brake, characterized by A_1, is not required by the present model. Therefore, the air-brake performance can be expressed independently of its size by the drag coefficient based on the fan inlet area $A_1 = A_{fan}$:

$$C_{D_{fan}} = \frac{\rho_1 u_1 (u_0 - u_3)}{\frac{1}{2}\rho_0 u_0^2}. \tag{4.24}$$

The pressure coefficient in the nozzle between stations 2 and 3 is also output by the model:

$$C_p = \frac{P_3 - P_2}{\frac{1}{2}\rho_2 u_2^2}. \tag{4.25}$$

4.3.3 Model Implementation for Compressor Operating Mode

In order to demonstrate the functionality of the meanline flow model, a fan map is generated and plotted in Figure 4-8. The following fan design parameters are chosen:

- P_0 and T_0: ISA sea level conditions
- $M_0 = 0.2$
- $M_{tip} = 1$
- $r = 0.3$

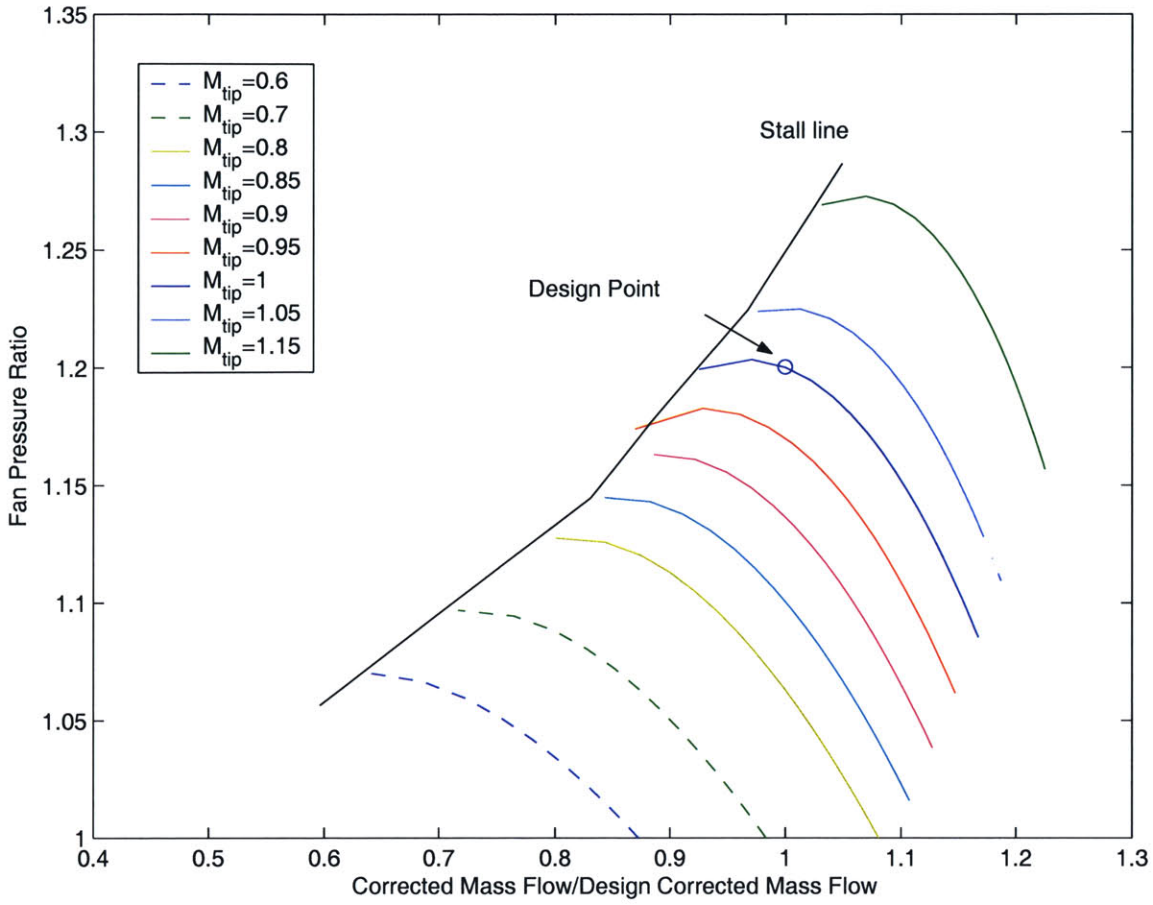

Figure 4-8: Generated fan map using compressible meanline flow model and generic blade row turning and loss characteristics.

- $\Psi = 0.153$ (adjusted such that the fan pressure ratio is $\pi_{fan} = 1.2$, a typical value for UHBPR engines (see Chapter 2).)
- $\Phi = 0.5$
- $\sigma = 1$

The blade tip Mach number is varied between $M_{tip} = 0.6$ and $M_{tip} = 1.15$. For a given tip Mach number, speed-lines are generated by varying the back-pressure between $0.4 \cdot P_0$ and $1.2 \cdot P_0$. The lowest back-pressure for which the calculation properly converges defines the stall line.

4.3.4 Results

The ducted fan designed in compressor mode in Section 4.3.3 is run in windmilling mode. A parametric study is performed by the model for stagger angles ranging from $\gamma = -160°$ to $\gamma = -100°$

and for blade tip Mach numbers ranging from $M_{tip} = 0.14$ to $M_{tip} = 0.65$. Figure 4-9 shows the resulting drag coefficient as a function of the stagger angle for various wheel speeds.

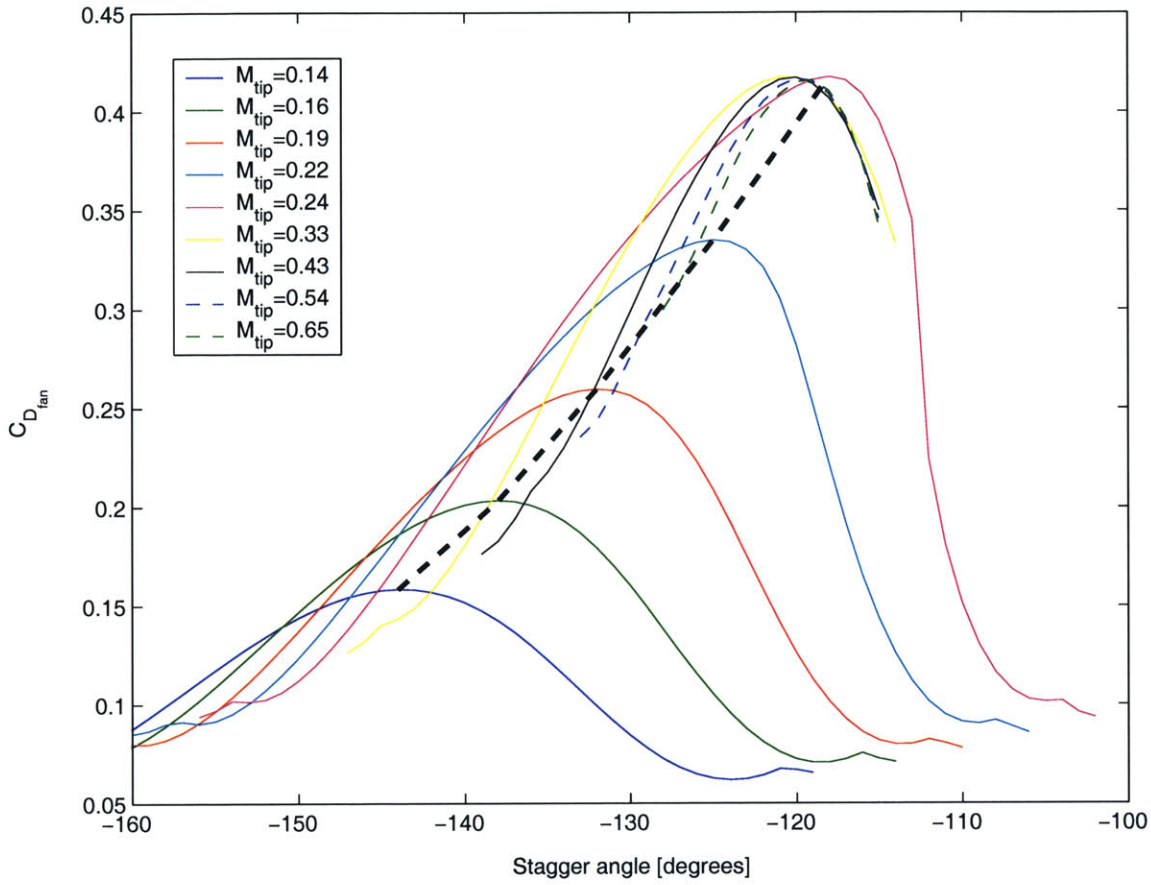

Figure 4-9: Prediction of the drag coefficient generated by the engine air-brake as a function of stagger angle and wheel speed using meanline flow model.

For each wheel speed a stagger angle exists that maximizes the generated drag. The corresponding stagger angles are marked by the thick dotted line in Figure 4-9.

For $M_{tip} < 0.24$, the maximum drag coefficient sharply increases with wheel speed. Here, the stagger angle can be adjusted to achieve $i_{TE} = 0$, for which the negative flow turning is maximum.

For $M_{tip} > 0.24$, the maximum drag coefficient reaches a maximum value $C_{D_{fan}} \approx 0.42$. At these blade tip Mach numbers, maximum turning yields too low a pressure at station 2 such that the back-pressure at the nozzle exit cannot be matched. As the wheel speed increases, the blade needs to be progressively unloaded in order to achieve a static pressure at the nozzle exit that can match the back-pressure. The minimum pressure that can be achieved at station 2 is set mainly by the area change between stations 2 and 3, which yields the maximum possible drag coefficient with this fixed geometry.

Thus, it is suggested that higher drag coefficients can be generated if the minimum possible pressure at station 2 can be further lowered. For this purpose, a variable-area nozzle is envisioned: by increasing the exhaust area, the nozzle behaves as a diffuser with a lower pressure at station 2 and a lower velocity at station 3, yielding higher drag coefficient. However, flow in a diffuser can stall if strong adverse pressure gradients are present. Since the model does not account for any losses in the nozzle, the study has to be limited to pressure coefficients between station 2 and 3 that are not likely to yield flow separation in the nozzle. In practice, an upper limit of $C_p \approx 0.5$ is considered (see Koch (1981)). If active flow control is used, this upper limit can be increased to $C_p \approx 0.65$ (see Coller et al. (2000) and McCormick (2000)). Figure 4-10 shows the maximum generated drag coefficient as a function of the pressure coefficient. The variable-area capability significantly enhances

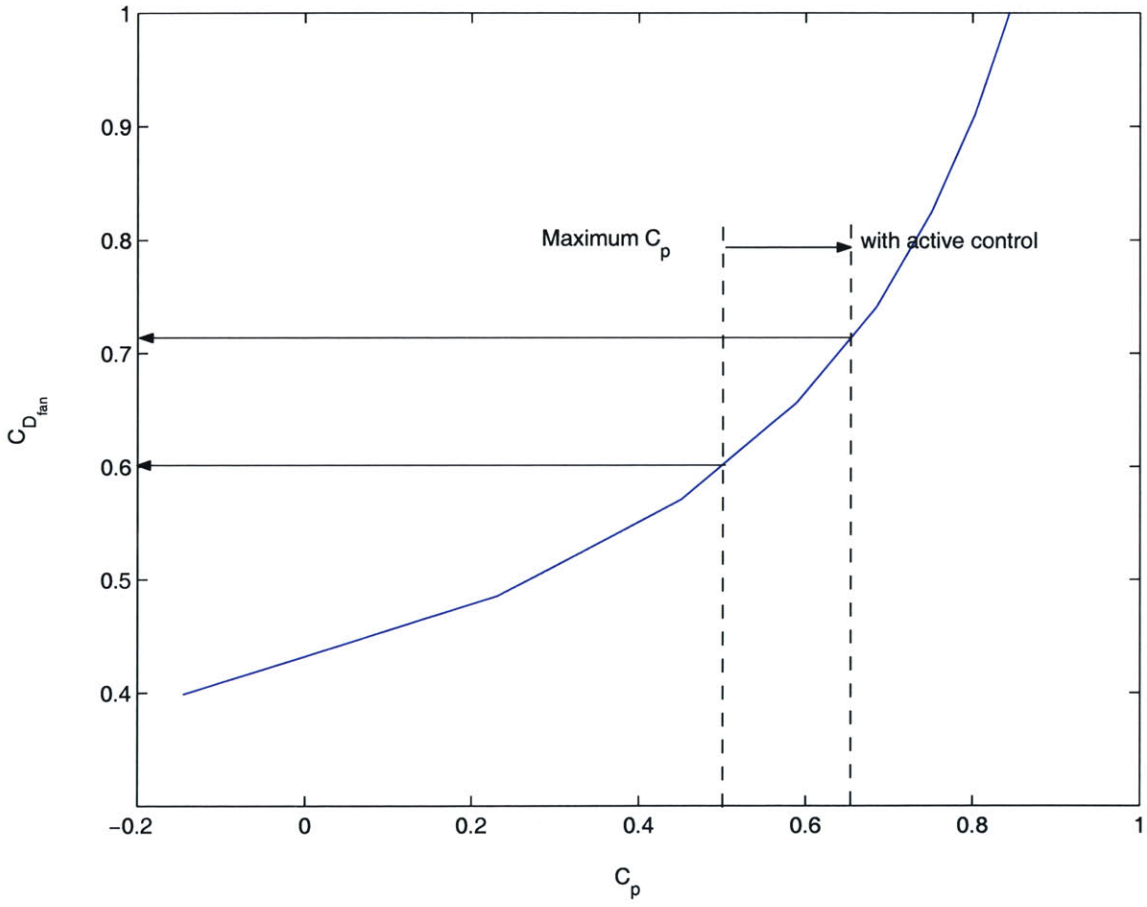

Figure 4-10: Drag coefficient generated by engine air-brake with variable-area exhaust nozzle as a function of the nozzle pressure coefficient.

the performance of the windmilling engine air-brake. The maximum drag coefficient increases from $C_{D_{fan}} = 0.42$ for the design exhaust area (converging nozzle) up to $C_{D_{fan}} = 0.6$ for $C_p = 0.5$ and even to $C_{D_{fan}} = 0.7$ with active flow control.

4.3.5 Conclusions

The meanline flow model enables the assessment of the drag generation capability of the windmilling engine air-brake on a preliminary basis. The results suggest that a maximum drag coefficient based on fan inlet area of 0.42 can be achieved for a stagger angle of approximately $-120°$ and a blade tip Mach number larger than 0.25. Further drag generation can be achieved by reducing the exhaust velocity using a variable-area nozzle as a diffuser.

Another possibility to increase the maximum generated drag coefficient would consist in lowering the static pressure at station 2 by adjusting the stator stagger angle. This would require a modification to the model to account for the stator blade row.

4.4 Blade-to-Blade Engine Air-Brake Analysis

4.4.1 Introduction

The main assumption of the meanline flow model used in Section 4.3 is the modeling of the rotor blade-row as an actuator disk with generic turning and loss characteristics.

In order to refine the assessment of the drag generated by the engine air-brake, this modeling is replaced by a blade-to-blade calculation using MISES (see Drela and Youngren (1998)).

4.4.2 Methodology

MISES Computation and Required Inputs

MISES performs a two-dimensional viscous computation of the blade-to-blade passage flow field. The domain in which the flow is computed is a stream surface characterized by a radius distribution, a thickness distribution, and a pitch-wise extent corresponding to one blade passage. The code requires the blade profile at the radius corresponding to the stream surface (for more details, see Drela and Youngren (1998)). For this study, the stream surface is set at the meanline radius.

The blade-row characteristics and the duct geometry are determined at design point using the meanline compressible analysis presented in Section 4.3. The blade camber, the blade leading edge and the blade trailing edge metal angles are calculated. Assuming hub-to-tip ratios at stations 1 and 2 and a blade tip radius of 1 m, the axial distribution of meanline radius is determined. From the blade-row solidity σ and the number of blades N, the blade chord c is given by $c = \sigma \cdot \frac{2\pi r_m}{N}$, where r_m is the meanline radius. From the flow-path area at stations 1 and 2, the axial distribution of stream surface thickness is computed. Assuming a NACA65 type airfoil and a blade thickness-to-chord ratio, the thickness distribution along the camber line is determined. For a given stagger angle, the appropriate rotation is applied, and the blade geometry is imported in MISES's grid generation program. The pitch-wise extent of the stream surface is $\Delta\theta = 2\pi/N$.

The Reynolds number based on the blade chord and the flow velocity relative to the blade needs to be specified for viscous computations.

For a design blade tip Mach number of one, the relative blade Mach number at meanline radius is expected to be subsonic for most operating conditions. For this type of inlet conditions, prescribing the upstream relative flow angle and Mach number creates a well-posed problem in MISES.

Off-Design Performance Computation

In order to compute the off-design behavior of the blade-row using MISES computations, a procedure similar to that implemented in the meanline model is applied:

- For a given stagger angle, the computational grid is generated based on the blade geometry.
- An initial guess of the inlet axial Mach number is made based on a meanline calculation or a previous flow field computation, and the relative flow angle is deduced from the blade speed.
- MISES is run until the computation converges, i.e. the residuals on global variables are below 10^{-6} (see Drela and Youngren (1998) for more details). The mixed-out flow angle, Mach number, and total pressure at the blade-row exit are obtained. The flow state at the nozzle exit is determined, and the exhaust mass flow is computed based on the nozzle area determined at the design point.
- If the exhaust mass flow does not match the inlet mass flow, the inlet Mach number is adjusted. This process is repeated until mass conservation is satisfied from the blade row inlet to the nozzle exit.
- Finally, the drag coefficient is computed from the axial flow velocity at the nozzle exit and the mass flow at the blade-row inlet, as in the meanline model.

In compressor operating mode, the computation properly converges for a range of operating conditions close to the design point. Starting from a converged computation, the blade-row performance can be computed by progressively changing the stagger angle, the wheel speed or the back-pressure to reach the desired operating condition. The same method can be used in windmilling mode, however an appropriate initial guess is more difficult to find.

4.4.3 Model Implementation for Compressor Operating Mode

The blade-to-blade analysis is used to evaluate the blade-row off-design performance in compressor mode. The same fan blade design parameters as in Section 4.3.3 are selected. The fan pressure ratio and corrected mass flow are computed along speed-lines for blade tip Mach numbers between 0.85 and 1.15. Figure 4-11 depicts the resulting fan map and operating line.

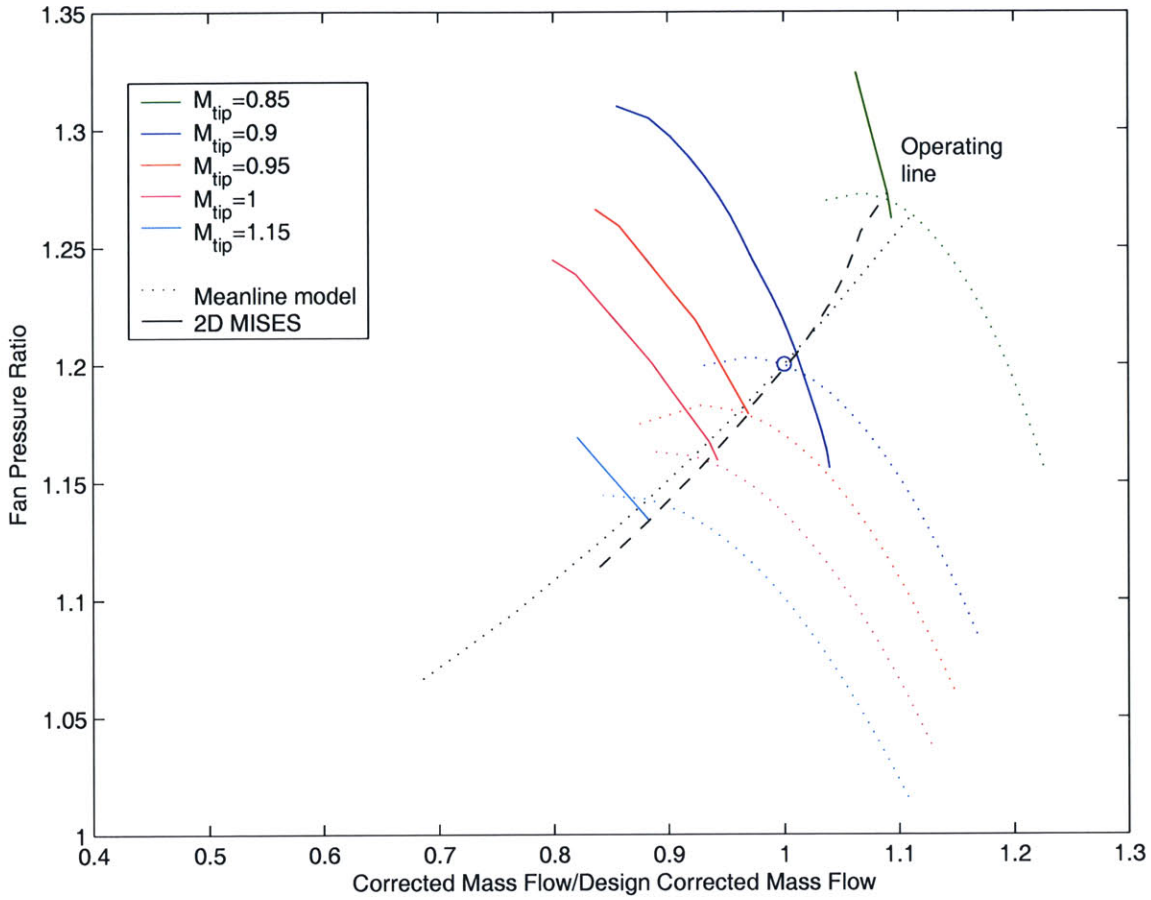

Figure 4-11: Fan map generated from blade-to-blade viscous computations using MISES . Dotted lines: results from the meanline model for the same operating conditions.

At design conditions (i.e. $M_{tip} = 1$ and back pressure equal to ambient pressure at design point), the blade-to-blade analysis yields $\pi_{fan} = 1.2037$ and $\dot{m}_{c1}/\dot{m}_{c1_{des}} = 1.009$, both within 1% of the design values:$\pi_{fan} = 1.2$ and $\dot{m}_{c1}/\dot{m}_{c1_{des}} = 1$ (by definition). Contours of constant Mach number at design point are shown in Figure 4-12.

The analysis using MISES computation and the meanline flow model prediction yield significantly different results. In the meanline model, the loss buckets and turning characteristics are selected to render typical trends in off-design blade-row performance, but do not correspond to a particular blade geometry. On the contrary, the blade-to-blade analysis computes the viscous losses and the flow turning for a given blade profile. Thus, the blade-to-blade analysis is expected to give a more accurate prediction of the drag generation capability of the windmilling engine air-brake compared to the meanline flow model.

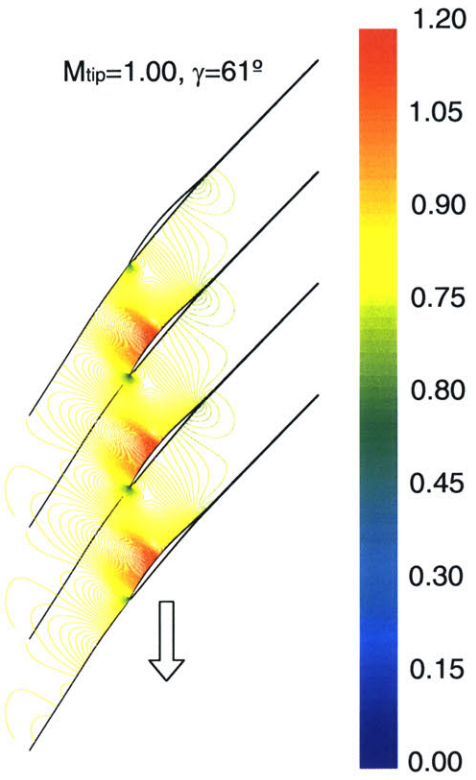

Figure 4-12: Contours of constant Mach number at design point: $M_{tip} = 1$, $\gamma = 61°$.

4.4.4 Results

The blade-row performance is computed in windmilling mode for blade tip Mach numbers ranging from 0.1 to 0.5 and stagger angles ranging from $\gamma = -140°$ to $\gamma = -105°$. However, for a given wheel speed, the computation does not successfully converge over the entire range of stagger angles; as the wheel speed increases, higher stagger angles can be achieved but remain limited below $\gamma = -108°$. For $\gamma > -108°$, the blades do not overlap such that the blade passage is not well defined, which leads to meshing and convergence issues.

Drag coefficients generated by the engine air-brake are computed using Equation 4.24 and are plotted in Figure 4-13 as a function of the stagger angle setting. For a given wheel speed, the stagger angle can be adjusted to maximize the drag coefficient, as previously observed in Section 4.3.4. The sensitivity of generated drag with respect to wheel speed is low over the range of blade tip Mach numbers covered here. The maximum drag coefficient increases from 0.44 to 0.46 as the wheel speed increases from $M_{tip} = 0.16$ to $M_{tip} = 0.5$. Contours of constant Mach number are shown for stagger angles of $-130°$, $-120°$, $-115°$, and $-110°$ in Figure 4-14. These selected stagger angles yield the maximum drag generation for the respective blade tip Mach numbers.

Drag generation yields a lower engine exit velocity (u_3 or u_{ex}) compared to the flight velocity

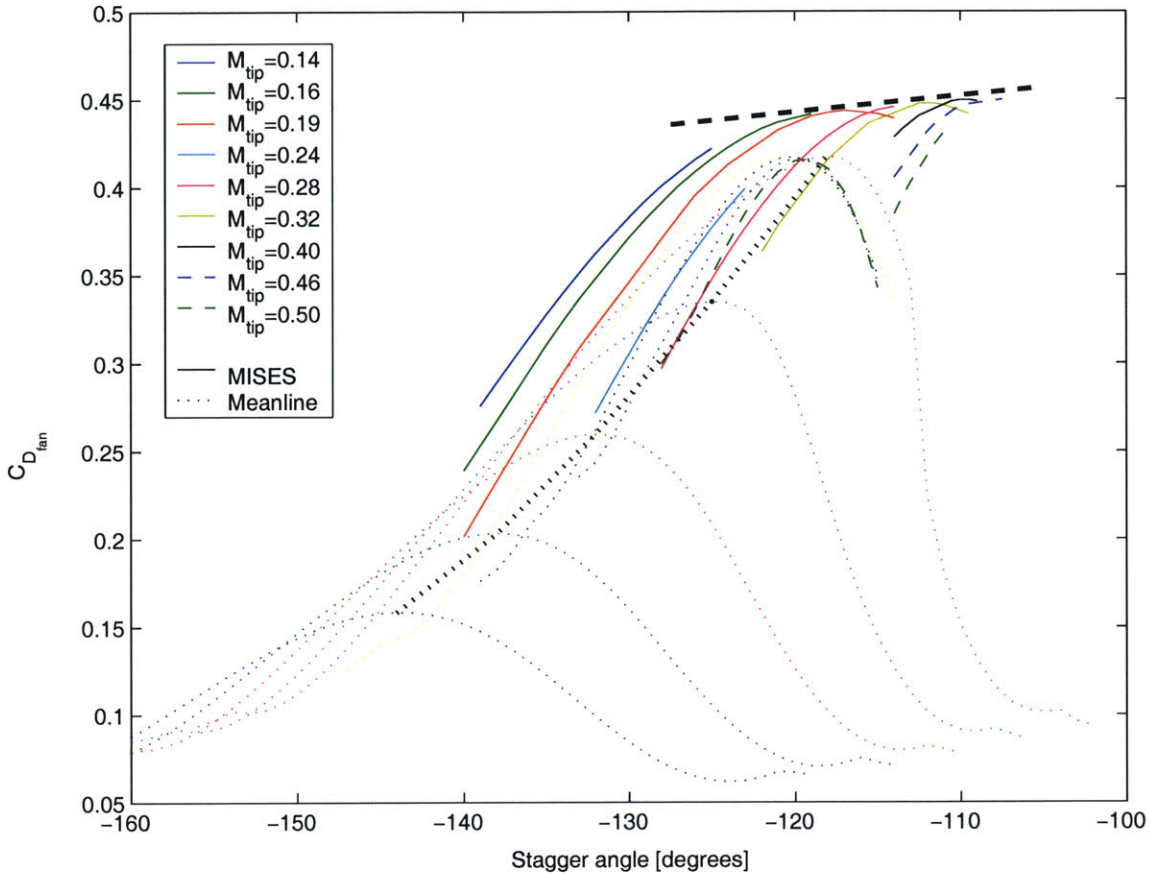

Figure 4-13: Drag coefficient generated by the engine air-brake as a function of stagger angle and wheel speed. MISES computation.

(u_0). Large velocity differences ($u_{ex} \ll u_0$) inevitably entail unsteady flow structures due to vortex shedding at the nozzle exit. Such unsteady flow structures are expected to generate undesirable low-frequency noise. Drag coefficients obtained by both meanline and two-dimensional models are plotted as a function of the ratio of the exit velocity u_{ex} to the flight velocity u_0 in Figure 4-15. According to both methods, maximum drag is generated for $u_{ex}/u_0 = 0.5$. This inevitably yields low-frequency vortex shedding, hence a potentially increased noise signature on approach. To reduce this noise component, u_{ex}/u_0 needs be increased, leading to a lower generated drag coefficient.

4.4.5 Conclusions

The blade-to-blade analysis allows a refined assessment of the drag generation capability of the engine air-brake. In windmilling mode, a typical fan blade profile can generate approximately 45% of the drag generated by a bluff body of the same cross-sectional area. For blade tip Mach numbers ranging from 0.2 to 0.5, the maximum drag is obtained by adjusting the stagger angle setting between

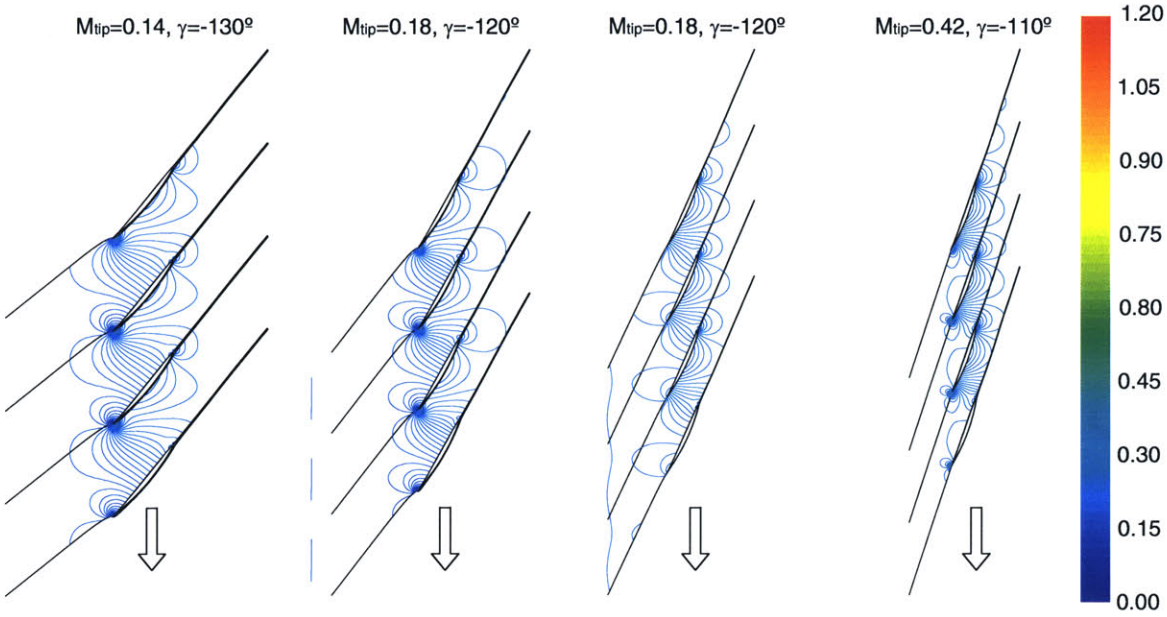

Figure 4-14: Mach number contours in windmilling mode for $M_{tip} = 0.14$, $\gamma = -130°$; $M_{tip} = 0.18$, $\gamma = -120°$; $M_{tip} = 0.30$, $\gamma = -115°$; and $M_{tip} = 0.42$, $\gamma = -110°$.

$-120°$ and $-110°$. The axial velocity at the nozzle exit is then half the flight velocity, generating undesirable low-frequency noise due to vortex shedding. Increasing the exit flow velocity yields lower drag coefficients, hence shallower approach glide slope angles, but mitigates the noise penalty due to vortex shedding.

4.5 Preliminary Assessment of Engine Air-Brake Noise Signature

4.5.1 Introduction - Engine Air-Brake Noise Sources

The engine air-brake appears as a promising concept to generate required drag on approach. However, in order to enable a functionally-silent aircraft, the engine air-brake must generate this drag in a quiet manner. The purpose of this section is to conduct a preliminary assessment of the noise signature of the engine air-brake.

Fan noise is the dominant propulsion system noise source on approach (see Groeneweg et al. (1991)). At low engine power settings, the fan blades operate at off-design conditions. This yields thick airfoil boundary layers and wakes which generate broadband and tonal noise. In windmilling mode, the fan blades are turned by approximately 180°. At such off-design conditions, thicker airfoil boundary layers and wakes can be expected compared to compressor mode, yielding potentially

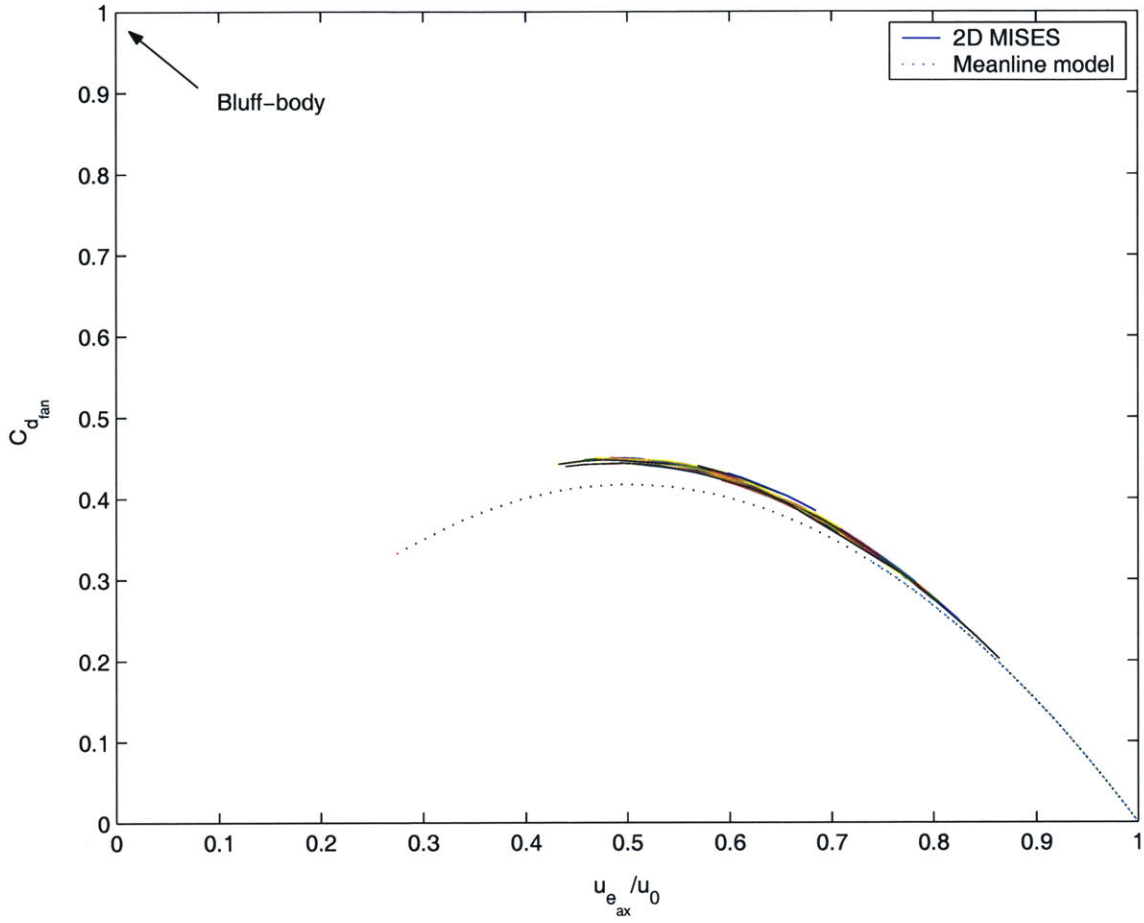

Figure 4-15: Drag coefficient generated by the engine air-brake as a function of the exhaust to free stream velocity ratio $\frac{u_{ex}}{u_0}$. Solid: MISES computation. Dashed: Meanline model.

higher noise levels.

A preliminary estimate of the fan noise radiated by the engine air-brake is first obtained using Heidmann's fan noise prediction method (Heidmann (1975)). The broadband rotor self-noise component of fan noise is then evaluated using an improved version of the Mugridge-Morfey model reported by Gliebe (2002).

For maximum drag generation, $u_{ex}/u_0 \approx 1/2$, and vortex shedding inevitably occurs at the engine exit. In order to reduce this source of low-frequency noise, either the engine exit velocity needs to be increased or means to mix the engine flow with the ambient air in a quiet manner need to be developed.

4.5.2 Fan Noise Estimate

Heidmann's turbomachinery noise prediction method (Heidmann (1975); Zorumski (1982)) is based on empirical scaling laws. The acoustic power of broadband and tonal noise sources is:

$$W \propto (\Delta T_t)^a M_{ax} M_{tip}^b, \tag{4.26}$$

where M_{tip} is the blade tip Mach number and M_{ax} is the axial Mach number at the fan inlet. For fan noise, $a = 2$. The exponent b is different for broadband and tonal components of fan noise. According to Groeneweg et al. (1991), turbine noise follows a similar scaling law but with different exponents.

The operation of a fan in windmilling/turbine mode raises the issue of how the noise signature will be modeled. This problem is addressed by considering the precision of available fan and turbine noise prediction methods and their means of calibration. The importance of fan noise has led to more refined noise prediction methods than those for turbines. Also, turbine noise prediction methods are calibrated for high hub-to-tip ratio blade geometries and high temperature flow conditions encountered in low-pressure turbines. A windmilling fan has the same general geometry and sees the same conditions as a fan in compressor operating mode. Though fan noise prediction method may not accurately capture the effect of the flow field for a windmilling fan, it is clear that a fan noise model is a superior choice to a turbine model in addressing the windmilling fan noise signature on a preliminary basis.

	Design point	Low power setting	Windmilling mode			
Airbrake $C_{D_{fan}}$	-	-	0.383	0.438	0.442	0.449
Stagger Angle	61°	61°	−130°	−120°	−115°	−110°
M_{tip}	1	0.52	0.14	0.18	0.3	0.42
M_{ax}	0.5	0.22	0.13	0.11	0.11	0.11
Ψ	0.2	0.14	-0.6	-0.51	-0.22	-0.12
M_{rel} (at meanline)	0.89	0.44	0.17	0.17	0.24	0.32
Airfoil C_D	0.024	0.03	0.168	0.186	0.055	0.03
T-E BL Thickness [cm]	0.4	0.5	2.9	3.3	1.0	0.5

Table 4.2: Inputs required by Heidmann's fan prediction method and the improved version of Mugridge-Morfey model for rotor self noise reported by Gliebe (2002). Trailing edge boundary layer thicknesses deduced from airfoil drag coefficients and air-brake drag coefficients are also presented.

In compressor mode, the fan noise is computed at design point and at a typical approach low engine power setting. In windmilling mode, fan noise is computed for blade tip Mach numbers of 0.14, 0.18, 0.3 and 0.42. For each wheel speed, the stagger angle is adjusted to generate maximum drag, yielding stagger angles of −110°, −115°, −120°, and −130°, respectively. The total temperature change across the blade-row and the axial Mach number are given by the blade-to-blade analysis

performed in Section 4.4. The inputs corresponding to these different cases are reported in Table 4.2. A fan diameter of 2 m and a hub-to-tip ratio of 0.3 are assumed. The number of blades is set to 22.

The resulting third-octave noise spectra are plotted in Figure 4-16. The observed peaks in sound pressure level correspond to tonal noise based on the blade passing frequency.

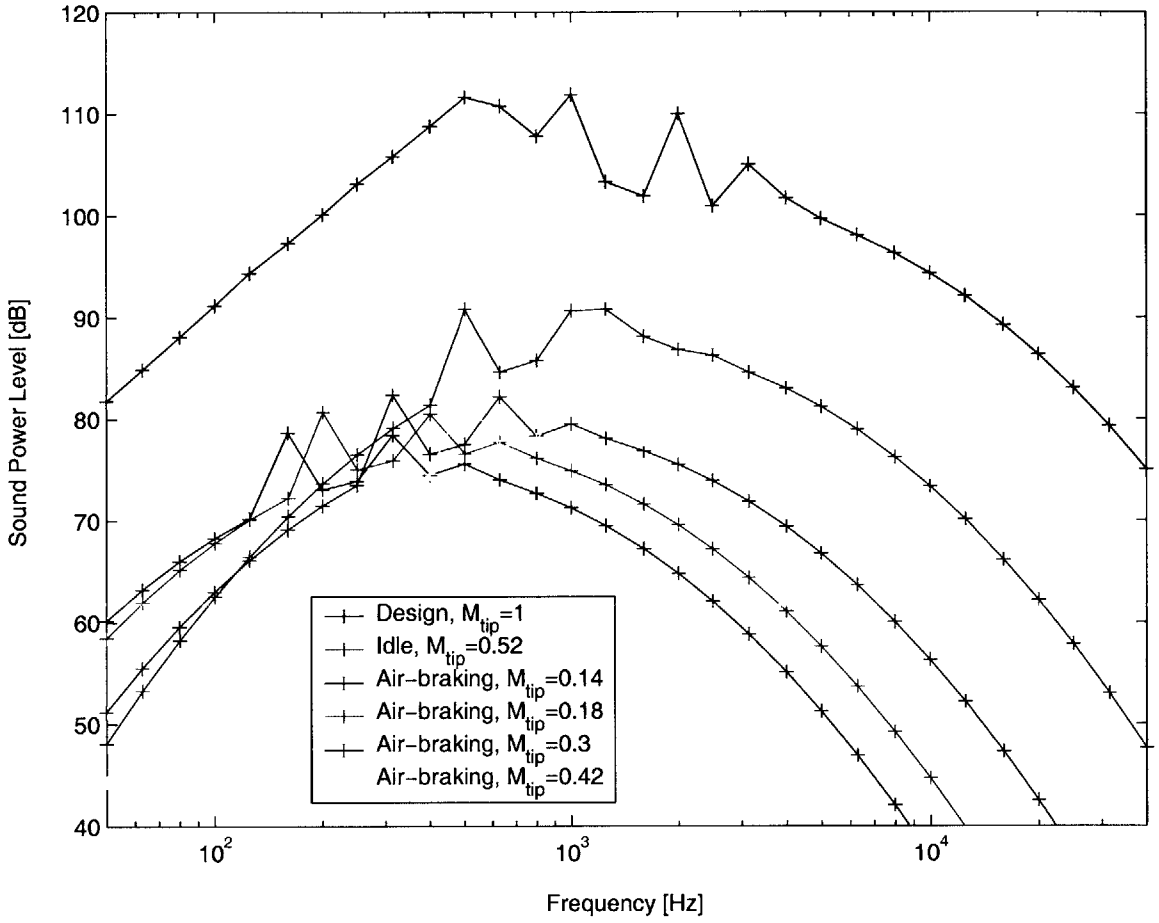

Figure 4-16: Fan noise third-octave band spectra predicted by Heidmann's prediction method at design point (blue), low power setting (green), and in windmilling mode.

Compared to the fan operated at low power setting in compressor mode, the engine air-brake operates at a lower rotating speed, a lower mass flow, and with lower total temperature changes $|\Delta T_t|$. According to the fan noise scaling laws determined by Heidmann, this yields lower fan noise levels at lower frequency. Present results suggest that the peak noise levels are approximately 10 dB lower in windmilling mode than at low engine power setting, and peak frequencies decrease from 500 Hz to approximately 150 Hz as the blade tip Mach number decreases from $M_{tip} = 0.5$ to $M_{tip} = 0.14$.

4.5.3 Rotor Self-Noise Prediction

In windmilling mode, the fan blades operate at highly off-design conditions. This inevitably creates thicker boundary layers, hence higher broadband self-noise levels. This effect is not taken into account by Heidmann's fan noise prediction method. In order to more accurately evaluate the broadband component of fan noise in windmilling mode, an improved version of the Mugridge-Morfey model for rotor self-noise reported by Gliebe (2002) is used.

Rotor self-noise is modeled by compact dipole acoustic sources radiating from an airfoil with an unsteady, random spanwise loading. The boundary layer thickness at the rotor blade trailing edge is deduced from the blade drag coefficient using the correlation $\delta^* \approx 2C_D b$, where b is the blade half-chord. The original Mugridge-Morfey model yields the following scaling law for the sound power spectral density at the peak frequency:

$$\omega \frac{dW}{d\omega} \approx K \cdot \rho \cdot c^3 \cdot B \cdot 2b \cdot h \cdot M_{rel}^6 \cdot C_D, \tag{4.27}$$

where $K = 8 \cdot 10^{-6}$, h is the blade span, B is the number of blades, and M_{rel} is the flow Mach number relative to the blade. Note that this scaling law has no dependence on frequency. The spectral shape must be empirically deduced. In the improved model suggested by Gliebe (2002), refined correlations for chord-wise loading, trailing edge surface pressure spectra, turbulent eddy convection speed, and length scale are used. The shape of the spectrum can then be deduced from the sound power spectral density.

The improved version of the model requires the following inputs:

- blade span, $h = r_{tip} - r_{hub}$
- blade half-chord, b
- number of blades, B
- blade drag coefficient, C_D
- flow Mach number relative to the blade, M_{rel}

The rotor self-noise spectra are computed for the same operating conditions as in Section 4.5.2. A chord of 20 cm is selected. Other geometrical parameters remain unchanged from Section 4.5.2. The blade drag coefficients and relative flow speeds are calculated from the blade-to-blade computations performed in Section 4.4. The inputs required by the rotor self-noise prediction are reported in Table 4.2. Corresponding trailing edge boundary layer thicknesses are also presented. Figure 4-16 shows the predicted third-octave noise spectra.

This study suggests that the windmilling engine air-brake generates self-noise levels 8 to 18 dB below those emitted by the fan operating in compressor mode at a low engine power setting. As the

performed in Section 4.4. The inputs corresponding to these different cases are reported in Table 4.2. A fan diameter of 2 m and a hub-to-tip ratio of 0.3 are assumed. The number of blades is set to 22.

The resulting third-octave noise spectra are plotted in Figure 4-16. The observed peaks in sound pressure level correspond to tonal noise based on the blade passing frequency.

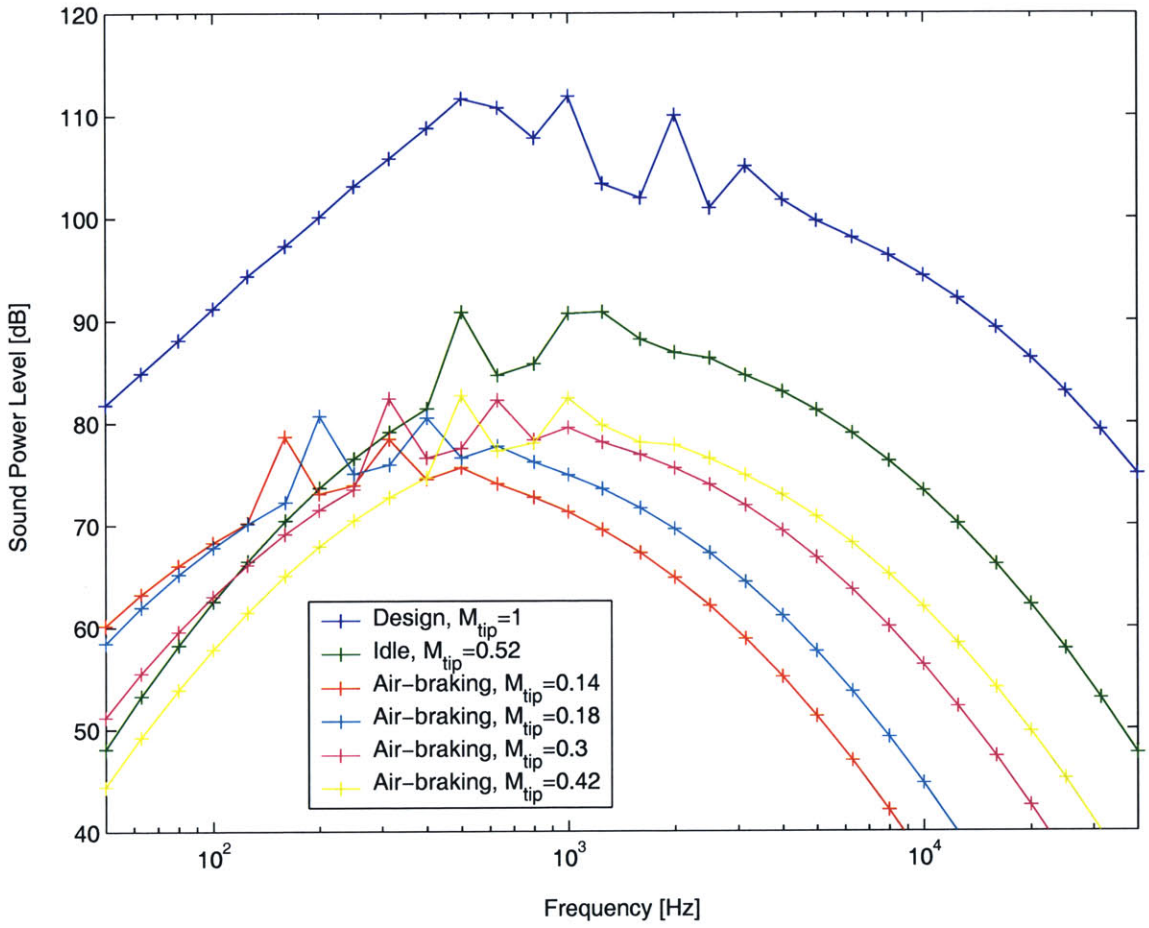

Figure 4-16: Fan noise third-octave band spectra predicted by Heidmann's prediction method at design point (blue), low power setting (green), and in windmilling mode.

Compared to the fan operated at low power setting in compressor mode, the engine air-brake operates at a lower rotating speed, a lower mass flow, and with lower total temperature changes $|\Delta T_t|$. According to the fan noise scaling laws determined by Heidmann, this yields lower fan noise levels at lower frequency. Present results suggest that the peak noise levels are approximately 10 dB lower in windmilling mode than at low engine power setting, and peak frequencies decrease from 500 Hz to approximately 150 Hz as the blade tip Mach number decreases from $M_{tip} = 0.5$ to $M_{tip} = 0.14$.

with a 30% stall margin. Under the same conditions, a blended-wind-body aircraft requires lower approach speeds ($u_0 \approx 85$ m/s), yielding lower airframe noise levels. To keep a blended-wing-body aircraft on a glide slope angle of $\theta = 4.5°$, the required silent drag that must be generated by the engine air-brake is approximately 40% of the drag generated by a bluff body of the same cross-sectional area. Both meanline and blade-to-blade analyses suggest that such a magnitude in drag can be achieved using a windmilling engine air-brake. Drag coefficients up to $C_{D_{fan}} \approx 0.6$ can be achieved with a variable area exhaust. Increasing the glide slope angle from 3° for a standard approach to 4.5° is expected to yield a 2 dB reduction in airframe noise perceived on the ground (see Pilczer (2003)).

Operating fan blades in windmilling mode entails thicker airfoil boundary layers and wakes than in compressor mode. However, the engine air-brake is expected to achieve a reduction of approximately 10 dB in fan noise level on approach compared to the noise level of a fan running at low engine power setting. This noise reduction is mainly due to the lower blade tip Mach numbers required by the engine air-brake to achieve a drag coefficient of 0.4.

The engine air-brake inherently yields a lower engine exit velocity compared to the flight velocity. If the engine exit velocity is significantly lower than the flight velocity, vortex shedding inevitably occurs at the nozzle exit and generates undesirable low-frequency noise. To alleviate this noise penalty, the engine exit velocity needs to be increased at the cost of a lower drag coefficient. This trade-off suggests that a minimum noise approach can be achieved if the engine air-brake is used to generate the highest drag coefficient for which vortex shedding does not occur.

Means to mix the engine flow with the ambient air in a quiet manner can also be considered to mitigate vortex shedding.

4.6.1 Preliminary Design Implications for a Silent Aircraft with Engine Air-Braking Capability

The windmilling engine air-brake concept greatly increases the complexity of the turbomachinery in the following ways:

- Variable-pitch fan blading is required.
- The power extracted by the windmilling fan needs to be dissipated by a hydrodynamic brake.
- A clutch is required to disengage the fan from the low-pressure spool.
- For $u_{ex} \ll u_0$, vortex shedding must be avoided by mixing the engine flow with the ambient air using an appropriate exhaust nozzle geometry.
- A variable exhaust area is required to generate drag coefficients larger than 0.4.

These requirements raise challenging issues from an engine control, safety, and reliability standpoints. The weight of the propulsion system is also expected to increase.

4.6.2 Modeling Limitations and Suggested Improvements

A more accurate drag polar of the blended-wing-body airframe on approach in clean configuration is required to refine the silent drag requirements.

The present two-dimensional assessment of the drag generation capability of the engine air-brake considers only the blade geometry at meanline. However, the tip and the hub of a fan blade behave differently at off-design conditions. This effect is expected to have a large impact on the engine air-brake performance. The actual drag coefficient generated by the engine air-brake is likely to be lower than the value of 0.45 obtained here. A quasi three-dimensional analysis of the engine air-brake can be obtained by considering a spanwise stack of MISES computations, coupled to a streamline curvature code (e.g. MTFLOW). Airfoil profiles other than a NACA65 profile can be considered. It is also suggested that the fan stator can be appropriately used to further reduce the pressure at the fan stage exit by increasing the flow swirl. Reducing the fan stage exit pressure is expected to enable further drag generation, as in the case of variable exhaust area.

In order to assess the engine air-brake noise signature, it is assumed in this chapter that noise radiated by a windmilling fan is similar to that radiated by a fan operating in compressor mode. A more detailed prediction method for broadband and tonal fan noise accounting for the blade-to-blade flow field and airfoil geometry is necessary to refine the preliminary noise assessment of this study.

Chapter 5

Conclusions and Future Work

5.1 Conclusions

The objective of the "Silent Aircraft Initiative" is to achieve a step-change in aircraft noise reduction. In order to reduce airframe and propulsion system noise levels below the background noise level in well-populated areas, noise must be a prime design variable and it is clear that departures from conventional aircraft configurations are necessary. According to Pilczer (2003), a blended-wind-body type aircraft configuration with aerodynamically-smooth lifting surfaces is a promising candidate to achieve the airframe noise reduction goals. However, this inevitably entails a decrease in drag on approach.

The work presented in this thesis focuses on low-noise propulsion system concepts potentially enabling a functionally-silent aircraft. Ultra-high bypass ratio engine cycles are envisioned to achieve a step-change in propulsion system noise reduction at takeoff. To enable such engine cycles, distributed propulsion system concepts with integrated airframe/exhaust system are considered. A windmilling engine air-brake is proposed to generate required drag on approach quietly.

Ultra-High Bypass Ratio Engine Cycles for a Step Change in Jet Noise Reduction

In Chapter 2, the jet noise reduction potential of ultra-high bypass ratio turbofan engine cycles is assessed. For this purpose, a modeling framework evaluating propulsion system performance and predicting propulsion noise levels emitted at takeoff is developed, validated, and calibrated. This model consists of a first-principles-based turbofan engine cycle deck (cycle analysis/engine sizing/off-design performance modules) coupled to NASA's Aircraft Noise Prediction Program (ANOPP). ANOPP is used to simulate the aircraft takeoff maneuver (flight dynamics module) and perform propulsion system noise predictions based on semi-empirical methods (Stone's jet noise and Heidmann's fan noise modules).

The potential noise reductions using separate flow and mixed flow exhaust nozzles combined with ultra-high bypass ratio engine cycles are assessed. For an advanced technology engine cycle reported by Liebeck et al. (1996), the noise goal is achieved for a bypass ratio of 70 to 80 with separate flow exhaust nozzles. With a mixed flow exhaust nozzle, bypass ratios of order 40 are required. The impact of such configurations on cycle performance is analyzed. With separate exhaust nozzles, the drop in specific fuel consumption relative to the baseline blended-wing-body engine is 25%. An engine cycle with a bypass ratio of order 42 and a mixed flow exhaust nozzle meeting the noise goals yields an 18% reduction in TSFC relative to the baseline engine. However, increasing the bypass ratio to ultra-high values inevitably entails a large drop in specific thrust. With separate exhaust nozzles, a 60% drop in specific thrust is predicted, yielding a threefold increase in engine cross-sectional area relative to the baseline engine. This is expected to entail detrimental propulsion system integration issues. With the mixed flow exhaust nozzle, this drop in specific thrust is 40% and requires a twofold increase in engine cross-sectional area.

The influence of engine technology level on the noise reduction potential of ultra-high bypass ratio cycles is assessed. Current technology engine cycles require approximately 50% lower bypass ratios compared to the advanced technology engine cycle. The specific thrust drops with increasing bypass ratio such that both engine technology levels yield similar engine sizes for a given noise goal. However, specific fuel consumption levels achieved by current engine technologies are 40 to 60% higher compared to advanced engine technology levels. The reduction in specific fuel consumption enabled by the latter tends to mitigate the weight and drag penalties associated with larger engine diameters and the mixer nozzle. With a current engine technology level, the penalty in overall propulsion system efficiency relative to the baseline blended-wing-body engine and the installation losses have a detrimental impact on aircraft performance.

Thus, an advanced technology level turbofan engine cycle with a bypass ratio of 42 and mixed flow exhaust nozzle is suggested as a promising cycle configuration to achieve the jet noise reduction goal of 30 EPNdB.

Distributed Propulsion System Concepts

Chapter 3 addresses issues related to the integration of ultra-high bypass ratio engine cycles in the airframe. A distributed propulsion system embedded in the blended-wing-body airframe is envisioned. Multiple engine/fan propulsion system configurations and integrated airframe/exhaust systems are assessed based on their noise signature and their impact on aircraft and propulsion system performance.

To enable the embodiment of ultra-high bypass ratio engines, the propulsion system must satisfy physical constraints imposed by the blended-wing-body airframe geometry. In particular, fan diameters need to be significantly reduced. A total of thirty 1.37m-diameter fans is required to both

provide the flow-path area necessary for the UHBPR engine cycle at the fan inlet and to enable the propulsion system embodiment in a blended-wing-body airframe.

In order to achieve such configurations, distributed propulsion systems with a large number of small engines and multiple fans driven by a common core engine are envisioned. Various configurations are analyzed based on their predicted impact on propulsion system performance. With multiple small engines, the required size of each core engine decreases. As a consequence, the reduction of core engine size entails increased viscous losses (Reynolds number effect). The concept of multiple fans driven by a common core engine allows a larger core size for a given fan diameter compared to multiple small engines. This mitigates the drop in efficiency due to Reynolds number effects but requires a transmission train and high-power gearboxes, which are expected to introduce shaft power transmission losses and weight penalties. It is suggested that a propulsion system configuration with 6 core engines driving 5 fans each, or 10 core engines driving 3 fans each, meets the installation specifications with a trade-off between gearbox weight penalties and turbomachinery losses. Gearboxes with a power rating of 12 to 18 MW are necessary to meet the power transmission requirements.

Potential benefits in perceived noise reduction resulting from multiple-fan configurations are estimated. Relative to the 3-fan baseline configuration, the prediction suggests that an array of 30 small fans yields a perceived noise reduction in fan noise of order 2 EPNdB. This is due to a shift in fan noise peak frequency towards higher frequencies where the human ear is less sensitive.

Splitting the total exhaust area into more than 100 jets yields a detrimental frequency shift effect because of the low jet noise peak frequency of the baseline 3-jet configuration. On the other hand, it is predicted that reducing the number of jets from 3 to 1 can yield a 3 EPNdB reduction in perceived jet noise from the resulting shift of the jet noise spectrum toward lower frequencies.

A literature review of high aspect ratio jet noise studies determines trends in jet noise with increasing aspect ratio. The noise levels radiated by jets of aspect ratios below 10 to 20 are similar to those radiated by round jets. For aspect ratios between 10 and 100, the jet noise decreases by approximately 4 dB. For aspect ratios larger than 100, the length scale of the mechanisms responsible for jet noise emissions decreases with increasing aspect ratio ($L_{eq} \approx \sqrt{A_j} AR^{-\frac{1}{4}}$) such that the jet noise levels decrease at a rate of 5 dB per decade (i.e. tenfold increase in aspect ratio). These trends are used to modify Stone's jet noise prediction method to estimate jet noise reduction benefits using high aspect ratio nozzles. For jet aspect ratios of 30 to 50, a jet noise reduction of 2 to 3 dB in overall sound pressure level in the plane containing the minor axis of the nozzle is suggested.

High aspect ratio nozzles are envisioned to facilitate engine integration into the blended-wing-body airframe. Thrust losses for simple nozzle geometries of various inlet and exit aspect ratios are estimated using three-dimensional CFD. The axial cross-sectional area distribution of the nozzle geometries investigated in this study yield a diverging-converging gas path. For geometries with large variations in aspect ratio between the inlet and the exit ($AR_1/AR_0 > 5$), flow separation

occurs in the diffusing section, resulting in large thrust losses (ranging from 10 to 30% and more). However, flow separation does not occur for geometries with lower values of the ratio of exit to inlet aspect ratio. In the absence of flow separation, thrust losses are driven by the increase in internal wetted area (skin friction losses) relative to axisymmetric nozzles. In this case, shorter nozzles are more efficient compared to longer nozzles. To avoid flow separation, it is suggested to select a ratio of exit to inlet aspect ratio below 1.5. Nozzle exit aspect ratios of 20 to 40 can then be achieved such that the thrust losses are kept below 5%.

To satisfy the constraints imposed by the blended-wing-body airframe and the flow-path area required by the UHBPR engine cycle, a single jet exhausted through a nozzle of aspect ratio 41 along the trailing edge of the blended-wing-body airframe is envisioned. This integrated airframe/exhaust system is predicted to entail a 5% loss in thrust but suggests an additional 4 dB reduction in perceived jet noise.

Silent Drag - Windmilling Engine Air-Brakes

In Chapter 4, silent drag requirements are quantified and the windmilling engine air-brake concept is evaluated based on drag generation capability and noise signature.

Assuming that wing loading is kept constant as the aircraft wing area varies, the required Silent Drag coefficient ($C_{SD_{req}}$) and the drag coefficient produced by the engine air-brake (C_D) are independent of aircraft size. The blended-wing-body aircraft can achieve approach velocities of 84 m/s in clean configuration with a 30% stall margin, whereas a conventional aircraft configuration requires an approach velocity larger than 100 m/s. This result is essentially due to the proportionally larger wing area of the blended-wing-body configuration. The study suggests that if 40% of the drag of a bluff body can be generated by engine air-brakes, an approach glide slope angle of 4.5° can be achieved. According to Pilczer (2003), this yields a 2 dB reduction in airframe noise perceived on the ground relative to a standard 3° approach.

The drag generation potential of the windmilling engine air-brake is assessed using a one-dimensional compressible meanline flow model of a ducted blade-row with variable pitch. For a given wheel speed, the stagger angle can be adjusted to maximize the drag generated. For blade tip Mach numbers below 0.25, the power extraction is limited by the maximum negative flow turning that the blade can generate in windmilling mode. Thus, according to Euler's turbine equation, the drag coefficient of the engine air-brake increases with wheel speed. For blade tip Mach numbers between 0.25 and 0.4, a maximum drag coefficient of 0.4 based on fan inlet area (i.e. 40% of the drag of a bluff body of same cross-sectional area) can be generated. The power extraction is limited by the pressure at the blade-row exit, which must be sufficiently high to drive the flow through the converging duct. With a variable exhaust area, the nozzle can be used as a diffuser to further lower the pressure at the blade-row exit. This yields a lower exhaust velocity, hence a higher drag coef-

ficient. However, this effect is limited to configurations for which diffuser stall does not occur. For a typical diffuser pressure coefficient of 0.5, the drag coefficient generated by the engine air-brakes increases to 0.6.

In order to refine the generated drag estimate, a viscous blade-to-blade analysis is used to compute the blade-row performance in windmilling mode. For blade tip Mach numbers larger than 0.2, the results suggest that drag coefficients of 0.45 can be achieved almost independently of the wheel speed provided that the blade stagger angle is properly adjusted.

According to both meanline and blade-to-blade computations, maximum drag is generated when the exhaust flow velocity (u_{ex}) is approximately half the flight velocity (u_0). This is expected to entail vortex shedding at the nozzle exit, generating undesirable low-frequency noise. To reduce vortex shedding, the engine exit velocity needs to be increased at the cost of a lower drag coefficient. Means to mix the exhaust flow with ambient air in a quiet manner need to be developed.

The noise signature of the windmilling engine air-brake is estimated on a preliminary basis. According to Heidmann's fan noise prediction method, a reduction of approximately 10 dB in sound pressure level can be expected compared to a fan running at a low engine power setting in compressor mode. This reduction is essentially due to the lower blade tip Mach numbers achieved in windmilling mode.

The rotor self-noise component of the broadband fan noise is predicted using an improved version of the Mugridge-Morfey model reported by Gliebe (2002). This model accounts for the thickness of the boundary layer at the blade trailing edge. In windmilling mode, fan blades are operated at highly off-design operating conditions. This yields thicker airfoil boundary layers than in compressor mode, and hence potentially higher broadband self-noise levels. However, the lower blade tip Mach numbers at which the engine air-brake is suggested to operate are expected to entail a reduction in rotor self-noise between 8 dB and 18 dB in sound pressure level compared to a fan operating at low engine power setting.

5.2 Propulsion System Design Implications for a Silent Aircraft - Predicted Noise Reduction

Based on the conclusions of this work, the following design implications for the propulsion system of a silent aircraft can be inferred.

In order to achieve the jet noise reduction goal at takeoff, an ultra-high bypass ratio turbofan engine cycle with a mixed flow exhaust nozzle is suggested. Based on the advanced engine technology level of the baseline blended-wing-body engine cycle reported in Liebeck et al. (1996), a bypass ratio of 42 and a fan pressure ratio of 1.18 are required to achieve a 30 dB reduction in EPNL. This engine cycle enables an 18% decrease in uninstalled fuel consumption compared to the baseline blended-

wing-body engine. However, the drop in specific thrust of 42% resulting from the increase in bypass ratio requires a twofold increase in engine cross-sectional area. This area increases from 7.3 m^2 for the baseline engine to 14.8 m^2 for the ultra-high bypass ratio engine.

The embodiment of such engines in the trailing edge of the blended-wing-body airframe requires a distributed propulsion system with high aspect ratio exhaust nozzles. A configuration with 10 core engines driving a total number of 30 fans is envisioned.

A mail-slot inlet that extends over 41 m in the spanwise direction is necessary. This corresponds to 48% of the aircraft span. Ingesting the boundary layer of the wing surface through this inlet is predicted to entail a 2 dB reduction in trailing edge noise and a 4 to 6% increase in aircraft range depending on engine inlet Mach number (see Pilczer (2003)).

The required fan diameter for such a distributed propulsion system is suggested to be 1.37 m. A 2 EPNdB reduction in perceived fan noise is expected from the frequency shift due to the increase in total number of fans relative to the baseline configuration. Each core engine drives 3 fans via gearboxes and shafts. Gearboxes must be able to take a maximum power input of 12 MW at takeoff. The core mass flow at takeoff is 17 kg/s.

All core and bypass flows exhaust into a single high aspect ratio nozzle of inlet aspect ratio of 34 and exit aspect ratio of 41. The core and bypass flows are assumed fully-mixed in the nozzle. This nozzle geometry is expected to yield a 5% thrust penalty, but it is suggested that improved nozzle designs can yield lower thrust losses. Exhaust areas required by the ultra-high bypass ratio engine cycle yield a nozzle height of 0.94 m, distributed over 38.5 m in the spanwise direction, i.e. 45% of the aircraft span. Exhausting a single jet of aspect ratio 41 is expected to yield an additional reduction of 4 EPNdB in perceived jet noise.

To generate required drag on approach, windmilling engine air-brakes are envisioned. Variable pitch turbomachinery is required to enable fan operation in windmilling mode. The power extracted by the windmilling fan must be dissipated in a hydrodynamic brake, and a clutch is required to disengage the fan from the low-pressure spool. Using the engine air-brake to generate a drag coefficient of 0.4, a glide slope angle of 4.5° can be achieved by a blended-wing-body aircraft in clean configuration with a stall margin of 30%. Compared to a typical aproach at a 3° glide slope angle, a 2 EPNdB reduction in airframe noise perceived on the ground is expected. However, the engine exhaust velocity is lower than the flight velocity ($u_{ex} < u_0$). This velocity profile creates unsteady flow structures due to vortex shedding, which are expected to generate undesirable low-frequency noise. To mitigate this noise penalty, the engine exhaust velocity can be increased or a nozzle geometry enabling mixing of engine flow with ambient air in a quiet way can be used. Increasing the engine exhaust velocity decreases the drag generated by the engine air-brake, yielding lower approach glides slope angle. A fan noise reduction of 8 dB to 10 dB relative to a fan operating at a low engine power setting is suggested due to the lower fan rotational speeds of the engine air-brake.

	Distributed Propulsion System For Silent Aircraft	Baseline BWB engine
Engine technology level	Advanced	Advanced
Installation	Embedded	Pod-mounted
Flow exhaust	Mixed	Separate
Fan blades	Variable Pitch	Fixed
BPR	42	19.5
FPR	1.183	1.34
TSFC	-18%	0%
Specific Thrust	-41.9%	0%
Total Inlet Area	30.2 m^2	23.3 m^2
Total Exhaust Area	34.3 m^2	21.9 m^2
Number of engines	10	3
Core mass flow	16.9 kg/s	68 kg/s
Fan gearbox power	11.6 MW	48.7 MW
Inlet (h x w, AR)	0.78 m x 41.2 m, 53	-
Total number of fans	30	3
Fan diameter	1.37 m	3.3 m
Exhaust (h x w, AR)	0.94 m x 38.5 m, 41	-
Nozzle AR_1/AR_0	1.2	-
Nozzle C_{fg}	0.95	-
Jet noise reduction (takeoff)	-34 EPNdB	-5 EPNdB
Fan noise reduction (takeoff)	-2 EPNdB	0 EPNdB
$C_{D_{fan}}$ in windmilling mode	0.45	-
Approach profile	84 m/s, 4.5°	84 m/s, 3°
Airframe noise reduction (approach)	-32 EPNdB	-
Fan noise reduction (approach)	-10 dB	0 dB

Table 5.1: Characteristics and predicted noise reduction of the candidate distributed propulsion system for a silent aircraft compared to the ones of the baseline blended-wing-body engine (from Liebeck et al. (1996)).

The candidate propulsion system for a silent aircraft is sketched based on the design implications outlined here. The characteristics of this propulsion system and predicted noise reductions are summarized in Table 5.1. For comparison, the baseline blended-wing-body propulsion system (from Liebeck et al. (1996)) is also presented. Figure 5-1 shows three-dimensional views of this distributed propulsion system.

5.3 Recommendations for Future Work

In order to refine the assessment of ultra-high bypass ratio engines, the cycle performance should be evaluated at cruise conditions. For this purpose, the current model needs to be refined to reliably compute engine performance for operating points far from the design point. It is suggested to include component maps in the off-design performance module. The accuracy of the cycle analysis and the off-design performance modules currently implemented may be improved by taking into account

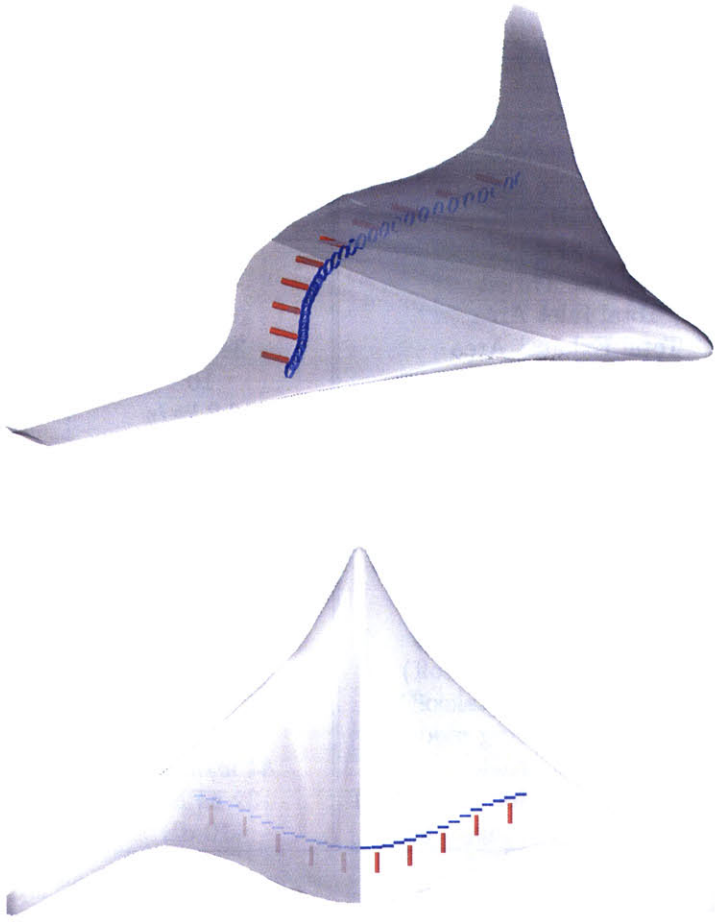

Figure 5-1: Three-dimensional views of the candidate distributed propulsion system for a silent aircraft.

variable gas properties across engine components.

Variable engine cycles are suggested to both enhance the performance of ultra-high bypass ratio engine cycles at cruise and meet the jet noise reduction goals at takeoff. In addition, fan noise needs to be significantly reduced to achieve the noise goals of the silent aircraft. Passive and active noise control methods and low-noise fan designs are envisioned to address this issue. Potential turbomachinery noise shielding due to the blended-wing-body airframe must be estimated and high aspect ratio jet noise needs to be further studied to refine the prediction models. In particular, the study should focus on jets of aspect ratio between 20 and 50, and the effects of directivity should be quantified. It is suggested that high aspect ratio nozzles with relatively low thrust losses can be designed using, for example, curved walls to minimize diffusion in the diverging part of the nozzle. A distributed propulsion system embedded in the blended-wing-body airframe is expected to significantly deteriorate the performance of the ultra-high bypass ratio engine cycle. A refined

study should include the following aspects:

- higher inlet total pressure losses due to engine embodiment,
- Reynolds number effects,
- shaft power transmission losses,
- thrust losses due to high aspect ratio nozzles,
- weight penalties due to mixer nozzles and gearboxes,
- impact of nozzle exit height on airframe aerodynamic performance.

System-level metrics such as aircraft takeoff weight and maximum range should be used to evaluate the impact of distributed propulsion system configurations on aircraft performance. Embedding the propulsion system is expected to yield increased inlet distortion levels. This raises key issues related to:

1. the estimation of inlet distortion levels due to the ingestion of the wing surface boundary layers through a mail-slot inlet,
2. turbomachinery design robust to increased inlet distortion levels.

To refine the assessment of drag generation capability using engine air-brakes, a quasi three-dimensional analysis of a windmilling fan should be conducted considering a spanwise stack of MISES computations coupled to a streamline curvature code (e.g. MTFLOW). The effects of engine embodiment on air-brake drag generation capability should also be evaluated. A more detailed prediction of fan broadband noise and blade-row interaction noise should be carried out for the proposed engine air-brake system. The noise generated by vortex shedding at the engine exhaust needs to be investigated and means to enhance the mixing of the exhaust flow with ambient air in a quiet manner need to be developed.

Issues related to the safety, the reliability, the maintenance, and the operation of an embedded distributed propulsion system (gearboxes, shafts) and engine air-brakes (variable-pitch blading, clutch, hydrodynamic brake, control system) must be addressed.

Appendix A

Engine Cycle Deck and Takeoff Noise Prediction

This appendix presents the modeling framework developed to assess propulsion system noise reduction concepts potentially enabling a functionally-silent aircraft in Chapters 2 and 3.

The modeling framework consist of four modules: cycle analysis (A.1.1), engine sizing (A.1.2), off-design performance computation (A.2) and propulsion system noise prediction at takeoff (A.3). The first three modules form a first-principles-based turbofan engine cycle deck that predicts engine cycle performance at takeoff. These modules generate the inputs required by the noise prediction module which uses semi-empirical propulsion system noise prediction methods implemented in NASA's Aircraft Noise Prediction Program (ANOPP).

A.1 Cycle Analysis at Design Point and Engine Sizing

Engine cycle design parameters and output computed by the cycle analysis and sizing modules are summarized in Table A.1.

A.1.1 Two-spool Turbofan Cycle Analysis

The cycle analysis first consists in computing the total pressure and temperature ratio across the different components. This is done by applying conservation of energy across the combustor, the high-pressure spool, and the low-pressure spool. The flow state at the exhaust of the engine can then be determined for a known exhaust configuration (separate or mixed flow), allowing to compute specific thrust (ST), fuel consumption (TSFC), and jet characteristics (Mach number, temperature, velocity, pressure, density). Figure A-1 shows the engine stations used in the cycle analysis for both separate exhaust nozzles and mixed flow exhaust.

Name	Symbol	Typical value
Engine Cycle Design Parameters		
Bypass ratio	α	19.5
Fan pressure ratio	π_{Fan}	1.34
Total Thrust (or Core mass flow)	F (or $\dot{m}$)	$F = 800000$ N
Number of engines (cores)	N_{eng}	3
Number of fans per engine	N_f	1
Ambient conditions	T_0, P_0	ISA+15 K
Flight Mach number	M_0	0.2
LPC pressure ratio (including π_{Fan})	π_{LPC}	2.7
HPC pressure ratio	π_{HPC}	25
HPT inlet total temperature	T_{t4}	2000 K
Inlet pressure recovery	π_d	0.99
Fan polytropic efficiency	η_{Fan}	0.94
LPC polytropic efficiency	η_{LPC}	0.925
HPC polytropic efficiency	η_{HPC}	0.92
Combustor pressure drop	π_b	0.96
HPT polytropic efficiency	η_{HPT}	0.9
LPT polytropic efficiency	η_{LPT}	0.9
Bypass nozzle pressure drop	π_{nb}	0.99
Core nozzle pressure drop	π_{nc}	1
Axial Mach number at fan inlet	M_2	0.5
Fan blade tip/hub ratio	r	0.3
Fan blade tip Mach number	M_{tip}	1.1
Cycle Analysis Outputs		
Specific Thrust	ST	
Thrust Specific Fuel Consumption	$TSFC$	
Fuel fraction	f	
Core&bypass/mixed jet(s) characteristics	T_t, T, P_t, P, M, u	
Core mass flow (or Total Thrust)	$\dot{m}$ (or F)	
Core&bypass/mixed flow noz. area	A_6, A_8, A_9	
Total inlet area	A_0	
Fan inlet area	A_2	
Fan blade tip and hub radii	r_{tip}, r_{hub}	

Table A.1: Turbofan engine cycle design parameters and cycle analysis outputs. Typical values are for advanced technology engines reported by Liebeck et al. (1996).

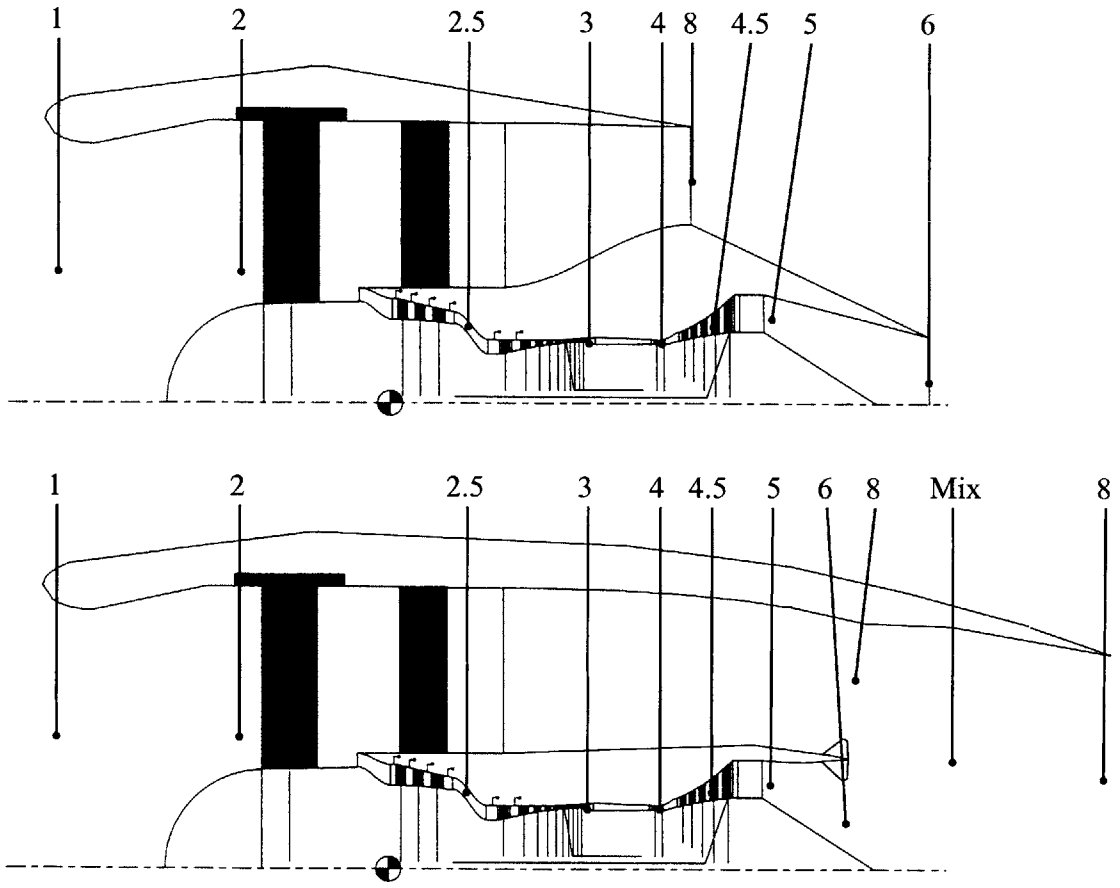

Figure A-1: Engine stations for turbofan engine with separate exhaust nozzles (top) and mixed flow exhaust (bottom).

Fuel Combustion Heat Addition. The net enthalpy flux across the combustor equals the heat added by the fuel combustion:

$$\dot{m}_f h_f = (\dot{m}_f + \dot{m}) c_{p_t} T_{t4} - \dot{m} c_{p_c} T_{t3}, \tag{A.1}$$

where h_f is the fuel heating value, $\dot{m}_f$ the fuel mass flow rate, c_{p_c} and c_{p_t} are the specific heat of air for constant pressure at the compressor exit and the turbine inlet, respectively. Introducing the fuel-to-air ratio $f = \dot{m}_f / \dot{m}$,

$$f = \frac{c_{p_t} T_{t4} - c_{p_c} T_{t3}}{h_f - c_{p_t} T_{t4}}. \tag{A.2}$$

Finally:

$$f = \frac{T_0 (c_{p_t} \theta_t - c_{p_c} \theta_0 \tau_{LPC} \tau_{HPC})}{h_f - T_0 c_{p_t} \theta_t}, \tag{A.3}$$

where $\theta_0 = T_{t0}/T_0 = 1 + \frac{\gamma_c - 1}{2} M_0^2$, $\delta_0 = P_{t0}/P_0 = \theta_0^{\gamma_c/(\gamma_c - 1)}$ and $\theta_t = T_{t4}/T_0$.

High-Pressure Spool Power Balance. Balancing the power required to drive the HPC with the power delivered by the HPT yields:

$$\dot{m}c_{p_c}(T_{t3} - T_{t2.5}) = (1+f)\dot{m}c_{p_t}(T_{t4} - T_{t4.5}), \tag{A.4}$$

which can be rewritten:

$$c_{p_c}(\tau_{LPC}\tau_{HPC} - \tau_{HPC}) = (1+f)c_{p_t}(\theta_t/\theta_0 - \tau_{HPT}\theta_t/\theta_0). \tag{A.5}$$

Thus:

$$\tau_{HPT} = 1 - \frac{c_{p_c}(\tau_{LPC}\tau_{HPC} - \tau_{LPC})}{(1+f)c_{p_t}\theta_t/\theta_0} \tag{A.6}$$

where τ_{LPC} and τ_{HPC} are calculated from the total pressure ratios and polytropic efficiencies of the components by:

$$\tau_C = \pi_C^{\frac{\gamma_c - 1}{\gamma_c \eta_{pol}}}. \tag{A.7}$$

Low-Pressure Spool Power Balance. Balancing the power required to drive the Fan and the LPC with the power delivered by the LPT gives:

$$\alpha\dot{m}c_{p_c}(T_{t8} - T_{t2}) + \dot{m}c_{p_c}(T_{t2.5} - T_{t2}) = (1+f)\dot{m}c_{p_t}(T_{t4.5} - T_{t5}). \tag{A.8}$$

The low and high spool power balances lead to the overall power balance:

$$c_{p_c}(\tau_{LPC} - 1) + \alpha c_{p_c}(\tau_{Fan} - 1) = (1+f)c_{p_t}(\tau_{HPT}\theta_t/\theta_0 - \tau_{HPT}\tau_{LPT}\theta_t/\theta_0). \tag{A.9}$$

Using the expression of τ_{HPT} yields:

$$\tau_{LPT} = 1 - \frac{c_{p_c}(\tau_{LPC} - 1) + \alpha c_{p_c}(\tau_{Fan} - 1)}{(1+f)c_{p_t}\theta_t/\theta_0 - c_{p_c}(\tau_{LPC}\tau_{HPC} - \tau_{LPC})}. \tag{A.10}$$

Stagnation Properties at the Core and Bypass Exits. At stations 6 and 8, the cycle analysis yields:

$$\frac{P_{t6}}{P_0} = \delta_0\pi_d\pi_{LPC}\pi_{HPC}\pi_b\pi_{HPT}\pi_{LPT}\pi_{nc}, \tag{A.11}$$

where π_{HPT} and π_{LPT} are calculated from the total temperature ratios determined using Equations A.6 and A.10 by $\pi_T = \tau_T^{\frac{\gamma_t}{(\gamma_t - 1)\eta_{pol}}}$

$$\frac{T_{t6}}{T_0} = \theta_t\tau_{HPT}\tau_{LPT}, \tag{A.12}$$

and

$$\frac{P_{t8}}{P_0} = \delta_0\pi_d\pi_{Fan}\pi_{nb}, \tag{A.13}$$

$$\frac{T_{t8}}{T_0} = \theta_0 \tau_{Fan}, \tag{A.14}$$

where τ_{Fan} is calculated from π_{Fan} and η_{Fan} using Equation A.7.

Nozzle Exit Conditions

In order to compute cycle characteristics such as specific thrust and fuel consumption, flow conditions at the exhaust of the engine have to be specified. Two different exhaust conditions are considered here:

- Separate flow exhaust through converging nozzles
- Ideal mixing of both bypass and core flows in a constant area mixer, exhaust through a single converging nozzle

In both cases, stagnation properties determined by cycle analysis at stations 6 and 8 remain the same, but static quantities, jet velocities, and exhaust areas have to be calculated according to the exhaust conditions.

Separate Flow Exhaust Nozzles. Core and bypass flows directly exhaust into the atmosphere through separate flow converging nozzles. This type of nozzle is acceptable for subsonic applications, where the nozzle pressure ratio (P_{t6}/P_0 or P_{t8}/P_0) is less than 4 (see Mattingly (1996)). Then, each nozzle is either choked (sonic ($M = 1$), underexpanded ($P/P_0 > 1$) flow) or ideally expanded (subsonic ($M < 1$), fully expanded to atmospheric pressure ($P = P_0$) flow). Choking occurs when

$$\frac{P_t}{P_0} \geq (1 + \frac{1}{2}(\gamma - 1))^{\gamma/(\gamma-1)}. \tag{A.15}$$

If this condition is satisfied, static properties are computed using stagnation properties by setting $M = 1$ in

$$\frac{T}{T_0} = \frac{T_t/T_0}{(1 + \frac{1}{2}(\gamma - 1)M^2)}, \tag{A.16}$$

$$\frac{P}{P_0} = \frac{P_t/P_0}{(1 + \frac{1}{2}(\gamma - 1)M^2)^{\gamma/(\gamma-1)}}. \tag{A.17}$$

On the other hand, if the nozzle pressure ratio is not sufficient to choke the converging nozzle, the static pressure ratio is $\frac{P}{P_0} = 1$ and the flow Mach number is

$$M = \sqrt{\frac{2}{\gamma - 1}(\frac{P_t}{P_0}^{(\gamma-1)/\gamma} - 1)}. \tag{A.18}$$

Static temperatures are then obtained from total temperatures using the same equation as in the choked case.

Once M, P/P_0 and T/T_0 are determined for both nozzles, both jet velocities are known ($u = M\sqrt{\gamma RT}$) and exhaust areas per unit mass flow can be determined from the mass flow conservation through the core and the bypass ducts:

$$A_6/\dot{m} = \frac{(1+f)}{\rho_6 u_6} = \frac{(1+f)R_t T_6}{P_6 u_6} \tag{A.19}$$

and

$$A_8/\dot{m} = \frac{\alpha}{\rho_8 u_8} = \frac{\alpha R_c T_8}{P_8 u_8}. \tag{A.20}$$

All quantities on the right hand side of Equations A.19 and A.20 are known from the cycle analysis. At this point $A_8/\dot{m}$ and $A_6/\dot{m}$ are completely determined by cycle characteristics, but the knowledge of $\dot{m}$ is required to obtain the physical areas of the exhaust nozzles. This engine core mass flow is determined by sizing the engine in Section A.1.2.

The net momentum flux across the engine is the thrust produced by the turbofan cycle. With separate exhausts, the thrust is:

$$F = (1+f)\dot{m}u_6 - \dot{m}u_0 + A_6(P_6 - P_0) + \alpha\dot{m}u_8 - \alpha\dot{m}u_0 + A_8(P_8 - P_0). \tag{A.21}$$

Thus,

$$\frac{F}{\dot{m}} = (1+f)u6 - u_0 + A_6(P_6 - P_0)/\dot{m} + \alpha u_8 - \alpha u_0 + A_8(P_8 - P_0)/\dot{m}, \tag{A.22}$$

which can be rewritten independently of the exhaust areas and the core mass flow:

$$\frac{F}{\dot{m}} = (1+f)\left[u_6 + \frac{R_t T_6}{u_6}\left(1 - \frac{P_0}{P_6}\right)\right] - u_0 + \alpha\left[u_8 + \frac{R_c T_8}{u_8}\left(1 - \frac{P_0}{P_8}\right)\right] - \alpha u_0. \tag{A.23}$$

The specific thrust is:

$$ST = \frac{1}{a_0(1+\alpha)}\frac{F}{\dot{m}}, \tag{A.24}$$

where a_0 is the speed of sound at ambient conditions. The specific impulse can also be computed:

$$I = \frac{F}{g\dot{m}_f} = \frac{F}{\dot{m}}\frac{1}{gf}. \tag{A.25}$$

This specific impulse leads to the thrust specific fuel consumption:

$$TSFC = \frac{1}{gI} = \frac{f}{F/\dot{m}}. \tag{A.26}$$

Mixed Flow Exhaust. It is assumed that the bypass and the core flows are fully mixed in a forced mixer located between stations 6 and 8 (upstream) and station Mix (downstream). The resulting flow then exhausts in the atmosphere through a converging nozzle at station 9. The cross-sectional

area of the mixer is assumed constant: $A_{Mix} = A_6 + A_8$. Conservation of mass, momentum and energy are applied to the control volume defined by:

- stations 6 and station 8 as upstream boundary,
- station Mix as downstream boundary, where both bypass and core flows are fully-mixed.

Conservation of mass flow during the mixing process gives:

$$\dot{m}_{Mix} = \dot{m}_6 + \dot{m}_8 = (1 + f + \alpha)\dot{m} = \rho_{Mix} u_{Mix} A_{Mix}. \tag{A.27}$$

This allows to calculate the static pressure at the mixer exhaust provided that the static temperature and the flow velocity at this station are known:

$$P_{Mix} = \frac{(1 + f + \alpha)\dot{m} R_c T_{Mix}}{A_{Mix} u_{Mix}}. \tag{A.28}$$

Applying conservation of momentum to the control volume previously defined gives:

$$(1 + f)\dot{m}u_6 + A_6 P_6 + \alpha\dot{m}u_8 + A_8 P_8 = (1 + f + \alpha)\dot{m}u_{Mix} + A_{Mix} P_{Mix}. \tag{A.29}$$

Using Equation A.28, Equation A.29 becomes:

$$(1 + f)\left[u_6 + \frac{R_t T_6}{u_6}\right] + \alpha\left[u_8 + \frac{R_c T_8}{u_8}\right] = (1 + f + \alpha)\left[u_{Mix} + \frac{R_c T_{Mix}}{u_{Mix}}\right]. \tag{A.30}$$

Assuming an adiabatic mixing process, conservation of energy gives:

$$(1 + f)\dot{m}c_{p_t} T_{t6} + \alpha\dot{m}c_{p_c} T_{t8} = (1 + f + \alpha)\dot{m}c_{p_c} T_{tMix}. \tag{A.31}$$

This can rewriten this as:

$$T_{tMix} = \frac{(1 + f)c_{p_t} T_{t6} + \alpha c_{p_c} T_{t8}}{(1 + f + \alpha)c_{p_c}}. \tag{A.32}$$

In order to completely determine the mixed flow state, two additional equations are required:

- At the mixing plane, bypass and core static pressures have to be equal (no radial pressure gradient, Kutta condition at the splitter plane):$P_8 = P_6$. This requires that the core and bypass flows at stations 6 and 8 respectively are not choked.
- A quantity has to be prescribed upstream of the mixer, either M_6 or M_8 or A_8/A_6. Here, M_6 is chosen.

From M_6 and P_{t6}, P_6 is found, hence P_8. From P_{t8}, M_8 can be calculated. Then, T_6 and T_8 are deduced from T_{t6} and T_{t8}. Finally u_6, u_8, $A_6/\dot{m}$ and $A_8/\dot{m}$ can be determined.

At this stage, the left hand side of Equation A.30 is entirely known. B is defined as the following quantity:

$$B = \frac{1}{(1+f+\alpha)}\left[(1+f)\left[u_6 + \frac{R_t T_6}{u_6}\right] + \alpha\left[u_8 + \frac{R_c T_8}{u_8}\right]\right]. \tag{A.33}$$

T_{tMix} is known using Equation A.32. Since $T_{Mix} = T_{tMix} - \frac{u_{Mix}^2}{2c_{p_c}}$, substituting T_{Mix} and B in Equation A.30, yields the following quadratic equation for u_{Mix}:

$$\left(1 - \frac{R_c}{2c_{p_c}}\right) u_{Mix}^2 - B u_{Mix} + R_c T_{tMix} = 0, \tag{A.34}$$

using $1 - \frac{R_c}{2c_{p_c}} = \frac{\gamma_c+1}{2\gamma_c}$. Solving for u_{Mix} yields two solutions, one is supersonic (+), and the other is subsonic (−):

$$u_{Mix} = \frac{\gamma_c}{\gamma_c+1} B\left[1 \pm \sqrt{1 - 2\frac{\gamma_c+1}{\gamma_c}\frac{R_c T_{tMix}}{B^2}}\right]. \tag{A.35}$$

Only the subsonic solution is considered here. The following quantities describing the mixed jet can then be calculated:

$$T_{Mix} = T_{tMix} - \frac{u_{Mix}^2}{2c_{p_c}}, \tag{A.36}$$

$$M_{Mix} = \frac{u_{Mix}}{\sqrt{\gamma_c R_c T_{Mix}}}, \tag{A.37}$$

and the mixer exit static pressure P_{Mix} using Equation A.28 assuming constant area mixer ($A_{Mix} = A_6 + A_8$).

Finally, the total pressure at the mixer outlet is given by:

$$\frac{P_{tMix}}{P_0} = \frac{P_{Mix}}{P_0} \cdot \left(1 + \frac{\gamma_c - 1}{2} M_{Mix}^2\right)^{\frac{\gamma_c}{\gamma_c - 1}}. \tag{A.38}$$

Assuming that no total pressure losses between stations Mix and 9 yields $\frac{P_{tMix}}{P_0} = \frac{P_{t9}}{P_0}$. Based on this nozzle pressure ratio, the flow state at the throat of the converging nozzle (station 9) is either choked or fully expanded. Thus, the mixed jet exhaust static pressure P_9 and Mach number M_9 can be determined. Assuming $T_{t9} = T_{Mix}$, the static temperature T_9 and the mixed jet velocity u_9 are then found. Conservation of mass between stations Mix and 9 yields

$$\dot{m}_{Mix} = (1+f+\alpha)\dot{m} = \dot{m}_9 = \rho_9 u_9 A_9. \tag{A.39}$$

Exhaust area per unit core mass flow can then be determined from:

$$A_9/\dot{m} = \frac{(1+f+\alpha) R_c T_9}{P_9 u_9}. \tag{A.40}$$

The thrust per unit mass flow produced by this single, fully mixed jet is:

$$\frac{F_{Mix}}{\dot{m}} = (1 + f + \alpha)u_9 - (1 + \alpha)u_0. \tag{A.41}$$

Finally, the specific thrust and the specific fuel consumption are:

$$ST = \frac{1}{a_0(1+\alpha)} \frac{F_{Mix}}{\dot{m}}, \tag{A.42}$$

$$TSFC = \frac{1}{gI} = \frac{f}{F_{Mix}/\dot{m}}. \tag{A.43}$$

A.1.2 Engine Sizing

The following quantities depend only on cycle characteristics and are independent of engine size: static and stagnation properties at engine stations, jets Mach numbers, specific thrust, TSFC and $A/\dot{m}$. In order to determine the engine thrust, the fuel mass flow, and the exhaust areas, the size of the engine needs to be determined by setting the engine core mass flow $\dot{m}$.

Engine Core Sizing

The engine core mass flow $\dot{m}$ can either be imposed (existing core) or determined from the specific thrust in order to meet a given thrust requirement, using:

$$\dot{m} = \frac{1}{a_0(1+\alpha)} \frac{F}{ST}, \tag{A.44}$$

where F is the required thrust for a single engine and ST is the specific thrust which depends only on cycle characteristics.

Engine Exhaust Areas

The physical exhaust areas A_6 and A_8 in the case of separate flow exhaust nozzles or A_9 in the case of mixed flow exhaust are:

$$A_i = \left(\frac{A}{\dot{m}}\right)_i \dot{m}, \tag{A.45}$$

where $\left(\frac{A}{\dot{m}}\right)_i$ are determined from Equations A.19 and A.20 or Equation A.40.

In the case of separate exhaust flow exhaust nozzles, A_6 and A_8 are respectively the areas of core and bypass converging nozzles. In the case of the fully mixed jet, A_6 and A_8 are the areas of the core and bypass flows at the inlet of the mixer, and A_9 is the exhaust area of the single exhaust nozzle.The cross-sectional area of the constant area mixer is $A_{Mix} = A_6 + A_8$.

Fan Inlet Area and Fan Blade Dimensions

The total mass flow ingested by the engine is $(1+\alpha)\dot{m}$. Conservation of mass at the fan inlet (station 2) yields:

$$(1+\alpha)\dot{m} = A_2\rho_2 u_2 = A_2\frac{P_{t2}}{\sqrt{T_{t2}}}D(M_2,\gamma_c,R_c), \tag{A.46}$$

where

$$D(M,\gamma,R) = \sqrt{\frac{\gamma}{R}}M(1+\frac{\gamma-1}{2}M^2)^{-\frac{1}{2}\frac{\gamma+1}{\gamma-1}} \tag{A.47}$$

is the corrected flow function, $P_{t2} = P_{t0}\pi_d = \delta_0 P_0 \pi_d$ and $T_{t2} = T_{t0} = \theta_0 T_0$. Equation A.46 shows that A_2 depends only on M_2 for a given total engine mass flow and design point ambient conditions. Usually, a value of M_2 between 0.45 and 0.65 is chosen and A_2 is found (see Mattingly (1996)). In the case of an engine with a number of fans driven by a common core N_f, the flow area at the inlet of each fan is:

$$A_{fan} = \frac{A_2}{N_f}. \tag{A.48}$$

The dimensions of the fan blades are linked to the fan inlet area by:

$$A_{Fan} = \pi(r_{tip}^2 - r_{hub}^2) = \pi r_{tip}^2(1-r^2), \tag{A.49}$$

where $r = r_{hub}/r_{tip}$ is the hub/tip ratio of the fan blades, usually between 0.3 and 0.4 (see Mattingly (1996)). For a given value of r, r_{tip} is found from Equation A.49, and r_{hub} is finally determined.

Introducing the rotational speed of the low-pressure spool ω_1 (in rad/s, or $N1 = \frac{60\omega_1}{2\pi}$ in RPM), the blade tip Mach number is:

$$M_{tip} = r_{tip}\omega_1/a_2, \tag{A.50}$$

where $a_2 = \sqrt{\gamma_c R_c T_2}$ is found from $T_{t2} = T_{t0}$ and M_2. In practice, M_{tip} is chosen between 1 and 1.5, and ω_1 is then determined. The relative flow Mach number at the blade tip becomes $M_{r2} = \sqrt{M_{tip}^2 + M_2^2}$.

A.1.3 Cycle Analysis Validation with Engine Data and GasTurb

The results of the cycle analysis and the sizing procedure are first compared to data measured on real engines. Then, the baseline blended-wing-body engine cycle reported in Liebeck et al. (1996) is compared to the predicted cycle computed in GasTurb (Kurzke (2001)).

Cycle Analysis of JT9D Engine

Engine cycle parameters required by the cycle analysis and sizing tools are reported in Table A.2 for the Pratt&Whitney engine JT9D (data from Mattingly (1996)). The design point is chosen at

Quantity	Value
α	5.0
π_{Fan}	1.54
π_{LPC} (including π_{Fan})	2.18
π_{HPC}	9.84
T_{t4}	1350 K
π_d*	1
η_{Fan}	0.958
η_{LPC}	0.874
η_{HPC}	0.925
π_b	0.956
η_{HPT}*	0.86
η_{LPT}*	0.86
π_{nb}	0.991
π_{nc}*	1
$\dot{m}$	113 kg/s

Table A.2: JT9D engine cycle parameters from Mattingly (1996), when available (*: estimated).

Quantity	Data	GasTurb	Model	Δ_{data} [%]	$\Delta_{GasTurb}$ [%]
$P_{t2.5}$ [Pa]	221321	221316	221324	0	0
$T_{t2.5}$ [K]	372	371.750	371.99	0	0
P_{t3} [Pa]	2178736	2178634	2178700	0	0
T_{t3} [K]	744	736.160	744.38	0	1
P_{t4} [Pa]	2082209	2082774	2082200	0	0
T_{t4} [K]	1350	1350	1350	0	0
P_{t5} [Pa]	144100	170930	157630	9	-8
T_{t5} [K]	728	800.2	746.55	3	-7
P_{t6} [Pa]	144100	170930	157630	9	-8
T_{t6} [K]	728	800.2	746.55	3	-7
P_{t8} [Pa]	154442	154435	154420	0	0
T_{t8} [K]	328	327.55	327.6	0	0
Thrust [N]	193498	208940	201792	4	-3
$\dot{m}_f$ [kg/s]		1.9761	1.8121		-9
TSFC [kg/s/N]		9.46E-06	9.36E-06		-1
M_6		0.910	0.824		-9
M_8		0.800	0.7997		0
A_6 [m^2]		0.480	0.4977		4
A_8 [m^2]		1.701	1.7		0

Table A.3: JT9D engine cycle characteristics predicted by the cycle analysis tool and GasTurb, and engine data reported in Mattingly (1996).

Quantity	Value
α	19.5
π_{Fan}	1.34
π_{LPC} (including π_{Fan})	2.7
π_{HPC}	25
T_{t4}	2000 K
π_d*	0.99
η_{Fan}	0.94
η_{LPC}	0.925
η_{HPC}	0.92
π_b*	0.96
η_{HPT}	0.9
η_{LPT}	0.9
π_{nb}*	0.99
π_{nc}*	1
Thrust	60000 lbf

Table A.4: Baseline blended-wing-body engine cycle parameters from Liebeck et al. (1996), when available (*: estimated).

takeoff conditions (sea level static, ISA atmospheric conditions). Cycle analysis results and relative errors are tabulated in Table A.3.

Relative errors of order 5 to 10% are mostly due to:

- uncertainty in components polytropic efficiencies,
- the assumption that gas properties are constant upstream and downstream of the combustor.

Cycle Analysis of Baseline Blended-Wing-Body Engine

The main engine cycle parameters for the turbofan engine suggested to propel the baseline blended-wing-body aircraft reported in Liebeck et al. (1996) are summarized in Table A.4. The design point is chosen at $M_0 = 0.2$ on a hot day (ISA+15 K).

Cycle analysis results and relative errors are tabulated in Table A.5. Discrepancies of order 5 to 10% are moslty due to the assumption that gas properties are constant upstream and downstream of the combustor.

A.2 Off-Design Engine Performance Prediction

During a takeoff maneuver, the aircraft first accelerates from static conditions to rotation velocity ($V_{rot} \approx 80$ m/s, $M_0 \approx 0.2$), then starts to climb at an approximately constant climb rate and accelerates to $M_0 \approx 0.3-0.4$. The engine performance significantly varies over the range of operating conditions encountered at takeoff. For typical turbofan engines ($\alpha \approx 8$), the thrust at $M_0 = 0.4$ is approximately 70% of the sea level static (SLS) thrust. Fan rotational speed, jet velocities and

Quantity	GasTurb	Model	$\Delta_{GasTurb}$ [%]
P_{t3}/P_0	68.54	68.71	0.2
T_{t3}/T_0	3.48	3.51	0.8
$P_{t4.5}/P_0$	14.53	15.21	4.7
$T_{t4.5}/T_0$	4.89	4.94	10.1
P_{t6}/P_0	1.82	1.98	8.8
T_{t6}/T_0	3.16	3.24	2.5
P_{t8}/P_0	1.35	1.35	0
T_{t8}/T_0	1.10	1.10	0
$\dot{m}$ [kg/s]	71.7	71.1	-0.8
TSFC [$\cdot 10^{-6}$ kg/s/N]	8.23	9.39	14
M_6	0.98	1	2
M_8	0.67	0.67	0
A_6 [m^2]	0.32	0.29	9.4
A_8 [m^2]	5.38	5.13	4.6

Table A.5: Blended-wing-body engine cycle characteristics predicted by the cycle analysis tool and GasTurb.

temperatures also vary during take-off. Therefore, the off-design performance of the engine is crucial to accurately assess the propulsion system noise levels at takeoff. The computation of the effective perceived noise level (EPNL) at takeoff requires the knowledge of the noise sources trajectory and characteristics (see Section A.3).

Inputs required by the off-design performance prediction module are:

- operating conditions at design point: T_{t4r}, M_{0r}, T_{0r}, P_{0r}
- cycle characteristics at design point: α_r, π_{Fanr}, π_{HPCr}, τ_{LPTr}, $\dot{m}_r$, ω_{1r} ...
- off-design operating conditions: T_{t4}, M_0, T_0, P_0

The outputs of the off-design performance computation are:

- Off-design cycle characteristics: α, π_{Fan}, π_{HPC}, τ_{LPT}, $\dot{m}$, ω_1.
- Off-design performance: Total thrust, specific thrust, TSFC.

A.2.1 Methodology for Off-Design Performance Prediction

In Section A.1, the engine cycle characteristics are computed at a given design point, specified by reference operating conditions (T_{t4r} and flight conditions M_{0r}, T_{0r}, P_{0r}), for given values of the design variables such as π_{Fan}, π_{LPC}, π_{HPC}, α.

In this section, the engine geometry is frozen, and its off-design performance is predicted for various operating conditions T_{t4}, M_0, T_0, and P_0. Reference quantities computed or given at design point are denoted with subscript r.

Method and Key Assumptions

The method used to compute engine off-design performance is based on the engine performance analysis presented in Mattingly (1996). At early stages of the preliminary design of an engine, detailed off-design behavior of the different engine components, usually in the form of component performance maps, is not necessarily available.

However, engine off-design performance can be estimated with reasonable accuracy by applying first principles (mass conservation and energy conservation) and using simplifying assumptions to render the off-design performance of the engine components.

The following assumptions are made:

- Polytropic efficiencies of rotating components (η_{Fan}, η_{HPC}, η_{HPT}, η_{LPC}, η_{LPT}) are kept constant and equal to the values at the design point.
- Total pressure ratios across the combustor, the core exhaust nozzle and the bypass exhaust nozzle (π_b, π_{nc}, π_{nb}) are kept constant and equal to the values at the design point.

Furthermore, the following assumptions are required:

- The flow is always choked at the high-pressure turbine inlet (station 4) and the low-pressure turbine inlet (station 4.5): $M_4 = M_{4.5} = 1$.
- The term $1 + f$ is constant and equal to its value at the design point $1 + f_r$. However, the fuel-to-air ratio f can vary relative to its value at the design point f_r.
- Turbine cooling and power extraction are neglected.

Off-Design Engine Performance Calculation with Separate Flow Exhaust Nozzles

The following equations govern the off-design performance of a turbofan engine with separate flow exhaust nozzles. Similar equations can be obtained in the case of a mixed flow exhaust. Equations governing the off-design performance of a turbofan engine with mixed flow exhaust are reported in Mattingly (1996). Using the corrected flow function $D(M, \gamma, R)$ given by Equation A.47, the mass flow at any station i, $\dot{m}_i = \rho_i u_i A_i$ can be rewritten as:

$$\dot{m}_i = \frac{P_{ti}}{\sqrt{T_{ti}}} A_i D(M_i). \tag{A.51}$$

High-Pressure Turbine. Conservation of mass through the high pressure turbine yields:

$$\dot{m}_4 = \frac{P_{t4}}{\sqrt{T_{t4}}} A_4 D(M_4) = \dot{m}_{4.5} = \frac{P_{t4.5}}{\sqrt{T_{t4.5}}} A_{4.5} D(M_{4.5}). \tag{A.52}$$

Since the flow-path geometry is frozen and the flow is assumed always choked at station 4 and 4.5, the ratio

$$\frac{P_{t4}/P_{t4.5}}{\sqrt{T_{t4}/T_{t4.5}}} = \frac{\sqrt{\tau_{HPT}}}{\pi_{HPT}} \tag{A.53}$$

is also constant, equal to its value at the design point. The assumption of constant polytropic efficiency η_{HPT} yields $\pi_{HPT} = \pi_{HPT_r}$ and $\tau_{HPT} = \tau_{HPT_r}$.

Low-pressure turbine. Conservation of mass from the low-pressure turbine (station 4.5) to the core exhaust nozzle or the inlet of the mixer (station 6) leads to:

$$\dot{m}_{4.5} = \frac{P_{t4.5}}{\sqrt{T_{t4.5}}} A_{4.5} D(M_{4.5}) = \dot{m}_6 = \frac{P_{t6}}{\sqrt{T_{t6}}} A_6 D(M_6). \tag{A.54}$$

With $P_{t6} = \pi_{nc} P_{t5}$ and $T_{t6} = T_{t5}$, one can write:

$$\frac{P_{t4.5}/P_{t5}}{\sqrt{T_{t4.5}/T_{t5}}} \frac{1}{D(M_6)} = \frac{\sqrt{\tau_{LPT}}/\pi_{LPT}}{D(M_6)} = \frac{A_6 \pi_n}{A_{4.5} D(M_{4.5})}. \tag{A.55}$$

Since the flow at station 4.5 is choked and π_n, $A_{4.5}$, A_6 are fixed, the left-hand side of Equation A.55 is equal to its value at the design point. This yields:

$$\pi_{LPT} = \pi_{LPT_r} \sqrt{\frac{\tau_{LPT}}{\tau_{LPT_r}}} \frac{D(M_{6r})}{D(M_6)}. \tag{A.56}$$

The low-pressure turbine temperature ratio is then given by:

$$\tau_{LPT} = \pi_{LPT}^{\frac{\gamma-1}{\gamma}\eta_{LPT}}. \tag{A.57}$$

High-Pressure Compressor. The power balance between the high-pressure turbine and the high-pressure compressor yields:

$$\dot{m}_2 c_{p_c} (T_{t3} - T_{t2.5}) = \dot{m}_4 c_{p_t} (T_{t4} - T_{t4.5}). \tag{A.58}$$

This can be rewritten as:

$$(\tau_{LPC}(\tau_{HPC} - 1))\theta_0/\theta_t = c_{p_t}/c_{p_c}(1 - \tau_{HPT})(1 + f). \tag{A.59}$$

Since τ_{HPT} and $1 + f$ are fixed, the left-hand side of Equation A.59 is equal to its value at the design point.

Thus, solving for τ_{HPC} gives:

$$\tau_{HPC} = 1 + \frac{\theta_t/\theta_0}{\theta_{tr}/\theta_{0r}} \frac{\tau_{LPCr}}{\tau_{LPC}} (\tau_{HPCr} - 1). \tag{A.60}$$

The high-pressure compressor pressure ratio is then given by:

$$\pi_{HPC} = \tau_{HPC}^{\frac{\gamma-1}{\gamma}\eta_{HPC}}. \tag{A.61}$$

Fan and Low-Pressure Compressor. The power balance between the fan, the low-pressure compressor and the low-pressure turbine can be written as:

$$\dot{m}_8 c_{p_c}(T_{t8} - T_{t2}) + \dot{m}_2 c_{p_c}(T_{t2.5} - T_{t2}) = \dot{m}_{4.5} c_{p_t}(T_{t4.5} - T_{t5}). \tag{A.62}$$

Similarly to the high pressure spool, Equation A.62 can be rewritten in terms of total temperature ratios. Introducing the fuel-to-air ratio f and the bypass ratio α, and rearranging terms yields:

$$\frac{\alpha(\tau_{Fan} - 1) + (\tau_{LPC} - 1)}{1 - \tau_{LPT}} \theta_0/\theta_t = c_{p_t}/c_{p_c} \tau_{HPT}(1 + f), \tag{A.63}$$

where the left-hand side of this equation is found from its value at the design point.

At this point, another equation is needed to link τ_{LPC} and τ_{Fan}. Since the fan and the low-pressure compressor are rotating at the same speed, the enthalpy rise across the two components can be assumed proportional: $T_{t2.5} - T_{t2} = K(T_{t8} - T_{t2})$, or $\tau_{LPC} - 1 = K(\tau_{Fan} - 1)$. The proportionality constant is found using the design point conditions, and the low-pressure compressor temperature ratio becomes:

$$\tau_{LPC} = 1 + (\tau_{Fan} - 1)\frac{\tau_{LPCr} - 1}{\tau_{Fanr} - 1}. \tag{A.64}$$

The low-pressure compressor pressure ratio is then given by:

$$\pi_{LPC} = \tau_{LPC}^{\frac{\gamma-1}{\gamma}\eta_{LPC}}. \tag{A.65}$$

Substituting $\tau_{LPC} - 1$ obtained from Equation A.64 in Equation A.63, τ_{Fan} is found:

$$\tau_{Fan} = 1 + (\tau_{Fanr} - 1)\left[\frac{1 - \tau_{LPT}}{1 - \tau_{LPTr}} \frac{\theta_t/\theta_0}{\theta_{tr}/\theta_{0r}} \frac{\tau_{LPCr} - 1 + \alpha_r(\tau_{Fanr} - 1)}{\tau_{LPCr} - 1 + \alpha(\tau_{Fanr} - 1)}\right]. \tag{A.66}$$

The fan pressure ratio is then given by:

$$\pi_{Fan} = \tau_{Fan}^{\frac{\gamma-1}{\gamma}\eta_{Fan}}. \tag{A.67}$$

Bypass Ratio. Core and bypass mass flows can be written as:

$$\dot{m}_2 = \frac{\dot{m}_4}{1 + f} = \frac{P_{t4}}{\sqrt{T_{t4}}} A_4 \frac{D(M_4)}{1 + f}, \tag{A.68}$$

and

$$\dot{m}_8 = \frac{P_{t8}}{\sqrt{T_{t8}}} A_8 D(M_8), \tag{A.69}$$

respectively. Since A_4, M_4, $1+f$ and A_8 are fixed, Equations A.68 and A.69 can be written as:

$$\dot{m}_2 \frac{\sqrt{T_{t4}}}{P_{t4}} = \frac{D(M_4)A_4}{1+f} = \dot{m}_{2r} \frac{\sqrt{T_{t4r}}}{P_{t4r}} \tag{A.70}$$

and

$$\dot{m}_8 \frac{\sqrt{T_{t8}}}{P_{t8}} / D(M_8) = A_8 = \dot{m}_{8r} \frac{\sqrt{T_{t8r}}}{P_{t8r}} / D(M_{8r}). \tag{A.71}$$

With $P_{t4}/P_{t8} = \pi_{LPC}\pi_{HPC}\pi_b/\pi_{Fan}$ and $T_{t4}/T_{t8} = \theta_t/(\theta_0\tau_{Fan})$, the ratio Equations A.70 and A.71 yields:

$$\frac{\dot{m}_8}{\dot{m}_2} \frac{\pi_{LPC}\pi_{HPC}\pi_b/\pi_{Fan}}{D(M_8)} \sqrt{\frac{\theta_0\tau_{Fan}}{\theta_t}} = \frac{\dot{m}_{8r}}{\dot{m}_{2r}} \frac{\pi_{LPCr}\pi_{HPCr}\pi_b/\pi_{Fanr}}{D(M_{8r})} \sqrt{\frac{\theta_{0r}\tau_{Fanr}}{\theta_{tr}}}. \tag{A.72}$$

From Equation A.72, the bypass ratio $\alpha = \dot{m}_8/\dot{m}_2$ is found to be:

$$\alpha = \alpha_r \frac{\pi_{LPCr}\pi_{HPCr}/\pi_{Fanr}}{\pi_{LPC}\pi_{HPC}/\pi_{Fan}} \frac{D(M_8)}{D(M_{8r})} \sqrt{\frac{\theta_t/(\theta_0\tau_{Fan})}{\theta_{tr}/(\theta_{0r}\tau_{Fanr})}}. \tag{A.73}$$

Using Equation A.70, the off-design core mass flow can be written:

$$\dot{m} = \dot{m}_2 = \dot{m}_r \sqrt{\frac{T_{t4r}}{T_{t4}}} \frac{P_0\delta_0\pi_d\pi_{LPC}\pi_{HPC}}{P_{0r}\delta_{0r}\pi_{dr}\pi_{LPCr}\pi_{HPCr}}, \tag{A.74}$$

where $\dot{m}_r$ is determined at design point. From Equations A.73 and A.74, the total engine mass flow at off-design conditions is: $\dot{m}_0 = (1+\alpha)\dot{m}$.

Separate Flow Exhaust Nozzle Conditions. The flow stagnation properties at the core and bypass exhaust nozzles are

$$\frac{P_{t6}}{P_0} = \delta_0\pi_d\pi_{LPC}\pi_{HPC}\pi_b\pi_{HPT}\pi_{LPT}\pi_{nc} \tag{A.75}$$

and

$$\frac{P_{t8}}{P_0} = \delta_0\pi_d\pi_{Fan}\pi_{nb}, \tag{A.76}$$

respectively. The flow through each of the exhaust nozzles is either choked or ideally expanded. In both cases, the core and bypass exhaust flow static properties can be computed.

A.2.2 Solution Procedure

The computation of the off-design performance of a turbofan engine with separate flow exhaust nozzles requires to solve a system of 11 non-linear governing equations (Equations A.56, A.57, A.60, A.61, A.64, A.65, A.66, A.67, A.73, A.75 and A.76) for the 11 dependent variables: π_{Fan}, τ_{Fan}, π_{LPC}, τ_{LPC}, π_{HPC}, τ_{HPC}, π_{LPT}, τ_{LPT}, α, M_6 and M_8.

In the case of a mixed flow exhaust nozzle, a system of 14 non-linear equations and 14 dependent variables is obtained. Additional equations are required to capture the off-design performance of the constant-area mixer. Additional variables are the total pressure and temperature ratio across the mixer and the mixer bypass ratio. The computation of the off-design performance of a turbofan engine with mixed flow exhaust is reported in Mattingly (1996).

The above system of equations is solved using a Newton iteration method. A least-square technique is used to minimize the residuals of the non-linear system of equations. The design point is used as an initial guess.

The core mass flow is then computed from Equation A.74, and the following results are output:

- fuel-to-air ratio,
- flow velocity, static temperature and pressure at stations 6, 8, and 9,
- specific thrust and TSFC.

The shaft rotational speeds of both spools are computed with respect to the design point conditions. Assuming that enthalpy rise across the fan and the high-pressure compressor scale with the square of their rotational speed yields

$$T_{t8} - T_{t2} = K_1 \omega_1^2 \tag{A.77}$$

and

$$T_{t3} - T_{t2.5} = K_2 \omega_2^2, \tag{A.78}$$

where ω_1 and ω_2 are the rotational speeds of the low-pressure spool and the high-pressure spool, respectively. Eliminating K_1 and K_2 using the design point conditions yields

$$\frac{\omega_1}{\omega_{1r}} = \sqrt{\frac{T_0 \theta_0 (\tau_{Fan} - 1)}{T_{0r} \theta_{0r} (\tau_{Fanr} - 1)}}, \tag{A.79}$$

and

$$\frac{\omega_2}{\omega_{2r}} = \sqrt{\frac{T_0 \theta_0 \tau_{LPC} (\tau_{HPC} - 1)}{T_{0r} \theta_{0r} \tau_{LPCr} (\tau_{HPCr} - 1)}}. \tag{A.80}$$

As ω_{1r} is determined by the fan sizing procedure, a dimensional value of ω_1 at off-design conditions can be obtained. This quantity is used in Heidmann's fan noise prediction method implemented

in ANOPP (see Heidmann (1975) and Zorumski (1982)). However ω_{2r} is not determined and only the ratio ω_2/ω_{2r} can be computed at this level of details.

A.2.3 Model Limitations and Validation with GasTurb

In order to assess the accuracy of off-design engine performance prediction, the baseline blended-wing-body engine sized at design point in Section A.1.3 is operated under the following off-design conditions:

- T_{t4} ranging from 1700 K to 2100 K, $M_0 = 0.2$, ISA+15 K.
- M_0 ranging 0 from 0.4, $T_{t4} = 2000$ K, ISA+15 K.

The results of the off-design engine performance prediction are compared to GasTurb's output in Figures A-2 and A-3.

Compared to GasTurb's results, the off-design performance prediction accurately renders the trends observed for most of the engine cycle characteristics. However, for some quantities such as the low-pressure spool rotational speed (ω_1), the trends are not captured by the performance prediction. This is mainly due to the assumption of constant polytropic efficiencies of the rotating components. To remove this assumption, component performance maps are required.

A significant part of the error is also due to the assumption that the gas properties upstream and downstream of the combustor are constant. For the results reported in Figures A-2 and A-3, the prediction has been significantly improved by introducing local gas properties at stations 2, 2.5, 3, 4 and 5. For comparison, the results obtained assuming constant gas properties upstream and downstream of the combustor are plotted in green in Figure A-4.

Implementing component performance maps and variable gas properties would yield a more accurate off-design engine performance prediction. However, it is suggested that the method presented in this section is reliable and accurate enough for preliminary off-design performance prediction at takeoff.

A.3 Propulsion System Noise Prediction at Takeoff

The first-principles-based engine cycle deck presented in Sections A.1.1, A.1.2 and A.2 generates the inputs required by the propulsion system noise prediction at takeoff. This noise prediction is performed by NASA's Aircraft Noise Prediction Program (ANOPP).

For given airframe characteristics, the takeoff trajectory is first computed by a flight dynamics module. The characteristics of the jet noise and/or fan noise sources along this trajectory are then predicted using semi-empirical methods. Finally, the noise is propagated to the observer and the effective perceived noise level is computed.

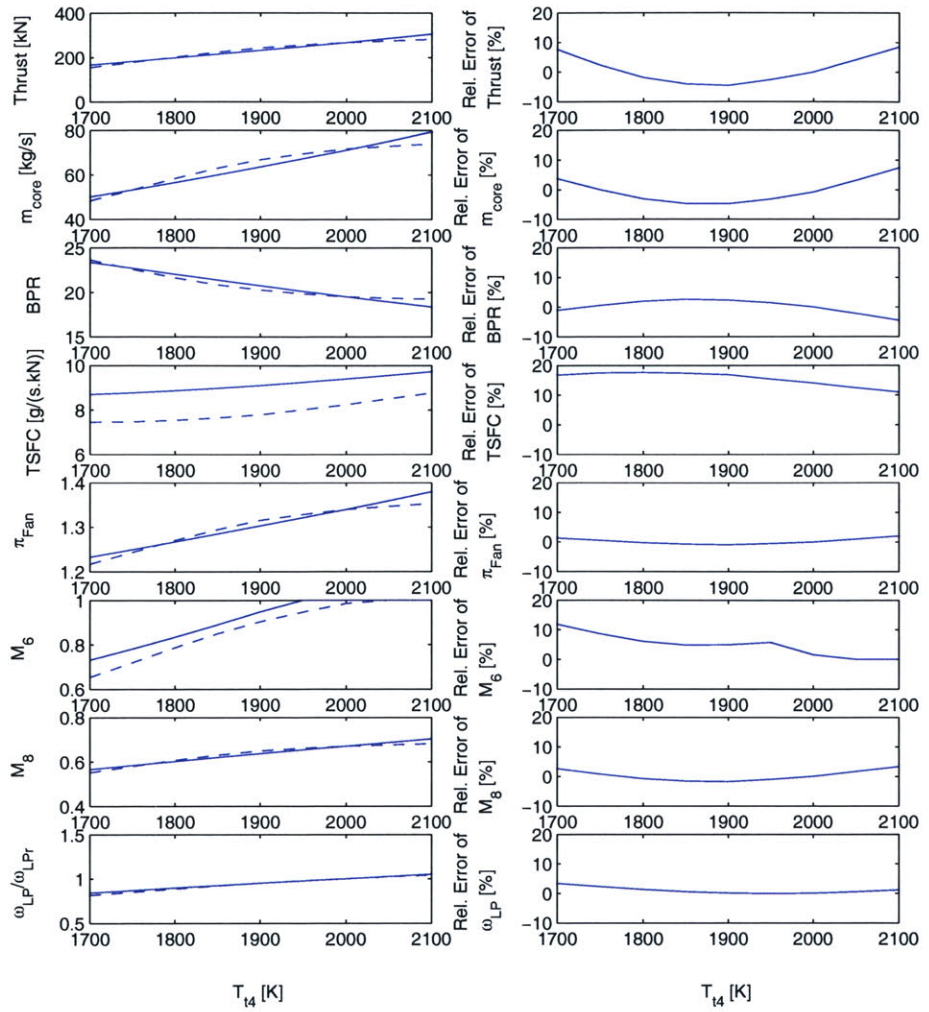

Figure A-2: Predicted off-design performance of the baseline engine for the blended-wing-body aircraft (solid) as a function of T_{t4} compared to GasTurb (dashed). Right column shows the model prediction error relative to the prediction using GasTurb.

A.3.1 Takeoff Noise Prediction Using ANOPP

Appropriate Noise Metric

In order to certify an aircraft to noise standards (see FAR Part 36 (1988)), the acoustic signature at takeoff is quantified by the Effective Perceived Noise Level (EPNL) at two distinct locations:

- the flyover measurement point, located on the extended centerline of the runway, 6500m from the start of the takeoff roll, and
- the sideline measurement point, located on a line parallel to and 450m from the runway extended centerline, where the noise after lift-off is at a maximum during takeoff.

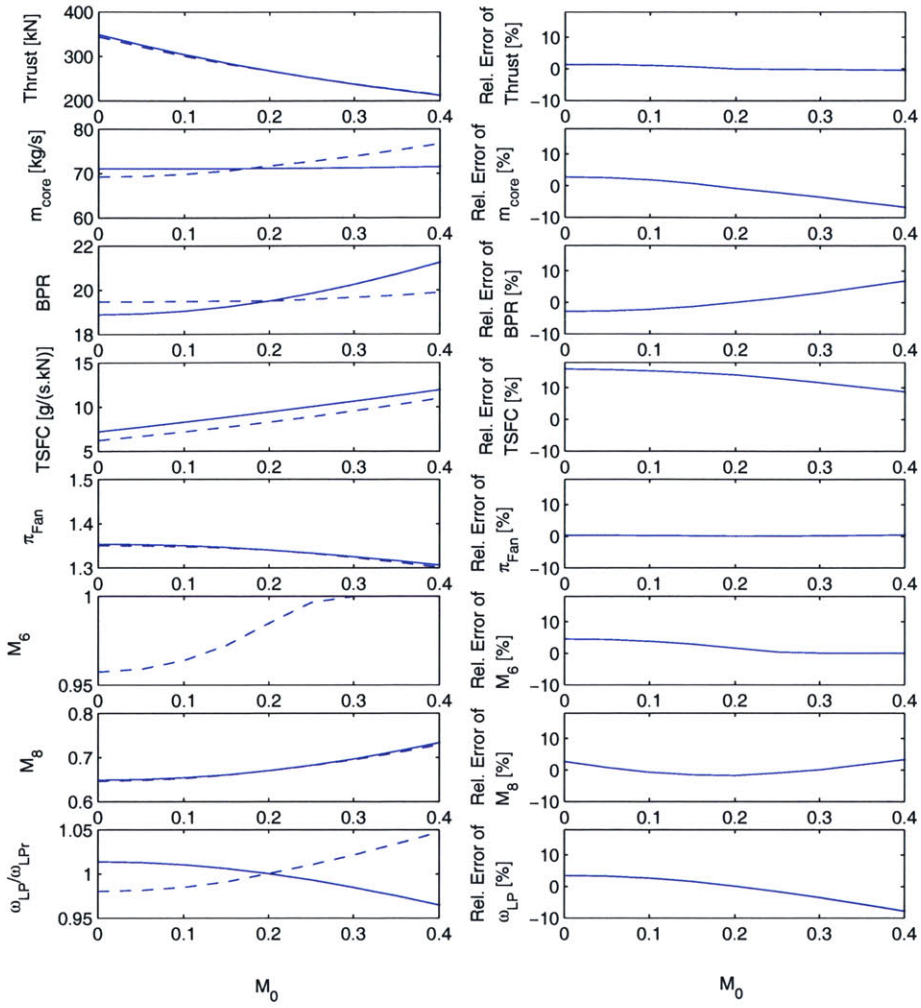

Figure A-3: Predicted off-design performance of the baseline engine for the blended-wing-body aircraft (solid) as a function of M_0 compared to GasTurb (dashed). Right column shows the model prediction error relative to the prediction using GasTurb.

EPNL metric quantifies the annoyance of an aircraft maneuver by integrating the duration of the maneuver, the sound pressure level (SPL), and the frequency and tonal content of the perceived noise at a given location. In this study, the EPNL is computed at the flyover and sideline measurement points, such that the noise predictions can be compared to the certification data. All measurement points are placed 1 m above the ground.

Aircraft Trajectory at Takeoff

The computation of EPNL requires knowledge of the position of the noise source relative to the observer as a function of time. In ANOPP, the trajectory of the aircraft during takeoff is computed using the jet takeoff module. This module requires the following inputs:

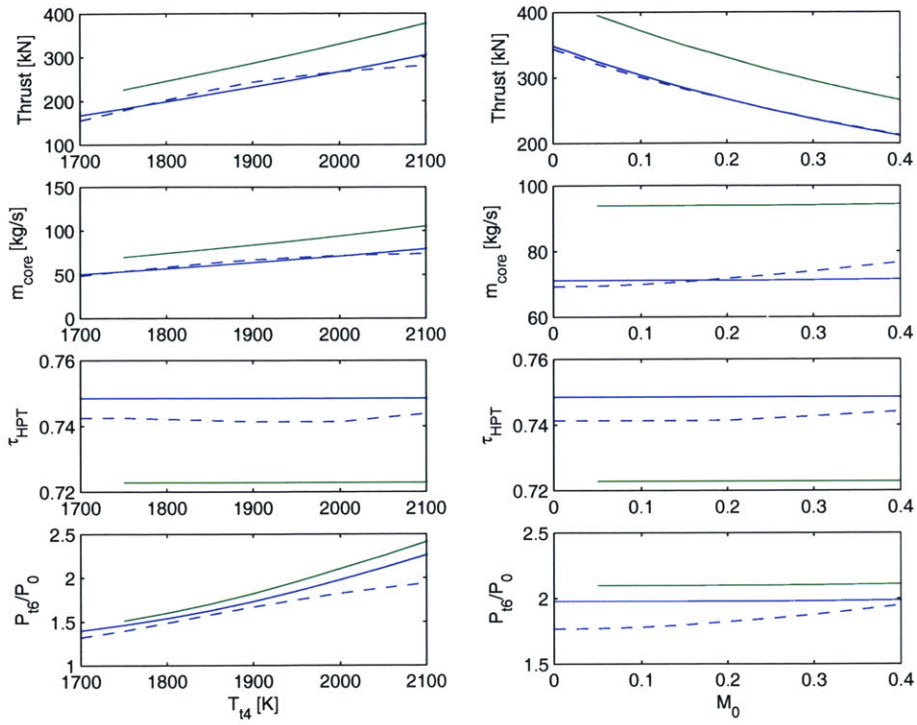

Figure A-4: Predicted off-design performance of the baseline engine for the blended-wing-body aircraft as a function of T_{t4} (left) and M_0 (right) for locally constant gas properties (solid blue) and constant gas properties upstream and downstream of the combustor (solid green), compared to GasTurb's results (dashed blue).

- engine thrust as a function of flight Mach number and power setting, previously computed by the engine cycle deck
- number of engines
- aerodynamic characteristics of the airframe (C_l and C_d as a function of angle of attack and flap setting)
- landing gear drag coefficient as a function of lift coefficient ($C_{d,Lg}(C_l)$)
- initial flap setting
- aircraft wing reference area (used to non-dimensionalize C_l and C_d, in m^2)
- aircraft takeoff weight
- rotation velocity (V_{rot})
- desired climb velocity (V_{climb}) and climb angle

The rotation velocity must be larger than the stall speed, and the climb velocity should be at least 20% larger than the stall speed (see Zorumski (1982) for more details). The total aircraft weight is assumed constant during takeoff and the effect of wind is neglected. The trajectory is computed until the aircraft reaches a horizontal distance of 9 km from the start of the takeoff roll. The EPNL computation requires knowledge of the instantaneous noise level over a sufficiently long time period. In practice, this time period is selected such that the noise level is always higher than 20dB below the maximum level.

Noise Sources

The propulsion system is the main noise source during takeoff. At takeoff, engines are operating at maximum power conditions, generating high turbomachinery noise and jet mixing noise levels. On the other hand, the aircraft velocity is relatively low during most of the ground roll and initial climb (0 to approximately 100 m/s), such that airframe noise is relatively low compared to propulsion system noise.

Only jet mixing noise and fan noise are considered in this analysis. Other noise sources generated by the propulsion system such as compressor noise, combustion noise and turbine noise are neglected.

The thrust produced by the engine drops as the aircraft accelerates from static conditions to $M_0 \approx 0.3 - 0.4$. According to Lighthill's acoustic analogy (Lighthill (1952)), the acoustic power radiated by jet mixing varies as the fourth power of the thrust, such that jet noise emissions vary during takeoff. Moreover, the flight effect (Doppler effect resulting from the convection of turbulent eddies) has a significant impact on jet noise. Similarly, the fan is operated at various off-design conditions during takeoff. Variations in engine mass flow, fan blade loading and rotational speed entail variations in fan noise radiated along the takeoff path.

In order to account for the above mentioned effects, noise source characteristics are computed at each time step, under the instantaneous flight conditions and engine power setting determined by the takeoff flight dynamics module.

The following noise prediction modules are used:

- Stone's Jet Noise module is capable of computing jet noise for single jets as well as co-annular jets. This module is considered more accurate than the Single Jet noise module based on the SAE method (see Stone (1974)). The modeling of the flight effect has been improved (see Stone and Montegani (1980)). This prediction method has been extensively validated (Stone (1974); Stone and Montegani (1980)).

- Heidmann's fan noise module, based the fan noise prediction method reported in Heidmann (1975). The original method has been modified by adjusting constants and parameters to better render fan noise experimental measurements. Two improvements are available:

  - the Allied Signals Small engines method (see Hough and Weir (1996))
  - the GE method (see Kontos et al. (1996))

The following input quantities are required by Stone's jet noise module:

- engine reference area (AE, in m^2)
- flight Mach number (MA)
- density (RHOA, in kg/m^3), speed of sound (CA in m/s) and static temperature (TA in K) at ambient conditions
- number of engines (NENG) (number of noise sources, ie. number of jets)
- nozzle type (two coaxial jets or a single circular jet)
- primary and secondary nozzle flow states, ie. for each jet a lookup table as a function of flight Mach number and engine power setting containing:
  - nozzle area (in case of variable exhaust area, relative to AE)
  - fuel-to-air ratio
  - jet mass flow rate (relative to $AE \cdot PA/\sqrt{R \cdot TA}$)
  - jet total pressure (relative to PA)
  - jet total temperature (relative to TA)

The following input quantities are required by the Heidmann's fan noise module:

- engine reference area (AE, in m^2)
- flight Mach number (MA)
- density (RHOA, in kg/m^3), speed of sound (CA in m/s) and static temperature (TA in K) at ambient conditions
- number of engines (NENG) (number of noise sources, ie. number of fans)
- fan inlet cross-sectional area (AFAN, relative to AE)
- fan rotor diameter (DIAM, relative to $\sqrt{AE}$)
- fan rotor relative tip Mach number at design point (MD)
- rotor-stator spacing (RSS, relative to the mean rotor blade chord)
- number of rotor blades and stator vanes (NB and NV)

- fan with (IGV=1) or without (IGV=2) IGVs
- distorted (DIS=2) or non-distorted (DIS=1) inlet flow (for IGV=1)
- prediction method (HDNMTH=1, 2 or 3)
- fan inlet and exit flow states, ie. for each location, a lookup table as a function of flight Mach number and engine power setting containing:
  - mass flow rate (relative to $AE \cdot PA/\sqrt{R \cdot TA}$)
  - total temperature (relative to TA)
  - rotational speed ($N = \omega_1/(2\pi)$ in Hz, relative to $\sqrt{R \cdot TA}/DIAM$)

ANOPP Output

From the trajectory and the noise sources characteristics along the takeoff path, the propagation module computes the sound pressure level (SPL) as a function of time at each measurement point. Atmospheric conditions and ground reflection are taken into account. Finally, the EPNL is computed based on the SPL history, the noise spectral content and the duration of the takeoff maneuver.

A.3.2 Method Validation

The noise signature of an aircraft at takeoff is very sensitive to

1. takeoff trajectory, which depends on airframe aerodynamic characteristics, aircraft takeoff gross weight (TOGW) and takeoff procedure (flaps settings),
2. noise sources intensity and directivity, which depend on engines characteristics and takeoff procedure (engine power setting schedule).

The aircraft configuration for which most of the required parameters are available is an A300B (aerodynamic data from Boiffier (2000)), powered by Pratt&Whitney JT9D-59A engines (cycle data from Mattingly (1996)). Aerodynamic coefficients and airframe characteristics of this aircraft are presented in Table A.6. Lift and drag coefficients are computed using

$$C_l(\alpha, \delta) = C_{l_\alpha} \cdot (\alpha - \alpha_0(\delta)) \tag{A.81}$$

and

$$C_d(\alpha, \delta) = C_{d_0} + \Delta C_{d_0}(\delta) + k_i C_l(\alpha, \delta)^2, \tag{A.82}$$

where k_i is the induced drag coefficient. Additional drag $\Delta C_{d,LG}$ is due to the landing gear and is assumed independent of the lift coefficient.

Parameter	Value			
C_{l_α}	0.087 (for α in °)			
C_{d_0}	0.0175			
$\Delta C_{d,LG}$	0.0175			
k_i	0.055			
Flaps setting (δ)	0°	15°	22°	41°
α_0	−2°	−8°	−11.4°	−16.6°
ΔC_{d_0}	0	0.0185	0.0243	0.0583
TOGW	142 tons to 165 tons			
Wing Area	260 m^2			

Table A.6: Aerodynamic coefficients and main airframe characteristics of an A300B (Boiffier (2000)).

The following takeoff profile is assumed. A typical rotation velocity of 82 m/s ($\sim$ 164 kts) and an initial climb velocity of 95 m/s (190 kts) are chosen. The flap setting during takeoff is constant to 15°. The engine power setting increases from approximately 80% (corresponding to $T_{t4} = 1250$ K) at the start of the takeoff roll ($M_0 = 0$) to 100% ($T_{t4} = 1350$ K) when the aircraft reaches $M_0 = 0.2$ and stays constant at maximum power setting during the initial climb. Thus, no cutback is performed. Figure A-5 depicts the takeoff trajectories computed by the flight dynamics module for various takeoff gross weights. The aircraft lifts off in 2000 m to 2800 m, depending on the takeoff gross weight. The required runway length is consistent with the takeoff field length of 2400 m specified for this aircraft (Jane's All the World's Aircraft (2003)).

The noise prediction includes both fan and jet noise sources. The GE version of Heidmann's fan noise prediction method is used. Figure A-6 compares results of the noise prediction to the certification data reported in FAA (2002), as a function of the takeoff gross weight.

Independently of the takeoff gross weight, the sideline noise is overestimated by approximately 2.5 dB and flyover noise by 6.5 dB. The predicted trends are consistent with certification data. The sideline noise is almost independent of the takeoff gross weight, whereas the flyover noise increases with the takeoff gross weight. According to Figure A-5, a heavier aircraft requires a longer runway length to takeoff and climbs at a lower angle compared to a lighter aircraft. Thus, the heavier aircraft passes over the flyover measurement point at a lower altitude, and generate a higher EPNL. Quantitatively, the predicted increase of 3 dB is consistent with certification data.

The discrepancy of 6.5 dB is acceptable considering the uncertainty in engine power and flap setting schedules. The prediction does not take into account potential noise reduction due to the shielding of fan noise by the nacelles. Reconstructing the exact conditions of the certification measurement requires more accurate data on the takeoff profile, and airframe and engine characteristics. However, this study shows that the modeling framework captures the relative variations in propulsion system noise level at takeoff.

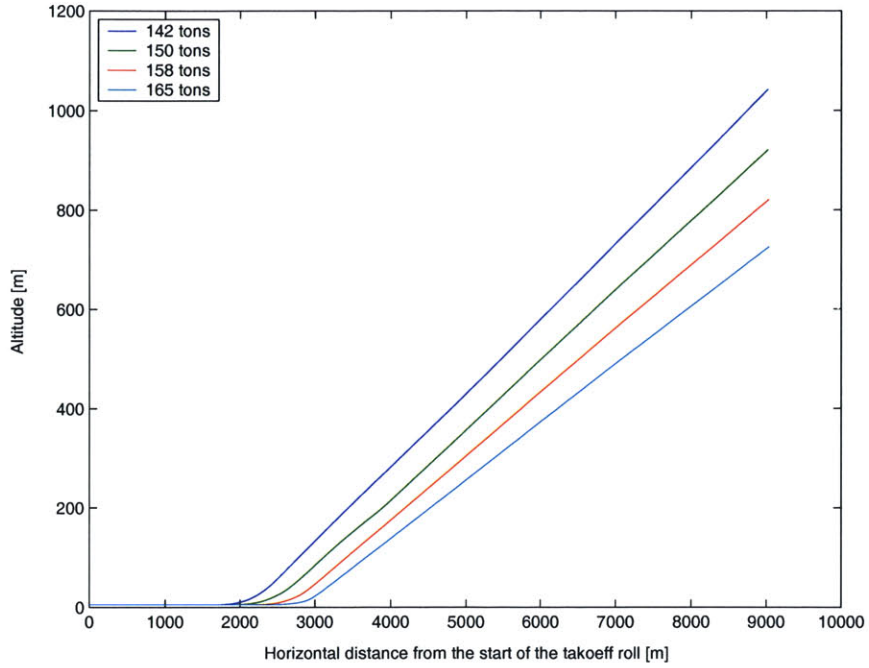

Figure A-5: Computed takeoff trajectories of an A300B for TOGW of 142 tons (dark blue), 150 tons (green), 158 tons (red), and 165 tons (light blue).

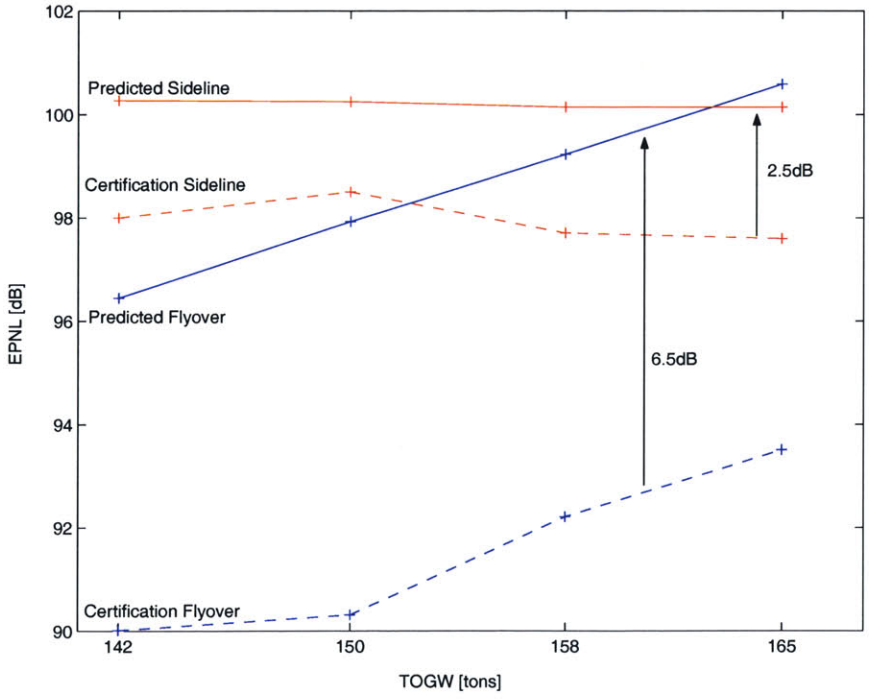

Figure A-6: Predicted noise (solid) and certification data (dashed) of the A300B, powered by the JT9D-59A as a function of the takeoff gross weight. Blue: flyover noise - Red: sideline noise.

Appendix B

High Aspect Ratio Jet Nozzles

B.1 High Aspect Ratio Jet Noise

B.1.1 Previous Work on High Aspect Ratio Jet Noise

Coles (1959) investigates the jet noise produced by two slot nozzles of aspect ratios 14 and 100 mounted at the back of a full-scale turbojet. With respect to the reference circular nozzle of same area, both slot nozzles appear to decrease sound-pressure levels in the plane containing the major axis and to increase it in the plane containing the minor axis. Low and middle frequency levels are reduced, and high frequency levels are increased. Polar directivity is also strongly influenced by the nozzle shape: a round jet shows a peak around 150°, whereas the slot nozzles of aspect ratio 14 and 100 show peaks at 135° and 105°, respectively. The total sound power is decreased by 3 dB with the slot nozzle of aspect ratio 100, but is not significantly modified by the nozzle of aspect ratio 14. Adding a flap parallel to the major axis of the slot leads to a further 1.5 dB reduction in total sound power, essentially due to shielding effect at certain angles.

Compared to a circular nozzle of same area, the increased perimeter of the slot nozzle leads to a larger region of high shear, but also to a more rapid mixing, as the core length is greatly decreased and the jet surface exposed to secondary air is increased. According to Coles (1959), these changes are similar to the ones obtained by replacing the large circular nozzle by a large number of small, widely separated, circular nozzles of the same total area. For a sufficiently large aspect ratio slot nozzle, Coles uses Lighthill's analogy to demonstrate that a jet noise reduction of 3 dB is expected, provided that mean and turbulent velocities in the mixing region follow the same similarity relations for both circular and slot nozzles. This assumption is validated by flow field data of circular nozzle and slot nozzle of aspect ratio 40, and the expected 3 dB reduction is observed for a slot nozzle of aspect ratio 100. In his discussion, Coles argues that the largest proportion of the noise is generated in the initial mixing region that extends from the nozzle exit to the end of the jet core. In practice,

this initial mixing region extends 8 nozzle radii downstream of the nozzle exit for circular jets, and 8 nozzle heights downstream of the slot exit for high aspect ratio jets.

Maestrello and McDaid (1971) compare acoustic characteristics of jets produced by a rectangular nozzle of aspect ratio 20 with respect to a round nozzle of same area. Similar to Coles (1959), Maestrello and McDaid (1971) observe that the rectangular nozzle alters both the directional pattern and the spectral content of the sound field. The spectrum is shifted toward higher frequencies in the plane containing the minor axis but remains almost unchanged in the plane containing the major axis. At a polar angle of 135°, the peak sound pressure level in the plane containing the minor axis is 3 dB lower than in the plane containing the major axis. In terms of total acoustic power, no significant reduction (-0.1 dB) is observed with respect to the round partially turbulent flow nozzle. This result is consistent with the one reported by Coles (1959) for the slot nozzle of aspect ratio 14. Coles and Maestrello and McDaid (1971) observe that low aspect ratio nozzle redirect and modify the spectral content of the noise without significantly altering the total acoustic power radiated by the jet. It appears from both studies that the azimuthal redirection of jet noise by high aspect ratio nozzles is not yet fully understood.

According to Maestrello and McDaid (1971), the two distinct regions of the jet are the mixing region, extending from 1 to 4 nozzle diameters downstream of the nozzle exit, and the transition and fully turbulent region, starting at 5 nozzle diameters downstream of the nozzle exit. Jet flow fields generated by nozzles of different geometries but same areas and momentum fluxes tend to become increasingly alike as they develop downstream the nozzle. Thus, noise suppression must come from differences in the initial stages of the jet development. This statement is consistent with Coles's assumption that the noise is mainly radiated by sources situated between the nozzle exit and the end of the potential core.

Gruschka and Schrecker (1972) present measurements of total acoustic power radiated from jets generated by rectangular nozzles of aspect ratios 30, 60 and 120 with and without flaps. Noise measurements for a reference circular nozzle are also given. All nozzles have the same exit area. For Mach numbers above 0.5, the acoustic power follows the eighth power of the velocity scaling law independently of the nozzle geometry. Compared to the round nozzle, the nozzle of aspect ratio 30 shows a reduction of about 1 dB at a Mach number of 0.5 to about 3 dB at high subsonic Mach number (0.87). Further reductions of 1 dB and 2 dB are observed for nozzles of aspect ratio 60 and 120, respectively.

According to Gruschka and Schrecker (1972), changing the nozzle geometry from a circular to a rectangular shape increases the jet surface in contact with the outer flow. This leads to an increased mixing and a reduced core length. Referring to Coles's calculation, a 3 dB noise reduction is expected for sufficiently high aspect ratios nozzles. For jet aspect ratios of 30 and 60, the data agree with Cole's prediction. However, for a jet aspect ratio of 120, a 4 to 6 dB reduction in jet noise is observed.

It seems that Coles's calculation underestimates the noise reduction for jet aspect ratios larger than 100. This suggests that reductions of more than 3dB can be achieved by high aspect ratio nozzles.

Tam and Zaman (2000) report jet noise spectra of a circular and two rectangular nozzles of aspect ratios 3 and 8, at polar angles of 90° and 155° in the planes containing the major and minor axes of the nozzle. Jet noise spectra do no significantly depend on the azimuthal angle. The sound levels are approximately the same as those of a circular jet with same exit area.

Tam and Zaman (2000) conclude that the jets generated by nozzles of different geometries reach a common asymptotic state characterized by an approximately circular cross section and self-similar flow and turbulence characteristics. This common state is reached after a few equivalent diameters downstream the nozzle exit. Tam and Zaman (2000) argue that the dominant jet noise sources must therefore be located near the end of the potential core which yields an axisymmetric sound field independent of the nozzle geometry. From this study, rectangular nozzles of low aspect ratio (less than 10 in practice) do not yield significant jet noise reduction compared to conventional circular nozzles. This is consistent with the results reported by Maestrello and McDaid (1971) for $AR = 20$ and by Coles (1959) for $AR = 14$.

Munro and Ahuja (2003a,b) study the noise generated by jets of aspect ratios ranging from 60 to 3000. The Overall Sound Pressure Level (OASPL) at polar angle of 90° in the plane containing the minor axis of the nozzle follows the V_{jet}^8 scaling law reasonably well and shows a significant dependence to the jet aspect ratio. The appropriate characteristic length to describe the jet noise generation by high aspect ratio jets is found to be:

$$L_{eq} = h^{3/4} w^{1/4} = \sqrt{A} A R^{-1/4}, \tag{B.1}$$

where A is the jet area. At a polar angle of 90°, the experimental data are reasonably well rendered if L_{eq} is used to form the Strouhal and L_{eq}^2 is used to computed the sound pressure level.

At other polar angles, according to Lighthill's theory, the directivity pattern is given by the convection amplification term $(1 - M_c \cos(\theta))^{-5}$. For conventional round jets, a value of $M_c = 0.65 M_{jet}$ is generally used. For high aspect ratio jets, the spectra at a polar angle of 160° suggest that a value of $M_c = 0.36 M_{jet}$ is more appropriate to render the noise measurements. The region of noise generation for high aspect ratio jets appears to extend from the nozzle exit to 20 heights of the nozzle downstream. The core length is of the order of 4 nozzle heights.

Stone (1974) reports that the overall sound pressure levels at a polar angle of 90° generated by rectangular jets of aspect ratios 4.8 and 69 are in good agreement with the OASPL predicted for circular nozzles of the same area for all azimuthal directions. Spectral distributions measured at azimuthal angles of 0 (plane containing the minor axis) and 45° are well captured by the spectra predicted for a round jet. However, at an azimuthal angle of 90°, the lower frequencies are over-

predicted. Stone concludes that his jet noise prediction method valid for circular nozzles can directly be applied to equivalent slot nozzles with a reasonable accuracy.

B.1.2 Analysis of Available Data

It is suggested that the data reported by Coles (1959), Maestrello and McDaid (1971), Gruschka and Schrecker (1972), Tam and Zaman (2000), and Munro and Ahuja (2003a,b) can be gathered to determine the trends in jet noise for jet aspect ratios ranging from 1 to approximately 1000. To determine these trends in jet noise, available data must be first converted to a single common measure. Once these trends are found, existing jet noise prediction methods can be modified to predict high aspect ratio jet noise.

All available data except the ones reported by Tam and Zaman (2000) are integrated over the entire spectrum. Coles, Maestrello et al. and Grushka et al. report total acoustic power measurements (W). Munro et al. report OASPL at 90° of polar angle, normalized by the eighth power of jet velocity V and jet area A:

$$S = OASPL(90°) - 80log(V/100) - 10log(A). \tag{B.2}$$

Using

$$W = \int_S I(\vec{r})d\vec{r} \tag{B.3}$$

and

$$\overline{p^2(\vec{r})} = \rho_a c_a I(\vec{r}), \tag{B.4}$$

and assuming that the mean square pressure can be expressed as:

$$\overline{p^2(\vec{r})} = \frac{1}{r^2} \cdot \overline{p^2_{90°}}(A_{jet}, V_{jet}, \rho_{jet}, T_{jet}, ..., \theta = 90°, \phi = \phi_0) \cdot D(\theta, \phi) \tag{B.5}$$

with $D(\theta = 90°, \phi) = 1$, the total acoustic power becomes, integrating on a sphere of radius r:

$$W = \frac{\overline{p^2_{90°}}(A_{jet}, V_{jet}, ..., \theta = 90°, \phi = \phi_0)}{\rho_a c_a} \cdot \int_{\theta,\phi} D(\theta, \phi) sin(\theta) d\phi d\theta \tag{B.6}$$

Thus, W and $\overline{p^2_{90°}}$ are proportional and

$$OASPL(r, \theta = 90°, \phi) = 10log\left(\frac{\overline{p^2_{90°}}/r^2}{p^2_{ref}}\right) = 10logW + K, \tag{B.7}$$

where K is constant at given r. Using this method, total acoustic power measurements are converted to overall sound pressure levels at 90° of polar angle. In the case of different jet velocities or nozzle areas, data are normalized using the scaling used by Munro et al. given in Equation B.2. However,

it is not possible to accurately extract absolute noise levels from all available data sets, and all data cannot directly be reduced to a single curve. This would require a more detailed knowledge of the setup of each of experiment, such as the distance of measurement.

Thus, only the relative variations in jet noise over the range of aspect ratios covered by each data set are conserved. The constant K associated with each data set is adjusted to match the absolute levels reported by Munro and Ahuja (2003a,b). To determine K, the range of aspect ratios covered by the considered data set must overlap with the range covered by Munro and Ahuja (2003a,b), i.e. from 60 to 3000. This is the case for one of the data points reported by Coles (1959) ($AR = 100$) and two data points reported by Gruschka and Schrecker (1972) ($AR = 60$ and $AR = 120$). These two data sets allow to link high aspect ratio jet noise ($AR > 100$) to low aspect ratio jet noise ($AR \approx 10$ to 30) and even round jet (i.e. $AR = 1$).

The data reported by Maestrello and McDaid (1971) and Tam and Zaman (2000) do not overlap with the data reported by Munro and Ahuja (2003a,b), but both data sets give results for round jets. For these data, the constants K are adjusted to match the data reported by Coles (1959) and Gruschka and Schrecker (1972) at $AR = 1$. The data set reported by Maestrello and McDaid (1971) provide an additional data point at $AR = 20$. Data reported by Tam and Zaman (2000) are narrow band jet noise spectra. In order to calculate the OASPL, it would be required to integrate these spectra over all frequencies. However, the main result of this study is that there is no significant change in noise spectra for $AR = 3$ and $AR = 8$ compared to a round jet ($AR = 1$).

The corrected OASPL obtained by converting the available noise data are shown in Table B.1 and are plotted as a function of $10log(AR)$ in Figure B-1.

B.1.3 Modifications to Stone's Method for High Aspect Ratio Jet Noise Prediction

The trends in corrected OASPL observed in Figure B-1 links the jet noise generated by high aspect ratio jets to the noise generated by conventional circular jets. This suggests that existing jet noise prediction methods validated for round jets can be modified to predict high aspect ratio jet noise. The following modifications are made to Stone's jet noise prediction method to predict high aspect ratio jet noise:

- $MSP90$
  - unchanged if $AR < 10$
  - multiplied by $\left(\frac{AR}{10}\right)^{-1/3}$ if $10 < AR < 100$
  - multiplied by $\left(\frac{100}{10}\right)^{-1/3}\left(\frac{AR}{100}\right)^{-1/2}$ if $100 < AR$
- SM (Strouhal number)

AR	$Data$	S [dB]	Data Conversion
75	42	42	Munro and Ahuja (2003a,b), Fig. 3
100	40.8	40.8	$Data = OASPL(90°) - 80log(V/100) - 10log(A)$
178	39.5	39.5	$S = Data$
316	37.5	37.5	
562	35.5	35.5	
1	165	44	Coles (1959) p.5-6
14	165	44	$Data = total\ sound\ power\ level$
100	162	41	$S = Data + K_1$, $K_1 = -121$
1	$2.1.10^{-4}$	45.2	Maestrello and McDaid (1971), Table in Fig. 18
1	$1.6.10^{-4}$	44.0	$Data = W_{ac}/(\rho_0 A_j U_j^8/a_0^5)$
20	$1.56.10^{-4}$	43.9	where W_{ac} is the total radiated acoustic power
5	$1.80.10^{-4}$	44.6	$S = 10log(Data) + K_2$, $K_2 = 82$
5	$1.58.10^{-4}$	44.0	
1	91.4 (L_1)	44.5	Gruschka and Schrecker (1972), Fig. 3a
1	102.1 (L_2)	44.5	$Data = 10log(\frac{w}{w_{ref}})$ vs L
1	110.6 (L_3)	45.2	where $L = \rho_0 A_j U_j^8/a_0^5$ is the Ligthill parameter,
30	90.7 (L_1)	43.8	w is the total sound power
30	99.6 (L_2)	42.0	and $w_{ref} = 10^{-12}W$
30	107.6 (L_3)	42.2	$S = Data - 10log(L) + K_3$, $K_3 = -64.9$
60	89.7 (L_1)	42.8	$L_1 = 43$
60	98.7 (L_2)	41.1	$L_2 = 500$
60	106.5 (L_3)	41.1	$L_3 = 3000$
120	88.5 (L_1)	41.6	
120	97.6 (L_2)	40.0	
120	105.4 (L_3)	40.0	
1	93	44.6	Tam and Zaman (2000), Fig. 5
3	93	44.6	$Data = peak(10log(\frac{SU_j}{D_j P_{ref}^2}))$ in minor axis plane
8	93	44.6	$S = Data + K_4$, $K_4 = -48.4$

Table B.1: Rectangular jet noise data reported in literature. S is the area- and velocity-corrected OASPL at 90° of polar angle.

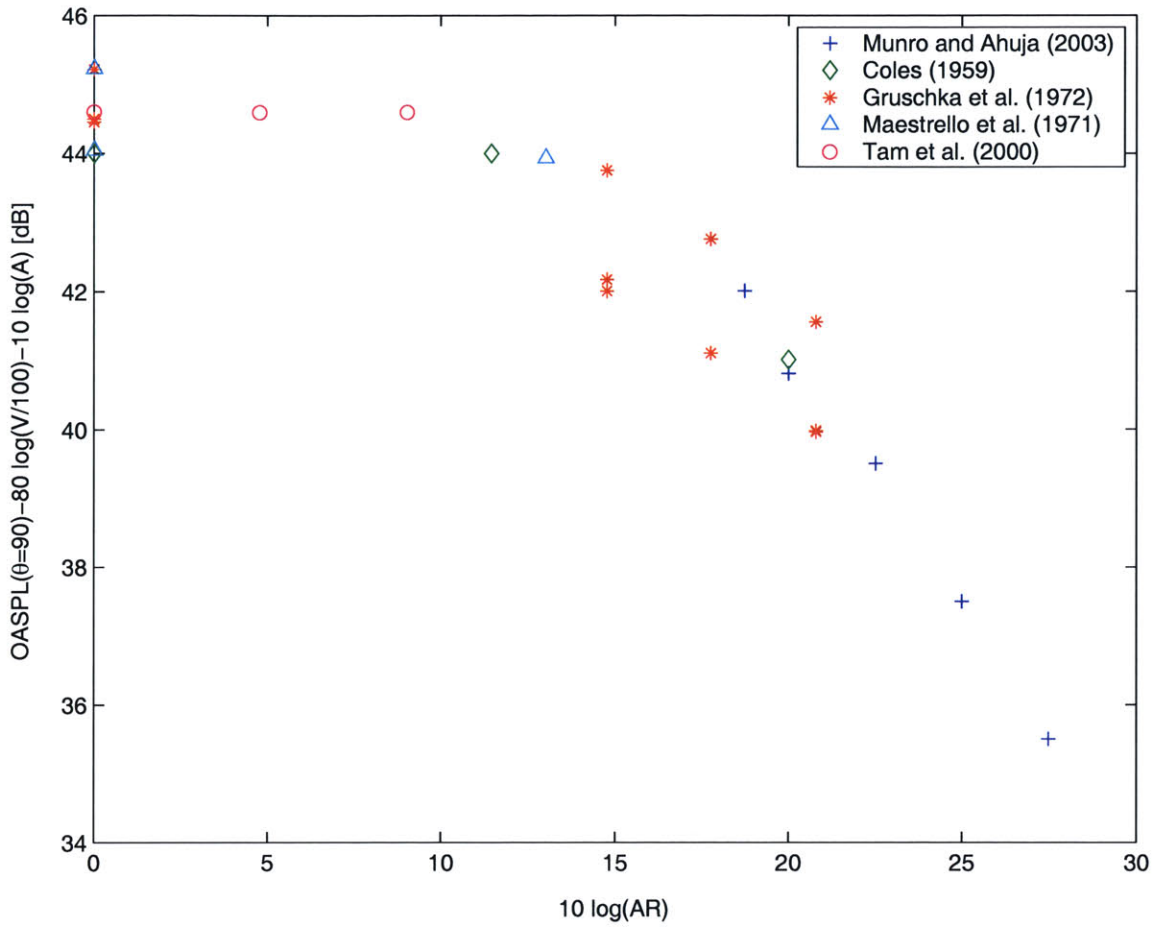

Figure B-1: Area- and velocity-corrected jet noise OASPL at a polar angle of 90° as a function of jet aspect ratio

  - unchanged if $AR < 10$
  - multiplied by $\left(\frac{AR}{10}\right)^{-1/6}$ if $10 < AR < 100$
  - multiplied by $\left(\frac{100}{10}\right)^{-1/6}\left(\frac{AR}{100}\right)^{-1/4}$ if $100 < AR$

- k (Convection coefficient: $M_c = kV_{jet}/c_a$)
  - unchanged if $AR < 60$
  - replaced by 0.36 (initial value: 0.62) if $60 < AR$ (k is also modified in the term $\alpha k = 0.2k$. Instead of 0.124, this term becomes 0.072.)

In ANOPP, the modified source files are stnpar.f and stnsub.f.

B.2 Thrust Losses in High Aspect Ratio Nozzles

B.2.1 Computation of Nozzle Performance

A one-dimensional viscous and compressible flow model of the high aspect ratio nozzle (HARN) was first developed. In this one-dimensional flow model, the only source of losses is skin friction. Thus, losses are proportional to the internal wetted area of the nozzle, such that HARNs show lower performance compared to axisymmetric nozzles. However, these additional viscous losses are relatively small even for high aspect ratio geoemtries, and the one-dimensional flow model clearly over-predicts nozzle performance. This is attributed to the fact that losses due to flow separation in HARNs are neglected in the one-dimensional model. Flow separation cannot be modeled by a simple one-dimensional flow model. Thus, a three-dimensional viscous computation of the flow in HARNs is performed to account for thrust losses due to both skin friction and flow separation.

Three-Dimensional Fluent Calculation

The steady three-dimensional Reynolds-Averaged Navier-Stokes equations solver coupled to the standard $k-\epsilon$ turbulence model is used to compute the flow in HARNs. The fluid is considered as a perfect gas of constant C_p, constant dynamic viscosity, and constant thermal conductivity.

HARN Geometry

For a choise of design parameters (L, A_0, A_1/A_0, AR_0 and AR_1/AR_0), the nozzle geometry is constructed as follows. First, height and width at the nozzle inlet and exit are deduced from areas and aspect ratios using: $h_i = \sqrt{A_i/AR_i}$ and $w_i = \sqrt{A_i \cdot AR_i}$.

Assuming straight walls, the local height and width are then interpolated linearly from the inlet to the exit: $h(z) = h_0 + (h_1 - h_0)\frac{z}{L}$ and $w(z) = w_0 + (w_1 - w_0)\frac{z}{L}$. The local cross-sectional area $A(z) = h(z) \cdot w(z)$ and the local aspect ratio $AR(z) = w(z)/h(z)$ are also computed. These quantities are plotted for different values of AR_1/AR_0 in Figure B-2 to illustrate the HARN geometry. Note that the high aspect ratio nozzle behaves first as a diffuser, and then as a converging duct.

The nozzle geometry is then meshed using Gambit (Fluent's meshing program). The mesh is refined at the nozzle walls to enable the flow solver to capture the boundary layers. The maximum boundary layer thickness in the HARN can be estimated to approximately 1 cm. A cell thickness of 0.5 mm (i.e. 5% of the boundary layer thickness) is selected at the nozzle walls. The grid resulting from this meshing process is a structured mesh.

Boundary Conditions

The no-slip condition is imposed at the nozzle walls. The flow total pressure $P_{t_{inlet}}$ and temperature (T_{t0}) are prescribed at the nozzle inlet. The ambient static pressure P_a is given for the nozzle exit.

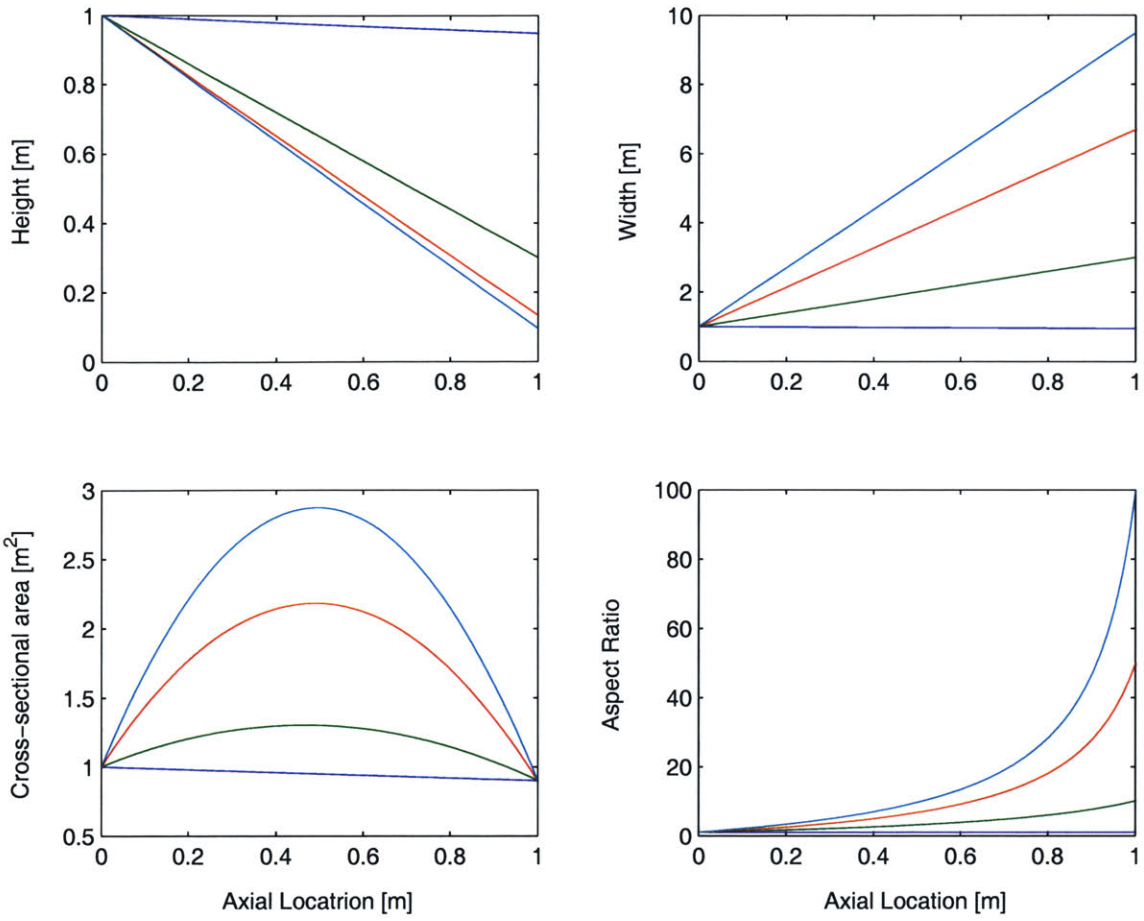

Figure B-2: Axial variations of nozzle height, width, cross-sectional area and aspect ratio are marked in dark blue, green, red and light blue for $AR_1/AR_0 = 1$, 10, 50 and 100 respectively. Other nozzle geometrical parameters are: $AR_0 = 1$, $A_0 = 1$ m^2, $A_1/A_0 = 0.9$, and $L = 1$ m.

Total pressure and temperature at the nozzle inlet can be determined for given engine operating conditions, i.e. ambient conditions P_a and T_a, flight velocity, and engine power setting. The solver computes the flow that develops through the nozzle under these operating conditions.

Post-Processing and Outputs

Once convergence is reached, the actual mass flow and the actual thrust produced by the nozzle are computed by integrating the flow state over the nozzle exit:

$$\dot{m}_{actual} = \int_{Exit} d\dot{m}, \tag{B.8}$$

$$\vec{F}_{actual} = \int_{Exit} d\vec{F} = \int_{Exit} \left[\vec{V} d\dot{m} + (P_s - P_a) dA\right]. \tag{B.9}$$

The nozzle discharge coefficient $C_D = \dot{m}_{actual}/\dot{m}_{ideal}$ and the nozzle gross thrust coefficient $C_{fg} = F_{actual}/F_{ideal}$ are then computed. $\dot{m}_{ideal}$ is the ideal mass flow that the nozzle would pass without total pressure losses. For a converging nozzle, $\dot{m}_{ideal} = D(M_t) \cdot A_1 \cdot NPR \cdot P_a / \sqrt{T_{t0}}$, where M_t is the Mach number at the throat of the nozzle, $NPR = P_{t_{inlet}}/P_a$ is the nozzle pressure ratio, and $D(M)$ is the corrected flow function given by Equation A.47. $F_{ideal} = \dot{m}_{ideal} \cdot V_s$ is the ideal thrust that the nozzle would produce if the flow were ideally expanded to ambient pressure without total pressure losses. The isentropic exit velocity is found from $V_s = M_s \cdot \sqrt{\gamma R T_s} = M_s \cdot \sqrt{\gamma R T_{t0}} \cdot NPR^{\frac{1-\gamma}{2\gamma}}$.

In order to validate the post-processing, a typical HARN configuration is run using an inviscid solver. This yields C_{fg} and C_D very close to 1 (with a precision of 10^{-3}) as expected for non-choked nozzle operation.

B.2.2 Accuracy of the Results

Appropriate Mesh Refinement

In order to determine the appropriate mesh refinement, the computation of the nozzle flow for the following geometry is performed: $A_1/A_0 = 0.6$, $AR_0 = 1$, $AR_1/AR_0 = 120$. This worst case situation is similar to the HARN configuration reported by Munro and Ahuja (2003a,b), although without knife-edges. A_0 is arbitrarily set to 1 m^2 and L is computed such that the dimensionless length $L^* = L/\sqrt{A_0}$ is the same as reported in Munro and Ahuja (2003a,b). Nozzles of same A_1/A_0, AR_0, AR_1/AR_0 and L^* have all the same geometry, but differ only by their size, which is set by the dimensional value of L or A_0. The same nozzle geometry is computed for a coarse mesh with 48000 cells and a fine mesh with 252000 cells. The results obtained with the two different meshes are summarized in Table B.2. Considering the fine mesh computation as the reference, the accuracy of the coarse mesh computation is approximately 0.1% for the mass flow (and the C_D), and approximately 0.5% for the thrust (and the C_{fg}) except for high nozzle pressure ratio, where the error of the coarse mesh computation increases to approximately 2-3%.

Choked Nozzle Operation

Choked nozzle operation yields a static pressure at the nozzle exit that cannot satisfy the ambient pressure imposed by the exit boundary condition, such that the computation cannot properly converge (in practice, the residuals do not decrease below 10^-3).

In order to assess the accuracy of the results for choked nozzle operation, the corrected mass flow is computed for a simple converging nozzle geometry ($A_1/A_0 = 0.9$, $A_0 = 1$ m^2, $L = 1$ m) of square cross section ($AR_0 = 1$, $AR1/AR_0 = 1$) under 6 different operation conditions and is plotted in Figure B-3. The choking of the nozzle flow clearly occurs for $NPR \approx 1.9$, which is consistent with the theoretical value of $1.2^{3.5} = 1.893$ that can be expected for geometries inducing small total

NPR	op. cond.	$\dot{m}_i$	$\dot{m}_f$	$\dot{m}_c$	C_{D_f}	C_{D_c}	$\frac{\Delta\dot{m}}{\dot{m}_f}$ (%)
1.2	takeoff	123.6	114.7	114.8	0.928	0.929	0.09
1.5	takeoff	193.4	182.6	182.6	0.944	0.944	-0.01
1.8	takeoff	242.2	234.8	234.8	0.969	0.970	0.04
2	cruise	60.1	59.2	59.3	0.984	0.985	0.10
2.5	cruise	75.2	74.8	74.7	0.995	0.994	-0.15
3	cruise	90.2	90.0	90.1	0.998	0.999	0.09
NPR	op. cond.	F_i	F_f	F_c	C_{fg_f}	C_{fg_c}	$\frac{\Delta F}{F_f}$ (%)
1.2	takeoff	23211	20075	19998	0.865	0.862	-0.39
1.5	takeoff	53315	47397	47117	0.889	0.884	-0.59
1.8	takeoff	79377	73093	72678	0.921	0.916	-0.57
2	cruise	21272	19922	19874	0.937	0.934	-0.24
2.5	cruise	30107	28084	29072	0.933	0.966	3.52
3	cruise	39072	37376	36586	0.957	0.936	-2.11

Table B.2: Comparison of the results obtained with the fine and the coarse meshes. Units: mass flows in kg/s, forces in N, relative error in percent - Subscripts: i: ideal, f: fine mesh, c: coarse mesh.

pressure losses. This suggests that the convergence issue due to choked nozzle operation does not significantly impact the computation the nozzle performance.

Flow Separation

For the HARN geometries considered in this study, the nozzle first behaves as a diffuser, and then as a converging nozzle. For large values of the design parameter AR_1/AR_0, strong flow separation occurs in the diffusing section. The flow field visualizations presented in Figures B-4 and B-5 illustrate this flow separation phenomenon. Strong flow separation yields values of the ratio of turbulent viscosity (μ_t) to dynamic viscosity (μ) of order 10^5, such that the limit allowed by the flow solver for this ratio is reached.

To assess the impact of this numerical limit on the accuracy of the results, lower flow Reynolds numbers are achieved by scaling down the nozzle. The viscosity ratio in the region of strongly separated flow is proportional to the flow Reynolds number, such that the viscosity ratio is not limited for scaled-down nozzles. For these scaled-down nozzles, a 0.2% increase in nozzle gross thrust coefficient is observed for a tenflod increase in Reynolds number. Thus, the nozzle performance is almost insensitive to the nozzle size. By extrapolating this trend in gross thrust coefficient to the full-scale nozzle, it can be concluded that the error on the nozzle performance coefficients due to the numerical limit is less than 0.1%. This error is of the same order as the error due to the grid refinement observed above. An accuracy of 0.5% in C_{fg} and C_D is acceptable for the preliminary study conducted here.

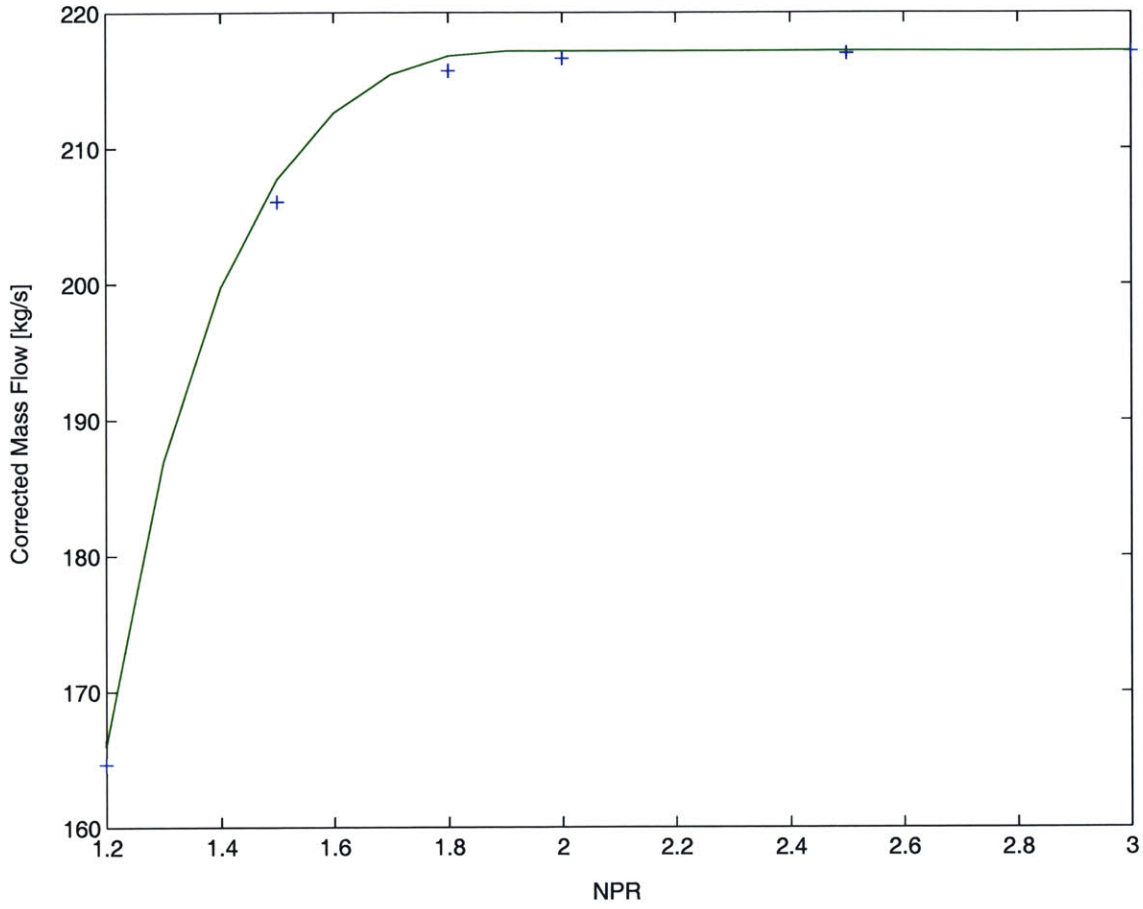

Figure B-3: Computed (blue cross) and ideal (green) corrected mass flow through a converging nozzle of square cross section as a function of the nozzle pressure ratio (NPR).

Sensitivity of Results to Nozzle Inlet Conditions

In the nozzle performance computations presented above, a uniform total pressure profile is prescribed at the nozzle inlet. However, in a real engine, endwall boundary layers develop through the upstream turbo-machinery, leading to a non-uniform velocity distribution and a momentum deficit close to the walls at the nozzle inlet. In order to assess the impact of ingesting such a boundary layer on the performance of the HARN, a duct of variable length (L_{duct}) and same cross-section as the nozzle inlet is added upstream of the nozzle. The uniform total pressure pressure is prescribed at the inlet of the duct, and a boundary layer can develop in this duct before it enters the high aspect ratio nozzle.

Figure B-6 shows the gross thrust coefficient based on the pressure losses across the nozzle only (dashed) and based on the pressure losses across the duct and the nozzle (solid) as a function of the duct length. As the duct length is increased, two different behaviors in nozzle performance can be

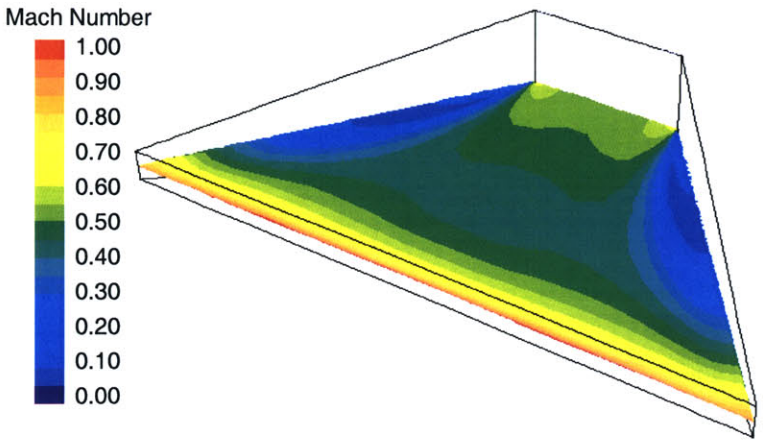

Figure B-4: Contours of Mach number showing the separation and recirculation region.

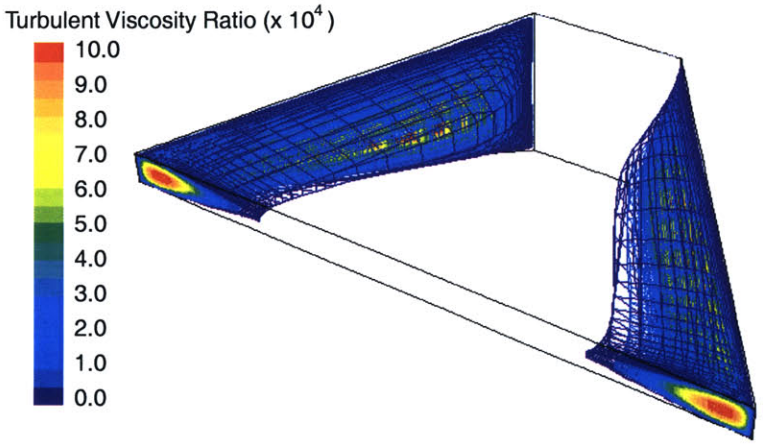

Figure B-5: Contours of high viscosity ratio showing the separation and recirculation region.

distinguished:

- For high-performance nozzles ($C_{fg} > 0.95$), the skin friction in the duct and the ingestion of the boundary layer by the HARN yield a total drop in gross thrust coefficient of approximately 0.4%. This drop in gross thrust coefficient is of the order of the accuracy of the computations. Therefore, it is considered that these high-performance nozzles are almost insensitive to the inlet conditions.

- For low-performance nozzles ($0.75 < C_{fg} < 0.9$), the addition of a duct section yields a 2% increase in gross thrust coefficient due to a decrease in the strength of the flow separation. The flow field visualizations in Figures B-7 and B-8 show the impact of the upstream duct on the strength of the separation and the size of the recirculation region. Without the duct, the boundary conditions at the nozzle inlet impose a velocity normal to the nozzle inlet plane

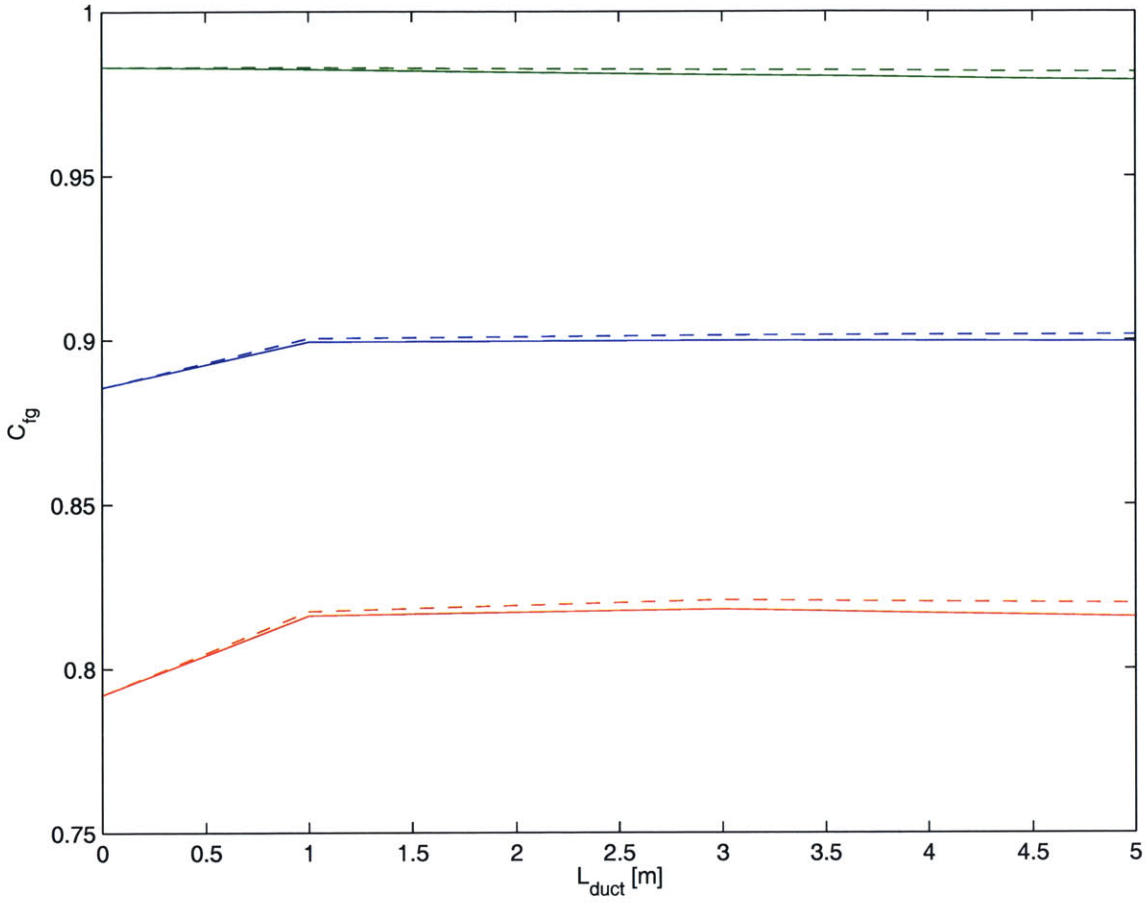

Figure B-6: Gross thrust coefficient as a function of duct length for HARN geometries corresponding to $C_{fg} \approx 0.98$ in green, $C_{fg} \approx 0.89$ in blue, and $C_{fg} \approx 0.79$ in red. Dashed lines show the thrust coefficient of the nozzle only. Solid lines show the thrust coefficient including losses in the duct.

such that separation in the initial diverging section of the nozzle is stimulated. The upstream duct allows the flow to more closely follow the nozzle walls as it enters this diverging section, which mitigates flow separation. This situation is more representative of the conditions in a real engine. Thus, it is considered that the predicted nozzle performance coefficients are underestimated by approximately 2% for nozzles with $C_{fg} < 0.9$.

Conclusions on the Accuracy of the Results

Finally, the prediction of the nozzle performance is altered by two major sources of error:

- In the case of a large Reynolds number computation with strong flow separation, the turbulent viscosity reaches the upper limit allowed by the flow solver in the regions of recirculation. As a result, the nozzle gross thrust coefficient is underestimated by approximately 0.5%.

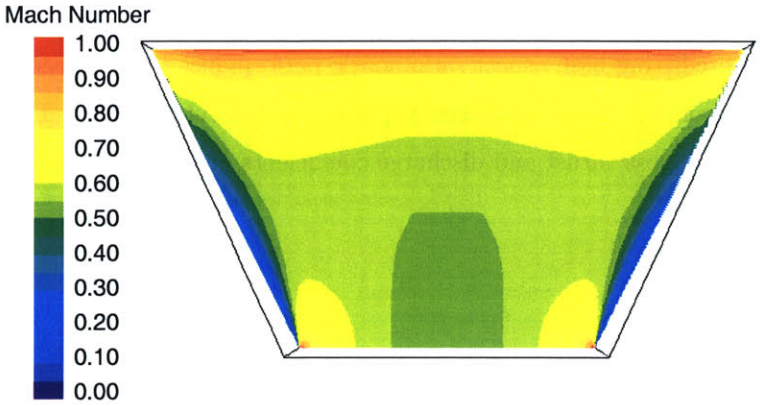

Figure B-7: Contours of Mach number, $L_{duct} = 0$

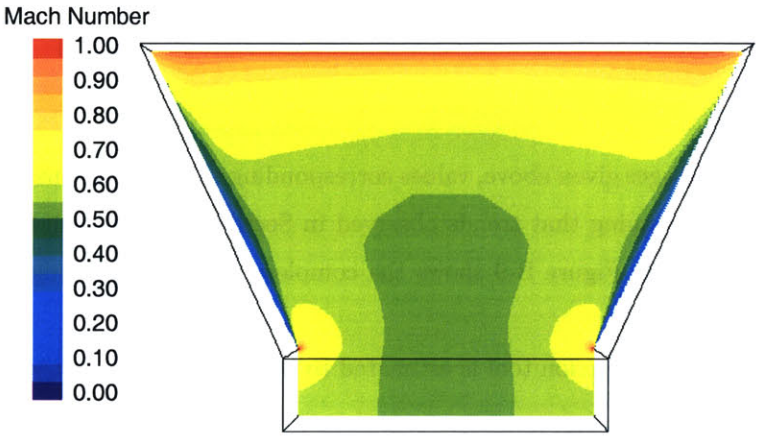

Figure B-8: Contours of Mach number, $L_{duct} = 1$ m

- For nozzle geometries yielding $C_{fg} > 0.9$, the gross thrust coefficient is almost insensitive to upstream boundary conditions, and the ingestion of a boundary layer entails a reduction in C_{fg} of less than 0.5%. However, for nozzles geometries yielding $0.75 < C_{fg} < 0.9$, the normal velocity prescribed at the nozzle inlet artificially stimulates flow separation, such that both discharge and gross thrust coefficients are underestimated by approximately 2%.

Finally, the accuracy of the nozzle performance computations is of the order of 1 to 2% in C_D and C_{fg} for high-performance nozzles (i.e. $C_{fg} > 0.9$) and of 3 to 4% for low-performance nozzles (i.e. $C_{fg} < 0.9$). This accuracy is acceptable since the purpose of this study is to understand the mechanisms driving the thrust losses in high aspect ratio nozzles, and to obtain a first estimate of the performance of the nozzle over a large range of nozzle geometries.

B.2.3 Prediction Tool for Thrust Losses in High Aspect Ratio Nozzles

A tool capable of predicting high aspect ratio nozzle performance is developed by interpolating the data set obtained from the parametric study presented in Section 3.6.3. This prediction tool is capable of computing gross thrust and discharge coefficients of high aspect ratio nozzles for:

- $1.3 < NPR < 2.8$
- $1 < L^* < 2$
- $1 < AR_1/AR_0 < 20$
- $1 < AR_0 < 10$
- $0.3\ \text{m}^2 < A_0 < 20\ \text{m}^2$
- $A_1/A_0 = 0.8$
- $T_{t0} = 346\ \text{K}$

In order to cover the ranges given above, values corresponding to computations that did not converge are extrapolated by assuming that trends observed in Section 3.6.3 are valid for these geometries and operating conditions. Figure B-9 shows the complete data set including extrapolated values, denoted by black circles.

The accuracy of the prediction tool is estimated to be: (in % of C_{fg} or C_D)

- $1\% - 2\%$ for low AR_1/AR_0
- $3\% - 5\%$ for high AR_1/AR_0, high AR_0, and $L^* = 2$ (long nozzles)
- $6\% - 10\%$ for high AR_1/AR_0, high AR_0, and $L^* = 1$ (short nozzles), and for extrapolated data

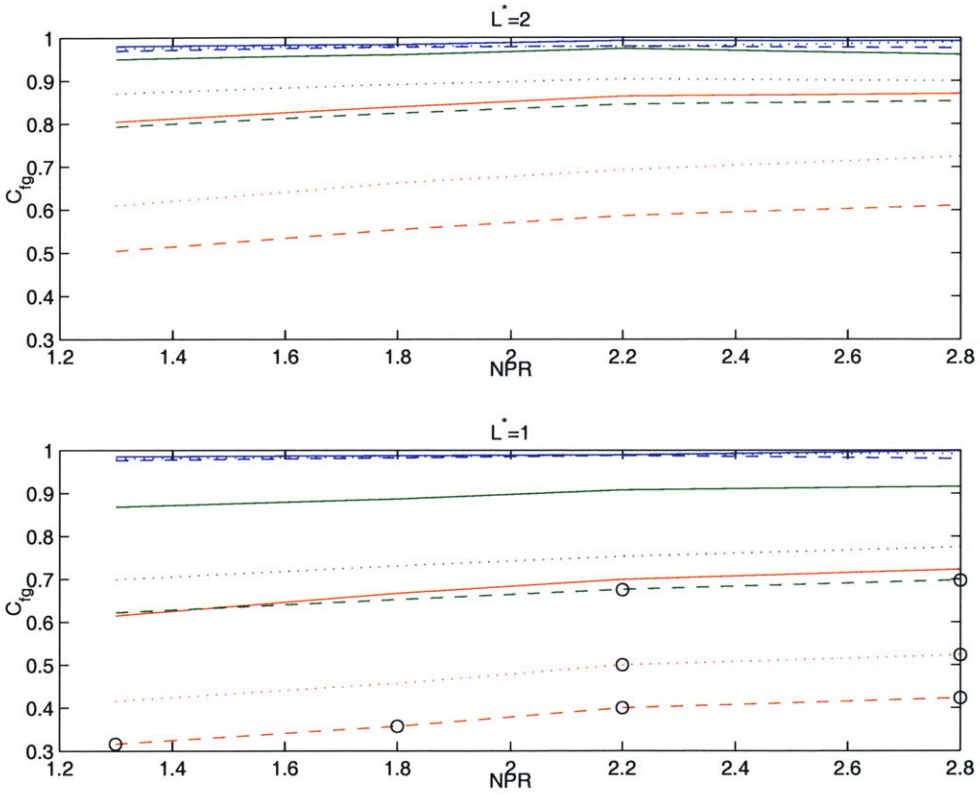

Figure B-9: C_{fg} as a function of NPR for $AR_0 = 1$, 5, and 10 in solid, dotted, and dashed lines, respectively and $AR_1/AR_0 = 1$, 5, and 20 in blue, green, and red, respectively. Black circles show the extrapolated values.

Bibliography

American Superconductor, 2003. "Ship Propulsion Motors and Generators." `www.amsuper.com/html/products/motorsGenerators/shipPropulsion.html`.

Antoine N., 2003. "Aircraft Optimization for Minimal Environmental Impact." `www.stanford.edu/~nantoine/lectures_files/PresentationSnecmaDec03.pdf`.

Antoine N. and Kroo I., 2002. "Aircraft Optimization for Minimal Environmental Impact." In *9th AIAA/ISSMO Symposium on Multidisciplinary Analysis and Optimization, Paper No. 2002-5667.*

Boiffier J., 2000. "Dynamique du Vol de l'Avion." Supaéro, Département Aéronefs - Notes de Cours.

Clark L. and Gerhold C., 1999. "Inlet Noise Reduction by Shielding for the Blended-Wing-Body Airplane." AIAA 1999-1937.

Coles W., 1957. "Full-Scale Investigation of Several Jet-Engine Noise-Reduction Nozzles." NACA TN 3974.

Coles W., 1959. "Jet-Engine Exhaust Noise from Slot Nozzles." NASA TN D-60.

Coller B., Noak B., Narayanan S., Banaszuk A., and Khibnik A., 2000. "Reduced-Basis Model for Active Separation Control in a Planar Diffuser Flow." In *Fluids 2000, Paper No. 2000-2562.*

Cumpsty N., 1989. *Compressor Aerodynamics.* Addison-Wesley Publishing Company.

Darmofal D., 2003. "Final Project Report for the Boeing Blended Wing Body Design Project." 16.100-Aerodynamics class project report prepared for Professor David Darmofal - MIT - Department of Aeronautics and Astronautics.

Drela M. and Youngren H., 1998. "A User's Guide to MISES 2.53." MIT Computational Aerospace Sciences Laboratory.

Erickson J., 2000. "Environmental Compatibility." FAA - William J. Hughes Technical Center - `home.hh.tc.faa.gov/presentations/jerickson.ppt`.

FAA, 2002. "FAA Noise Certification Data." www.aee.faa.gov/Noise/aee100_files/AC36-1H/nonuscert_appendix_02.xls%.

FAR Part 36, 1988. "FAR Part 36 - Noise Standards: Aircraft Type and Airworthiness Certification." www.airportnet.org/depts/regulatory/farparts/part36far3.html.

Flug Revue, 1998. "Pratt & Whitney Develops Geared Turbofan." www.flug-revue.rotor.com/FRheft/FRH9810/FR9810h.htm.

Flug Revue, 2002. "Engine Alliance GP7200 scores on A380." www.flug-revue.rotor.com/FRheft/FRH0210/FR0210d.htm.

Gaeta R. and Ahuja K., 2002. "Large Jet-Noise Reductions Through Distributed Nozzles." In *8th AIAA/CEAS Aeroacoustics Conference and Exhibit, Paper No. 2002-2456.*

Gliebe P., 2002. "Fan Broadband Self Noise Prediction Model." In *8th AIAA/CEAS Aeroacoustics Conference and Exhibit, Paper No. 2002-2490.*

Groeneweg J., Sofrin T., Rice E., and P.R. G., 1991. "Aeroacoustics of Flight Vehicles: Theory and Practice - Volume 1: Noise Sources - Chapter 3: Turbomachinery Noise." NASA Reference Publication 1258, Vol. 1 WRDC Technical Report 90-3052.

Gruschka H. and Schrecker G., 1972. "Aeroacoustic Characteristics of Jet Flap Type Exhausts." AIAA Paper No. 72-130.

Hanlon C., 2003. *Engine Design Implications for a Blended Wing-Body Aircraft with Boundary Layer Ingestion.* Master's thesis, Department of Aeronautics and Astronautics, MIT.

Heidmann M., 1975. "Interim Prediction Method for Fan and Compressor Source Noise." NASA TM X-71763.

Hough J. and Weir D., 1996. "Aircraft Noise Prediction Program (ANOPP) Fan Noise Prediction for Small Engines." NASA Contractor Report 198300.

Huff D., 2000. "Technology Development for Aircraft Noise Alleviation - Engine Noise Reduction Research." presented to The Hiller Aviation Museum - www.grc.nasa.gov/WWW/5900/5940/Research/2001Hiller.pdf.

Jane's Aero-Engines, 2003. *Jane's Aero-Engines.* Jane's Information Group.

Jane's All the World's Aircraft, 2003. *Jane's All the World's Aircraft.* Jane's Information Group.

Jaworski J., 2004. "Personal Communication."

Johnson R. (editor), 1998. *The Handbook of Fluid Dynamics.* CRC Press.

Kinzie K., Schein D., and Solomon W.J., 2001. "Measurements and Predictions for a Distributed Exhaust Nozzle." In *7th AIAA/CEAS Aeroacoustics Conference and Exhibit, Paper No. 2001-2236.*

Kinzie K., Schein D., and Solomon W.J., 2002. "Experiments and Analyses of Distributed Exhaust Nozzles." In *8th AIAA/CEAS Aeroacoustics Conference and Exhibit, Paper No. 2002-2555.*

Ko A., Schetz J., and Mason W., 2003. "Assessment of the Potential Advantages of Distributed-Propulsion for Aircraft." In *16th International Symposium on Air Breathing Engines, Paper No. 2003-1094.*

Koch C., 1981. "Stalling Pressure Rise Capability of Axial Flow Compressor Stages." *ASME J. of Engineering for Power*, vol. 103 pp. 645–656.

Kontos K., B.A. J., and Gliebe P., 1996. "Improved NASA-ANOPP Noise Prediction Computer Code for Advanced Subsonic Propulsion Systems - Volume 1: ANOPP Evaluation and Fan Noise Model Improvements." NASA Contractor Report 195480.

Kurzke J., 2001. "GasTurb 9 - User's Manual."

Liebeck R., Rawdon B., Scott P., Bird R., Hawley A., Page M., Girvin R., Potsdam M., Wakayama S., and Rowland G., 1996. "Configuration Control Document CCD-2, BWB Blended-Wing-Body, Prepared by McDonnel Douglas Aerospace." NASA Contract NAS1-20275.

Lighthill M., 1952. *On Sound Generated Aerodynamically. I. General Theory.* Proceedings of the Royal Society of London.

Maestrello L. and McDaid E., 1971. "Acoustic Characteristics of a High-Subsonic Jet." *AIAA Journal* pp. 1058–1065.

Mattingly J., 1996. *Elements of Gas Turbine Propulsion.* McGraw-Hill Book Company.

McCormick D., 2000. "Boundary Layer Separation Control with Directed Synthetic Jets." In *38th Aerospace Sciences Meeting and Exhibit, Paper No. 2000-0519.*

Munro S. and Ahuja K., 2003a. "Aeroacoustics of a High Aspect-Ratio Jet." In *9th AIAA/CEAS Aeroacoustics Conference and Exhibit, Paper No. 2003-3323.*

Munro S. and Ahuja K., 2003b. "Development of a Prediction Scheme for High Aspect-Ratio Jet Noise." In *9th AIAA/CEAS Aeroacoustics Conference and Exhibit, Paper No. 2003-3255.*

Munro S. and Ahuja K., 2003c. "Fluid Dynamics of a High Aspect-Ratio Jet." In *9th AIAA/CEAS Aeroacoustics Conference and Exhibit, Paper No. 2003-3129.*

Pilczer D., 2003. *Noise Reduction Assessments and Preliminary Design Implications for a Functionally-Silent Aircraft.* Master's thesis, Department of Aeronautics and Astronautics, MIT.

Stone J., 1974. "Interim Prediction Method for Jet Noise." NASA TM X-71618.

Stone J. and Montegani F., 1980. "An Improved Prediction Method for the Noise Generated in Flight by Circular Jets." NASA TM-81470.

Tam C. and Zaman K., 2000. "Subsonic Jet Noise from Non-Axisymmetric and Tabbed Nozzles." *AIAA Journal*, vol. 38 pp. 592–599.

Zorumski W., 1982. "Aircraft Noise Prediction Program - Theoretical Manual." NASA TM-83199 - Part 1 and 2.